WARSAW UNIVERSITY
OF TECHNOLOGY

Faculty of Mechatronics

UNIVERSITÈ
de FRANCHE-COMTÈ

Faculté des Sciences et des Techniques

Ph.D. THESIS
in “co-tutelle”

Katarzyna Krupa, M.Sc.

“Opto-numerical analysis of AlN piezoelectric thin film operating as an actuation layer in MEMS cantilevers”

Supervisors

Prof. Romuald JÓŹWICKI,
Prof. Christophe GORECKI,

Warsaw & Besançon, 2009

The research presented in this dissertation was supported by
European Network of Excellence in Microoptics (NEMO)
and grant no. N505 004 31/0670 of the Polish Ministry of Science and Higher Education.

To my family …

Acknowledgements

First of all, I would like to express my deepest gratitude to my supervisors Prof. Romuald Jóźwicki and Prof. Christophe Gorecki, for all their support, valuable advice and encouragement throughout my Ph.D. studies. I thank them for their understanding and patience during my research and writing this dissertation.

I would like to thank the Warsaw University of Technology and l'Université de Franche-Comté for enabling me to follow the Ph.D. work in the frame of "co-tutelle", which gave me the opportunity to gain the important experience during my long stay in the Départment d'Optique P.M. Duffieux of the FEMTO-ST at l'Université de Franche-Comté in Besançon.

I also would like to sincerely thank Dr Patrick Delobelle and Dr Laurent Hirsinger (Département LMARC of FEMTO-ST) and underline their significant contribution to the work presented in this dissertation. I thank them for their fruitful co-operation and valuable advice.

Special thanks go to Dr Michał Józwik (Department ZIF), who considerably helped me to accomplish this work with his valuable advice, discussions and suggestions on my research project. I would like to deeply thank him for his co-operation, support, assistance and comradeship. I am very grateful for taking his time for revision of my dissertation making it more complete and valuable.

I also would like to deeply thank Dr Alexandru Andrei (Département LOPMD of FEMTO-ST) for his agreeable co-operation, comradeship and especially for fabrication of the AlN driven microcantilevers becoming the objects of my Ph.D. studies.

I am very much obliged to all members of my dissertation committee for their critical reviews, as well as their insightful comments and valuable suggestions on my Ph.D. thesis.

Many thanks also go to the staff members and my Ph.D. student colleagues of the Départment d'Optique at the FEMTO-ST, the Department of Photonics Engineering and the Department of Applied Mechanics at the Institute of Micromechanics and Photonics. Thank you for your co-operation, advice, assistance, and also the excellent amicable atmosphere.

I would like to take this opportunity to also sincerely thank my family and my friends for their patience, faithful support and confidence in my ability to complete this work.

Finally, I thank all other people not mentioned, who contributed to creation of this dissertation.

Abstract

The goal of this Ph.D. thesis is the analysis and the determination of the properties of aluminium nitride (AlN) piezoelectric thin film operating as an actuation layer within bimorph microcantilevers and the evaluation of their micromechanical performances. The research described in this thesis was accomplished with the use of a hybrid methodology combining the optical interferometry, the techniques of nanoindentation, the numerical simulations as well as the analytical considerations meaning the association in which the interactions between the physical and mathematical models of the studied objects were investigated.

This research was performed within the framework of the “co-tutelle” Ph.D. thesis between l’Université de Franche-Comté and the Warsaw University of Technology. In France, this work was accomplished in the Département d’Optique P.M. Duffieux of the Institute FEMTO-ST. In Poland, the work was caried out by the Institute of Micromechanics and Photonics.

The present manuscript proposes the development of hybrid opto-numerical methodology to study the MEMS structures. This methodology allows a complex characterisation of samples by identifying and explaining the main sources of the discrepancies between their physical and mathematical models. This hybrid approach was applied to study the silicon microcantilevers actuated by a piezoelectric transducer containing a thin film of AlN sandwiched between two metal electrodes. The properties of AlN thin films as well as micromechanical behaviours and life time of the tested samples were determined. The physical model of these multilayer elements was created with a help of full field and non-contact Twyman-Green interferometry, offering high-resolution data. Thus, the data concerning static as well as dynamic performances, information on geometry as well as material and mechanical properties of the investigated microobjects were obtained. To complete this data, some reliability tests of the studied samples were realised. The mathematical models combining the analytical calculations and the Finite Element Method (FEM) calculations (ANSYS software) were performed taking into account the multilayer structure of mentioned elements. They allowed to understand better the functionality of the real microdevices with special emphasis on the identification of their mechanical failures. Moreover, the research focused also on some in-use problems dealing with both the ageing and fatigue accelerated life tests and the operational stability of the samples. Resulting data allowed a better knowledge about the most likely failure modes affecting the operation of the microobjects and the factors that invoke these failures. They led to determine the operational conditions and helped in analysis and evaluation of the AlN-driven microcantilever technology in order to improve their manufacturing process.

The proposed hybrid methodology has extended the metrological capability of the laser interferometry techniques. It has allowed to develop the methods serving to characterise microstructures, determine their reliability and support their technology in realisation of the reliable devices with required parameters. Implementation of the mentioned methodology within the framework of this Ph.D. thesis also allowed to obtain knowledge about the properties of the AlN thin films and the performances of the piezoelectric microcantilevers leading to increase a number of their applications with improve their quality and controllability.

Streszczenie

Celem rozprawy doktorskiej jest analiza i wyznaczenie właściwości piezoelektrycznej warstwy azotku glinu (AlN) w zastosowaniu do aktywnych mikrobelek jako piezoaktuatorów będących podstawowymi elementami składowymi urządzeń MEMS/MOEMS. Praca została wykonana z wykorzystaniem hybrydowej metody bazującej na interakcji fizycznego i matematycznego modelu badanego obiektu.

Doktorat był realizowany w systemie „co-tutelle" pomiędzy l'Université de Franche-Comté a Politechniką Warszawską. Badania i analizy zostały przeprowadzone w le Département d'Optique P.M. Duffieux Instytutu FEMTO-ST Uniwersytetu w Besançon oraz w Instytucie Mikromechaniki i Fotoniki Politechniki Warszawskiej.

W ramach pracy doktorskiej została opracowana hybrydowa, opto-numeryczna metoda do badania struktur w skali mikro. Pozwala ona na identyfikację głównych źródeł niezgodności pomiędzy teoretycznymi rozważaniami dotyczącymi testowanych mikroobiektów, a rzeczywistą ich realizacją, umożliwiając w ten sposób kompleksową analizę ich funkcjonowania. Hybrydowe podejście polega na współzależności wzajemnie uzupełniających się danych doświadczalnych uzyskanych metodami optycznymi i nanoindentacyjnymi z wynikami symulacji numerycznych oraz rozwiązań analitycznych. Podejście to zostało zastosowane do zbadania krzemowych mikrobelek aktywowanych piezoelektrycznie za pomocą cienkiej warstwy AlN naparowanej pomiędzy dwie metalowe elektrody. W pracy wyznaczono właściwości warstwy AlN, parametry działania wspomnianych mikroelementów i ich powtarzalność, a także stabilność i trwałość tych obiektów. Fizyczny model wielowarstwowych struktur będących przedmiotem badań został stworzony z wykorzystaniem polowych, bezkontaktowych oraz wysokoczułych optycznych metod pomiarowych zastosowanych w wielofunkcyjnej platformie bazującej na interferometrze Twyman-Green'a. System ten umożliwia szczegółową charakteryzację badanych mikroelementów dostarczając danych na temat ich statycznych i dynamicznych, a także geometrycznych, materiałowych oraz mechanicznych parametrów. Pozwolił on dodatkowo na przeprowadzenie testów niezawodnościowych wspomnianych obiektów poprzez monitorowanie i wyznaczanie zmian w ich właściwościach. Matematyczny model bazuje natomiast na rozważaniach analitycznych oraz Metodzie Elementów Skończonych (MES) i został opracowany z uwzględnieniem wielowarstwowości struktury badanych elementów. Numeryczne symulacje wytworzonych mikroaktuatorów wykonane w środowisku ANSYS pozwoliły na głębsze poznanie i zrozumienie funkcjonowania rzeczywistych mikrourządzeń oraz mechanizmów ich uszkodzeń poprzez identyfikację krytycznych obszarów uszkodzeń ich strukturze. Ponadto, w pracy przeprowadzona została także analiza niezawodności mikrobelek z warstwą piezoelektryczną. Skoncentrowano się na zagadnieniach wyznaczania niezawodności tych elementów już po ich wytworzeniu, a zatem w czasie ich eksploatacji. Wykonano jakościowe testy przyspieszone starzenia i zmęczenia oraz badania stabilności pracy powyższych mikroaktuatorów. Otrzymane wyniki pozwoliły na uzyskanie wiedzy na temat uszkodzeń możliwych do wystąpienia podczas działania testowanych urządzeń oraz czynników wywołujących te uszkodzenia. Umożliwiły one również określenie warunków pracy oraz oszacowanie czasu życia mikroobiektów. Ponadto, wykorzystując opto-numeryczne podejście do badań przeprowadzona została analiza i ocena technologii mikrobelek z warstwą AlN pod względem procesów ich wytwarzania oraz uzyskanych parametrów ich funkcjonowania umożliwiając optymalizację technologii tych struktur.

Zaproponowana hybrydowa metodyka pozwoliła na rozszerzenie możliwości metrologicznych technik interferometrii laserowej oraz na rozwój metod przeznaczonych do charakteryzowania mikrostruktur, wyznaczania ich niezawodności, a także wspomagania ich technologii, prowadząc do wytworzenia niezawodnych urządzeń o pożądanych właściwościach. Zastosowanie powyższej metodyki w ramach prezentowanej pracy doktorskiej wzbogaciło dotychczasową wiedzę na temat zachowania się materiału AlN w postaci cienkiej warstwy zastosowanej do mikrobelek. Uzyskano nowe możliwości poprawy jakości tych mikroelementów. Możliwe stało się też skuteczniejsze przewidywanie parametrów pracy rzeczywistych struktur pozwalające tym samym na zwiększenie liczby ich zastosowań.

Résumé

L'objectif de ce mémoire de thèse consiste à étudier et caractériser les propriétés de couche mince piézoélectrique de nitrure d'aluminium (AlN) utilisées comme une couche d'actionnement de micropoutres multimorphes actionnées piézoélectriquement et à évaluer leurs performances micromécaniques. Ce travail a été effectué en utilisant une méthodologie hybride basée sur l'interaction entre le modèle physique et mathématique des objets étudiés.

Ces recherches ont été faites dans le cadre d'une thèse de doctorat effectuée en cotutelle entre l'Université de Franche-Comté et l'Université Technologique de Varsovie. Les deux laboratoires qui ont porté ce projet sont le Département d'Optique P.M. Duffieux de l'Institut FEMTO-ST et l'Institut de Micromécanique et Photonique.

Une méthodologie hybride opto-numérique a été proposée pour étudier des microstructures. Cette méthodologie permet la caractérisation complèxe de ces échantillons en identifiant les divergences entre leur modèle physique et mathématique. Cette approche hybride, combinant les données expérimentales obtenues par l'interféromètrie optique et les techniques de nanoindentation avec les résultats de traitements numériques et les équations analytiques, a été appliquée pour étudier les micropoutres silicium où un film mince piézoélectrique d'AlN a été déposé entre les deux électrodes métalliques. Grâce à ces interractions, les propriétés de films AlN ainsi que les comportements micromécaniques de transducteurs piézoélectriques et leur fiabilité ont été déterminés. Nous avons bati un modèle physique de ces dispositifs multimorphes en utilisant la plateforme de métrologie basée sur l'interféromètre de Twyman-Green, offrant les avantages de mesure non-destructive et la haute résolution de techniques optiques. Ainsi, nous avons obtenu des données caractérisant les comportements statiques et dynamiques de micropoutres AlN, ainsi que les différentes propriétés physiques des éléments étudiés. Enfin, quelques mesures de fiabilité de nos microobjets ont permis l'évaluation de l'impact de certains paramètres géométriques et fonctionnels sur les comportements des échantillons et leur durée de vie. Le modèle mathématique proposé s'appuie à la fois sur l'utilisation d'équations analytiques et le calcul par la Méthode des Éléments Finis faisant appel au logiciel ANSYS. Ces calculs ont tenu compte de l'aspect multicouche des éléments étudiés. Ce travail de modélisation a permis d'identifier les paramètres critiques de ces microactionneurs piézoélectriques à la fois du point de vue dimensionel que matériau et de mieux comprendre leurs mécanismes de vieillisement. Par ailleurs, une étude de fiabilité a aussi été réalisée, en incluant des tests accélérés du vieillissement et de la fatigue, ainsi que une étude de la stabilité opérationnelle. Les résultats obtenus nous ont permis de mieux cerner quels sont les paramètres critiques de dommagement le plus probables de ces microobjets et estimer leur temps de vie. Enfin, l'approche opto-numérique proposée a permis d'identifier les étapes de fabrication critiques des micropoutres d'AlN afin d'optimiser leur fabrication.

La méthodologie hybride proposée au cours de la thèse de doctorat a étendu la capacité métrologique des techniques d'interférométrie laser. Elle permet de développer les méthodes pour la caractérisation des microstructures, la détermination de leur fiabilité et l'assistance de leur technologie dans la réalisation des dispositifs fiables des paramètres requis. L'application de cette méthodologie a permis de bien comprendre les propriétés de films d'AlN aussi bien que les performances des micropoutres piézoélectriques. Cela peut effectuer en une augmentation de nombre des applications possibles de ces microstructures d'AlN, en améliorant leur qualité et contrôle.

Table of contents

Introduction 11
Context and motivation of the research 11
Goal and scope of the thesis work 13
Thesis outline 15
1. From the overview of piezoelectric materials to the use of AlN thin films as an actuation material for MEMS 17
1.1. Overview of smart materials for MEMS actuators 17
1.2. Definition of parameters characterising piezoelectric materials 21
1.3. AlN among other MEMS piezoelectric materials 24
1.4. Properties of AlN thin films and their main applications 26
1.5. Impact of deposition parameters on quality of AlN thin films 28
1.6. Summary 32
2. Methodology of research work 33
2.1. Introduction to the methodology of hybrid analysis 33
2.2. Conceptual approach of analytical and numerical methods 34
2.3. Experimental set-up 35
2.3.1. Selection of metrological method 35
2.3.2. Experimental set-up 38
2.3.3. Completed metrology procedure 40
2.3.4. Measurement uncertainty determination 43
2.4. Implementation of hybrid methodology 47
2.5. Summary 49
3. AlN based microcantilevers – studied devices 50
3.1. Design 50
3.2. Principle of actuation 52
3.3. Analysis of fabrication technology 53
3.3.1. Identification of drawbacks of initial fabrication process 53
3.3.2. Critical analysis of the initial fabrication process and improvement proposals 60
3.3.3. Geometrical imperfections of final devices 64
3.4. Conclusions 65
4. Analytical and numerical analysis of AlN driven microcantilever 67
4.1. Analytical model based on tri-layer Si cantilever 67
4.2. Numerical model – FEM simulations 71
4.2.1. FEM simulations for homogeneous Si cantilever 72
4.2.2. FEM simulations for tri-layer Si cantilever 74
4.3. Conclusions 87
5. Material properties and electromechanical performances of AlN thin films incorporated in microcantilever actuators 89
5.1. Material behaviours – crystallographic and elastic properties 89
5.2. Static behaviours – shape and residual thin film stress 94
5.3. Dynamic behaviours – resonance frequency and transient mode shape 100
5.4. Electric behaviours – resistance 104
5.5. Piezoelectric behaviours and Joule effect 106
5.6. Thermal behaviours 110
5.7. Conclusions 112

6. Reliability study **114**
6.1. Introduction 114
6.2. Chosen problems of the reliability 118
6.3. Reliability study – results 119
6.3.1. Accelerated aging under electrical shock 120
6.3.2. Accelerated thermal aging 123
6.3.3. Accelerated aging under high humidity 127
6.3.4. Accelerated resonant fatigue under high voltage 131
6.4. Conclusions 135
Concluding remarks **137**
Novelty elements 138
Future research directions 140
Author's publications 141
Bibliography **142**
Appendix 1 .... **151**
Appendix 2 .... **154**
Appendix 3 .... **168**
Appendix 4 .... **173**

Introduction

Context and motivation of the research

In the 1960s it was observed that monolithic silicon showed excellent mechanical properties and could be used as a significant material for transducer and actuator construction. From this start microelectronics technologies were applied to manufacture simple, three-dimensional mechanical microscale structures in silicon, from which eventually developed complex micro-electro-mechanical (MEMS) or micro-opto-electro-mechanical (MOEMS) devices [Dziuban 2004, Józwik 2004 a]. Over the last decade, the significant progress in silicon technology has been fuelled by its advantages from scaling effect, i.e. miniaturization without loss of functionality: small size and low mass, fast response, cost-effectiveness because of batch fabrication possibility, increase of many important features like sensitivity, accuracy, efficiency, repeatability and reliability, etc. [Brown 1997, Wang 2000, Judy 2001, Samper 2003, Dziuban 2004, Banks 2006 a]. Nowadays, MEMS/MOEMS devices find a wide range of applications in automotive, telecommunications, electronics, photonics and also in biomedical, pharmaceutical, military market, etc. [Samper 2003, Ali 2004, Muratet 2006, Nexus, Yole]. One can expect that further development of microsystems will bring for these new generation devices a lot of new potential applications, replacing the bulky components with their micro counterparts.
However, to fabricate new type of microsystems with higher performances, it is necessary to overcome still existing limits in technology, design, etc., and improve the knowledge about used materials. World-tendency to mass-production of more perfect and smaller structures requires advanced research in materials engineering, MEMS reliability and metrology. The developing MEMS market makes the development of materials crucial, meeting the needs of this revolutionary Si-technology allowing to achieve demanded performances. However, it is very important also to determine the reliability of microsystems defined as a probability of performing certain functions within a set of pre-defined specifications for a given period in a required time [Wolf 2003 a, Berghmans 2006]. This is a significant issue, especially because of its fundamental influence on the competitiveness and on the successful commercialisation of microsystems technology. Manufacturers have to guarantee the correct operation of their products for a certain period of time. Therefore, it is essential to introduce into the market devices which are functional, reliable and safe [Kazinczi 2000, Wang 2000, Chang 2003, Moraja 2003, Muratet 2006]. This is especially crucial in applications involving human life, such as medical or automotive applications.
In the first years of microsystem growth, researchers were more interested in development of new fabrication technology than in microstructure metrology or investigation of their long-term stability and failure mechanisms [Miller 1999]. Nevertheless, in recent years, special attention has been given to studying the microsystem reliability and to developing the metrological techniques adapted to MEMS devices [Tanner 2000, Wolf 2003, Duong 2005, Sarihan 2006], what has been discussed in the numerous organised conferences. However, untill now, there has not been sufficient knowledge concerning the behaviour of these materials in the micro scale, which makes it necessary to examine the 'micro world'. Therefore, it is essential to investigate accelerated ageing or fatigue cycling and their influence on the materials and operation of the microsystems. Such studies could allow us to predict a life-time and possible to appear failure modes of the tested microstructures, leading to the improvement of their reliability and performance controllability by incorporating this information into the future development and fabrication of these microsystems.

As was previously mentioned, the key issue is to develop new materials meeting the requirements of microsystem technology and allowing for the fabrication of new and more demanding devices. One of the most important MEMS components are actuators, and especially those piezoelectrically driven, for which the choice of the active thin layer is crucial. The motivation of this Ph.D. thesis concerns then the study of piezoelectric material such as the thin film of aluminium nitride (AlN), used for MEMS/MOEMS systems. Here, it will be demonstrated that AlN is a very interesting material for microdevice applications. Aluminium nitride has a great number of advantages [Dubois 1999, Olivares 2005, Sanz-Hervás 2006, Vergara 2006] which favour its among other piezoelectric materials (i.e. PZT, ZnO, $LiNbO_3$, etc.). It exhibits good electrical and mechanical properties with an excellent chemical and thermal stability. Its high ultrasonic velocity and high electromechanical coupling coefficient associated with good piezoelectric properties cause that AlN is till now frequently used in surface acoustic wave devices (SAW) [Palacios 2002, Clement 2004]. However, for fabrication of bulk MEMS microctuators, PZT sol-gel films are more commonly applied because of their higher piezoelectric coefficient and the possibility of thick layer deposition. Nevertheless, even thought AlN does not exhibit the best piezoelectric properties, it still represents very interesting alternative for actuation purpose, mainly because of its excellent compatibility with standard silicon processes and low deposition temperature [Cattan 1999, Walter 2002, Clement 2004, Iborra 2004, Pantojas 2005, Sanz-Hervás 2006].
The primary advances in development of AlN active devices were focused on the appropriate choice of the best deposition methods. The objective was to create AlN thin film with controlled crystal orientation exhibiting good piezoelectric properties. In particular, during recent several years, a strong research effort was being made to deposit aluminium nitride films onto silicon by sputtering [Boeshore 2006] due to the advantages of this technological process [Clement 2004, Iborra 2004, Vergara 2006].
However, because of scaling effect arising from miniaturisation and fabrication based on the building of multilayer structures, the properties of aluminium nitride and then functionality of AlN-based transducers strongly depend on the technology. This dependency is precisely not crucial at the macro scale where the gravitational forces prevail, while at micro scale the surface forces are of great significance. Since, the microstructure of MEMS devices differs from that of bulk ones, the material parameters of thin films and their macroscale counterparts are quite different. In particular, Young's modulus of thin film material is lower than its bulky counterpart [Small, 1992, Brown 1997, Kazinczi 2000, Józwik 2004 a, Muratet 2006, Trimmer 2006]. It is difficult to simulate and then fabricate microobjects with required operational characteristics making crucial investigations of material properties at microscale. Since microsystem performances are strongly dependent on their mechanical design and materials used in their manufacturing [Sanz-Hervás 2006, Osten 2007, Kacperski 2008]. Scaling effect causes that in modelling, design and testing of MEMS, we cannot then use the same criteria like in macroscale. Moreover, experience and intuition acquired in macro designing are mostly useless. These result in poor characterisation of microscale objects and materials including AlN thin films, which microscale behaviours are still not well known [Palacios 2002] especially because we cannot apply our knowledge about "macro world" directly to its "micro" counterpart. Microelements require absolutely different approach in material engineering, design and technology [Brown 1997, Judy 2001]. All of these make that it is difficult to control the performances of microsystems, also those based on AlN and to maintain the high reproducibility of these devices through the entire wafer. Besides, interfaces interactions of multiple materials incorporated in thin films of multilayer structures, being particular components of MEMS systems, make a difficult, non-conventional situation requiring to use for its investigation a hybrid methodology combining experiments, theoretical calculations and numerical simulations [Duong 2005, Kujawińska 2005 b]. Because of using

thin film materials in combination with new structural designs, the performances of the microelements and their stability during entire life cycle of these devices, cannot be easily predicted and determined only by performing theoretical considerations, computational simulations or measurements. The new MEMS/MOEMS systems and their components characterised by high volume integration of differently combined variety of materials require to study interactions between the experimental and numerical solutions in order to obtain advanced functions. The knowledge gained in this way allows us to understand better the operation of these devices including structures based on the AlN material and also explain certain, hard in interpretation effects. It enables to optimise the technological process of these structures and achieve their required parameters and functionality by identifying the main source of behaviour discrepancy between the physical and numerical model of tested elements. Precise knowledge about technical characteristics of microstructures and properties of materials in microscale (in our case properties of AlN thin film) is necessary for further applications and can help the designer to improve quality, possibility to control, reliability and stability of fabricated objects.
Aluminium nitride thin film behaviour studies, consisting in interaction analysis of a physical and numerical model of structures, have not been still largely addressed. There are only a few known researches dealing with this task [Olivares 2005], but the scope of the presented subject area is not sufficient. It is necessary then to perform more complex and deeper studies, which are crucial for future microsystem market.

Goal and scope of the thesis work

The goal of this Ph.D. thesis is the analysis and the determination of the properties of piezoelectric aluminium nitride (AlN) thin film operating as an actuation layer within piezoelectrically driven bimorph microcantilevers and the evaluation of their micromechanical performances using a hybrid methodology basing on the interaction between the physical and mathematical models of investigated objects.

Realisation of this purpose required the implementation of the following tasks:

- developing the hybrid experimental-numerical research methodology and the procedures for determining the AlN thin film behaviours as well as the performances and the operational stability of the piezocantilevers;
- developing the procedures of aging and fatigue accelerated tests which allow to estimate the life-time and the quality of the investigated microcantilevers;
- developing of the analytical model of the investigated elements taking into account their multilayer structure;
- performing the FEM simulations of the AlN driven cantilevers, taking into considerations the environmental conditions and the experimental data as boundary conditions;
- performing the measurements aiming to determine the mechanical, piezoelectric, thermal, electrical, crystallographic and elastic properties for series of the microcobjects;
- carrying out chosen quality accelerated reliability tests allowing to estimate the device life-time as well as identify probable failure modes and understand their mechanisms;
- performing of the complex characterisation of the AlN thin film and the microcantilevers piezoelectrically actuated basing on the data obtained from the proposed hybrid methodology. The analyses of the technology will be included and their various geometrical dimensions of the investigated devices will be considered.

These tasks were realised by applying developed hybrid methodology of the research consisting in combination of the physical and computational models of the tested microobjects. Experimental data was obtained using the optical methods implemented in the Twyman-Green interferometer, allowing the measurement of static (shape, initial deflection, out-of-plane displacement, etc.) and dynamic (resonance frequencies, amplitude and phase distribution of vibrations, etc.) parameters, as well as the nanoindentation technique. Whereas, numerical data was received by performing the simulations using the ANSYS software based on the Finite Element Method (FEM). Analytical model applying the non approximated equations taking into account multiple film stacking of the investigated elements, was also developed. It allowed to extract the mechanical and material parameters, i.e.: residual stress σ, Young's modulus E, piezoelectric d_{31} and the thermal expansion coefficient α, etc.

Device performances and material behaviours depend on many factors such as geometry of elements, material components used in the multilayer structures, fabrication processes and their sequences. Therefore, it is difficult to develop general research methodology and studies for every microstructure. It concerns operating conditions and element applications, as well. Such a situation causes a large area of research work. Therefore, it is necessary to impose certain limitations concerning to the objects under test, the scope of the Ph.D. thesis work and the research techniques used in it.

Several authors have used cantilever microbeams or micromembranes as testing samples to study of thin film properties and reliability of materials [Sałbut 2005 b, Sharpe 2006]. These objects are often applied also as elements serving to prove correctness of proposed technology, measurement methods or device functionality [Kacperski 2008]. Moreover, these structures are used to model the behaviours of piezoelectric sensors and actuators. Most of microsystems contain mechanical elements in a form of cantilevers [Chang 1999, Kujawińska 2002, Dziuban 2004]. Therefore, regarding to the object tested in this thesis study, it was focused on the silicon microcantilevers with piezoelectric transducer containing the AlN thin film (see Chapter 3).

In the experimental part of work the multifunctional interferometric platform based on the Twyman-Green interferometer was used, providing the static and dynamic parameters of testing sample and indirectly their geometric, material and mechanical features basing on developed mathematical calculations (see Chapter 2).

Finally, the scope of performed studies investigated some simple aspects of the reliability, i.e. the ageing and fatigue quality accelerated life tests.

Obtained results and conclusions related to the study of the AlN thin films were exploited to optimise the technological process of piezocantilever leading to improve the design and the quality of fabrication process.

Thus, created data base, including parameters characterising AlN used in microcantilevers design, can be an information source for hybrid analyses, as well as for modelling and manufacturing of various piezoelectric actuators.

Thesis outline

The Ph.D. thesis consists of six chapters and two additional parts, which concern the introduction and the conclusions:

- Introduction - brief introduction, goal and scope of the doctor work;
- Chapter 1 - short overview of various types of smart materials used in MEMS actuators. The definitions of parameters characterising piezoelectric materials were shown focusing on the piezoelectric effect. The overview of piezoelectric materials applying in MEMS devices that emphasises the advantages of AlN and its main applications were presented. In the second part of this chapter the influence of sputtering process and microcantilever design on morphology, piezoelectric response and residual stress of the AlN thin film was discussed. The crystal structure corresponding to the piezoelectric behaviours was described, as well. In particular, the structure orientation, defects and impurities were considered. Finally, the influence of annealing process was shown;
- Chapter 2 – opto-numerical research methodology developed for characterisation of AlN piezoelectric thin film applied in the microcantilevers. Firstly, the hybrid analysis was presented. It consists in a study of the multilevel interactions between the mathematical model based on the analytical and numerical methods, and the physical model created by the experimental investigations of the real objects. The idea of the computational modelling techniques focusing on the Finite Element Methods (FEM) was discussed. Next, the metrology method implemented in the proposed experimental set-up was briefly presented with justification. The interferometric techniques (i.e. classical two-beam interferometry, time-average interferometry and stroboscopic interferometry) and the Temporal Phase Shift Algorithm (TPS) with 5 interferograms were considered. Finally, the analysis of performed measurement uncertainty was presented;
- Chapter 3 - detailed description of the investigated objects applied to the AlN thin film study containing their design and the principle of actuation. In the second section, the analysis of the microcantilever fabrication process was presented. Critical remarks and technology improvement were discussed. Experimentally noticed performance and technological imperfections were considered;
- Chapter 4 - analytical and numerical models of the AlN driven microcantilevers taking into account their multiple film structure. Performed in the ANSYS software the FEM simulations of device properties and their functionality were shown. The effect of the thin films on the object performances was discussed basing on the comparison between the results for the tri-layer structure and for the homogeneous one. The influence of the geometry and material parameters was analysed. Experimentally obtained geometrical imperfections of the fabricated device were considered and noticed performance discrepancies were explained;
- Chapter 5 – characterisation results of the AlN driven microcantilevers basing on the hybrid methodology implementation. The material properties and the electromechanical performances of the tested objects were presented. Namely, their optically measured static and dynamic parameters as well as calculated using these quantities the mechanical, piezoelectric and thermal behaviours were shown. Their deviations over entire wafer were analysed and the performance technological reproducibility was evaluated. The geometrical deviations of the cantilever length, silicon substrate thickness and thin film thicknesses were taking into account. The influence of the bottom electrode, AlN deposition conditions and this piezoelectric film thickness on the residual stress, the crystallographic, elastic and piezoelectric properties was described. The influence of environmental and electrical conditions focused on temperature and resistance effects was presented, as well. It allowed to determine the performance stability of the devices during

their operation in the standard weather conditions. The functionality analysis of the fabricated AlN thin film used in dedicated for MEMS actuator microcantilevers was then discussed and compared with the design values;

- Chapter 6 - general introduction to the reliability study and oriented on the dissertation problems the qualitative accelerated reliability tests. The resonant fatigue tests stimulated by high voltage as well as the ageing tests generated independently by electrical shock, high temperature and high humidity were considered. The procedures and the results were presented in detail. The operational stability, the durability (i.e. life time) as well as the probable damages, failures and behaviour changes were discussed including the explanations of the noticed effects;
- Concluding remarks - work summary, conclusions, novelty elements of the Ph.D. thesis and possible directions of the future research.

In addition to the main part, this Ph.D dissertation contains 4 appendices. In the Appendix 1 definitions of the most significant parameters usually determined to characterise piezoelectric materials were presented focusing on useful background for the late study of the AlN piezoelectric microcantilevers. However, because our experimental work focuses on the determination of piezoelectric coefficient this parameter was explained in the Chapter 1 of the main part of this Ph.D thesis. In the Appendix 2 the short overview of technological processes applied for manufacturing of the AlN-driven microcantilevers was presented to better understand the functionality of these devices. Moreover, the micromechanical properties of silicon as a substrate for the investigated cantilever fabrication were described to facilitate understanding of the used technological processes. While, in the Appendix 3 the analytical description of the techniques used in the proposed optical metrology was discussed. In particular, the two-beam interferometry with the use of time-average and stroboscopic methods and the application of the 5-frame Temporal Phase Shift Algorithm were shortly presented. Finally, in the Appendix 4 the analytical relations concerning the mechanical behaviours of homogeneous Si cantilever were shown.

Chapter 1

From the overview of piezoelectric materials to the use of AlN thin films as an actuation material for MEMS

This doctoral work covers piezoelectric materials and their applications in microactuators. Consequently, after short introduction to the various types of smart materials used in MEMS actuators this Chapter will be focused on the fundamental definitions of piezoelectricity, as well as the basics on the piezoelectric materials applied in the microdevices. In particular, the advantages and the applications of the AlN thin film will be presented. Since, the properties of thin films strongly depend on fabrication process, the influence of that process on the material and mechanical behaviours will be described in the second part of this Chapter. In particular, the effect of structure design and sputtering parameters, as well as the influence of annealing process will be presented. This discussion will be focused on the piezoelectric properties, residual stresses and morphology of the AlN film structure.

1.1. Overview of smart materials for MEMS actuators

The smart materials are materials that can significantly change their properties in a predictable or controllable manner in response to external loads. In particular, the smart materials used in MEMS actuators are the following:

1. Electrostrictive materials: they are all dielectrics that mechanically strain proportionally to the square of the applied electric field. However, unlike piezoelectric effect, electrostriction cannot be reversed meaning that mechanical deformation does not induce the electric field and the reversal of the electric field does not reverse the direction of the deformation. The reason is that the electrostrictive materials are not poled [Judy 2001, Dogheche 2005, Wiki];
2. Piezoelectric materials: they are some crystals, such as existing in nature quartz, which deform with the application of the electrical voltage. The direct piezoelectric effect is that these materials, when subjected to mechanical stress, generate the electric charge proportional to that stress. The converse one is also valid meaning that the same materials become strained when applying the electric field, and this strain again is proportional to the applied field. The first demonstration of the direct piezoelectric effect was given in 1880 by Curie brothers, but it was not fully used until the 1920s when first quartz sonar was proposed by Langevin [Argillon, Efunda, Matint, Piezomaterials]. Many crystalline materials exhibit the piezoelectric behaviour. However, a few of them show this phenomenon strong enough to be used in particular applications that take the advantageous of their properties. Nowadays, they have become very popular in passive and active control applications in both sensors and actuators. Thus, the piezoelectric materials can be divided in two main groups: crystals and ceramics, where those with perovskite structure are the most important. In addition, polymers revealing the piezoelectric effect have been developed recently [Azom, Efunda, Matint, Piezomaterials];
3. Magnetostrictive materials: they are ferromagnetic materials that change their shapes and lengths when subjected to the electromagnetic field, and inversely they can generate

the electromagnetic fields when they are deformed by the external force. The magnetostrictive materials can thus be used for both sensing and actuation purposes [Gilberstone 1996, Gahide 2001, Hodge 2001, Wiki];

4. Materials for magnetic actuators: they are magnetic materials incorporated in magnetic microactuators, which follow conventional macroscopic designs integrating ferromagnetic cores, rotors and cooper coils around cores. Such microactuators operate on the base of magnetic effect which determines remote interactions between components made from the magnetic materials [Gilberstone 1996, Judy 2001, Zheng 2004].
5. Materials for electrostatic actuators: these materials play a relatively small role because the electrostatic actuator contains movable part (usually in silicon) of the MEMS and metal electrode electrically isolated. The voltage applied to the electrode generates electrostatic forces causing displacement of these movable part [Wu 2003, Zheng 2004];
6. Shape memory alloys (SMA): they are materials that "remember" their shapes, and can be returned to those shapes after being deformed by applying thermal field [Gilbertson 1996, Gahide 2001, Hodge 2001, Judy 2001, Zheng 2004];
7. Materials for thermal actuators: they are usually two materials considerably differing in thermal properties, which are integrated in thermal microactuators. Because, such microactuators are commonly either of the "bimetallic" or bimorph type, or they rely on the expansion of liquid or gas. Their moving part (usually beam or membrane) is usually machined from one material (e.g. silicon) and a layer of material with a different thermal expansion coefficient (e.g. aluminium). When these two materials are heated, one of them expands faster than the other and this moving part bends. Heating can be accomplished by passing a current through the device heating it electrically [Gilberstone 1996, Judy 2001, Zheng 2004].

All of these smart materials allow to fabricate microactuators, which the most important properties vs. their actuation mechanisms are listed in the Table 1.1. From performed comparison, it can be seen that piezoelectric actuators (and thus piezoelectric materials) seem to be advantageous for MEMS applications because of the following features:

- good operational repeatability;
- operation with large forces and high speed response;
- high operational efficiency;
- voltage supply – fast and easy control, more efficient in relation to current supply;
- possibility of static and vibration actuation;
- lack of dust, radiation and temperature harmfulness.

Table 1.1: Comparison of various microactuators [Gilberstone 1996, Gahide 2001, Hodge 2001, Judy 2001, Wu 2003, Zheng 2004, Józwik 2004 a, Gambin 2005]

Actuator type	**Voltage**	**Supply**	**Response speed**	**Force**	**Compatibility**	**Repeatability**	**Temperature sensitivity**	**Efficiency**
Piezoelectric	±	Voltage	+	+	±	+	+	+
Magnetostrictive	±	External	±	+	±	+	+	±
Magnetic	–	Current	+	+	±	+	+	+
Electrostatic	–	Voltage	+	±	+	+	+	+
Thermal	+	Current	–	+	+	–	–	+

In practice, the electrostatic actuators are the most common and well-developed in the MEMS applications, easily fabricated by batch techniques of the IC-compatible micromachining technology [Thielicke 2000, Judy 2001, Zheng 2004]. They are suitable to perform positioning tasks, which can be completed within a chip. Other types of actuators may be more robust, may offer larger forces or larger displacements, but they ask more specialised processing and are not easily integrated with the microsystem technology due to material incompatibility [Gilbertson 1996, Wu 2003, Judy 2001, Józwik 2004 a, Zheng 2004, Gambin 2005]. The thermal actuators require, for example, relatively large electrical energy, and heat generated during their operation has to be dissipated. Also, the magnetic devices generally need relatively high currents and high energy. Therefore, here we focus our attention on the electrostatic and piezoelectric microactuators, considering that the use of the electrostatic microactuators is most suitable for positioning applications while the piezoelectric microdevices are appropriate for both the actuator and sensor applications. Moreover, the technology and the new material development lead to the improvement of the device performances, and in particular the actuator performances. It relates the AlN-based actuators, proposed here, whose one of the main advantages justifying the interest in the subject of the present doctoral work, is their easy fabrication by use of batch techniques of the IC-compatible micromachining technology (see section 1.3 and Chapter 5).

Piezoelectric actuators

A piezoelectric actuation arises from the effect of the dimensional changes (i.e. deformations), which are generated in certain crystalline materials when they are subjected to the electric field. The piezoelectric microactuators can be based on bulk piezoelectric materials such as zirconate titanate (PZT), quartz (SiO_2) or lithium niobate ($LiNbO_3$), and polymers such as polyvinyledene fluoride (PVDF) [Gilbertson 1996, Wu 2003, Zheng 2004], as well as on relatively new arrivals, which are thin film piezoelectric materials. The use of piezoelectric thin films (PZT, ZnO, AlN) for microactuation has certain advantages including the ability to use surface and bulk micromachining to fabricate complex mechanical structures that provide stable motion control at moderate voltage levels (in general above 100 V for displacements of few micrometers). Additional advantages are to have features such as large force generation over small displacements [Judy 2001, Wu 2003, Gambin 2005], high frequency responses, and compatibility with silicon electronics. These characteristics are used for example in medicine, in surgical applications (e.g. a smart force-feedback knife and an ultrasonic cutting tools) [Judy 2001, Józwik 2004 a]. Moreover, the other advantages of the piezoelectric devices are that they respond very quickly to changes in voltages with great repeatability [Gilbertson 1996, Thielicke 2000]. They operate with high force and speed, and return to a neutral position when unpowered. Alternating electric currents produce oscillation in the piezomaterial, and operation at the sample fundamental resonant frequency provides the largest elongation and the highest power efficiency [Gilbertson 1996]. When the voltage is applied, the expansion and contraction of the piezoelectric device is converted to up and down movements of the vibrating part [Zheng 2004]. Sometimes, the disadvantage of piezoelectric actuators is usually high (a few or tens of voltage), geometry-dependent supply voltage, which limits these structure operation with other IC devices [Wu 2003, Gambin 2005]. However, there are other relatively new materials which are currently developed that allow lower voltage, and also show other advantages and improve existing parameters (i.e. AlN) (see Chapter 5 and 6). In addition, the piezoelectric devices are insensitive to electromagnetic fields, radiation and temperature what enable them to work under harsh conditions. However the disadvantages include a more complex fabrication of the piezoelectrically driven elements (sometimes poling step is necessary for e.g. ferroelectric PZT) [Wu 2003].

Very interesting type of the piezoelectric microactuators are mechanical structures such as cantilevers, bridges or membranes, with deposited thin film piezoelectric transducer. They form voltage – control manipulators, which assist at positioning microelements or micropumps and microvalves in the case of membrane [Gilbertson 1996, Zheng 2004]. Other applications concern e.g. Scanning Tunnelling Electron Microscopes intended to rapidly move sensing tip over a very small range or ultrasonic transducers, digital watch beepers, and some small audio speakers [Gilbertson 1996].

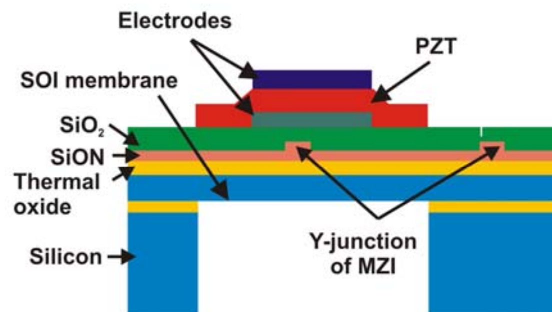

Fig.1.1: Schematic of membrane-based read out

Since the piezoelectric materials are appropriate also for sensor applications, one example of such devices is presented in the Fig.1.1 showing the membrane-based optomechanical sensor [Gorecki 2005 b]. This device consists of a thin PZT transducer integrated on a top of cladding layer of a Mach-Zenhder Interferometer (MZI). The piezoelectric layer of this transducer, sandwiched between the metal electrodes, is located in the center of 5-µm thick SOI (i.e. silicon-on-insulator) membrane. In the structure of MZI a waveguide channel is defined, which forms both arms of MZI. The sensing arm of MZI is placed on the membrane acting as the interrogation system. The other arm, the reference branch, is positioned outside the membrane. The membrane size is 1350 x 1350 μm^2. The total insertion loss of this demonstrator is about 12 dB. The coupling from optical fiber to waveguide is based on the etching of the waveguide substrate with the manufacturing of U-grooves, supporting fibers in the same substrate as the waveguide substrate. The packaged version of this demonstrator is shown in the Fig.1.2.

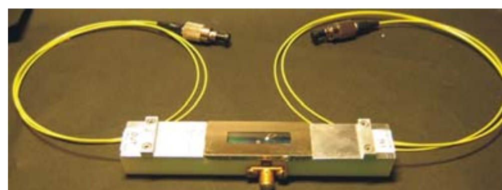

Fig.1.2: Packed version of membrane-based demonstrator

Laser beam that propagates through the MZI is used to interrogate the changes piezoelectrically induced because a portion of the optical waveguide is deformed. So, the MZI output signal contains the required information about the optical path change of the sensing arm produced by the membrane deformations accompanied by the local modifications of the waveguide refractive index, what permits the extraction of information about the effective mechanical performances of the membrane.

1.2. Definitions of parameters characterising piezoelectric materials

The piezoelectric materials can generate an electric potential in response to an applied mechanical stress (direct piezoelectric effect) and can produce the mechanical stress when subjected to the electrical field (converse piezoelectric effect). The main feature of the piezoelectric materials is energy transduction. One of most significant parameters characterising the efficiency of the piezoelectric material is the piezoelectric coefficient *d*. The experimental work will focus on the determination of piezoelectric coefficients and the evaluation of deformation-voltage characteristics. Therefore, only the piezoelectric parameters *d* will be explained in this section. The other important properties [Matint] including quality factor Q_m, coupling coefficient k^2, dissipation factor $tan\sigma$, hysteresis parameters, as well as dielectric relative constant ε_r and acoustic wave velocity v_s will be briefly presented in the Appendix 1 giving a useful background for the late study of the AlN piezoelectric microcantilevers.

Theoretical description of piezo-mechanism

Piezoelectricity consists in occurring reversible relation between dielectric polarisation and mechanical stress. There is a direct piezoelectric effect and a converse piezoelectric effect, both generally linear because of the proportionality between the electric field and the mechanical stress.

The crystalline piezoelectric material contains atoms that share electron density in some manner, e.g. ionic and covalent bonds. Because of this sharing, the electron density is not uniform throughout the crystal and there are separated positive and negative electrical charges forming periodic electric dipoles that reflect the periodic atomic arrangement of the crystal. In most crystals, the atoms are symmetrically distributed, so that the crystal overall is electrically neutral because the sum of the individual dipoles between all of the atoms is zero. Although, ferroelectric crystal has a nonzero dipole sum at equilibrium state. When the mechanical stress is applied, the generated strain creates small changes in the bond length between the atoms, resulting in a shift in the positions or directions of the individual dipoles. However, in many crystals, the sum of the dipoles still remains zero because of their centro symmetric structure even under the applied stress. Therefore, the piezoelectric effect appears only in particular crystals with ordered, non-centro symmetric atomic structure. It means that the mentioned symmetry is disturbed by the stress, resulting in the formation of a non zero dipole sum and a manifestation of piezoelectric effect. The converse effect is also observable and the applied electric field creates the strain in the piezoelectric material [Boeshore 2006, Pwr].

The piezoelectric effect can be expressed using equations describing the electric and structural behaviours of material. The components of the electric displacement field vector D_i are defined as

$$D_i = \varepsilon_0 \varepsilon_{ij} E_j \,, \tag{1.1}$$

where ε_{ij} are the elements of the relative permittivity tensor, ε_0 is a permittivity of a free space and E_j are the components of the applied electric field vector.

Similarly, Hooke's law for the elements of the mechanical strain tensor S_{ij} are

$$S_{ij} = s_{ijkl} \sigma_{kl} \,, \tag{1.2}$$

where s_{ijkl} are the elements of the elastic compliance tensor (defined as a inverse of stiffness tensor *c*, $s = c^{-1}$) and σ_{kl} are the elements of the stress tensor.

These equations can be combined into two, linear, so-called coupled constituent equations, which describe the relations between electrical and mechanical variables:

$$D_i = d_{ijk}\sigma_{jk} + \varepsilon_0 \varepsilon_{ij}^{\sigma} E_j$$ - for direct piezoelectric effect; (1.3a)

$$S_{ij} = s_{ijkl}^{E}\sigma_{kl} + d_{kij}E_k$$ - for converse piezoelectric effect. (1.4a)

And their strain – charge form is:

$$\{D\} = [d]\{\sigma\} + [\varepsilon^{\sigma}]\{E\}$$ - for direct piezoelectric effect; (1.3b)

$$\{S\} = [s^{E}]\{\sigma\} + [d^{t}]\{E\}$$ - for converse piezoelectric effect, (1.4b)

where d_{ijk} are the components of the piezoelectric (strain) coefficient tensor determining the piezoelectric properties of the material, the superscript E indicates a zero or constant electric field, and the superscript σ indicates a zero or constant stress field, and the superscript t stands for transposition of a tensor [Boeshore 2006, Wiki].
To understand better the piezoelectric effect described by the above equations, the Fig.1.3 shows the physical sense of the stress tensor components σ_{jk}, the values of which depend on the magnitude and direction of the external forces, which are apply to the particular surface of the crystal element. The first subscript informs about the direction of the mechanical stress and the second defines the axis direction perpendicular to the loaded crystal side-wall.

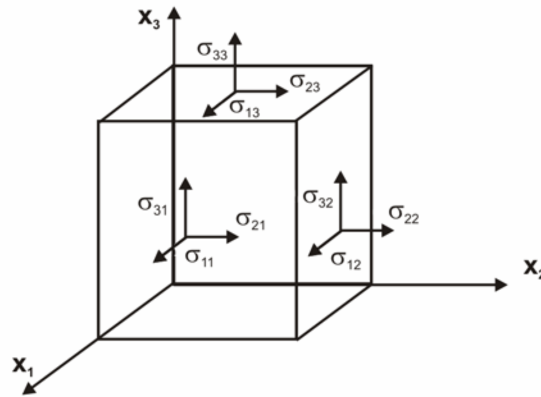

Fig.1.3: Physical sense of components of mechanical stress tensor

The components: σ_{11}, σ_{22}, σ_{33} denote then the normal stress, and others – the share stress. The shape of the piezoelectric coefficient matrix depends on the crystal system and the class of the piezoelectric material. For AlN the hexagonal crystal system with class of 6mm is valid [Pwr]. The strain-charge form of these coupled equations could be then written as:

$$\begin{bmatrix} D_1 \\ D_2 \\ D_3 \end{bmatrix} = \begin{bmatrix} 0 & 0 & 0 & 0 & d_{15} & 0 \\ 0 & 0 & 0 & d_{24} & 0 & 0 \\ d_{31} & d_{32} & d_{33} & 0 & 0 & 0 \end{bmatrix} \begin{bmatrix} \sigma_1 \\ \sigma_2 \\ \sigma_3 \\ \sigma_4 \\ \sigma_5 \\ \sigma_6 \end{bmatrix} + \begin{bmatrix} \varepsilon_{11} & 0 & 0 \\ 0 & \varepsilon_{22} & 0 \\ 0 & 0 & \varepsilon_{33} \end{bmatrix} \begin{bmatrix} E_1 \\ E_2 \\ E_3 \end{bmatrix}; \quad (1.5)$$

$$\begin{bmatrix} S_1 \\ S_2 \\ S_3 \\ S_4 \\ S_5 \\ S_6 \end{bmatrix} = \begin{bmatrix} s_{11}^E & s_{12}^E & s_{13}^E & 0 & 0 & 0 \\ s_{21}^E & s_{22}^E & s_{23}^E & 0 & 0 & 0 \\ s_{31}^E & s_{32}^E & s_{33}^E & 0 & 0 & 0 \\ 0 & 0 & 0 & s_{44}^E & 0 & 0 \\ 0 & 0 & 0 & 0 & s_{55}^E & 0 \\ 0 & 0 & 0 & 0 & 0 & s_{66}^E = 2\left(s_{11}^E - s_{22}^E\right) \end{bmatrix} \begin{bmatrix} \sigma_1 \\ \sigma_2 \\ \sigma_3 \\ \sigma_4 \\ \sigma_5 \\ \sigma_6 \end{bmatrix} + \begin{bmatrix} 0 & 0 & d_{31} \\ 0 & 0 & d_{32} \\ 0 & 0 & d_{33} \\ 0 & d_{24} & 0 \\ d_{15} & 0 & 0 \\ 0 & 0 & 0 \end{bmatrix} \begin{bmatrix} E_1 \\ E_2 \\ E_3 \end{bmatrix}. \quad (1.6)$$

Considering the notation, generally D and E are vectors – Cartesian tensor of rank 1. Permittivity ε is Cartesian tensor of rank 2. Strain S and stress σ are, in principle, also tensors of rank 2, because they represent symmetric tensors, their orders could be reduced by applying a multi linear algebra. There are a few different conventions for this idea depending on the field of application, which differ according to the weight attached to the selected entries of the tensor. In the Voight notation e.g. the re-labelling of the subscript is as following: 11→ 1, 22 → 2, 33 → 3, 23 → 4, 13 → 5, 12 → 6, while the Mandel notation uses 12 → 4, 23 → 5, 13 → 6. That is the reason why S and σ appear to be a vector of 6 components instead of 9. Consequently, s appears to be a 6 by 6 matrix instead of a rank 4 tensor, and piezoelectric constant d to be a 6 by 3 matrix instead of a rank 3 tensor. Hence, for example s_{1122} becomes s_{12}. In the AlN material which is the subject of this research, because of its crystal symmetry, the 18 – element matrix of d_{ijk} components is also reduced to

$$\begin{bmatrix} d_{11} & d_{12} & d_{13} & d_{14} & d_{15} & d_{16} \\ d_{21} & d_{22} & d_{23} & d_{24} & d_{25} & d_{26} \\ d_{31} & d_{32} & d_{33} & d_{34} & d_{35} & d_{36} \end{bmatrix} \to \begin{bmatrix} 0 & 0 & 0 & 0 & d_{15} & 0 \\ 0 & 0 & 0 & d_{24} & 0 & 0 \\ d_{31} & d_{32} & d_{33} & 0 & 0 & 0 \end{bmatrix} \to \begin{bmatrix} 0 & 0 & 0 & 0 & d_{15} & 0 \\ 0 & 0 & 0 & d_{15} & 0 & 0 \\ d_{31} & d_{31} & d_{33} & 0 & 0 & 0 \end{bmatrix}, \quad (1.7)$$

where $d_{32} = d_{31}$, $d_{24} = d_{15}$. In the doctoral research, the case of the converse piezoelectric effect is considered. Thus, the piezoelectric coefficients d_{ik} describe relations between the electric field applied in i – direction and the induced mechanical stress causing deformations specified by k subscript [Boeshore 2006, Pwr, Wiki]. In the wurtzite crystal structures representing by AlN material, the components d_{31} and d_{33} are in the following relation [Guy 1999]:

$$d_{31} = -\frac{1}{2} d_{33} \,. \quad (1.8)$$

Therefore, three kind of piezoelectric effects depending on the relations between applied voltage and stress induced could be distinguished: longitudinal, lateral and skew piezoelectric effect. The first two effects appear when the direction of electric field and stress perpendicularly applied to the crystal wall are respectively the parallel and the perpendicular. Whereas, the skew effect appears when the applied stress is parallel to the loaded crystal plane. These three piezoelectric effects correspond to the d_{33}, d_{31} (=d_{32}) and d_{15} (=d_{24}) of

the AlN piezoelectric coefficients, respectively and are illustrated in the Fig.1.4 [Guy 1999, Pwr]. Among these parameters, d_{31} and d_{33} are the most often determining for characterising the usable properties of the materials. In this research the case of d_{31} coefficient is taken into account and investigated as a result of the particular structure of the samples tested in this thesis work, and is described in the Chapter 3. Therefore, an explanation of the physical significance of these piezoelectric parameters only on the base of d_{31} component seems to be sufficient. The piezoelectric constant of d_{31} couples then the 3 – axis (<001>) or *c* – axis with the 1 – axis (<100>) (see Fig.1.5, section 1.4). Since, in the performed research the converse piezoelectric effect was studied, the electric field applied in 3 – direction results in the stress induced along 1 – axis and inversely, the voltage impressed in 1 – axis produces the stress along 3-axis. So, d_{31} is this piezoelectric coefficient that in particular, defines the operation of the cantilevers investigated in this work. Moreover, when piezoelectric coefficient exhibits a positive value, it means that, the piezoelectric material expands when a positive voltage is applied to it [Dubois 2001, Boeshore 2006]. Conversely, it contracts when d_{ik} is negative.

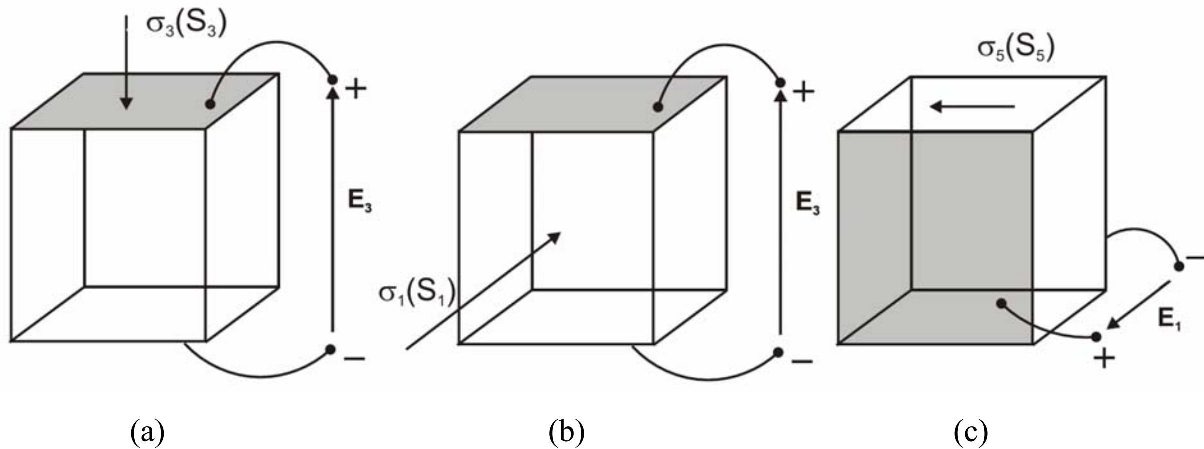

(a) (b) (c)

Fig.1.4: Three kind of piezoelectric effect: longitudinal (a), lateral (b) and skew (c)

1.3. AlN among other MEMS piezoelectric materials

There is a number of piezoelectric material types. However, a lot of them reveal too weak properties to be used in piezoelectric applications. The others reveal strong piezoelectric behaviours with piezoelectric coefficient exceeding that of AlN, sometimes even by order of magnitude. Although, many of them are not suitable for piezoelectric micro device fabrication, because of their incompatibility with the technological processes or specialised growth conditions [Muralt 2005, Bosseboeuf 2007, Efunda]. There are still some materials which are relatively compatible with the micro processing. Due to their relevant properties, they are used in a variety of applications as a piezoelectric film, especially in many acoustic wave devices, like for example acoustic and mechanical resonators, miniature high frequency (> 1 GHz) bypass filters for wireless communication market and also various kind of sensors, MEMS actuators, etc. [Choujaa 1995, Laurent 2000, Ruffieux 2000, Kim 2002, Clement 2004]. Four of them, the most frequently used require therefore a special attention. They are certain ceramics like lead zirconate titanium PZT, lithium niobate ($LiNbO_3$), zinc oxide (ZnO) and tested in this thesis aluminium nitride (AlN) [Choujaa 1995, Chang 1999, Dubois 1999, Palacios 2002, Clement 2004, Efunda]. Their properties, significant from their piezoelectric applications point of view, are presented in the Table 1.2.

Table 1.2: Material properties of four common piezoelectrics used for most piezoelectric MEMS applications [Carlotti 1995, Dubois 1999, Guy 1999, Palacios 2002, Dogheche 2005, Boeshore 2006, BPiezo, Edge, Matint, Roditi]

	AlN	**ZnO**	**PZT** **Pb(Zr, Ti)O₃**	**LiNbO₃**
Density ρ (kg/m^3)	3300	5610	757	4647
Young's modulus $E_{<002>}$ (*GPa*)	332	20	68	293
Thermal conductivity κ ($W/cm°C$)	1.75	0.6	0.018	0.056
Thermal expansion α ($1/°C$)	$\alpha = 4.3 \times 10^{-6}$	$\alpha = 6.5 \times 10^{-6}$	$\alpha = 2 \times 10^{-6}$	$\alpha = 15.0 \times 10^{-6}$
Band gap E_g (*eV*)	6.2	3.4	2.67	4.0
Resistivity r (Ωcm)	1×10^{11}	1×10^{7}	1×10^{9}	1×10^{10}
Acoustic velocity v_s (m/s)	10127	570	3900	3980
Electromechanical coupling coefficient k^2	0.25	0.3	0.57 hard PZT 0.61 soft PZT	5.5
Piezoelectric coefficient d_{31} (pm/V)	-2.0 (see Table 5.5, section 5.5)	-5.0	-120 hard PZT -175 soft PZT	-7.4
Relative dielectric constant ε_r	4.6	4.5	1300 hard 1760 soft	29

Among these piezoelectric materials, in particular, AlN has drawn researchers' strong attention turning out to be a powerful material, because of its great number of favoured advantages [Dubois 1999, Xu 2001, Palacios 2002, Iborra 2004, Sanz-Hervás 2006]. However, for being fully used it still demands an intense investigation in both the technology and the property domain. It results from facts, that until now they are not precisely known, especially in too small mature MEMS actuator applications. That is why, AlN has attracted a great interest, having potentially a big future in piezoelectrically driven MEMS market [Yole]. Aluminium Nitride is considered as the most preferred material for acoustic applications that allows to obtain due to its wide band gap E_g the high sound velocity v_s [Ishikara 1998, Kusaka 2000, Sanz-Hervás 2006]. This parameter and the high mechanical quality factor Q_m are also one of the demanded properties for fabrication filters of high frequency and wide band, respectively [Xu 2001, Auger 2004]. For both mentioned applications, the electromechanical coupling factor k^2 is the most limiting AlN property, which determines the bandwidth of the filter [Muralt 2005]. Other described materials i.e. PZT, $LiNbO_3$, ZnO, which belong to the ferroelectrics (high ε), exhibit much larger coupling coefficient k^2 (see Table 1.2), however they have not achieved high enough quality factor Q_m. Moreover, their acoustic velocities v_s are lower than that of AlN, which represent serious drawbacks in order to obtain band-pass filters with central frequencies higher than 1GHz [Xu 2001, Palacios 2002, Muralt 2005]. Nevertheless, as far as the piezoelectric properties are concerned, which are important for the microsystem applications, AlN exhibits lower piezoelectric coefficients d_{ik} than any other considered materials. It shows worse piezoelectric behaviours, particularly in comparison with PZT ferroelectric ceramic, which

because of that, has mostly been used for actuation purposes in MEMS devices [Walter 2002]. However, AlN is an excellent material for IC integration. It is, much more compatible with conventional Si manufacturing technology than other thin films. This is conditioned by its thermal stability, chemical compositions and possibility to achieve much lower film deposition temperature (<250°C at required temperature <500°C) [Dubois 2001, Clement 2004, Iborra 2004, Pantojas 2005, Sanz-Hervás 2006, Vergara 2006,]. This advantage, while including not the best, but still very good piezoelectric properties [Clement 2004, Sanz-Hervás 2006] and low dielectric permittivity ε, nearly 100 times lower than for PZT, is the principal benefit of AlN used in the piezoelectric MEMS fabrication, which makes this material a very good alternative for PZT sol-gel [Dubois 1999, Andrei 2008]. Regarding to the technological process, PZT, ZnO and $LiNbO_3$, on the contrary, have an isolating character which impedes monolithic integration with microelectronics [Palacios 2002]. In addition, AlN shows parameters which are difficult to achieve for any other piezoelectric materials. It can withstand much larger voltages without breaking-down, and exhibits much lower leakage currents and high electrical resistance. Therefore, as a wide band-gap material, the Aluminium Nitride thin films can be expected to be competitive in sensor, actuator, and acoustic applications where low dielectric loss, low thermal drift, and high signal-to-noise ratios are required [Dubois 1999, Xu 2001, Muralt 2005, Pantojas 2005, Andrei 2008]. AlN has attracted great interest also because of its high thermal conductivity and high resistance to temperature even within an hostile environment. This material shows low, almost negligible thermal expansion coefficient with opposite value to that of Si, what allows to achieve good temperature compensation with good thermal stability [Dubois 1999, Laurent 2000, Palacios 2002, Auger 2004, Choujaa 2005]. The AlN thin film has also several other advantages in comparison with zinc oxide (ZnO) and lead zironate titanate (PZT). Apart of its already mentioned excellent compatibility with standard MEMS processing techniques, it is very selective to many wet chemical and dry plasma etches, but can be readily etched in chlorine environment. Its chemical stability, very high hardness and melting point ensure that AlN thin layers do not degrade during processing [Dubois 1999, Iborra 2004]. Besides, AlN thin films with excellent crystallinity and orientation can be reproducibly deposited or grown on many different substrates and films, including dielectrics, semiconductors, and metals. Another advantage of AlN is that this material as a non ferroelectric, does not require poling for revealing piezoelectric phenomenon [Palacios 2002, Andrei 2008]. Moreover, both AlN and ZnO semiconductors are non toxic materials on the contrary to PZT ceramic containing lead compounds harmful for environment and health. They can be used then in bio-applications. Important research directions in the field of the piezoelectric materials comprise development of lead free materials exhibiting as good properties as PZT [Kaszuwara 2004, Matint].

1.4. Properties of AlN thin films and their main applications

The AlN is a III-V semiconductor compound crystallised in an hexagonal wurtzite structure. However, AlN can take a cubic rocksalt form induced by very high pressure (< 14 GPa). Moreover, in spite of the fact that this material is generally reported to be non-polymorphous, several authors report the occurrence of AlN metastable zinc blende polytype. The AlN wurtzite structure including crystallographic directions enclosed in angle brackets and crystallographic planes – in round brackets, is shown in the Fig.1.5. Here, the crystallographic notation using Miller indexes (*hkl*) is applied [Xu 2001, Madou 2002, Dziuban 2004]. Presented crystal structure has two lattice constant *c* and *a*, and consists of two interpenetrating hexagonal sublattices, each with one type of atoms, offset along *c*-axis by

5/8 of the cell height (5/8c). For the ideal wurtzite structure the c/a ratio is 1.633, but for the real AlN crystals this parameter takes slightly less value in the range of 1.600 ÷ 1.602 [Edgar 1994, Boeshore 2006]. Depending on the deposition process, the AlN thin film could have amorphous or crystalline form with mostly (002) or (100) preferential orientation [Ishihara 1998, Xu 2001]. These two plane orientation mean that *c*-axis of hexagonal AlN is perpendicular or parallel to the substrate, respectively (see Fig.1.5). Moreover, the (002) plane is composed of bonds with energy relatively smaller and easier to break than that of the (100) plane bonds [Xu 2001].

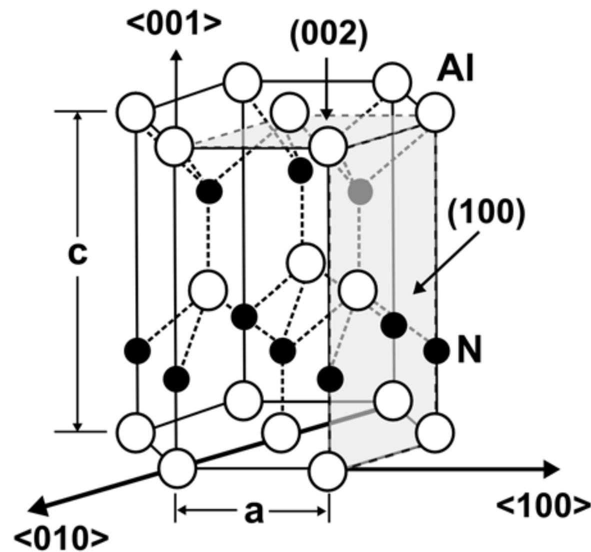

Fig.1.5: Hexagonal wurtzite crystal structure of AlN: crystallographic directions and planes indicated with Miller indexes and crystal unit cell [Edgar 1994, Xu 2001]

As previously mentioned, many of the AlN material properties are a result of its crystal structure. The close-packed lattice of III-V compound AlN results in its very high hardness, high elastic stiffness, high thermal conductivity (see Table 1.2, section 1.3) and excellent temperature stability. Moreover, low thermal expansion coefficient of AlN is well matched to the value for Si (111) substrate. All of these properties including also corrosion resistance cause that AlN is often used as a wear-resistant, anti-corrosive, protective coating as well as a radiator element. AlN is a chemically-resistant material, that can be etched by a number of wet and dry etching techniques especially using chlorine in gas, liquid and plasma phases [Palacios 2002, Auger 2004, Boeshore 2006].

The AlN is a wide band gap (6.2eV) material with electrical properties varying from semiconducting to insulating. This results in using AlN in a great number of photonic applications, i.e. as an active layer in a deep ultraviolet light-emitting diode or as a buffer layer for optical and electronic devices [Auger 2004, Boeshore 2006], etc. Moreover, as the wide band gap material (E_g = 6.2eV), AlN reveals high electrical resistivity r, high breakdown voltage (U_b > 800 kV/cm) and low dielectric losses (dissipation factor DF). Its high ultrasonic velocity v_s (see Table 1.2, section 1.3) makes it a very good candidate for high frequency (GHz) acoustic wave devices.

Finally, the AlN property that is important to take into consideration here is the relatively high piezoelectric coefficient d_{ik} of AlN [Iborra 2004], which strongly depends on the deposition technology influencing its preferred orientation (see section 1.5). To achieve a very good

piezoelectric activity, a perfect orientation of *c*-axis ((002) texture) is necessary [Iborra 2004, Sanz-Hervás 2006, Vergara 2006].

Main applications of AlN thin films

The AlN thin film has been used in a wide variety of piezoelectric applications, from the in-vitro biosensors, the pressure sensors to the actuators of precision components, capable of simulate locomotion [Boeshore 2006]. As a result of its piezoelectricity, AlN has been applied in acoustic wave devices. It concerns surface acoustic wave SAW devices [Palacios 2002, Clement 2004] and bulk acoustic wave BAW devices [Lakin 2001, Kim 2002]. The SAW applications are in a field of miniature high frequency bypass filters for wireless communication market, various chemical and physical (e.g. pressure, acceleration, gravimetric) sensors [Choujaa 1995, Laurent 2000] based on lamb-wave propagation over AlN/Si membranes, and acoustic actuators (e.g. Thin Film Bulk Acoustic Resonators TFBAR) [Choujaa 1995, Dubois 1999, Laurent 2000, Dubois 2001, Auger 2004, Clement 2004, Sanz-Hervás 2006, Vergara 2006]. Moreover, the AlN material can be used in MEMS [Ruffieux 2000, Dubois 2001, Vergara 2006] as an actuation film accordingly to this Ph.D. thesis goal. It can be then applied in various local probe microscopes, e.g. in scanning force microscopes or atomic force microscopes AFM. To improve the speed of scanning system of such microscopes, an array of scanning microcantilevers can be used [Cattan 1999].

1.5. Impact of deposition parameters on quality of AlN thin films

Since, the properties of thin films strongly depend on fabrication process, the influence of that process on the material and mechanical behaviours widely reported in the literature will be described in this section. In presented PhD thesis, there are tested the microcantilevers incorporating the AlN thin films deposited in two sputtering processes, which were realised by using different conditions. In addition, the investigated AlN structures have different design including different materials of electrodes and different thicknesses of the piezoelectric film. Therefore, the effect of certain sputtering parameters, as well as the influence of electrode nature and AlN film thickness will be discussed. Moreover, the piezoelectric properties of AlN thin films determined by the crystal structure orientation, as well as, the residual stress (see section 4.1) generated by the manufacturing process will be presented. They are the most important parameters that actuator layer should display when applying in microsystems [Iborra 2004] and one of the properties investigated in this doctoral work. Finally, because the other objective of our research is the reliability study and in particular the thermal aging, the influence of the annealing process will be discussed. Here, we will focus on the AlN thin films, which have thickness from 0.5 to 1 μm.

The influence of non-(002) preferred orientation of AlN thin film

To exhibit good piezoelectric properties thin films have to reveal a perfect (002)-oriented crystal structure and small value of full width at half maximum (FWHM) of rocking curve (rc) (for the concept of rc FWHM see Fig.5.1, section 5.1) [Sanz-Hervás 2006]. These properties decrease with increase of rc FWHM parameter. However, the AlN films with excellent (near epitaxial) crystal quality (high (002) peak of X-ray diffraction (XRD) spectrum and narrow rc FWHM of around 1º) can provide a negligible piezoelectric response. Inversely, the perfect (002)-oriented films with poor crystal quality (weak (002) XRD peak and wide rc FWHM of up to 20º) can still exhibit good piezoelectric coefficient [Sanz-Hervás 2006]. These behaviours are explained by a presence of other than (002)-oriented crystals in the structure of AlN films, what results in a presence of other than

(002) peaks in the XRD spectrum. Even very weak traces of non-(002) XRD are accompanied with a drastic deterioration of the AlN piezoelectric activity. Such peaks in the diffractive spectrum indicate the occurrence of some kind of defects in the thin film degrading the piezoelectric response. These defects can be related to the grains with opposite crystallographic polarities along the normal to the surface (or inversion domains), which significantly reduce the net piezoelectric field. In conclusion, the influence of crystallographic structure on the AlN piezoelectric properties is more critical than playing a secondary role rc FWHM [Iborra 2004].

The influence of sputtering parameters

The fabrication process strongly affects the properties of thin films. Therefore, many research works are focused on studying and developing the technology of microstructures. In particular, there were developed several methods to deposit high quality AlN films. There are chemical vapour deposition (CVD), molecular beam epitaxy (MBE), electron cyclotron resonance, and laser ablation deposition. However, most of these techniques require a substrate with a specific orientation (single crystal nature) and a high processing temperature (1000°C) to obtain the best crystal quality and texture in the deposited thin film [Ishihara 1998, Dubois 2001, Xu 2001, Madou 2002, Pantojas 2005, Banks 2006 c]. Microsystem applications for which piezoelectric thin films have to be grown on a polycrystalline surface (i.e. metal electrode film) with significantly lower temperature require a deposition temperature lower than 500°C to ensure compatibility with the standard IC technology. In this case deposition methods based on sputtering techniques have been developed. In particular, the pulsed reactive DC sputtering with plasma composed of an argon and nitrogen mixture in a presence of an aluminium target was applied to deposit the AlN thin films in the fabrication of the microcantilevers tested in this dissertation (see section 3.3). Sputtering techniques (see Appendix 2) were chosen because they can produce polycrystalline AlN films on many different substrates at a moderate temperature (200°C). They are well suited for MEMS applications also because they introduce other important advantages: low cost of process and possibility to adjust the material and mechanical characteristics to the thin film properties of the required microsystem applications: low residual stress and good piezoelectric behaviours [Ishihara 1998, Dubois 2001, Iborra 2004, Pantojas 2005, Boeshore 2006, Vergara 2006]. Moreover, according to the sputtering conditions, the resulting thin films may exhibit different crystal orientation from (002) to (100) and mixed texture (see section 1.5). However, not only deposition parameters but also design of manufactured microstructures including a nature of electrode and film thicknesses influence the obtained properties, what makes the fabrication of the AlN thin films a complex process. Nevertheless, there are some trends describing the impact of sputtering parameters on the material and mechanical behaviours of the AlN film. In particular, the effect of pressure p, target power P, substrate bias voltage V_s, and substrate temperature T on texture, piezoelectric properties and residual stress of the AlN thin film will be presented here. These parameters differentiate between the two sputtering processes (see section 3.3), which were used to deposit the AlN film during the fabrication of the investigated microcantilevers.
Thus, to grow thin films with the pure (002) preferred orientation, it is necessary to provide sufficient kinetic energy to the atoms absorbed on the growing film surface [Iborra 2004]. This energy is supplied through the bombardment of the growing surface with argon (Ar) gas ions. The deposition parameters have to be thus carefully controlled to change the bombardment energy in order to select the preferred orientation of the AlN films and then obtain optimal piezoelectric response. The energy required for forming (002)-oriented structure is greater than for growing (001)-plane. Thus, a lower sputtering pressure p allows to achieve the (002)-oriented AlN crystal structure with c-axis perpendicular to the substrate.

Inversely, a higher sputtering pressure p is beneficial for the growth of the (100)-oriented thin film, which c-axis is parallel to the substrate [Dubois 2001, Xu 2001, Iborra 2004]. Decrease of the pressure produces decrease of deposition rate and increase of directionality of sputtered atoms (Al and N) and growing of film favourable for the (002) preferred orientation [Pantojas 2005]. When the sputtering pressure p is increasing, AlN orientation is changing from purely (002), through mixed texture ((100), (101), (002) XRD peaks appear), until purely (100)-preferred orientation to finally becomes amorphous. The Al and N atoms interacting during the deposition process with sputtering gas, ions collide before reaching the substrate surface. Therefore at too high pressure, they do not have enough energy to form the crystalline structure at the substrate surface. When considering a target power P, to form the (002)-oriented crystal structure a grater value of this parameter is required than to form the (100)-texture of AlN. At higher power applied to the target, deposition rate increase causes increase of the preferred (002)-orientation. However, when the power is too high, part of the Al atoms sputtered from the target does not nitride being deposited directly on the substrate. This is because the deposition rate increases rapidly with the increase of the sputtering power, and the AlN thin film with a mixed preferred orientation and low piezoelectric properties is formed. Going to the substrate bias voltage V_s, for every gas pressure p there is a particular value of V_s above which the AlN thin films are perfectly (002)-oriented and exhibit good piezoelectric activity. This value increases with the pressure. However, with the further increase of V_s, the piezoelectric properties get worse even though the AlN retains the (002)-orientation because generated excessive ionic bombardment deteriorates the crystal quality of the AlN film [Ishihara 1998, Xu 2001, Iborra 2004]. Concluding presented data, the mechanisms for controlling this film growth to obtain the c-axis oriented AlN thin films are complex and complicated and they need careful investigation.

To obtain the optimum AlN material for certain MEMS structure, it is necessary to reach not only very good piezoelectric activity, but also desired amount (usually small) of residual stress σ. Considering the residual stress this is induced by the crystal surface defects appearing during the sputtering process through the ionic bombardment [Meng 1993, Iborra 2004, Martin 2004]. Discussing the influence of V_s, the residual stress σ changes from compressive values at high V_s to even tensile values at low V_s [Iborra 2004]. As V_s is increased, the ionic bombardment becomes more energetic, what produces a higher density of defects remaining inside the crystal lattice. Going to the pressure p, when this parameter decreases higher stress level is obtained due to the directionality of the ionic bombardment. At the low pressures the accelerated ions suffer fewer collisions than at the higher one reaching the AlN film surface at angles close normal to the surface (high directionality). Their interaction with the growing film and the generation of defect occur deeper and more efficiently. Therefore, it is necessary to choose appropriate value of the pressure to achieve the compromise between good piezoelectric properties and low stresses. Selected p parameter has to ensure the enough energetic ionic bombardment to allow the (002)-oriented material growth, but not so strong not to deteriorate the crystal quality and thus, not to reduce the piezoelectric response [Dubois 2001, Xu 2001, Iborra 2004]. Moreover, the residual stress is found to depend on the AlN thin film thickness. When the AlN crystal growth the interactions between dislocations at the atomic level combined with the anisotropy of the hexagonal structure of this crystal cause the evolution of the residual stress influencing on the stress final result. Therefore the residual stress changes from the highly compressive to highly tensile with increasing thickness of the AlN film. At low AlN thickness the very steep change is observed, being explained by large dislocation density at the beginning of nucleation [Martin 2004].

The AlN thin film orientation as a function of substrate temperature is discussed, as well. As the deposition temperature increases, the grain size and the crystal quality increases as

well as the degree of AlN crystal orientation. Usually the substrate temperature above 0.3 of the melting temperature is needed to cause substantial atomic rearrangement or alignment [Pantojas 2005].
The piezoelectric properties and the residual stress of the AlN thin films are also strongly influenced by the nature of electrode material. Here, the metallic thin film electrodes of cubic Pt and Al oriented along the <111> direction are considered according to the material used in the microcantilevers investigated in our work (see Chapter 3). Thus, as reported in the [Dubois 2001] the residual stress depends strongly on the growth conditions and its value can range from highly compressive to highly tensile. For the considered types of electrodes, the stress is primarily influenced by the deposition conditions rather than by their type of material. The films are certainly too thick to be affected by the lattice misfit between the AlN and the electrode material. Whereas, the piezoelectric properties are influenced by the columnar grains with antiparallel polarities, which can form during the early stages of the film growth. The presence of inversion domains decreases the piezoelectric behaviours. The largest piezoelectric response is obtained for the Pt electrode. It indicates that a large lattice mismatch (10.9% for Pt) is not an obstacle for formation the AlN film with high quality, but that a stable growth is required, what Pt ensures. The quality of the electrode surface is then thought to be responsible for the formation of the hexagonal structure of the AlN with (002) texture, significantly influencing its piezoelectric properties. However, the internal stress being very sensitive to the processing conditions is less dependent on the electrode material.

Influence of deposition time, deposition rate and AlN film thickness

The influence of various deposition times *t* (at a constant growth) rate on the preferred orientation of the AlN thin films is important to be discussed. As reported in [Dubois 2001, Auger 2004, Martin 2004] for short deposition times the film is formed by well oriented (i.e. textured) as well as by randomly ordered regions, while for long deposition times the texture is well developed. This difference can be caused by a different local growth rate of both textured and randomly oriented regions. The first of regions grow faster, at the expense of the randomly oriented ones. During the deposition process, the well oriented regions keep growing and spread, covering finally the randomly oriented regions. The film reaches then a homogeneous columnar texture. Under these conditions, the growth rate is similar at the whole growing surface. Thus, we can define the particular value of deposition time above which the AlN thin film show the (002)-preferred orientation and then very good piezoelectric activity (see section 1.4). Moreover, because the increase of the deposition time corresponds to the increase of the film thickness, the high piezoelectric coefficient is achieved for the thicker AlN film. However, the threshold value of the mentioned deposition time changes dependently on the AlN film growth rate (i.e. deposition conditions) shifting to the lower values for the higher rates. Therefore, the increase of the growth rate causes that better piezoelectric properties can be reached for the same AlN thickness.

Effect of thermal annealing

There are few works dealing with the reliability of structures driven by the AlN thin films. Some of them concern the influence of thermal annealing on the properties of the AlN devices, i.e. the similar problem, which is considered in this PhD thesis (see section 6.3.2). Therefore, some results related to the piezoelectric parameters and the residual stress will be here discussed. Thus, the presented data will concern the post-deposition rapid thermal annealing (RTA) process performed in N_2 atmosphere at 900°C, 1100°C and 1300°C during 90s, 60s and 30s, respectively. As reported in [Vergara 2006] the AlN polycrystalline films with mixed crystal structure are not significantly

affected by this annealing process. They do not undergo significant changes either in their morphological properties or in their piezoelectric response. However, in the films exhibiting *c*-axis preferred orientation, the annealing causes the improvement in their crystal quality, which is more evident for those with better (002)-orientation of their structure and at higher temperature. In that case, the RTA activates thecrystallisation process, i.e. an increase of the size of the original crystallite grain, a growth of the new small (002) textured grains, as well as a reduction (but not disappearing) of grains with orientations other than (002) and other defects. However, the new grains do not grow at the expense of the original ones, but they are the result of the crystallisation of amorphous material presented in the tested films. In addition, the re-growth of the original grains can also be attributed to the annihilation of some kind of defects. However, the enhancement of crystal quality of the films is not accompanied with a significant improvement of their piezoelectric response. Observed changes do not follow any particular trend. The dispersion in the piezoelectric activity is attributed to the presence of grains with opposite polarities (related to the influence of the substrate on the initial growth) producing poor piezoelectric activity, that cannot be rearranged through the thermal treatment. Additionally, the post-deposition thermal process can enhance some other AlN properties, such as the AlN residual stresses which are found to reduce.

1.6. Summary

According to this Chapter, the AlN thin film is very attractive material for applications in MEMS actuators, worth to be investigated and developed. However, the properties of the AlN thin films used in the microstructures strongly depend on the design and the fabrication processes. In particular, sputtering parameters, quality and nature of electrodes, as well as thickness of AlN film, which determines the piezoelectric properties and the residual stresses, are significant to be studied. Analysis of these parameters allowed a complex characterisation of the AlN-driven microcantilevers leading to the optimisation of their design and manufacturing processes in order to fabricate microactuators with better performances. The obtained results of the characterisation work will be presented in the Chapter 5 and of the optimisation work in the Chapter 3. Moreover, because the piezoelectric properties strongly depend on the morphology of thin film, the orientation of the AlN crystal structure was also taking into account during the investigations of the tested microobjects (see Chapter 5). According to this Chapter, the annealing process also influenced the performances of the structures based on the AlN thin film, and in particular the residual stresses. Thus, during the performed reliability studies the thermal ageing as well as the effect of ambient temperature changes were tested and the relevant results will be presented in the Chapters 5 and 6.

Chapter 2

Methodology of research work

In this chapter the methodology of the proposed opto-numerical technique will be discussed, aiming the characterisation of the AlN piezoelectric thin film applied in the microcantilevers. Thus, the hybrid analysis will be presented. It consists in a study of multilevel interactions between the mathematical and physical models. The modelling techniques will focus on the Finite Element Methods (FEM). The optical metrology method will be then briefly presented with their justification. Moreover, the analysis of the performed measurement uncertainty will be also discussed.

2.1. Introduction to the methodology of hybrid analysis

A combination of experimental data and modelling based on the advanced computer software (Finite Element Method FEM, Computer Aided Design CAD and Computer Aided Manufacturing CAM) has created an efficient tool to analyse, design and control the engineering structures. One of the mentioned tools concerns hybrid techniques, in which analytical and numerical methods with experimental ones are combined [Pryputniewicz 1982, Laerman 2002, Kujawińska 2005 b]. In some cases, the use of hybrid analyses is even crucial to be able to get knowledge about the behaviours of devices under investigation and evaluation of materials incorporated in their structures. It mainly concerns high-responsible objects or those, which are still not well characterised (i.e. without well proved design and modelling methods [Jüptner 1993]). The best example of the second ones are microsystems. The hybrid techniques are very often applied to study the properties of microobjects, where the fabrication is based on the combination of new materials [Poon 1993], includes new technological processes [Sałbut 1996], or request to study the reliability issues such as accelerated aging or fatigue [Kujawińska 1995].
In the field of MEMS and MOEMS there is a lack of knowledge concerning the impact of both material properties and mechanical performances of the microfabricated devices according to scaling laws in miniaturization. Microelements are different from their macro counterparts in smaller size, lower strength and they are much more dependent on surface forces. This makes more complicated the metrology procedures and promotes the use of hybrid techniques taking into account the interactions between the model and the experimental data. Geometric features, material parameters, boundary conditions etc. are usually taken from the existing data bases or the literature. Therefore, this input data is often approximated and even unavailable in case of thin film deposited in multilayer structures. Demanded methodology requires then an interaction between the results obtained on the base of two models of tested microstructure:

- physical material model being a result of design physical process based on experimental characterisation;
- mathematical model using geometrical parameters of physical model as its representation in the computer software environment created by analytical and numerical methods.

The techniques allowing to obtain these two models will be described in the next sections of this chapter. The analytical and numerical methods often give approximated results vitiated by errors. It results from the simplifying assumptions concerning for example the definition of

boundary conditions. It is true that the experimental methods introduce measurement errors too. In most cases of experimental techniques, the optical ones are used [Kujawińska 2005 b, Sarihan 2006]. However, they usually provide data about displacement or deformation fields determined on an external surface of the tested objects (available for light-beam), and do not give information about effects appearing inside these elements or their materials. To obtain more accurate and more reliable information about the microstructure behaviours, it is necessary to create the data base of modelling and experimental results and to find relations between them. The potentiality of this hybrid approach is to provide information about material parameters and to improve MEMS/MOEMS design as well as their operational behaviours. The hybrid methodology allows to identify the main sources of behaviour discrepancies between the physical and mathematical model. It results in a faithful description of the sample performances and an identification of the material defects. Thus, according [Kujawińska 2005 b] the discrepancy causes can come from the following reasons:

- differences between physical and numerical models;
- slightly different conditions of experiments (e.g. value of force or voltage, way of their application, etc.);
- errors of a numerical description of the effects occurring in a sample.

In the hybrid investigations, the applied numerical methods are often a first step of a micromechanical structure verification, allowing to select appropriate experimental methods, which serve for modification of the created theoretical models. The experiment data provide information about the values of real material constants, especially crucial in the case of the use not-well characterised materials in thin films. They determine the influence of the object microstructure [Józwik 2004 b, Kujawińska 1995] and the boundary conditions, as well. The accurate model of the real microstructure is then obtained. In order to understand the functionality of microobject with complicated mechanical design, the numerical simulations are often accomplished after its manufacturing. According [Kapkowski 1994, Kujawińska 2005 b], the techniques of hybrid methodology can be divided into three groups:

1. "basic hybrid technique", where experimental data are introduced into the constitutive equations making them possible to be solved;
2. "located hybrid technique", where experimental data are used as the boundary conditions in the mathematical model, allowing to solve problem of stress analysis in any area;
3. full hybrid technique realised when the analytical and numerical solutions and the experimental results interfere mutually by all stages of the performing analysis.

2.2. Conceptual approach of analytical and numerical methods

The most of engineering problems are solved by determining the fields of various quantities including displacement, stress, strain, temperature etc. [Zienkiewicz 1997, Józwik 2004 a]. Therefore, in order to describe them mathematically, an infinitesimal fragment of such a physical continuum is studied. However, the obtained differential equations that give the mathematical representation of these problems can be solved only for the relatively simple cases of the structure shape and initial – boundary conditions. Methods used to obtain this solution are called <u>analytical methods</u> and model formed on its basis - <u>analytical model</u>. Although, the real technical problems concern variously conditioned objects of complicated shapes and complex properties. Therefore, only approximated solutions localised in nodes (finite space points), which are performed by digitising process can be achieved. This digitising process results in creating a <u>digital computational model</u> of the tested object by using <u>numerical methods</u>. One of these methods is the Finite Difference Method (FDM), but the other one called the <u>Finite Element Method (FEM)</u> is the most often

used in engineering activity [Zienkiewicz 1977]. The FEM relies on dividing the investigated object on the finite number of elements with similar shape, on assuming the type of their connections in the nodes, on selecting node parameters and a type of a function interpolating results between the nodes, on establishing the relations between these parameters, and on integrating all elements. The proper selection of all these elements decides about the correctness and the accuracy of the received approximated solutions. Thus, the FEM is currently the standard of calculations in engineering analyses implemented in various professional softwares. The ANSYS, a software one of the most often used in the market [ANSYS], was also used for the numerical part of the presented work. However, the obtained numerical results depend on many aspects: boundary conditions, an accuracy of object geometry representation, a precise knowledge about material parameters, as well as a shape and size of elements used in a meshing process. Therefore, to obtain a reliable numerical model, its experimental verification is necessary. It allows completing or creating a new data base of material and mechanical properties of the investigated structures. These parameters in microscale are often different from those in macroscale, especially when they concern the new devices [Trimmer 2006]. The steps performed during numerical modelling and their interactions with experimental data are shown in the Fig.2.1.

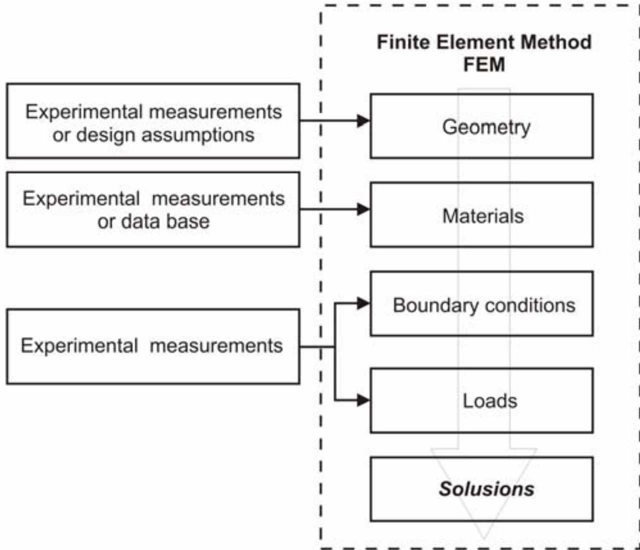

Fig.2.1: Block diagram of numerical method and interaction with experimental data

2.3. Experimental set-up

In this section, the proposed methods of optical metrology will be presented. The experimental set-up [Józwik 2004 a, Gorecki 2005 a, Gorecki 2006, Bosseboeuf 2007, Kacperski 2008] and the analysis of measurement uncertainty, as well as the fringe pattern analysis approach will be described, as well.

2.3.1. Selection of metrological method

Among existing metrological methods the non-destructive optical techniques are the most suitable for investigation of micro-systems [Józwik 2004 a, Kujawińska 2002, Patorski 2005 b, Osten 2007, Kacperski 2008]. In particular, the optical interferometry offers: (i) high sensitivity; (ii) non-contact and full-field measurement; (iii) automatic analysis of

results; as well as (iiii) reconstruction of exact 3D-shape of microstructures. Various techniques were developed [Kujawińska 2005 a, Patorski 2005 a, Sałbut 2005 a and b, Osten 2007] including classical interferometry, grating interferometry, holographic interferometry, speckle interferometry and white-light interferometry. The overview of all these interferometric methods is shown in the Table 2.1. According to the measurement principle and detection system, each of these techniques is mostly specialised in the characterisation of static or dynamic behaviours of microcomponents, measuring their out-of-plane deformation, in-plane deformation or both. Possibility to determine the static and dynamic parameters is very attractive because such properties allow to obtain geometrical, material and mechanical features of microobjects. However, the optical properties of the typical silicon and polysilicon MEMS structures can present difficulties for the describing interferometric methods. In particular, the low reflectivity of polysilicon plates combined with the unavoidable presence of scattered light, limits the contrast of fringes and can influence the accuracy of measurements. For instance, the two-beam interferometry requires mirror-like surfaces, while the speckle and holographic interferometry are well adapted to rough surfaces.

Table 2.1: Main parameters of full field, interferometric measurement methods [Osten 2007, Kacperski 2008]

Interferometric method	**Measured quantity**	**Complexity of measurement system and process**	**Surface object required ****	**Direct shape measurement ***	**Vibration object measurement**	**Accuracy**	**Remarks, requirements**
Classical, laser two-beam interferometry	Shape; out-of-plane displacement	low	reflective	Yes	Yes	20 nm	
Grating interferometry	in-plane displacement	moderate	with grating	No	Yes	20 nm	sample preparation; time of sample preparation; plane sample;
Holographic interferometry	Shape; in-plane and out-of-plane displacement	moderate	light scattering (reflective)	No	Yes	40 nm	
Speckle interferometry	Shape; in-plane and out-of-plane displacement	low	light scattering (reflective)	No	Yes	40 nm	measurement conditions
White-light interferometry	shape; roughness	high	arbitrary	Yes	Yes	50 nm (scanning) 10 nm; (phase shifting)	scanning; measurement time; measurement conditions; possibility of measuring object with discretely varying surface

* direct measurement – when it is possible to determine measured quantity without additional, special technique like contouring, just on the basis of registered interferograms
** reflective surface $R_z<0.05$, light scattering surface $R_z=0.4\div0.8$

We can see in the Table 2.1. that the laser two-beam interferometry is found as the most appropriate method for measurements of the AlN driven microcantilevers. The main advantages of this technique [Malacara 2001, Patorski 2005 b] that justify its selection for the experiments performed in the framework of this PhD thesis are the following:

- low complexity of system and measurement process allowing their easy alignment;
- easy modification of interferograms (possibility of working in homogeneous and fringe field);
- good quality of obtained interferograms (high contrast and visibility);
- wide range of well developed fringe pattern analysis algorithms;
- possibility to fulfil the requirements concerning demanded characterisation of the investigated microobjects, the AlN driven micocantilevers with features shown in the Table 2.2.

Table 2.2: Main features of AlN investigated microobjects and parameters which should be measured

	Dimensions: X – length, Y – width	**Out-of-plane displacement**	**Resonance frequencies**	**Amplitude and phase of vibration**	**Surface roughness**	**Reflection coefficient (for visible light)**
AlN – driven microcantilever	X =(100 μm ÷ 1 mm) ± x μm; Y ≈ 50 μm ± x μm	up to xx μm ± xx nm	(x kHz ÷ xx MHz) ± xx Hz	up to xx μm ± xx nm; (0º ÷ 360º) ± 10º	$R_z < 0.05$	R > 0.7

x – denote a few; xx – denote tens

In this doctoral contribution we propose then to use a low-cost multifunctional interferometric platform for testing MEMS/MOEMS devices based on a Twyman-Green interferometer [Józwik 2004, Gorecki 2007, Kacperski 2008], which will be presented in the next section. This system that can be used for relatively smooth surfaces like the surfaces of our piezoelectric objects, allows to directly measure the 3-D map of the out-of-plane displacements, providing the micromechanical and material properties of the AlN microcantilevers (e.g. stress σ, Young modulus E, thermal expansion coefficient α, piezoelectric coefficient d_{31}), as well as the quasi-static and vibration behaviours of these microactuators. Since, when operating under a stroboscopic regime [Petigrand 2001 a, Bosseboeuf 2007], this interferometric platform allows the full-motion measurements of the moving microstructures. Moreover, this platform allows to realise reliability test by monitoring the property changes of the tested AlN microcantilevers. Thus, this interferometric measurement tool gives us the possibility to perform complex characterisation of the investigated microobjects based on the AlN thin film.

2.3.2. Experimental set-up

For the measurements performed during this thesis, the multifunctional interferometric platform was selected. This kind of experimental set-up was available both at the Institute FEMTO-ST UFC [Józwik 2004 a] and at the Institute Micromechanics and Photonics WUT [Kacperski 2008], where the author stayed during Ph.D. thesis. These two metrological platforms have a little bit different construction, however they use the same measurement methods and provide the convergent technical parameters and extended uncertainties, justifying the use of both of these systems for the doctoral research. The experimental set-up will be then presented on the example of the instrument located at l'Université de Franche-Comté. Thus, the used metrological platform contains:

- two-beam Twyman-Green interferometer (TGI) and a variety of supporting devices for sample manipulation and loading – used for measuring a shape or an out-of-plane displacement of objects;
- possibility to operate in time-average interferometry regime – used for measuring resonance frequencies, a vibration mode shape and a vibration amplitude;
- possibility to operate in stroboscopic regime – used for measuring vibration transient shapes.

Interferometric data are processed by automatic fringe pattern analyser [Servin 2001, Kujawińska 2005 a], called the Fringe Application (commercially available Smarttech's software [Smarttech]). The selected experimental system allows to apply three algorithms: Time Phase Shift (TPS) algorithm, Spatial Carrier Phase Shift (SCPS) algorithm and Fast Fourier Transform (FFT) algorithm. However, in the frame of this thesis only the TPS algorithm with 5 interferograms phase-shifted of $\pi/2$ was exploited because of its advantages (see Appendix 3). The analytical description of these well-known metrological techniques including the two-beam interferometry with the use of time-average and stroboscopic methods and the application of 5-frame TPS [Servin 2001, Patorski 2005 b, Bosseboeuf 2007] will be shortly presented in the Appendix 3. The proposed multifunctional interferometric platform includes several modules containing optics, electronics, mechanics and software [Józwik 2004 a, Krupa 2007, Krupa 2009]. The main, optical part of this system is based on the well known and widely described in the literature [Malacara 2001, Patorski 2005 b, Bosseboeuf 2007] the Twyman-Green interferometer (TGI). This TGI is integrated with a microscope objective to adjust a measurement field to the tested object size. The scheme of describing multifunctional interferometric platform dedicated for microelement testing and its interferometric part is presented in the Figs.2.2a and b, respectively. The light source is a collimated laser diode ($\lambda = 658$ nm), which can be driven in continuous-wave or pulsed (up to 2 MHz) modes (see Appendix 3). The incident laser beam illuminates the interferometer in which it is divided into two part by a beam-splitter cube. After their reflections from both the reference flat mirror and the tested object, the two beams are recombined by the same beam-splitter cube and then interfere producing an interference pattern, which can be visualised by a microscope oculars or automatically acquired by a 768 x 576 CCD camera connected to a frame grabber card. The interferograms are processed by the automatic fringe pattern analyser. A used metallurgical Nikon microscope (with the objective of 5x and NA=0.13 for the presented measurements) integrated with the TGI ensures a magnification allowing to adjust measurement field to the tested object size. The presented TGI is inserted between this microscope objective and the measured sample and consists of the beam-splitter cube. One of beam-splitter facets is metal overcoated, playing a role of reference mirror in the interferometer, while other facets are coated with an anti-reflection coating. Moreover, a precise piezoelectric transducer (PZT) is used to translates the sample to acquire five phase-shifted ($\pi/2$) interferograms analysed next by the Temporal Phase Shift Algorithm (TPS). The photographs of the selected multifunctional

interferometric platform and its optical part (the T-G interferometer integrated with the microscope) are shown in the Figs.2.3a and b, respectively.

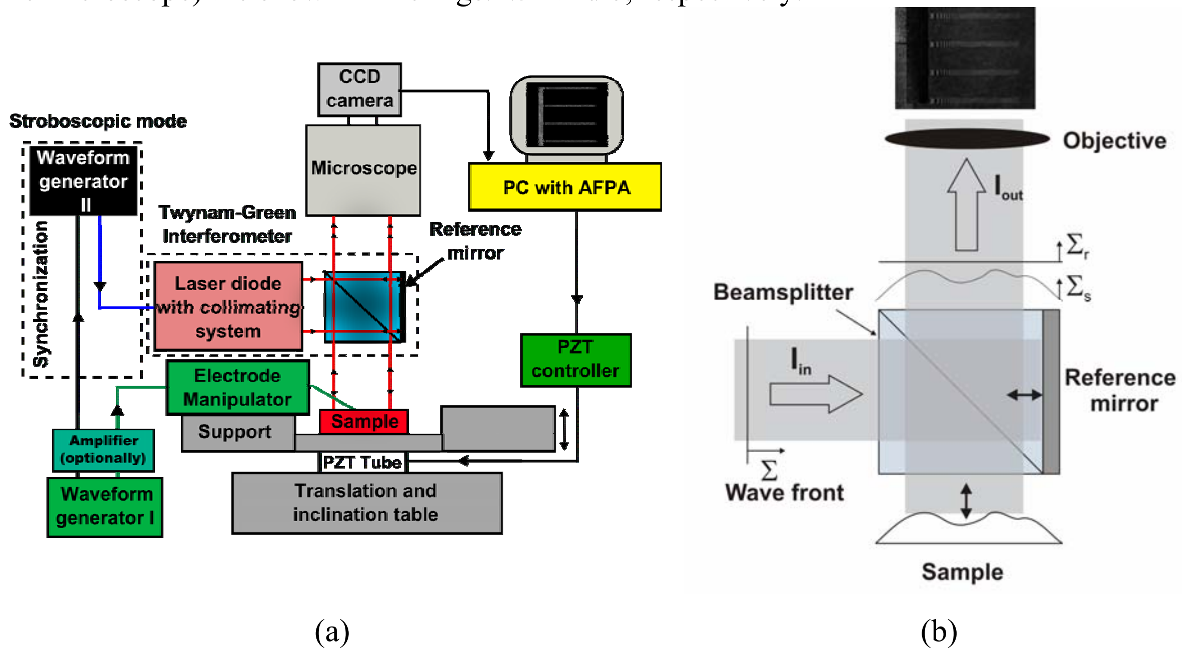

(a) (b)

Fig.2.2: Scheme of measurement system (a) [Gorecki 2007, Krupa 2007, Krupa 2009] and T-G interferometer (b)

Beside the main optical module, the measurement system contains also a lot of electronic and mechanical supporting devices, which are shown in the scheme and the photographs of this platform (see Figs.2.2 and 2.3). There are two manipulators equipped in wolfram needle arms serving to actuate the investigated microcantilevers by applying to them a voltage from the generator (with optional amplification by high voltage amplifier). To realise the measurement in stroboscopic mode, this generator is synchronised with an adjustable phase delay with the second generator used to strobe the laser diode. Changing this phase delay observed in the digital oscilloscope the all transient shapes of vibrating object can be obtained. Moreover, during the measurements the investigated microelements are horizontally simple-placed on the object table, what allows to test them without introducing undesirable deformation or damaging. This table can be aligned independently (see Figs.2.2a and 2.3b) allowing to readily manipulate interference fringes and work in either homogeneous or fringe field. Moreover, there is also special software utilised to automatically perform the measurement. The entire measurement part of the platform (all elements beside electronic module) is placed on the anti-vibration table to minimise transmitted by the floor mechanical vibration influence. The selected technical parameters of the multifunctional interferometric platform are presented in the Table 2.3.

Table 2.3: The main technical parameters of measurement system [Józwik 2004 a]

Features	Values
Field of view	0.13 x 0.10 mm ÷ 2.1 x 1.6 mm ***1.20 x 0.90 mm – for presented measurements***
Basic sensitivity	329 nm/fringe (for λ = 658 nm)
Extended uncertainty	± 40 nm (for conventional interferometry)
Measurement range	~ 40 µm (for conventional interferometry)
Lateral resolution	0.17 x 2.73 µm / pixel ***1.56 µm / pixel – for presented measurements***

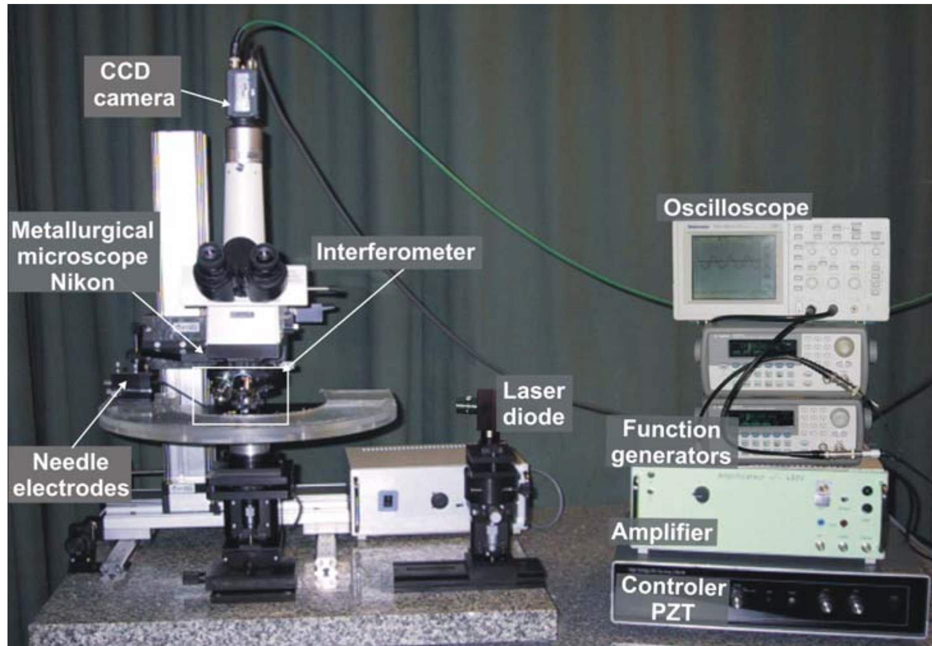

(a)

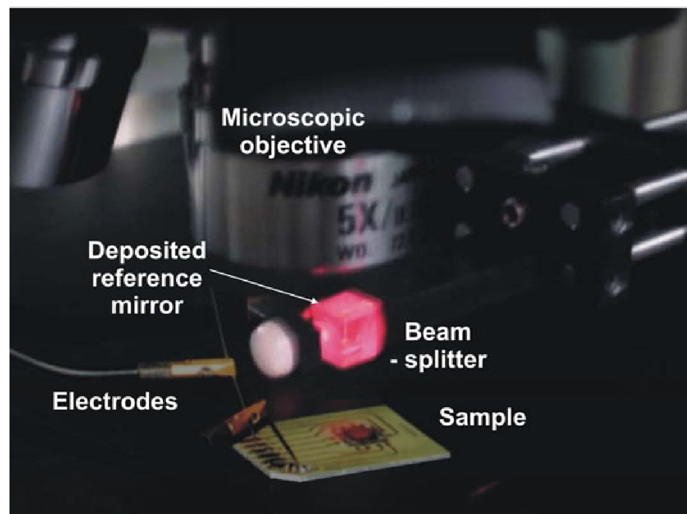

(b)

Fig.2.3: Photographs of multifunctional interferometric platform [Gorecki 2007] (a) and its optical part based on T-G interferometer [Józwik 2004 a] (b)

2.3.3. Completed metrology procedure

The Figure 2.5 represents the complete metrology procedure proposed in the frame of this doctoral research to measure the selected features of the thin film AlN microcantilevers. The experimental procedure starts from measuring object's shape in a static and unloaded state using the T-G interferometry. After the extraction of this initial shape of the sample (initial out-of-plane deflection), we study the out-of-plane displacement of the microcantilevers actuated by a constant or slowly-variable voltage, as well as the effects of a temperature or humidity load on the static behaviours of these structures. Such loads are usually imposed step by step in order to maintain the tested object shape stable during

the interferogram acquisition. Since, the flat mirror has been used as the reference element, the investigated out-of-plane displacement is calculated relatively to the static, unloaded state of the tested sample by subtraction process.

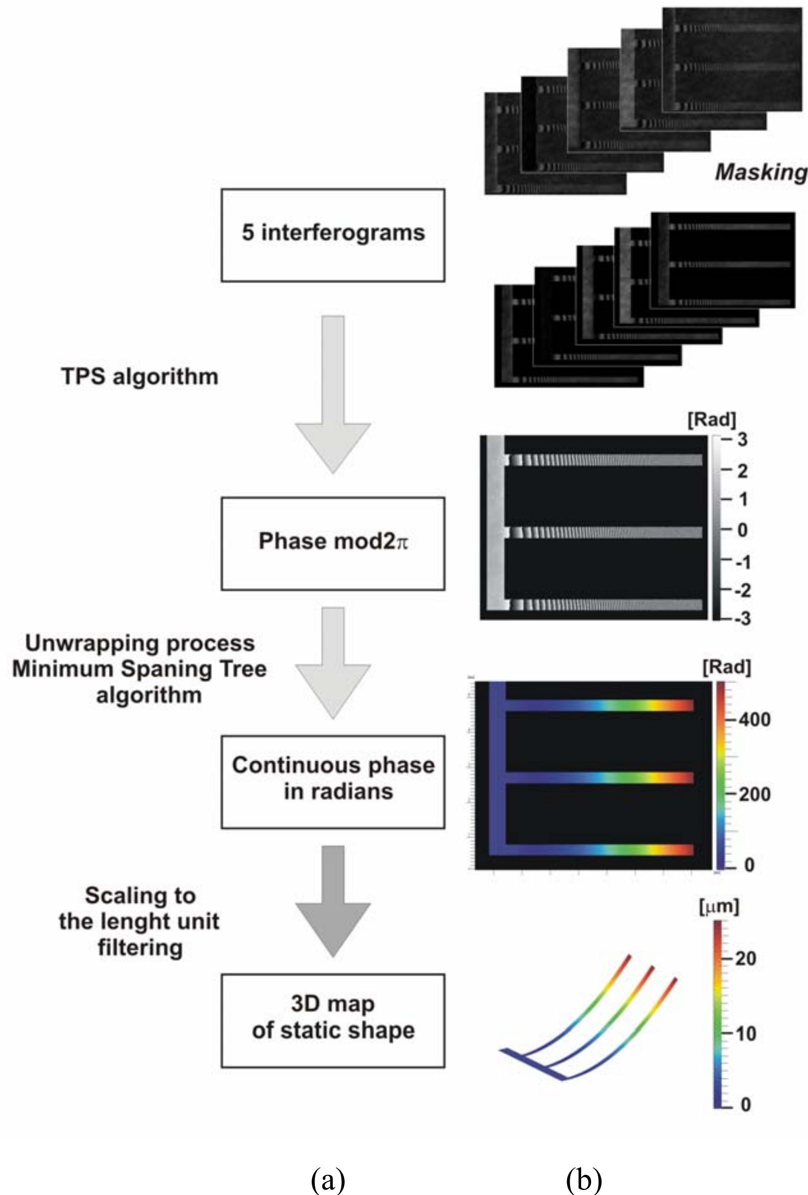

(a) (b)

Fig.2.4: Diagram of theoretical measurement procedure for static shape determination (a) and its experimental illustration (b)

The full procedure of measurement and fringe processing used in the static shape determination is presented in the Fig.2.4a. The process of retrieving unknown phase distribution consists of two steps:

- fringe patterns analysis (5-image TPS algorithm) and determination of phase distribution modulo 2π (see Appendix 3);
- unwrapping of the phase distribution modulo 2π (the Minimum Spanning Tree algorithm) and its scaling to the measured units restoring the 3D shape of sample (see Appendix 3).

In practical application of this procedure various additional processes like masking and filtering (see Fig.2.4b) were added. The masking process was used to facilitate the unique determination of the tip and the fixed ends of the cantilevers.

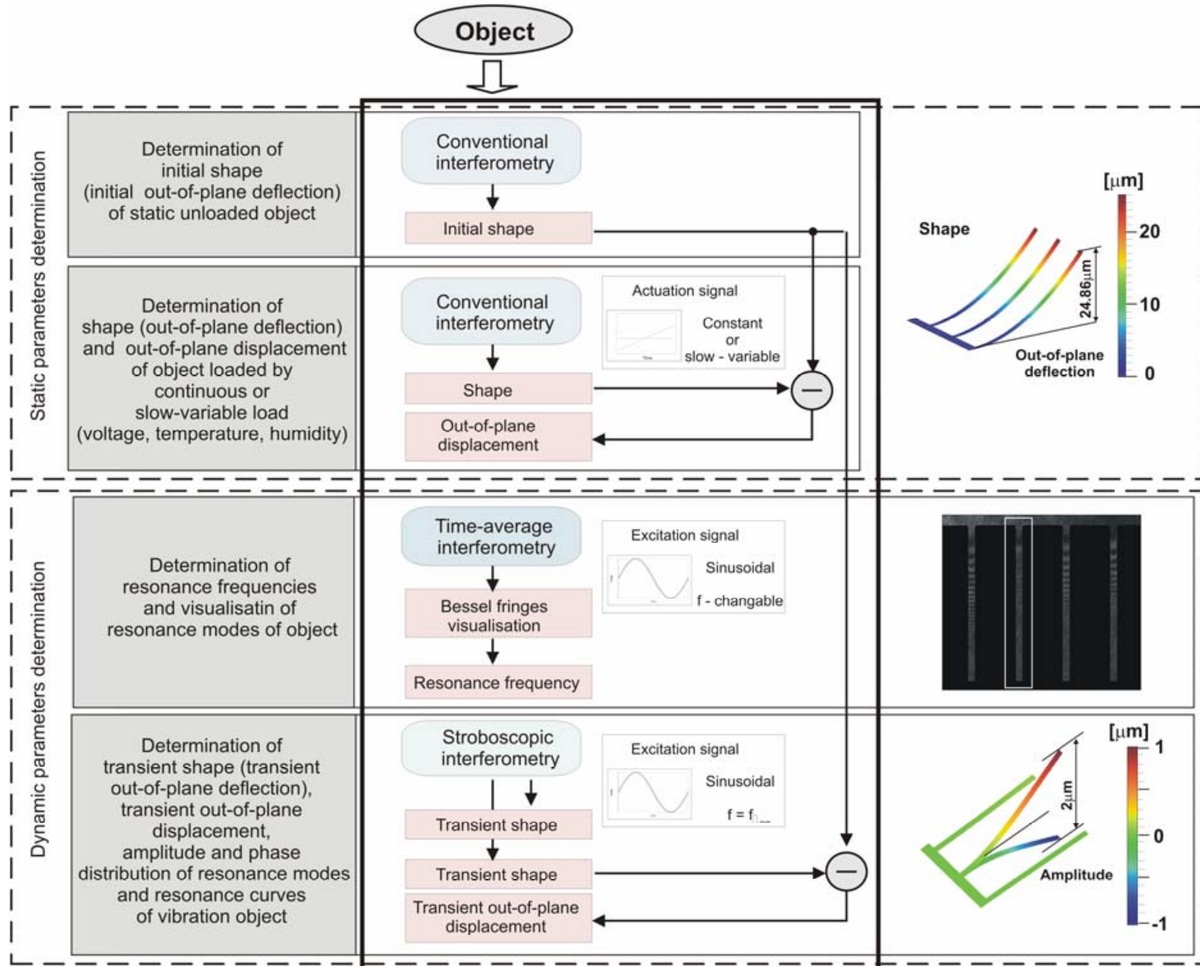

Fig.2.5: Complete procedure of optical metrology implemented in this Ph.D. thesis study

After obtaining the described static parameters the microcantilevers are excited by sinusoidal voltage signal to study the dynamic properties. The resonance frequencies are determined by monitoring a contrast of the obtained interference fringe and a number of Bessel fringes when adjusting a frequency value at constant amplitude of an excitation signal (time-average interferometry (see Appendix 3)). When the highest vibration amplitude (a maximum number of Bessel fringes) and the lowest visibility of the interference fringes are observed, then the object resonance frequency is identified. The number of the resonance mode is determined by visualisation of the Bessel fringes [Sałbut 2003, Patorski 2004]. The precise measurements of the transient shape, the transient out-of-plane displacement of vibrating microstructure and the amplitude and phase distribution of vibration modes are obtained in the stroboscopic regime (see Appendix 3). In that regime the measurement procedure is similar to the static case (see Fig.2.4) with a subtraction of the unloaded object state from the dynamic state. Thus, the amplitude of resonance modes is determined by measuring two of the most deflected (upwards and downwards) states during the vibration period. These two states are found by monitoring the fringe shapes and the numbers of these fringes in the interferogram during the adjustable time delay t_0 (see Appendix 3). Thus, the two maps of the two extreme out-of-plane transient deflections are measured and after subtracting from each of them the unloaded state, the obtained extreme displacement values are added to received the vibration amplitude. The stroboscopic interferometry allows to determine the amplitude at different applied voltages V_{pp} and the resonance curves. Moreover, the subtraction process

helps to decrease the systematic errors. Each out-of-plane deflection data of the AlN cantilevers are calculated as a difference between the free-end and the fixed-end of the object, determined in the masking process, i.e. between the highest and lowest points of the element (see Fig.3.1, section 3.1 and Fig.2.5, section 2.3.3). The interferograms are processed by the TPS algorithm previously mentioned, which is widely used by several authors [Bosseboeuf 2007, Patorski].

2.3.4. Measurement uncertainty determination

The metrological analyses of the multifunctional interferometric platforms used in this dissertation were performed in detail by M. Józwik and J. Kacperski in their Ph.D. theses [Józwik 2004 a, Kacperski 2008]. They concerned the determination of the error sources and the metrological parameters of the mentioned systems. However, because of the masking process included in the applied measurement procedure (see sections 2.3.3. and Appendix 3) the accuracy analysis was performed to determine the extended uncertainties of single measurements of every investigated quantity determined by using one of the interferometric systems. This analysis was accomplished in two steps:

- by the statistical analysis of the series of 10 measurements of the same, randomly chosen cantilever;
- by the comparative analysis with the commercially available interferometric system of Veeco company [Veeco].

The all measurements carried out in the framework of this doctor work were performed in the air conditioned laboratory room in the temperature of 25.5 ± 1°C and the relative humidity of 45 ± 5% using 1.2 x 0.9 mm field of view. To determine the extended uncertainty the coverage factor $k = 2$ was applied. This value is the most frequently used in technical problems ensuring that obtained measurement results are in the range of $< a_{median} - U; a_{median} + U>$ with the confidence level of 95.4%, where a_{median} is a median value of the results from the sample and U is an extended uncertainty [Niepewność 1999, Dobosz 2001]. The standardised skewness and the standardised kurtosis were calculated to determine whether the samples come from the normal distributions. Values of this statistics outside the range -2 to +2 indicate significant departures from normality. However, if the normality of the probability distribution could not be verified (e.g. when the measurement error was evaluated basing on the author's experiences) it was assumed that the probability distribution is uniform. Then, the standard deviation was calculated as:

$$s_{uniform} = \frac{RG}{\sqrt{3}}, \tag{2.1}$$

where RG is the range [Dobosz 2001]. The statistical analysis was performed using Statgraphics Plus 5.1 software.

The investigation results of the AlN driven microcantilevers performed basing on the statistical analysis were presented in the dissertation giving the median and the standard deviation values, i.e. statistics to estimate the concentration and the deviation of the determined data. The obtained results have allowed to infer statistically about the properties of the tested microcantilever parent population.

The statistical analysis – uncertainty determination

There were determined the interference measurement uncertainties of the following investigated quantities:

- the static and dynamic parameters determined directly from the interferometric measurements, i.e.:
  - out-of-plane deflection;
  - first resonance frequency and amplitude of resonance vibration;

- the mechanical and material parameters determined indirectly form the analytical equation basing on the interferometric measurements, i.e.:
  - residual stresses;
  - piezoelectric and thermal expansion coefficients.

Out-of-plane deflection

The accuracy of the determination of the single cantilever out-of-plane static deflection is related to the factors discussed by the Kacperski [Kacperski 2008]. However, the masking process applied during the measurement procedure (see section 2.3.3 and Appendix 3) was an additional factor which significantly influenced this accuracy. Assuming that all the measurements were performed for the following limitations:

- 1.2 x 0.9 mm – field of view (see section 2.3.2);
- proportionality of the initial deflection to the square of the cantilever length $\delta_m \sim L^2$ (see Chapter 5);
- ± 3 pixels – determined extended uncertainty of the masking process;

the extended uncertainty of the out-of-plane deflection measurement was found to be a linear function of the cantilever length considering the same value of the AlN thin film thickness. The statistically obtained extended uncertainties are given in the Table 2.4.

Table 2.4: Uncertainties of out-of-plane deflection measurement

Bottom electrode of cantilever	**AlN thin film thickness [µm]**	**Cantilever length *L* [µm]**	**Standard deviation SD [nm]**	**Extended uncertainty Δ*δ* (*k*=2) [nm]**
CrNi	1.4	800	110	220
		400	60	110
		200	30	60
CrNi, Al	1.0 (for CrNi) 0.4 (for Al)	800	90	180
		600	62	130
		400	50	95
		200	20	40
Au	1.0	200	30	60

First resonance frequency

The accuracy of the resonance frequency determined using the time-average interferometry depends mainly on the two factors, i.e. the accuracy of the function generator applied to object loading and especially the ability to detect the vibration amplitude change vs. the excitation frequency change. The accuracy of the resonance frequency evaluation depends thus on the detection of the amplitude change threshold [Petitgrand 2001 b] and on the width of the resonance curve. The vibration quality factor (see Appendix 1) is strictly related to the design and the material properties of the tested objects. The extended uncertainty of the resonance frequency should be thus determined individually for every investigated element. Therefore, omitting the generator accuracy (negligible value of $U_{gen} = \pm$ 20 ppm [Agilent]) the discussed metrological parameter was statistically analysed for all type of

the tested cantilevers. The obtained results are given in the Table 2.5 being in convergence with the theory about mechanical quality factor (see Eq.A1.5). While, the bigger values of the determined extended uncertainty found for the cantilevers with Al bottom electrode are caused by their wider resonance curve.

Table 2.5: Uncertainties of first resonance frequency measurement

Bottom electrode of cantilever	**Cantilever length *L* [µm]**	**Standard deviation SD [kHz]**	**Extended uncertainty Δf_{res} (*k*=2) [kHz]**
CrNi	800	0.0025	0.005
	600	0.0051	0.011
	400	0.012	0.023
	200	0.03	0.06
Al	800	0.06	0.12
	700	0.07	0.14
	500	0.11	0.21
	200	1.1	2.1
Au	200	0.05	0.1

Amplitude of resonance vibration

The metrological analysis of the used interferometric platform operated in the stroboscopic mode is presented in the literature [Kacperski 2008]. However, similarly to the static parameters, the applied masking process had to be also considered to determine the accuracy of vibration amplitude. Moreover, because the large amplitudes (i.e. greater than 2 µm) were also measured the uncertainty of the relevant quantities were evaluated, as well. Basing on the statistical analysis the extended uncertainties for both small and large amplitudes were found and presented in the Table 2.6. The limiting error was determined basing on the results obtained for the longest investigated cantilevers, for which the uncertainties were the highest.

Table 2.6: Measurement uncertainties of vibration amplitude at first resonance frequency

Bottom electrode of cantilever	**Cantilever length *L* [µm]**	**Vibration amplitude a_0**	**Standard deviation SD [nm]**	**Extended uncertainty (*k*=2) Δa_0 [nm]**
CrNi, Al	800	$a_0 \leq 2$ µm	26	51
		2 µm < $a_0 \leq 20$ µm	51	100

Indirectly determined mechanical and material parameters

The extended uncertainties of the mechanical and material parameters were calculated using the method of total differential of the relevant equations. These parameters concern the experimental results presented in the Chapters 3 ÷ 6 and their values are presented in the Table 2.7.

The mentioned extended uncertainties determined from the analytical equations were evaluated on the base of the extended uncertainties of the measured static (i.e. out-of-plane displacement) parameters. Since, the applied designed values of the object geometrical quantities and the mechanical properties (i.e. Young modulus and Poisson ratio) were assumed as constants.

Table 2.7: Extended uncertainties of indirectly calculated parameters (see section 4.1)

Bottom electrode of cantilever	**Quantities**	**Extended uncertainty (*k*=2)**
CrNi, Al, Au	global stress	$\Delta\sigma_0 = \frac{E_{eq}h_{eq}^2}{3(1-\upsilon)} \frac{E_s h_s + E_f h_f + E_e h_e}{E_s h_s^2 - (E_f h_f + E_e h_e)(h_e + h_f)} \frac{1}{L^2} \Delta\delta_m$
	stress in AlN film	$\Delta\sigma_f = \frac{h_{eq}}{h_f} \Delta\sigma_0$
	Piezoelectric coefficient	$\Delta d_{31} = \frac{E_{eq}h_{eq}^2}{3} \frac{E_s h_s + E_f h_f + E_e h_e}{E_f (E_s h_s + E_e h_e)} \frac{1}{L^2 U} \left(\Delta\delta_p - \frac{\delta_p}{U} \Delta U \right)$ for $\Delta U = k \frac{1}{\sqrt{3}} 2mV$, $k = 2$ [Agilent]
	Thermal expansion coefficient	$\Delta\alpha_f = \frac{1}{3L^2 T E_f h_f} \left(\Delta\delta_{Th} - \frac{\delta_{Th}}{T} \Delta T \right)$ for $\Delta T = k \frac{1}{\sqrt{3}} 2°C$, k = 2

The comparative analysis

It was performed series of 10 measurements of the initial deflection of the same randomly chosen cantilever using the two optical instruments: the interferometric platform applied in the doctor work and the commercially available Veeco interferometric system of NT2000 type [Veeco]. The Veeco optical interferometric profiler was used in the VSI mode (Vertical Scanning Interferometry). Moreover, both interferometric systems were operating with the similar technical parameters including the field of view, the magnification and the numerical aperture NA of the used objective, as well as the vertical and lateral resolutions. The obtained results are presented in the Table 2.8. They concern the longest (L = 800 µm) and the shortest (L = 200 µm) of the tested cantilevers (with the bottom electrode of CrNi), i.e. the objects having the maximal and minimal initial deflection.

To prove the correctness of the measurements presented in this dissertation, which were performed using the interferometric platform, the statistical tests were carried out. The hypotheses assuming the equality of the expected values EVs (i.e. medians as their estimators) determined basing on the series of 10 measurements of the same element obtained

from both mentioned optical systems were tested. It was found that there are not statistically significant differences between the medians of paired data samples at the 95.0% confidence level.

Table 2.8: Statistical measurement results of initial deflection performed on the interferometric platform and the Veeco interferometric system

	h_{AlN} [µm]	L [µm]	Initial deflection δ_m			
			Median value [nm]	Standard deviation SD [nm]	Standard error SE [nm]	Relative standard error [%]
Interferometric platform	1.0	200	1068	20	6	0.6
	1.4	800	25660	110	35	0.1
Veeco interferometric system	1.0	200	1066	36	12	1.1
	1.4	800	25590	91	30	0.1

2.4. Implementation of hybrid methodology

The research carrying out here focuses on characterisation of the AlN piezoelectric cantilevers playing the role of MEMS actuators. To achieve this objective the appropriate hybrid methodology is proposed and implemented. This hybrid approach (see Fig.2.6 [Krupa 2008 a]) is based on mixing analytical, numerical and measurement solutions. The experimental aspects of this methodology are based on the laser interferometric measurements yielding displacement and deformation fields, while the analytical and computational aspects are based on exact equations and approximate (FEM) solutions, respectively. Comparison of the analytical, numerical, and measurement results permits to obtain well approximated evaluation of the AlN cantilever operational behaviours.

During the first phase of that procedure shown in the Fig.2.6 the MEMS samples are modelled and designed. Thus, their geometry, as well as material properties and loading conditions are defined. The analytical and FEM models are created (see Chapter 4). These models represent the functionality of the investigated objects allowing to determine the influence of temperature, internal stresses and geometry discrepancies of these elements on their performances. During the second step of this procedure the microdevices are fabricated, while the third step aims at the sample characterisation. At the beginning of this characterisation, the conditions of tested element operation are defined. Then, the static and dynamic behaviours are determined. The measurements were performed in the air conditioned laboratory room allowing to control the temperature and the humidity by measuring these conditions. Thus, the environmental conditions were set to 25.5 ± 1°C of the temperature and 45 ± 5% of the relative humidity (see section 2.3.4). On the basis of experimentally obtained static and dynamic data, the micromechanical and material parameters (residual stresses, Young modulus, and piezoelectric and thermal expansion coefficients) are extracted. They are calculated with a help of the non-approximated analytical equations taking into account multilayer structure of the AlN cantilevers (see section 4.1). Combination of the analytical, numerical and experimental data allows to create data base of the "exploitable" results in strong relationship between them. Moreover, comparison between all received data leads to

the verification of the both theoretical models and then to their modifications by completing them with the parameters received from the characterisation of the studied devices. Such process permits to obtain exactly defined model representing the real microobject, and also the well approximated evaluation of this fabricated microstructure. In additions, the applied hybrid methodology allows the identification of the main source of behaviour discrepancy between the developed physical and numerical models that helps to understand better the operation of the tested elements and to optimise their technology in order to fabricate the high quality and reliable AlN driven microcantilevers with performances homogeneous on the entire wafer.
To complete the experimental results, the AlN microobjects are also tested by other methods [Oliver 1992, Banks 2006 d, Delobelle 2006, Osten 2007, Andrei 2008]. Namely, nanoindentation allows to obtain elastic behaviours; Scanning Electron Microscopy (SEM), mechanical profilometer and Atomic Force Microscopy (AFM) serve for topography measurements; as well as X-ray diffraction (XRD) is used to determine crystallographic properties. Moreover, a characterisation of the AlN material and microcantilevers is performed by a statistic analysis of collected data.
That is the first branch of the described methodology carried out in the framework of this Ph.D. thesis work. The second one concerns the reliability study of the AlN piezoelectric thin films applied in the microcantilevers, and it will be discussed in the Chapter 6.

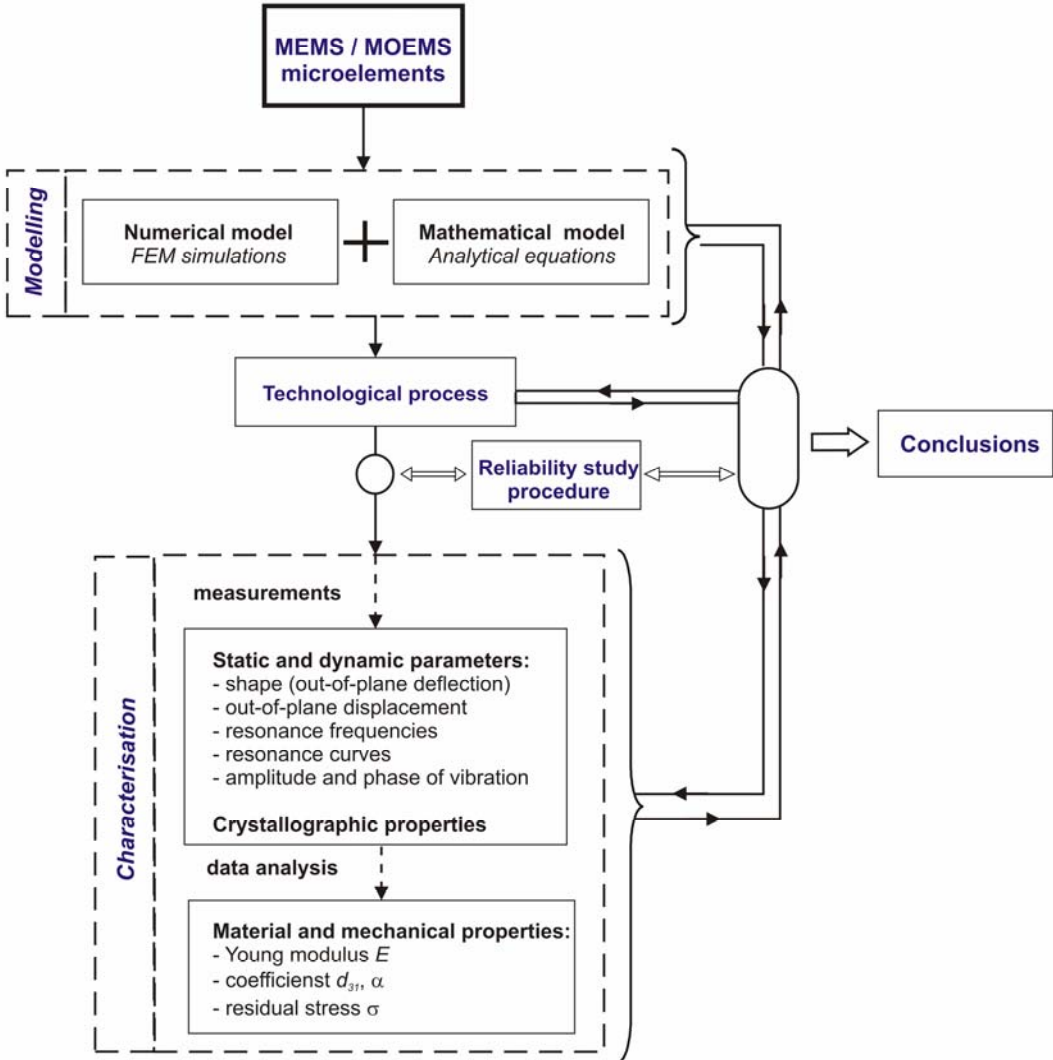

Fig.2.6: Block diagram of applied hybrid methodology

2.5. Summary

The choice of the hybrid approach for the study of AlN driven microcantilevers was justified as the most appropriate one for the investigated microstructures described in the next Chapter 3. The developed opto-numerical methodology combining the mathematical and physical models was discussed. The creation of the mathematical model, which will be presented in the Chapter 4, is based on the analytical considerations and FEM simulations performed in ANSYS software. While, the physical model shown in the Chapters 5 and 6 uses the interferometric techniques implemented in the described here multifunctional platform based on T-G interferometer. This choice of this experimental set-up was justified in this Chapter by the possibility to determine a wide range of significant mechanical and physical parameters of the tested microobjects, which could be measured in a non-destructive way with high accuracy. The classical two-beam interferometry and the exact analytical equations allow to obtain the shape (out-of-plane deflection), out-of-plane displacement, residual stress, as well as, piezoelectric and thermal properties of the tested objects. While, the time-average and stroboscopic interferometry allow to determine their resonance frequencies and transient shapes of vibration modes. Moreover, the measurement procedure concerning the mentioned optical methods was presented. This procedure basing on the 5-frame TPS algorithm is exploited during this PhD research. This algorithm provides high measurement accuracy because of its immunity of various noises. In this chapter the analysis of measurement uncertainty of studied quantities was also discussed.

Chapter 3

AlN based microcantilevers – studied devices

In this chapter, the design as well as the actuation mechanism of the investigated sample, the thin film AlN-driven microcantilever will be presented. AlN seems to be a promising material for MEMS actuators. Even if MEMS sensors using surface acoustic waves have already been proposed, the use of AlN films as an actuation layer requiring the bulk acoustic propagation is not yet common. The absence of deeper studies calls for investigations of the fatigue behaviour of such components, contributing to a better understanding of failure mechanisms in AlN-based bulk MEMS. The understanding of the failure physics is quite complex as multiple materials and interfaces are involved, all of them influencing the ways in which the system interacts with the local environment. This characteristic brings forward the need for a thorough study of the role of fatigue and environmental factors in the reliability assessment of MEMS. We will demonstrate here that there is a strong impact of the technological process on the operation of microcantilevers, modifying their static as well as dynamic behaviours. The MEMS actuator considered here, was designed and fabricated by the FEMTO-ST for reliability study purposes. On the basis of the experimental studies the analysis of microcantilever's technology will be proposed in this Chapter. In particular, the resulting geometrical imperfections and defects of the tested samples are measured, allowing the indication of most critical technology steps. We studied the influence of metal electrodes on the fabrication quality of the AlN microcantilevers, as well as the properties of the AlN material operating as a piezoelectric actuation layer. Such analysis is useful to improve the efficiency of fabrication process and to increase the quality as well as the operational behaviours of the investigated AlN-based actuators. Study of the actuators is essential, since they are the most often run a risk of damaging because of the material fatigue [Andersen 2004]. Therefore, in this dissertation as a test object, it was chosen the microelements in the form of cantilevers driven by AlN, dedicated for MEMS piezoelectric actuators. Our researches allow to acquire knowledge concerning not only to AlN material but also to behaviours of the tested cantilevers and effects accompanying their operations. It seems to be crucial, especially in 'microworld'. Drawn conclusions could then improve accuracy, reliability, life-time and performances of the fabricated AlN-based microsystems, contributing to increase a number of their applications.

3.1. Design

For the research needs of this doctoral work, the test – arrays of piezoelectric transducers were designed and fabricated at the FEMTO-ST by dr A.Andrei. The shape of such an elementary array is square (7.3 x 7.3 mm^2) with an internal square aperture (4.7 x 4.7 mm^2) including the free-standing AlN – driven microcantilever beams. These microcantilever samples were realised by several sequences of etching and deposition onto 3", 380 μm-thick, (100) orientated single crystal Si wafer. In the individual structure, the piezoelectric film of AlN is sandwiched between two metal electrodes. The dimensional parameters of these cantilever beams are:

- width: 50 μm;
- length: from 200 to 1000 μm;
- thickness of Si membrane: 15 μm;
- thickness of AlN film: from 0.4 to 1.4 μm.

The schematic cross-section of the individual microdevice showing its layout, as well as the schematic top view of whole test-structure are presented in the Figs.3.1 and 3.3, respectively. A single mirocantilever is composed of three thin layers deposited on the silicon substrate: the bottom electrode (pink colour), the thin film of AlN (green colour) and the top electrode (blue colour). The way of how the different test – chips are positioned on the surface of 3” wafer is shown in the Fig.3.2. We have here 3 structures with the lengths of 700 µm and 1000 µm and 5 other structures of different lengths. Several of single cantilevers of the same dimensions are grouped on each side of the array, as shown in the Fig.3.3.

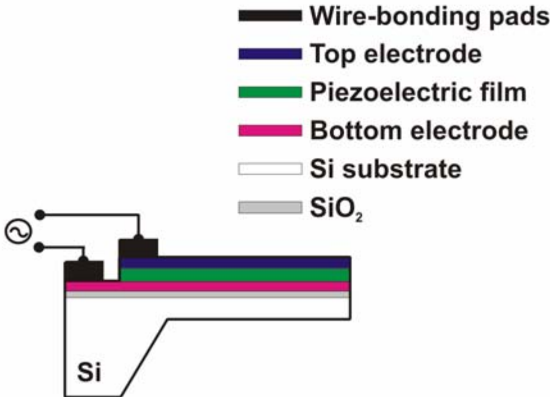

Fig.3.1: Layout of single cantilever

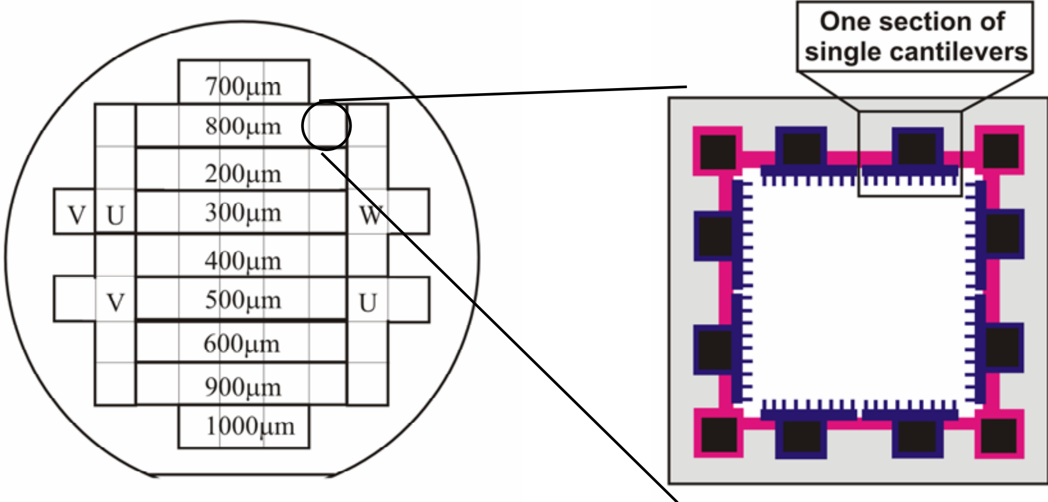

Fig.3.2: Wafer mapping

Fig.3.3: Schematic top view of single square chip

3.2. Principle of actuation

The actuation of the AlN sample is based on the converse piezoelectric effect, which appears in the AlN layer sandwiched between two metal electrodes when a voltage is applied. The purpose of these electrical contacts is to create a uniform electric field across the piezoelectric film thickness. Accordingly to the aluminium nitride as the piezoelectric material and the design of the tested cantilevers, a voltage is applied along the 3 – axis direction. It generates in-plane (x-y plane) strains, introducing stress to the AlN thin film and produces actuator functionality via the d_{31} (= d_{32}) coefficient of the piezoelectric matrix. The strains along the film thickness via the d_{33} are also generated. However, because lateral piezoelectric effect is dominant, the AlN film thickness change is extremely small, in the range of femtometers. The length of the cantilever is sufficient to cause an appreciable strain of the piezoelectric layer along the object length (see section 1.2). Because the cantilever is fixed at one end and the film is constrained by the much thicker Si substrate, a voltage between the contacts causes the vertical bending of the sample and the displacement of its free-standing tip. Therefore, it is important for the layers above and below the piezoelectric to have the different thickness' or compliances. Otherwise, the piezoelectric film is constrained by similar boundary conditions and the cantilever only stretches without bending. In our case, as previously mentioned the AlN films are deposited on the substrate and thus the d_{31} coefficient is considered as a clamped one d_{13}^{c}. Therefore, the value of d_{31} (i.e. d_{13}^{c}) is smaller than the value for the unconstrained bulk material d_{31}^{b} according to the relations:

$$d_{31}^{b} = d_{31}^{c}\left(\frac{s_{11}^{E}+s_{12}^{E}}{s_{11}^{E}+s_{12}^{E}+\alpha s_{13}^{E}}\right) \tag{3.1}$$

where α is a factor depending on the clamping amount ($0 \leq \alpha \leq 1$) and s_{ij} parameters are elastic compliances at constant electric field. Thus, as it was mentioned the Si substrate restricts the strain in the film plane reducing the strain along its thickness [Andrei 2008].

The actuation principle of the tested microdevice driven by the AlN piezoelectric thin film is then shown in the Fig.3.4. It is then necessary to maximise the value of d_{31} coefficient when considering the efficient application of the AlN cantilevers as MEMS actuators.

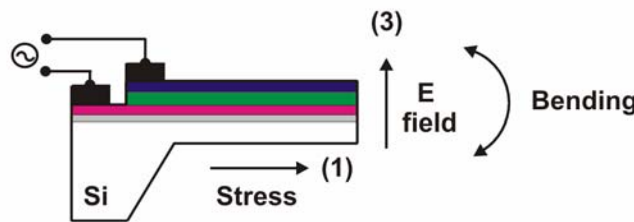

Fig.3.4: Actuation principle of silicon cantilever driven by AlN piezoelectric thin layer

3.3. Analysis of fabrication technology

Microstructure fabrication could be defined as a combination of manufacturing techniques and knowledge about materials, processes and their applications considering in micro scale. Proper selection of sequence and parameters of technological processes has acrucial significance in microstructure fabrication. The MEMS manufacturing process usually is composed of three basic techniques: a photolithography, a deposition and an etching which could be realised by various existing technological processes. These processes including those used in fabrications of the investigated microobjects are well-known and largely described in the literature [Petersen 1982, Beck 1991, Madou 1997, Thielicke 2000, Judy 2001, Madou 2002, Dziuban 2004, Józwik 2004 a, Zheng 2004, SSchool 2005, Banks 2006 a].

The IC compatible process including the sequences of etching and deposition was employed to fabricate the AlN driven microcantilevers [Andrei 2006 c]. This process has used 3", 380μm – thick and (100) orientated silicon wafers. The devices were designed and manufactured at the FEMTO-ST, l'Université de Franche-Comté in Besançon in France. Here, our purpose will be to demonstrate that the feedback from the experimental characterisation of critical technological steps is necessary to improve the quality and the reliability of fabricated devices.

3.3.1. Identification of drawbacks of initial fabrication process

The initial fabrication process of the AlN microcantilevers was a 5-mask process, shown in the Fig.3.5. Its successive steps are:

Step 1: Double-side thermal oxidation of Si wafer
The thin film of SiO_2 is playing a role of an electric insulator and hard mask for Si etch. A 1.3 μm - thick film of oxide was obtained by wet thermal oxidation of 380 μm – thick Si wafer (6 hours at 1050°C).

Step 2: Etch of a 15 μm – thick Si membrane
After the back-side photolithography (see Appendix 2) (mask 1) of the wafer, the etching window was opened in SiO_2 by buffered BHF solution. Then the unprotected silicon was anisotropically etched in a KOH solution, resulting in the 15 μm - thick (± 2 μm) membrane. The precise membrane thickness was monitored by a control of etch time.

Step 3: Patterning of a bottom electrode
On the top side of the wafer, thin metal film (100 nm of Au or 150 nm of Al – see Table 3.3) was deposited by PVD (Physical Vapour Deposition). The substrate was annealed in the atmosphere of Ar (pressure: 7 mTorr / 0.93 Pa) at 200°C and 230 W (0.5 A). Then, the photolithography (mask 2) and etching process of metal were performed to pattern the shape of a bottom electrode.

Step 4: Deposition of an AlN thin film
The piezoelectric film of AlN was deposited in a pulsed reactive DC sputtering machine using the *slow recipe*, i.e. one of the two available recipes presented in the Table 3.1.

Table 3.1: AlN deposition conditions according to two available recipes

	Slow recipe	**Fast recipe**
Ar / N_2 gas flow (sccm)	0.65 / 6	0.65 / 6
Pressure (mTorr)	4.9	4.9
Current (A)	0.5	2
Power (W)	150	640
Substrate Temp. (°C)	200	Non heated (1.2°C/min increase during deposition)
AlN deposition rate (nm/min)	3	17

Step 5: Patterning of a top electrode
A 100 nm – thick film of CrNi was deposited and patterned using the mask 3. This electrode was next used as a hard mask during the subsequent etching process, defining the shape of the final microcantilevers.

Step 6: Etch of AlN thin film
The AlN film unprotected by the top electrode was etched by RIE process (Reactive Ion Etching).The bottom electrode was playing a role of etch stop for AlN etching.

Step 7: Etch of central part of bottom electrode
The central part of bottom electrode was removed applying etching process with the mask 4.

Step 8: Release of the microcantilever structures
Structures were released using DRIE (Deep Reactive Ion Etching) (mask 5), removed the silicon unprotected by the bottom metal film.

Finally, cleaning and dicing processes were carried out. The square chips with tens of microstructures of the same dimensions were obtained. The described microcantilevers are formed from a metal/piezoelectric/metal stack on the Si substrate. They have width of 50 µm and length in the range of 200 ÷ 1000 µm.

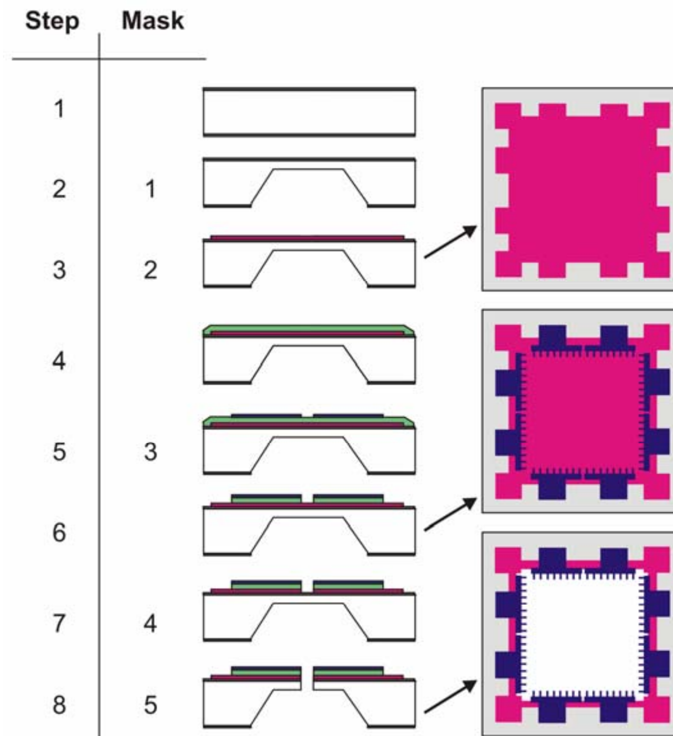

Fig.3.5: Flow-chart of initial technological process

The performances of the resulting AlN actuators strongly depend on the good quality of both metal electrodes: the top electrode playing the role of etch mask and the bottom electrode playing the role of etch stop for patterning of the AlN active layer. Consequently, the appropriate choices of such metal films and their behaviours during the AlN etching are crucial. In particular, the resistance of both mentioned electrodes against SF_6 plasma used in AlN film etching RIE process has to be taken into consideration. Moreover, the choice of material for one metal film limits the choice for the second one. The bottom electrode has to be partially etched without damaging the top one (step 7). Because $Cr_{50\%}Ni_{50\%}$ alloy is very resistive against SF_6 plasma, it was chosen for the top metal film. This CrNi metal property was also used during the microcantilever process flow (step 8). According to the Table 3.2 presenting the etch speeds of various metal films in the available etch solutions, Au and Al were selected for the bottom electrode as the most suitable metals.

Table 3.2: Etch speeds *s* (nm/min) of various metal films in the available etch solutions

	etch Al	**etch Cr**	**etch Ni**	**etch Cu**	**etch Au**
Al	60 ÷ 100	6	6	100	10
Cr	0	s > 100	0	0	0
Ni	100 > s > 0	0	23	s >100	0
Cu	100 > s >0	150	45	s >100	470
Au	0	0	0	0	s >100

However, only Au can be etched without attacking Cr and Ni, Al still represents the second possible choice. Since, it is better resistive on RIE of AlN thin film than Au showing very poor resistance on SF_6 plasma. Therefore, the first two prototypes of the AlN driven cantilevers had CrNi top electrode, and Au and Al bottom one, respectively (see Table 3.3).

According to the initial technological process described in the Fig.3.5, the two wafers containing the AlN driven microcantilevers with the designed (i.e. nominal) geometric parameters given in the Table 3.3 were fabricated.

Table 3.3: Designed geometry dimensions and materials used in cantilevers fabricated during initial technological process

Wafer	**Metal electrodes thickness**		**AlN film thickness**	**Si substrate thickness**	**Cantilever length**	**Cantilever width**
	bottom	**top**				
1	Au 100 nm	CrNi 100 nm	1.0 µm	15 µm	200÷1000 µm	50 µm
2	Al 150 nm	CrNi 100 nm	0.4 µm	15 µm	200÷1000 µm	50 µm

To estimate the quality of the fabricated piezoelectric devices the static and dynamic measurements were performed by using the Twyman-Green interferometer and the measurement procedures described in the Chapter 2. The first investigations were carried out on the 200 µm long microcantilevers. The initial deflection allowing to the calculate global residual stress introduced by the fabrication process (see Eq.4.2, section 4.1), the first resonance frequency and the amplitude of resonance vibration were determined. The median values are presented in the Table 3.4. They were calculated basing on the measurements of a serie of 10 randomly chosen microelements with the same structure. Whereas, the 3D representation of the initial deflection and the vibration amplitude of the exemplary microcantilever coming from the wafer 2 are shown in the Figs.3.6 and 3.7, respectively.

Table 3.4: Median static and dynamic measurement result values of 200 µm long cantilevers fabricated in initial fabrication process

Wafer	**Length** L **[µm]**	**Initial deflection** δ_m **[µm]**	**Global residual stress** σ_0 **[MPa]**	**First resonance frequency** $1^{st} f_{res}$ **[kHz]**	**Amplitude of resonance vibration [µm]**
1	200	-2.480	-99.48	319.90	1.837
		SD= 0.020	SD=0.96	SD= 0.05	SD= 0.044
2	200	-1.140	-34.54	566.0	0.459
		SD= 0.030	SD=0.84	SD= 8.9	SD= 0.075

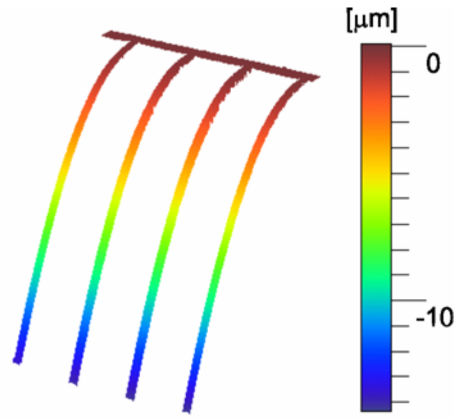

Fig.3.6: 3D view of initial deflection of 200 μm long cantilevers wit Al bottom electrode

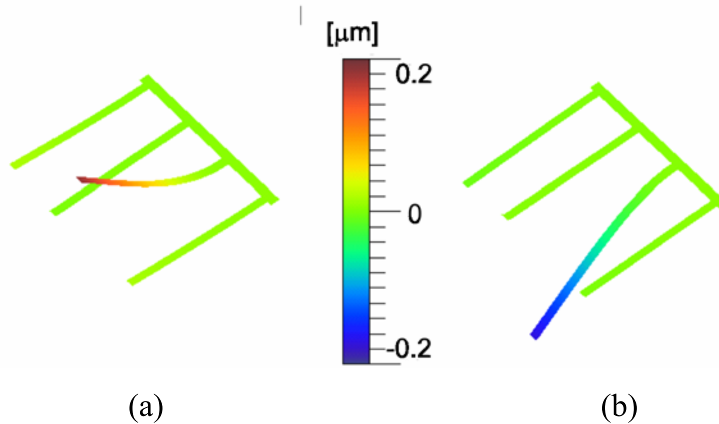

(a) (b)

Fig.3.7: 3D view shape of first resonant mode transient shape measured for 200 μm long cantilever with Al bottom electrode: upper (a) and lower (b) extremities

The technology process generates high compressive residual stresses in the thin films (see Table 3.4). Such an effect is harmful, because the stresses cause a large out-of-plane deflection of microcantilever undesirable in the case of the actuator applications.
The displacements measured at the extremity of the microcantilevers as a function of applied constant voltage for both wafers are presented in the Table 3.5. The graphical illustrations of these results for the 200 μm cantilevers are shown in the Fig.3.8. According to them the observed piezoelectric properties are relatively modest.

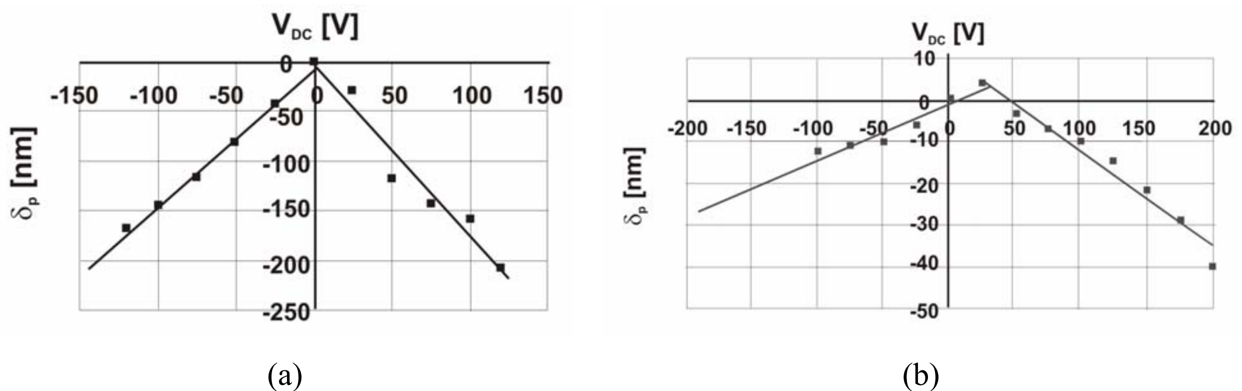

(a) (b)

Fig.3.8: Graphical illustration of sample piezoelectric displacement induced by constant voltage in the case of exemplary 200 μm long cantilevers with bottom metal film made of Au (a) and Al (b)

Table 3.5: Results of displacement vs. applied constant voltage performed for exemplary 200 µm microcantilevers coming from initial technological processes

Wafer 1		Wafer 2	
Constant voltage [V]	**Cantilever free-end displacement [nm]**	**Constant voltage [V]**	**Cantilever free-end displacement [nm]**
-120	-169	200	-40
-100	-145	175	-29
-75	-116	150	-22
-50	-81	125	-15
-25	-49	100	-10
0	0	75	-7
25	-28	50	-4
50	-118	25	4
75	-144	0	0
100	-160	-25	-6
120	-208	-50	-10
		-75	-11
		-100	-13

To obtain 150 nm of free-end displacement, the minimal constant voltage of 100 volts needs to be applied for the microcantilevers taken from the wafer 1. In the case of the wafer 2, the results are in the range of measurement uncertainty (see section 2.3.4) and therefore the tendency of the piezoelectrically induced displacements can have been not observed even for 100V of constant voltage. It could be explained by more than two times thinner AlN film deposited on the Al metal (see section 1.5) [Martin 2004]. Moreover, to notice the resonance vibration the high amplitude sinusoidal signal was required, i.e. 130 V_{pp} with 140 V_{offset} or 240 V_{pp} without offset for the actuators containing the Al and Au bottom electrode, respectively. However, the initial polarisation performed by the offset voltage was necessary for both device types. Such high voltage values were possible to obtain only through the amplification of the signal from the used functional generator. The presented results pointed out thus, that the operation signals in both the static and dynamic operation modes were very high. It is worth to emphasise that the surface quality of the tested structures was very low, what induced the low interferogram quality (see Fig.3.9).

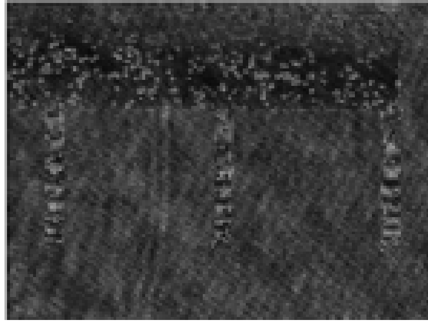

Fig.3.9: View of static interferogram for 200 µm long AlN microcantilevers with Au bottom electrode

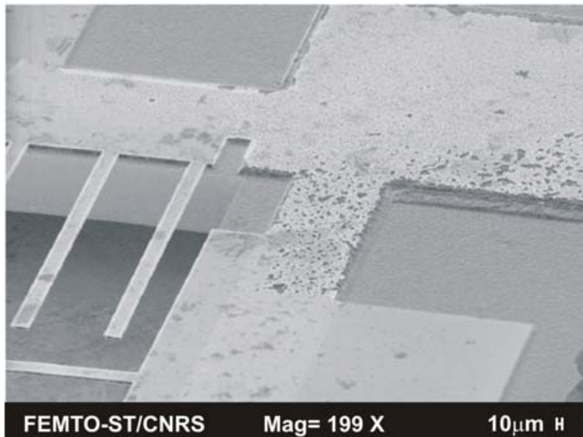

(a)

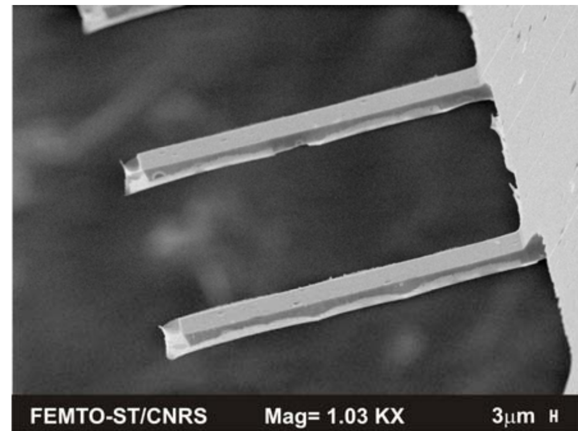

(b)

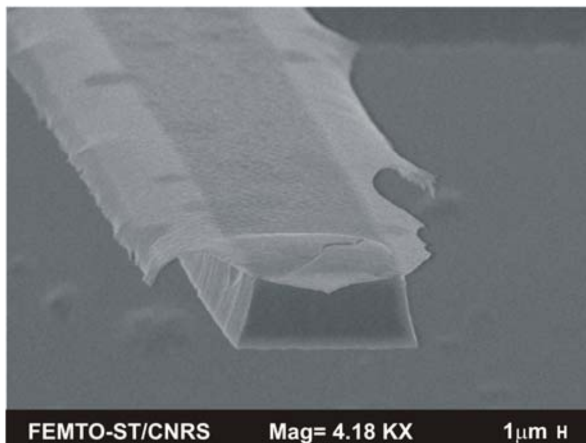

(c)

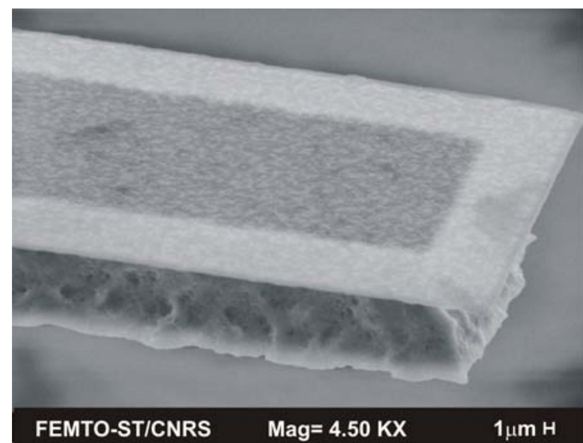

(d)

Fig.3.10: SEM images obtained for 200 µm long cantilevers with Al (a, d) and Au (b, c) bottom electrode

To better understand the source of low actuator quality, we analysed the geometric imperfections of the microcantilevers from the wafers 1 and 2 using Scanning Electron Microscope (SEM). The resulting SEM images are illustrated in the Fig.3.10 [Andrei 2006 c, Krupa 2009] showing several damages, namely:

- damages of the top and bottom electrodes induced by the etching processes (see Figs.3.9 and 3.10a). Here, the used metals of bottom electrode (Al and Au layers) have relatively low resistance during RIE etch of AlN layer.;

- changes of the cantilever profile because of the underetching process shown at the cantilever clamped-end and free-end (see Figs.3.10b÷d). It caused the changes of the microobject length and thickness. Moreover the voltage load during tests induced an irregular shape of thin film borders (see Fig.3.10c).

3.3.2. Critical analysis of the initial fabrication process and improvement proposals

The low piezoelectric efficiency as well as the presence of the geometrical imperfections mentioned before (see section 3.3.1), requested the modification of the initial fabrication process, where the metals of bottom electrode was Al and Au layers. In particular, the step 6 of the initial process (RIE etching of AlN film) had a destroyed effect on the integrity of the bottom electrode. In addition, the step 8 of this process (DRIE release of the structures) might introduce silicon underetching. The first mentioned problem was solved as follows:

- masks 2 and 4 were replaced with new ones allowing to eliminate the step 7 of the process (i.e. etching of the bottom electrode). Due to it the materials for both electrodes can have been chosen independently;
- CrNi alloy was chosen for the both metal films because of its very good resistance against RIE process (in SF_6 plasma and humid solution). However, as noticed after the fabrication process this resistance was over-estimated;
- AlN RIE etching process performed in a SF_6 plasma was replaced with a less aggressive humid RIE allowing to obtain better quality of vertical sidewalls of the AlN film.

The performed modifications allowed to reduce the damage of both metal electrodes induced before in the steps 6 and 7 of the initial fabrication process. However, the mentioned new masks generated simultaneously some advantages and drawbacks. The main drawback was loss of the self-alignment process performed in the initial technological process by the top electrode serving as a mask to pattern the bottom one. This effect is illustrated in the Fig.3.11. The introduced new technology modification (i.e. the dry AlN etching to humid one and the discussed below silicon DRIE to RIE process replacing) changed the cantilever profile, what is also shown in this figure.

Instead of the expected high anisotropic process, a nearly isotropic Si etching was observed (see Figs.3.10c and d). This problem in relationship with the Si substrate underetching was solved as follows:

- DRIE process was replaced with a classical SF_6 RIE, that was less anisotropic (see Fig.3.11).

This change produced the trapezoidal cross-section cantilever profile shown in the Figs.3.12c and d.

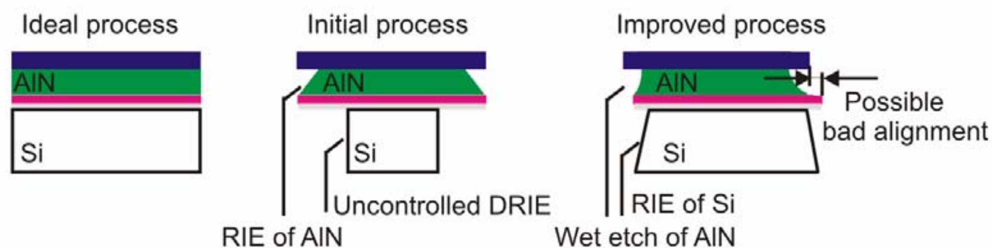

Fig.3.11: Cantilever cross sections, possible to obtain during initial and modified fabrication process in comparison to an ideal one

Besides the modifications related to the two mentioned critical fabrication steps, the other ones were introduced as well. In particular, the thickness of SiO_2 film (a highly compressive layer) was reduced to decrease the high residual stress observed in the tested initial microcantilevers. Moreover, the additional Al film was deposited and patterned to form pads facilitating subsequent packaging performed by an object wire-bonding (see Fig.3.14), because the old metal electrodes were too thin for this process. The packaging ought to supply the tested devices without damaging their metal film electrodes.

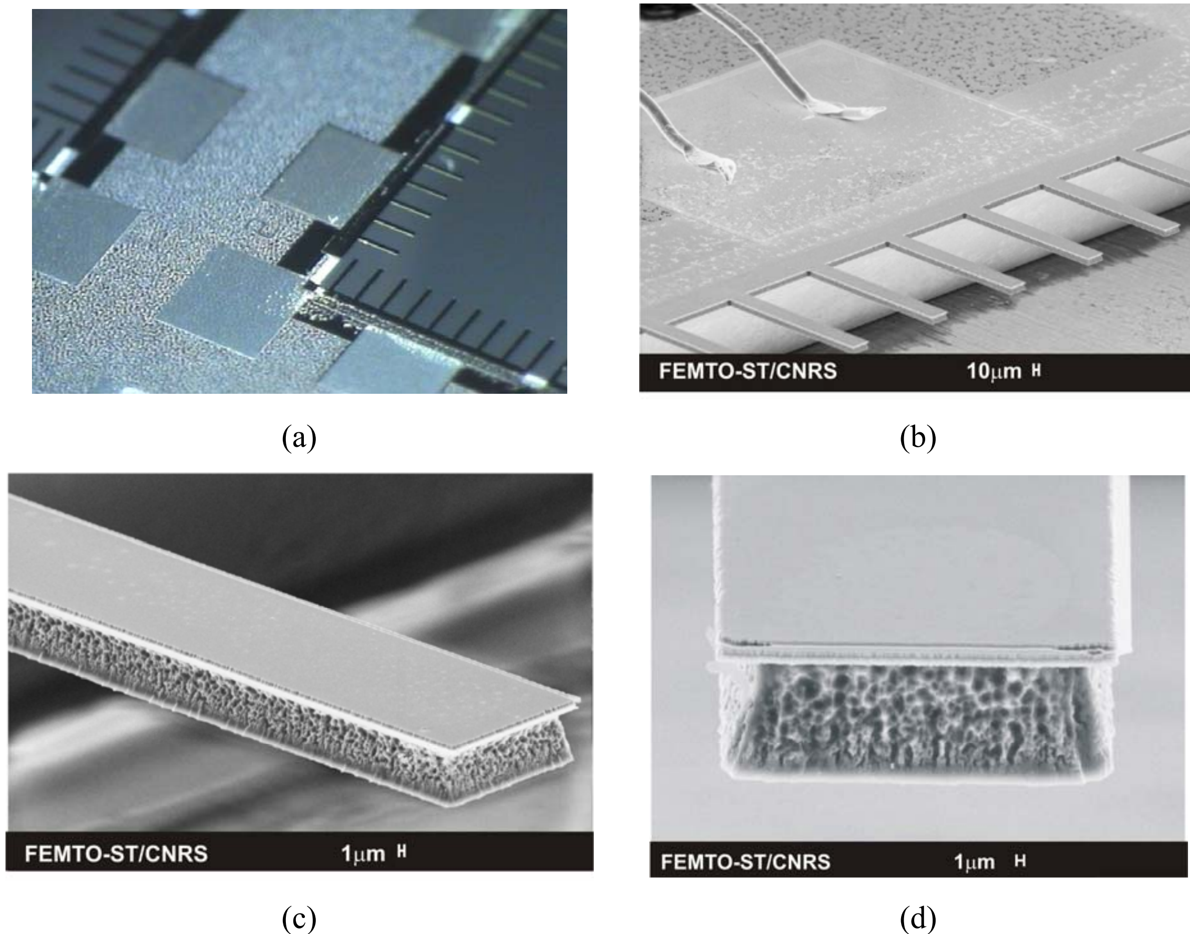

Fig.3.12: Optical microscope and SEM images obtained for 200 µm long microcantilevers fabricated during modified technological process

The critical analysis of the initial fabrication process led to the definition of improved fabrication process [Andrei 2006 b and c, Andrei 2007 a, Andrei 2008, Krupa 2009] allowing to manufacture significantly higher quality microactuators. The improved process is compared with the old one (see Fig.3.5, section 3.3.1) in the Fig.3.13. The consequences of the new process on the quality of the AlN microcantilevers are illustrated in the Fig.3.12. In particular, reducing of the Si substrate underetching (see Fig.3.12c and d) and better quality of the both electrodes (see Fig.3.12a and b). The successive steps of the improved process focusing on the introduced changes are as follows:

Step 1: Double-side thermal oxidation of Si wafer

Step 2: Etch of a 15 µm – thick Si membrane
The thickness of the SiO_2 film was reduced to 50 nm to decrease the residual stresses.

Step 3: Patterning of a bottom electrode
The new mask 2 was applied to pattern the bottom electrode.

Step 4: Deposition of an AlN thin film
The *fast recipe* (see Table 3.1) of deposition was used allowing to obtain deposition rate of about 17 nm/min, which is in accordance with the results of Kusaka et al [Kusaka 2000]. During this step, the substrate temperature was much lower with the comparison to the *slow recipe*.

Step 5: Patterning of a top electrode
Thicker top metal film (about 420 nm) was deposited (by the same process as in the initial fabrication flow) to assure better protection against AlN and Si etching (step 6 and step 8) and finally the demanded designed thickness of the top electrode.

Step 6: Etch of AlN thin film
The AlN film was etched in the humid RIE process.

Step 7: Realisation of wire – bonding pads
This step was proposed to facilitate the wire-bonding packaging. To deposit and pattern the thick aluminium pads (500 nm) a lift-off technique with the new mask 4 was applied.

Step 8: Release of microcantilevers
In the modified process, the last step was classical RIE etching of silicon substrate.

The two wafers containing the AlN driven microcantilevers were fabricated according the modified process. Their nominal (i.e. designed) geometric parameters are given in the Table 3.6 (negligibly thin SiO_2 film is not considered).

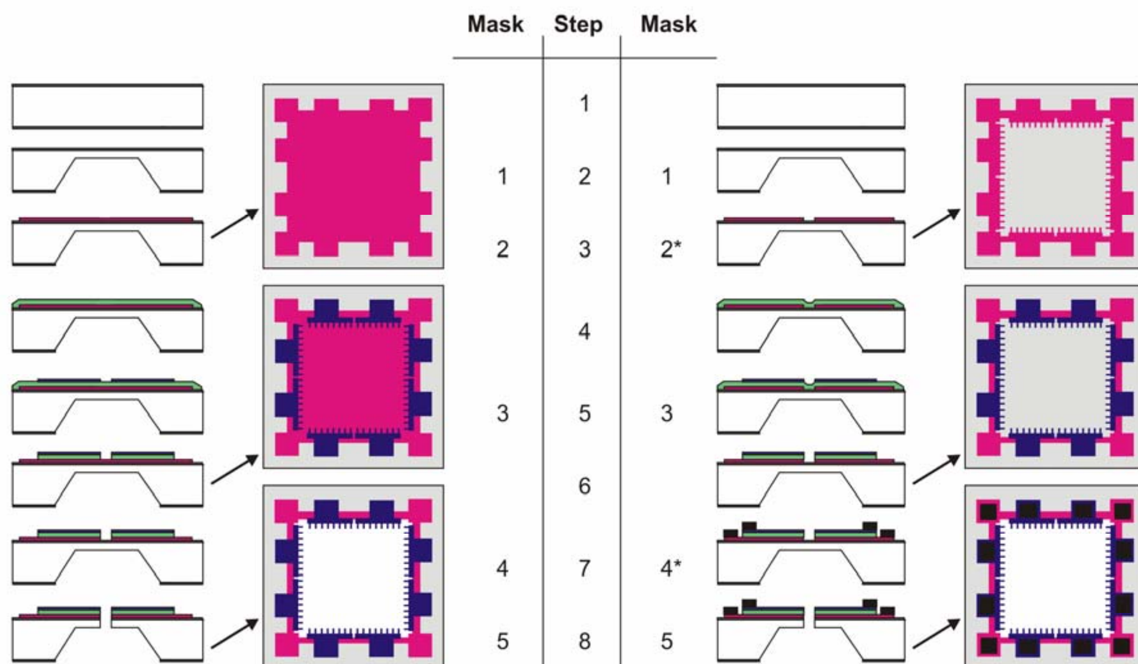

Fig.3.13: Flow chart of improved fabrication process compared to the initial one

Table 3.6: Nominal geometry dimensions and materials used in cantilevers fabricated during improved technological process

Wafer	**Metal electrodes thickness**		**AlN film thickness**	**Si substrate thickness**	**Al pads**	**Cantilever length**	**Cantilever width**
	bottom	**top**					
1	CrNi 150 nm	CrNi 350 nm	1.0 μm	15 μm	0.5 μm	200÷1000 μm	50 μm
2	CrNi 150 nm	CrNi 350 nm	1.4 μm	15 μm	0.5 μm	200÷1000 μm	50 μm

<u>Device packaging</u>

The microcantilever chips were packaged using a circuitry for SD card. For that purpose, Al pads were deposited, as shown in the Figs.3.1 and 3.3. The photographs of packaged microcantilever chip are shown in the Fig.3.14. This package was manufactured at the FEMTO-ST. The copper lines of this particular plate were insulated from the aluminium base by a thermally conductive electrical insulator. This plate resists up to 130°C (only 90°C maximum temperature for the classic epoxy plate), which is important and useful regarding the thermal reliability tests (see section 6.3.2). Before wire - bonding, the copper contact lines were covered with gold using electrochemical deposition process.

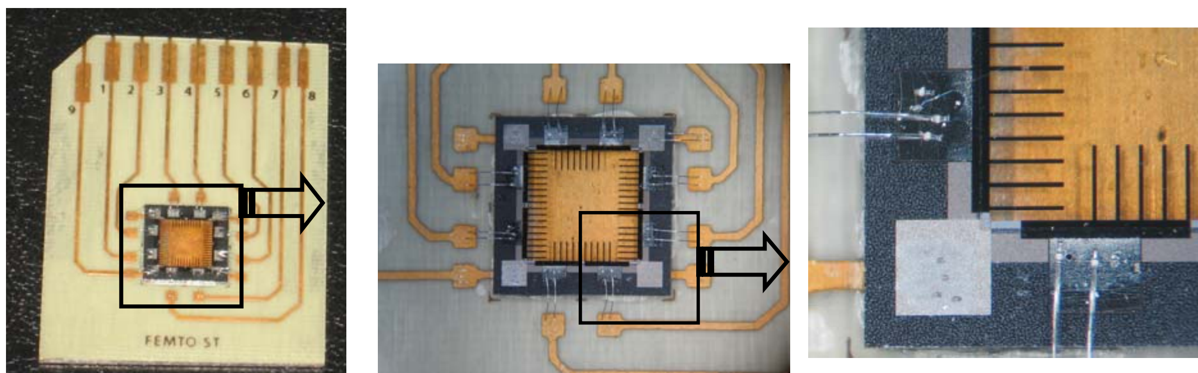

Fig.3.14: Photographs of packed arrays of microcantilevers coming from improved fabrication process

3.3.3. Geometrical imperfections of final devices

If the geometrical imperfections of the microcantilevers, as well as their piezoelectric efficiency were improved significantly with the modified fabrication process, the final devices still have exhibited some imperfections. They have concerned the material and mechanical properties and the operational functionality presented in the Chapters 5 and 6 as well as the relevant geometrical ones. The discrepancies corresponding to the design geometry were investigated using the SEM microscopy and the mechanical profilometry. They mainly have concerned the cantilever cross-section profile, the cantilever length and thickness' of the films. The SEM images of the sample extremity are shown in the Fig.3.15. The expected trapezoidal profile of the microcantilever was found due to the silicon underetching. Here, the effect of the electrode misalignment is well visible. This kind of imperfection could be considered as an object shortening what was explained in detail in the section 3.3.2. Moreover, the porosity (see Figs.3.15a and b) and the material defects (see Fig.3.15c) of the silicon substrate were found reducing its surface quality and then influencing the resonance frequency values of the cantilevers.

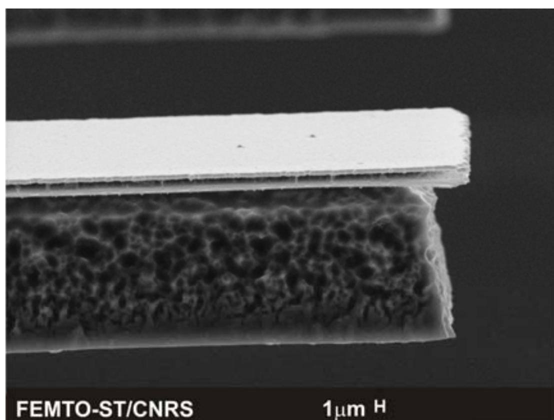

(a) SEM image

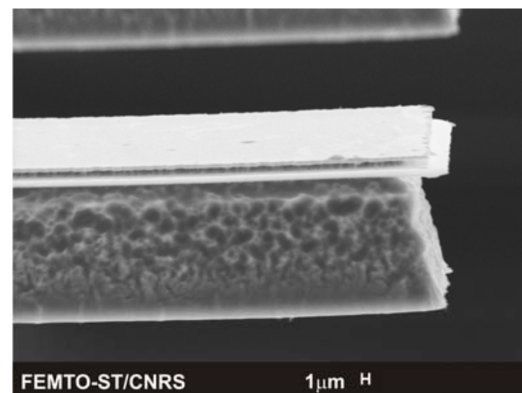

(b) SEM image

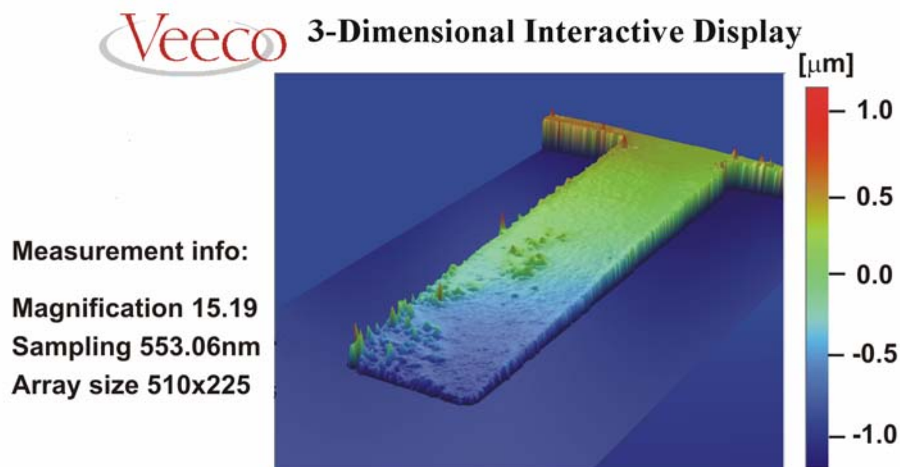

(c) image from Veeco interferometer system of NT2000 type

Fig.3.15: Final device geometrical imperfections induced by technology: cross-section profile (a,b) and Si substrate surface quality: porosity (a, b) and Si material surface defects - bottom view (c)

The thickness of the Si membrane and the thickness of the piezoelectric thin film of the microcantilevers are the most critical parameters of the fabrication which influence the object performances in operation (see Chapter 4). The measurement of the Si membrane thickness was performed by SEM with the accuracy of 0.2 µm. The median values of the results obtained for the serie of 10 randomly chosen objects were found to be 16.37 µm ± 0.11 µm and 16.41 µm ± 0.26 µm for the wafers with 1.0 µm and 1.4 µm thick AlN film, respectively. However, because the AlN film thickness determines the piezoelectric response of the investigated actuators the more detailed measurement of its thickness variations were carried out including whole Si wafer (see Fig.3.2, section 3.1). The mechanical profilometry (operating with the accuracy of few nm) was applied and the results are shown in the Fig.3.16a and b for the wafers with designed values of the AlN film thickness of 1.0 µm and 1.4 µm, respectively.

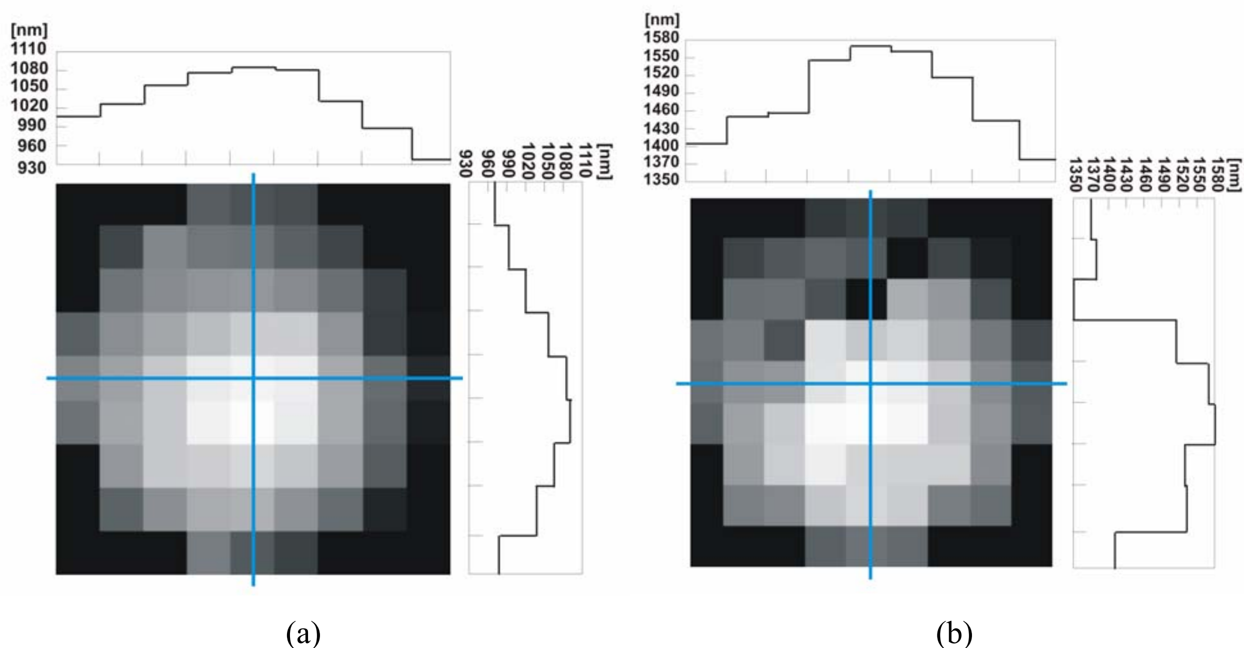

(a) (b)

Fig.3.16: AlN film thickness measurement mapping over wafers with designed values of 1.0 µm (a) and 1.4 µm (b)

More important AlN film thickness was found in the centre of the wafers with about 15% variations between the center and the borders (the wafer areas containing the cantilever structures were considered). The asymmetrical thickness distribution over the wafers was also noticed. Whereas, the median values calculated from the measurements of a serie of 10 randomly chosen microelements were found to be 1.023 µm ± 0.012 µm and 1.480 µm ± 0.030 µm for the wafer with design values of 1.0 µm and 1.4 µm, respectively.

3.4. Conclusions

The performed analyses and measurements of the AlN-based microcantilevers allowed to indicate the most critical technological steps basing on the technological and operational imperfections of the investigated objects. It was found that the devices fabricated during the initial process have exhibited very low piezoelectric properties and they have required high supply voltage and the initial polarisation (the offset voltage). Moreover, the damages of the top and bottom electrodes and the changes of the cantilever profile were observed and

explained by the AlN thin film and Si substrate etching, being the most critical processes. The improvement of the fabrication was then discussed consisting mainly in the application of the new masks, the different materials for the bottom electrode and the different etching techniques. This new technological process allowed to fabricate microcantilevers with considerably better performances (see Chapters 5 and 6).

Chapter 4

Analytical and numerical analysis of AlN driven microcantilever

In this chapter the results of electromechanical modelling will be presented for the AlN driven microcantilevers. This analytical and numerical modelling will take into account the multilayer structure of the piezoelectric transducers. The comparison of such tri-layer structure with those for a homogeneous one will demonstrate the impact of thin film structure on the device performances. The influence of geometrical imperfections as well as the influence of material parameter on the performances of the measured samples will be analysed on the basis of the measurement data (see section 3.3 and Chapter 5). Thus, due to the convergence study between the experimental results and the modelling data, the model of piezoelectric microactuator could better match the real device.

4.1. Analytical model based on tri-layer Si cantilever

Since the pioneering work of Stoney in 1909 on stress analysis, several theoretical models of a single thin film deposited on an elastically isotropic substrate have been proposed [Stoney 1909, Röll 1976]. In the 1980s, stress models for multilayered structures were introduced. The mechanics of a heterogeneous piezoelectric bimorph loaded by an external applied electric field has been analysed by Smits and Choi [Smits 1991] and its extensions to various configuration of multilayer piezoelectric actuators with bending deformation has also been considered by various authors [Chang 1999, Wang 1999]. In particular, the Département de Mécanique Appliquée (LMARC) of the FEMTO-ST performed a study of tri–layer cantilevers with piezoelectric film demonstrating linear behaviours [Walter 2001, Walter 2002]. According the theoretical considerations for the homogeneous Si cantilever (see Appendix 4) the authors from LMARC brought to establish the linear constitutive equations for the piezoelectric materials allowing to calculate the deflection of the multilayer structures as functions of the applied or residual stress, the applied voltage and as a function of the temperature. These equations (see Eqs.4.2÷4.5 and Eqs.4.10÷4.13) were then applied to create the analytical model of mechanical, piezoelectrical and thermal behaviours of the AlN driven microcantilevers. This model has served then to characterise the AlN thin film incorporated in the microactuators. The developed analytical model of tri-layer structure with piezoelectric film showing linear properties will be discussed in this section. However, to obtain the reference for the static and dynamic behaviours of such multilayer object the analytical relations governing the mechanical properties of the homogeneous silicon cantilever structure will be presented in the Appendix 4. Then, the impact of the thin films on the stress distribution and the resonant response will be studied.

Mechanical behaviours of AlN driven microcantilevers

The mechanical properties of the thin film structures differ significantly from those of the relevant bulk counterparts. They are determined by a microstructure and a defect location. Fabrication technology, environment, functional behaviour and various applications requiring different approach of packaging of microsystems produce various situation of loading, generating mechanical stress. The identification and the reduction of the magnitude of this stress are crucial to manufacture reliable microsystems. A choice of appropriate thin films matching the mechanical, thermal as well as chemical parameters becomes crucial. In particular, an optimal selection of the thermal expansion coefficients is important both during fabrication process (because of the different temperature of the applied processes) and during operational use (because of the interlayer stresses generated at the different temperature) of the microsystem. According the multilayer structure of cantilever, the different deposition processes of the thin films introduce the intrinsic stresses because of the differences in the thermal properties of the thin film and substrate materials. The resulting residual stress value could be expressed by the sum of the three components [Madou 2002]:

$$\sigma = \sigma_{Tf} + \sigma_{wew} + \sigma_{zew}, \tag{4.1}$$

where σ_{Tf} represents thermal (unintentional) stresses, σ_{wew} – sum of any intrinsic stresses (unintentional) and σ_{zew} – sum of any external applied stresses (intentional and unintentional). The stresses resulting from the difference between the thermal expansion coefficient of the substrate and the thermal expansion coefficient of the thin film are one of the main stress sources, which moreover often are difficult to eliminate. The intrinsic stresses generated during the film growth are the other important source of the residual stresses. For example, in the case of CVD techniques (see Appendix 2), they are mostly caused be the ionic bombardment inducing various defects to the crystal structure of the thin film. The analysis of this type of stresses is difficult because they depend on a thin film thickness, substrate properties and conditions of deposition process (see section 1.5) etc. The extrinsic stresses correspond to object fixation and probable additional mechanical or thermal loading. The discussed residual stress could be assumed as constant and independent on the film thickness. The residual stress generates the bending moment producing the initial deflection of the cantilever beam structure. The technological process has then a strong influence on the magnitude of such initial deflection. To estimate the magnitude of stress, we developed the analytical model of simplified cantilever taking into account its multilayer structure. The use of the same metallic alloy (CrNi) for both the top electrode and the bottom electrode, allows to consider that the silicon cantilever has on its surface only two films: the AlN film and the metal electrode film with a thickness equal to the sum of thicknesses of the top and the bottom electrode. The stress induced in the AlN transducer causes a mechanical deflection δ_m of the cantilever that can be written as [Andrei, Józwik 2008, Krupa 2008 a, Krupa 2009]:

$$\delta_m = \frac{3(1-\upsilon)}{E_{eq}h_{eq}^2} \frac{E_s h_s^2 - \left(E_f h_f + E_e h_e\right)\left(h_e + h_f\right)}{E_s h_s + E_f h_f + E_e h_e} L^2 \sigma_0 \tag{4.2}$$

with the global stress σ_0 induced by manufacturing:

$$\sigma_0 = \frac{\sigma_f h_f + \sigma_e h_e + \sigma_s h_s}{h_{eq}} , \tag{4.3}$$

where E is a Young's modulus, h is a thickness and σ is a residual stress of the silicon *substrate (s)*, the AlN *film (f)* and the metal *electrodes (e)*. L represents a cantilever's length and υ is a Poisson coefficient considered the same for all the materials. An equivalent thickness h_{eq} is equal to the sum of h_s, h_f, and h_e, while E_{eq} represents an equivalent modulus that can be written as:

$$E_{eq} = \frac{K_1 + K_2 + K_3 + K_4 + K_5}{\left(E_f h_f + E_s h_s + E_e h_e\right) h_{eq}^3} \tag{4.4a}$$

with

$$K_1 = E_f^2 h_f^4 + E_s^2 h_s^4 + E_e^2 h_e^4 \tag{4.4b}$$

$$K_2 = 2 E_s E_e h_s h_e \left(2h_s^2 + 2h_e^2 + 3h_s h_e\right) \tag{4.4c}$$

$$K_3 = 2 E_f E_e h_f h_e \left(2h_f^2 + 2h_e^2 + 3h_f h_e\right) \tag{4.4d}$$

$$K_4 = 2 E_f E_s h_f h_s \left(2h_s^2 + 2h_f^2 + 3h_s h_f\right) \tag{4.4e}$$

$$K_5 = 12 E_s E_f \, h_s h_f h_e \, h_{eq} \tag{4.4f}$$

It is interesting that, assuming in the above equations (see Eqs.4.2÷4.4) that h_e=0 and σ_s=0, a first term of the expansion of the Eq.4.2 gives the relation written as [Andrei, Krupa 2009]:

$$\sigma_f = \frac{E_s h_s^2 \delta_m}{3(1-\upsilon) h_f L^2} \left[1 + 4 \underbrace{\frac{E_f h_f}{E_s h_s}}_{A} \left(1 + \underbrace{\frac{3h_f}{2h_s}}_{B} \right) \right], \tag{4.5}$$

The last equation is in agreement with the formula established by Röll [Röll 1976], where only the term B is different. Moreover, the first term of the Eq.4.5 gives a generalized form of the Stoney's formula.

Fig.4.1: Stress distribution in cross-section of multilayer bending cantilever [Brissaud 2003]

We see that the residual stress induces the bending of the multilayer cantilever. Analysing the normal stress distribution in the bending element, it is found that the neutral plane position is shifted by y_0 value from the middle of the Si substrate (see Fig.4.1) as characteristic for the homogeneous structure (see Appendix 4).

$$y_0 = \frac{E_{e1}h_{e1}\left(h_{e1}+h_s\right)+c_{11}^E h_c\left(h_f+2h_{e1}+h_s\right)+E_{e2}h_{e2}\left(h_{e2}+2h_f+2h_{e1}+h_s\right)}{2\left(E_s h_s+E_{e1}h_{e1}+c_{11}^E h_c+E_{e2}h_{e2}\right)}, \tag{4.6}$$

where c_{11}^E is an elastic constant of the piezoelectric material, the letters *s, f, e1, e2* corresponds to the silicon *substrate (s)*, the AlN *film (f)* and the metal *electrodes: bottom (e1)* and *top (e2)* [Brissaud 2003]. Therefore, the normal stress distribution becomes non-symmetric as presented in the Fig.4.1. Assuming that the technologically induced bending moment M_g of the multilayer cantilever is:

$$M_g = M_s + M_{e1} + M_f + M_{e2}. \tag{4.7}$$

the stress in the film distanced of (y-y_0) from the neutral layer can be given by:

$$\sigma = \int_{y1}^{y2}\frac{M_s}{I_{x_s}}\left(y-y_0\right)dy + \int_{y2}^{y3}\frac{M_{e1}}{I_{x_{e1}}}\left(y-y_0\right)dy + \int_{y3}^{y4}\frac{M_f}{I_{x_f}}\left(y-y_0\right)dy + \int_{y4}^{y5}\frac{M_{e2}}{I_{x_{e2}}}\left(y-y_0\right)dy, \tag{4.8}$$

with $I_{x_i} = \int_{A_i} y^2 dA \quad \text{for} \quad i = s, e1, e2, f,$ (4.9)

where z_i for i=1÷5 are the coordinates of the lower and upper surfaces of the Si substrate *(s)*, the electrodes *(e1, e2)* and the AlN film *(f)*, respectively.

The bending resonance frequency conditions (see Eq.A4.13, Appendix 4) are the same as obtained for the homogeneous cantilever [Brissaud 2003]. Thus, according to the Eq.A4.15 (see Appendix 4) the value of first resonance frequency of the tri-layer bending structure can be written as [Andrei, Józwik 2008, Krupa 2008 a, Krupa 2009]:

$$f_{res1} = \frac{p_1^2}{4\pi\sqrt{3}}\frac{h_{eq}}{L^2}\sqrt{\frac{E_{eq}}{\rho_{eq}}} \tag{4.10}$$

where h_{eq} is the equivalent thickness and E_{eq} is the equivalent Young modulus defined in the Eq.4.4. The term p_1 is 1.875 and the equivalent density term ρ_{eq} is:

$$\rho_{eq} = \frac{\rho_s h_s + \rho_f h_f + \rho_e h_e}{h_{eq}}. \tag{4.11}$$

Piezoelectric behaviour and influence of temperature on AlN driven microcantilevers

Under a driving voltage U, the piezoelectric properties of the AlN film cause an additional deflection δ_p that can be related to the AlN piezoelectric coefficient d_{31} by [Andrei, Józwik 2008, Krupa 2008 a, Krupa 2009]:

$$\delta_p = \frac{3}{E_{eq}h_{eq}^2} \frac{E_f\left(E_s h_s + E_e h_e\right)}{E_s h_s + E_f h_f + E_e h_e} d_{31} L^2 U \; . \tag{4.12}$$

This expression is in agreement with that developed by Wang et al [Wang 1999] for a symmetric triple film bender. Assuming in the above equation that $h_e=0$ leads to the classic equations for a piezoelectric film deposited on a thick cantilever [Walter 2002].

Under a thermal loading ΔT, an additional deflection δ_{Th} appears. This is related to the thermal expansion coefficients of films α_e, α_f, α_e incorporated in the cantilever structure by the following equation [Andrei 2007 a, Andrei 2008, Krupa 2008 a, Krupa 2009]:

$$\delta_{Th} = 3\frac{\left[E_s h_s^2 - \left(E_f h_f + E_e h_e\right)\left(h_e + h_f\right)\right]\left[\alpha_s\left(E_f h_f + E_e\, h_e\right) - \left(E_f \alpha_f h_f + E_e \alpha_e h_e\right)\right]}{E_{eq}h_{eq}^3\left(E_f h_f + E_s h_s + E_e h_e\right)} L^2 \Delta T \tag{4.13}$$

4.2. Numerical model – FEM simulations

The use of modelling methods based on the Finite Element Method (FEM) is a common technique to obtain predictions of the functionality of MEMS devices. Such computational approach helps to evaluate micromechanical parameters. Numerous models of thermal and electrostatic actuators can be found in the literature [Chauffleur 2004]. However, certain aspects of simulations of piezoelectrically driven structures need to be completed and improved [Zinc 2004, Olivares 2005]. Here, the FEM simulations of the AlN-based microcantilevers were proposed to complete the hybrid methodology (see section 2.4). In particular, the 3D model of the rigid one-side-clamped Si microcantilever with three thin films (two metal electrodes and piezoelectric AlN thin film) was proposed. Its numerical simulations of the static and dynamic responses were performed using the commercially available ANSYS software [ANSYS]. This tool was based on the FEM calculation, i.e. using the numerical method presented in the section 2.2. The general algorithm of the numerical modelling process consists of the following main three steps:

1. Preprocessor

First, the object model is proposed. Data containing its geometry, material properties and element type appropriate for performed analyses is defined. To obtain proper results the used element type has to reflect the constituent equations governing behaviours of materials incorporated into the modelled structure according to desired analysis type. After that, the mesh grid is generated to divide it into connected by nodes discrete elements. The number of nodes depends on the chosen element type and the generated mesh density. Meshing process allows thus to increase the number of nodes for which algorithm finds the solutions causing an increase of the result resolutions. In ANSYS software a free or a mapped meshing can be performed. First type of mesh grid has no restrictions in terms of chosen element shapes, and has no specified pattern applied to it. While, the second one is restricted in terms of the contained element shape and the mesh pattern [ANSYS]. The choice of the mesh type appropriate for the desired analysis is important and should be considered before the model.

2. Processor

Then, boundary conditions and loads (displacement constraints, forces, etc.) are applied to the nodes of the generated mesh. The analysis type (i.e. static, modal, etc., and structural, thermal, piezoelectric, etc.) is defined and the finite element solution is obtained. Appropriate mathematical formulas are implemented in the ANSYS software, which operates in multiphysics mode to solve the system of differential equations governing the mesh behaviours.

3. Postprocessor

Finally, the received solution results are analysed using the ANSYS software, which allows their graphic presentation, as well.

The described algorithm seems to be simple and easy to accomplish it. However, the correct simulations using numerical methods require the suitable knowledge. The proper data preparation and correct interpretations of the obtained results are crucial. The modelling process requires its control in any step of performed algorithm. Therefore, the knowledge of the mechanics and the material strength is indispensable for ANSYS software users.

The following numerical simulations of the 3D microcantilever model were carried out:

a) out-of-plane displacement distribution under force application;
b) stress distribution under various loads (e.g. force and temperature);
c) effect of temperature on shape and deflection;
d) piezoelectric response, i.e. out-of-plane displacement induced by constant voltage load;
e) vibration modes: resonance frequencies and displacement distributions;
f) effect of initial deflection (i.e. internal stress present in the thin films);
g) effect of geometrical and material constant imperfections (observed during the measurements).

The simulations of the homogeneous and tri-layer silicon cantilevers were performed. The comparison between the received results allowed to study the effect induced by the thin films. Moreover, according to the multilayer element, the modelling of the ideal structure was carried out. The notion *ideal* means with the nominal geometry dimensions, (i.e. assumed in design process), material constants (reported in the literature) and no residual stress (i.e. flat object profile). Such a modelling process allowed to obtain the reference to the subsequent analyses, which concerned the simulations including the relevant measurement data. The interactions between the numerical and experimental results were accomplished. They led to understand better the behaviours observed in the real devices (see section 6.3 and Chapter 5). Moreover, they allowed to identify the performance affected cantilever areas considered as the most critical ones because of the stress concentration. Thus, it was developed the 3D numerical model of the investigated cantilever, which corresponds strictly to the fabricated object in regard to its real geometry, material properties, boundary conditions and loads.

4.2.1. FEM simulations for homogeneous Si cantilever

To evaluate the impact of the thin film transducer on the cantilever operation, the simulations of the static, as well as dynamic behaviours were conducted for the homogeneous silicon structure. The modelled fixed – free Si cantilever had the same geometrical dimensions as those of the multilayer device simulated in the section 4.2.2, i.e.:

- length: L = 200 and 800 μm (i.e. minimal and maximal value of the real cantilever length);
- width: w = 50 μm;
- Si thickness: h_{Si} = 15 μm.

In the simulations the *SOLID95* element type representing the 3D structural solid element defined by 20 nodes [ANSYS], as well as the material properties of silicon given in Table 4.3

were used. Moreover, the mapped meshing with hexahedron elements was applied, generating a regular and symmetrical mesh grid with equal node distance.

Structural analysis: out-of-plane displacement distribution versus force

Using the ANSYS finite element solver, the theoretical out-of-plane displacement of the cantilever free-end induced by a force was determined. The mentioned force was applied to the free-end of the device as shown in the Fig.4.3b. Such a concentrated force value was chosen to induce to the model the same cantilever deflection as those measured for the real multilayer devices (see Table 4.1, section 4.2.2). The simulation results of the 800μm long cantilever, i.e. the out-of-plane displacement induced by 282 μN load and the corresponding von Mises stress [ANSYS] distribution are presented in the Figs.4.2a and b, respectively. The modelled map of stress in the homogeneous Si cantilever served as a reference to therelevant results for the tri-layer structure. The comparison of these data allowed to evaluate the influence of the thin films on the cantilever mechanical behaviours (see section 4.2.2).

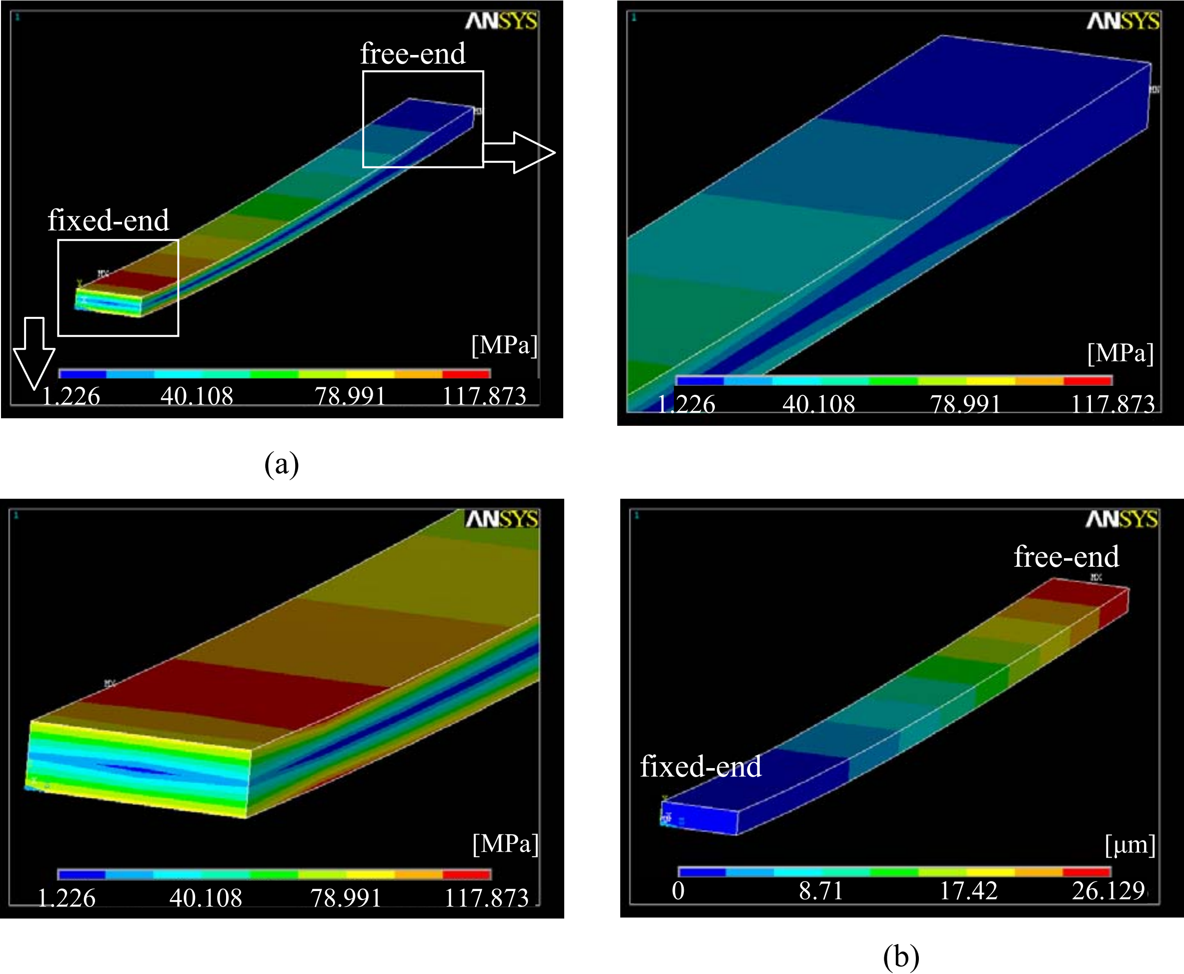

Fig.4.2: Results of loading of 800 μm long Si cantilever by F = 282 μN force applied to its free end: von Mises stress map (a), out-of-plane displacement map (b)

Table 4.1: Applied force total values relating to the measured cantilever initial deflections

Cantilever length L [µm]	**Numerically obtained force F [µN]**	**Deflection δ_m [µm]**
800	282	26.130
	178	16.430
200	1400	2.000
	720	1.020

Modal analysis: determination of resonance frequencies and distribution of vibration modes

Because the fundamental resonance mode is the mode of bending, the bending resonance frequencies and the relevant mode shapes were modelled. The results related to the first three frequencies, determined using an implemented in the ANSYS iterative process, are presented in the Table 4.2. The obtained resonance modes have the same shapes as those of the multilayer cantilevers described in the section 4.2.2.

Table 4.2: Resonance frequencies obtained from FEM modelling

L [µm]	**1st f_{res} [kHz]**	**2^{sd} f_{res} [kHz]**	**3th f_{res} [kHz]**
800	28.451	178.41	500.47
200	459.22	2817.00	7675.30

4.2.2. FEM simulations for tri-layer Si cantilever

We modelled a 3D tri-layer Si cantilever with the same geometrical dimensions as the dimensions presented in the section 3.3.2 (see Table 3.6). Moreover, the effect of the geometrical imperfections noticed in the fabricated cantilevers (see Figs.3.15a and b, section 3.3.3) was also analysed. Therefore, more complicated 3D model was also built basing on the object SEM measurements (see section 3.3.2). In the simulations there were used following element types depending on the performed analysis:

a) *SOLID95* – the 3D structural solid element defined by 20 nodes having three degrees of freedom per node: translations in the nodal x, y, and z directions [ANSYS]. This element was used to carry out the static and modal structural analysis to simulate an out-of-plane displacement distribution under force loading and vibration modes;
b) *SOLID226* – the 3D coupled field solid element defined by 20 nodes having up to five degrees of freedom per node [ANSYS]. Having many capabilities, e.g. structural-thermal and piezoelectric one, this element additionally reflects structural changes (induced by electric field and temperature) allowing to simulate piezoelectric and thermal behaviours.

The properties of the materials incorporated in the modelled structure are presented in the Table 4.3. They are taken from the literature. These materials were considered as

mechanically and thermally isotropic. According to the elastic material constants, the orientation of used silicon substrate (100) and the orientation of sputtered AlN thin film (002) were aligned on the direction of the operational out-of-plane cantilever displacement (see Chapters 3 and 5). This situation permitted to assume the constant values of Young modulus ($E_{<100>}$ and $E_{<002>}$ for silicon and aluminium nitride, respectively). However, the geometrical dimensions of the relevant structure (length >> other dimensions) justified the assumption of thermal isotropy. The perspective view of the modelled structure with the defined materials is shown in the Fig.4.3a.

Table 4.3: Nominal material constants used in structure modelling [Guy 1999, Carlotti 1995, Madou 2002, Dziuban 2004, Andrei 2008, Krupa 2008 a, Edge, Memsnet b]

	Density ρ **[kg/µm³]** **DENS**	**Young modulus** E **[GPa]** **EX**	**Poisson coefficient** ν **PRXY**	**Piezoelectric matrices** d_{ik} **[pm/V]** **PIEZ**	**Thermal expansion coefficient** α **[1/K]** **ALPX**	**Thermal conductivity** k **[pW/µmK]** **KXX**
Si	$2.33 \cdot 10^{-15}$	129.5	0.3		$2.44 \cdot 10^{-6}$	$167 \cdot 10^{6}$
AlN	$3.30 \cdot 10^{-15}$	332	0.3	$d_{31} = -2$	$4.30 \cdot 10^{-6}$	$175 \cdot 10^{6}$
CrNi	$8.05 \cdot 10^{-15}$	237	0.3		$9.50 \cdot 10^{-6}$	$90.3 \cdot 10^{6}$

The mapped version of meshing with hexahedron elements was applied [ANSYS] generating a regular and symmetrical equidistant mesh grid on the modelled structure consisted then of 2925 20-node discrete elements (see Fig.4.3b). Such meshing allowed to obtain a sufficient resolution of the simulated data received within a reasonable amount of time. According to the design of the modelled device, fully-rigid one-side-clamped cantilevers with various loads were realised (see Fig.4.3b). The example of symmetric concentrated force applied to the cantilever free-end is shown in the Fig.4.3b.

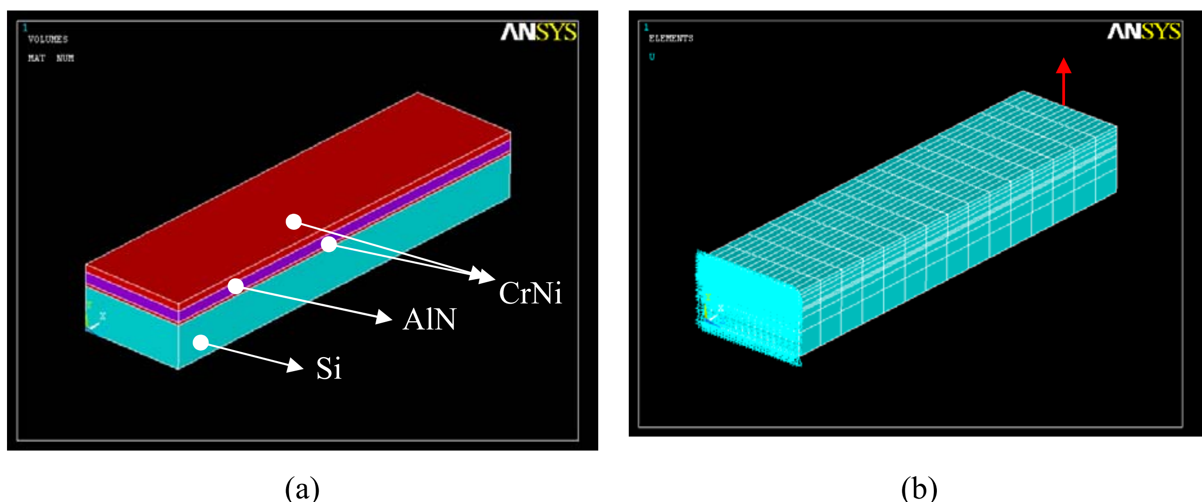

(a) (b)

Fig.4.3: Perspective view of 3D cantilever primary model: presentation of structure and used materials (a), as well as boundary conditions and force loading (b)

Structural analysis: out-of-plane displacement distribution vs. force

The theoretical out-of-plane displacement of the cantilever free-end induced by force was determined using the ANSYS finite element solver. The force was applied to the free-end of cantilever beam as shown in the Fig.4.3b. The Table 4.4 includes the values of applied forces causing initial deflections of the cantilevers. The illustration of 3D map of the out-of-plane displacement is shown in the Fig.4.4b, obtained for the 800 μm long cantilever loaded by a force of 529 μN. Modelling the resulting distribution of stress allowed thus to identify the localisation of stress concentration in the sample, with emphasis to identify the most critical areas from the point of view of failure and damage generation. The Fig.4.4a shows the example of von Mises stress distribution [ANSYS], obtained for the 800 μm long cantilever. Here, the AlN film is 1.4 μm thick and the measured initial deflection is 26.13 μm. The comparison of these results with those for the homogeneous Si structure (see section 4.2.1) allowed to determine the influence of the thin films on the mechanical behaviours of the cantilevers. The results were in a good agreement with the theory (see section 4.1 and Appendix 4). In particular, the expected maximal stress concentration was noticed in the clamped area for both considered structures. Moreover, the symmetrical stress distribution, observed in the homogeneous cantilever (see Fig.4.2a), became nonsymmetrical for the multilayer devices (see Fig.4.4a). The neutral plane (related to the zero stress level) was thus shifted from the middle position in the Si substrate (valuable for homogeneous structure) with value depending on the thin film geometrical and material parameters (see Eq.4.6, section 4.1). In this model, the maximal stresses were generated in the thin films (see Fig.4.4a) what is important according to the device reliability.

Table 4.4: Total values of applied force relating to the measured cantilever initial deflections

AlN film thickness h_{AlN} [μm]	**Cantilever length L [μm]**	**Numerically obtained force F [μN]**	**Initial deflection δ_m [μm]**
1.4	800	529	26.130
	400	1120	6.990
	200	2700	2.000
1.0	800	298	16.430
	600	465	10.880
	400	750	5.164
	200	1200	1.020

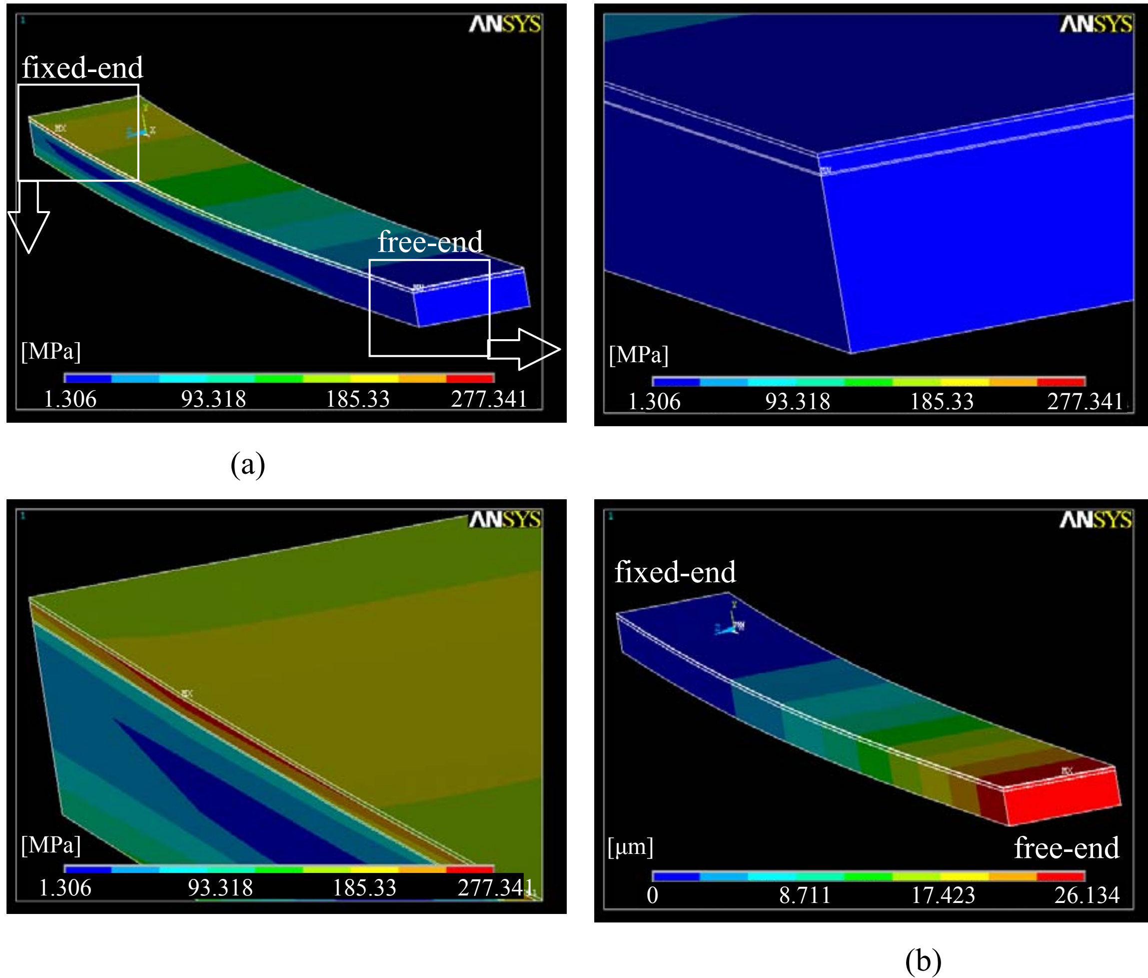

Fig.4.4: Exemplary results of loading of 800 μm long cantilever with h_{AlN} = 1.4 μm by F = 529 μN force applied to its free end: von Mises stress map (a), out-of-plane displacement map (b)

Modal analysis: determination of resonance frequencies and vibration mode distributions

Modelling of the dynamic response of the piezoelectric microcantilevers consisted of identifying of their resonant frequencies and shape of vibration modes. The fundamental resonance is a bending vibration mode in the direction of the out-of-plane displacement. Therefore, the resonant frequencies of higher orders correspond also to this kind of modes. The resonance frequencies were found using an iterative process implemented in the ANSYS, allowing to solve the system of equations over an appropriate range of frequency. Thus, the first four resonance frequencies were modelled for the investigated samples with consideration of various electrode materials and different AlN film thicknesses. The results obtained for the cantilevers made by the initial fabrication process and the cantilevers fabricated by the optimised manufacturing process (see section 3.3) are given in the Tables 4.5 and 4.6, respectively. However, the deepest analysis, taking into account the static, thermal and piezoelectric properties, was performed for the final version of the cantilevers, i.e. manufactured using the improved technology. Therefore, further considerations will concern the final structures only. The shape of four elementary vibration modes for the 800 μm long cantilever are illustrated in the Fig.4.5. The comparison of these results with those obtained for the homogeneous cantilevers (see Table 4.2) permits to conclude that

the resonance frequency is mainly depending on the thickness of silicon substrate, sample dimensions (length and thickness) and material parameters.

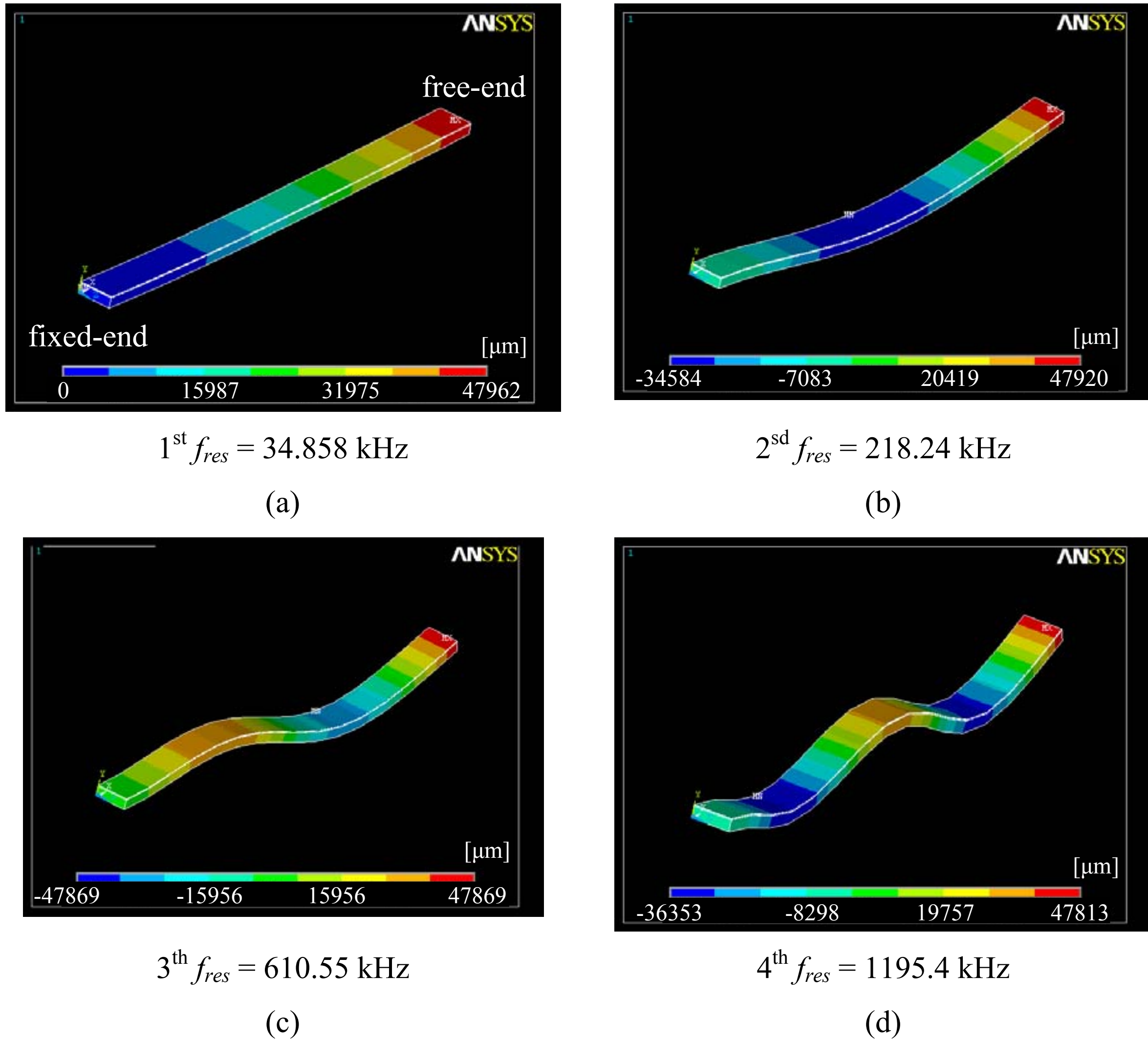

1st f_{res} = 34.858 kHz

(a)

2sd f_{res} = 218.24 kHz

(b)

3th f_{res} = 610.55 kHz

(c)

4th f_{res} = 1195.4 kHz

(d)

Fig.4.5: FEM simulations of four elementary bending resonance modes obtained for 800 µm long final ("improved") cantilever (with h_{AlN} = 1.4 µm)

Table 4.5: Resonance frequencies obtained from FEM modelling of initial devices

Bottom electrode	h_{AlN} **[µm]**	L **[µm]**	**1st** f_{res} **[kHz]**	**2sd** f_{res} **[kHz]**	**3th** f_{res} **[kHz]**	**4th** f_{res} **[kHz]**
Al	0.4	800	30.817	193.13	541.17	1062.1
		700	40.257	252.07	705.30	1381.4
		500	78.946	492.81	1372.4	2669.9
		200	493.95	3004.0	8066.6	14977
Au	1.0	200	478.80	2910.5	7810.7	14494

Table 4.6: Resonance frequencies obtained from FEM modelling of final devices

Bottom electrode	h_{AlN} [μm]	L [μm]	1st f_{res} [kHz]	2sd f_{res} [kHz]	3th f_{res} [kHz]	4th f_{res} [kHz]
CrNi	1.4	800	34.858	218.24	610.55	1195.4
		600	61.986	387.12	1078.7	2100.0
		400	139.53	866.05	2391.0	4595.8
		200	557.67	3360.2	8912.0	16318
CrNi	1.0	800	33.494	209.76	587.08	1150.3
		600	59.563	372.13	1037.6	2021.8
		400	134.08	832.9	2302.2	4432.3
		200	536.14	3239.2	8621.4	15848

The measurement data concerning the initial deflection of the cantilevers were introduced to the simulation procedure. The influence of the initial deflection, obtained experimentally, on the first three resonance frequencies is presented in the Table 4.7 and in the Fig.4.6b. This table includes the microelements of various lengths and different thicknesses of the AlN film. The variation of first resonance frequency vs. initial deflection of the 800 and 200 μm long cantilevers is illustrated in the Fig.4.6a. To justify the observed resonant behaviour discrepancies, the changes obtained from the FEM analyses in the range of relevant deflection values seemed to be too small (see Table 4.7). The differences between the measured and simulated resonance frequencies (see Table 5.4, section 5.3) were found to be about 3.32 kHz and -23.80 kHz for the 800 μm and 200 μm long objects, respectively. According to the numerical modelling, stresses introduced to the thin films during fabrication process do not provide significant resonance frequency changes.

Table 4.7: Influence of relevant measured cantilever initial deflection on dynamic response: resonance frequency changes (the case of final devices)

h_{AlN} [μm]	L [μm]	Initial deflection δ_m – measured values [μm]	Δ1st f_{res} [kHz]	Δ2sd f_{res} [kHz]	Δ3th f_{res} [kHz]
1.4	800	26.130	0.011	0.03	0.03
	400	6.990	0.04	0.1	0.1
	200	2.000	0.22	0.50	0.50
1.0	800	16.430	0.007	0.02	0.02
	600	10.880	0.013	0.02	0.0
	400	5.164	0.04	0.07	0.0
	200	1.020	0.1	0.2	0.2

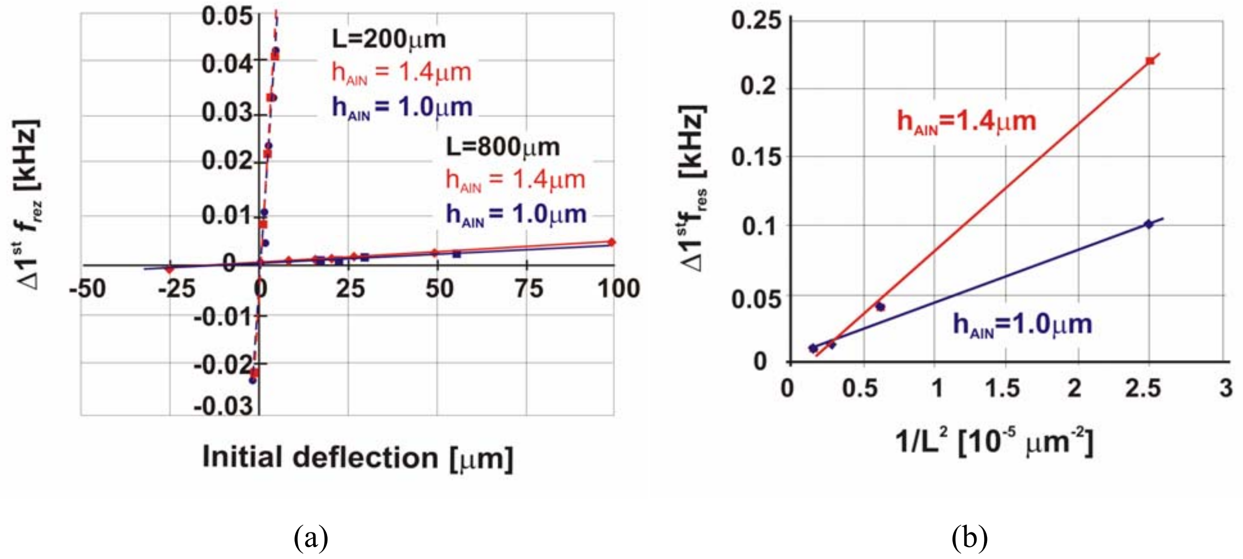

(a) (b)

Fig.4.6: Variation of first resonance frequency versus initial deflection (a) and length^{-2} determined at measured value of initial deflection (b)

Temperature effect analysis: deflection changes vs. temperature variations

Thermal simulations were performed using the ANSYS solver to determine the environment stability of the AlN samples. The influence of the temperature on the cantilever deflection, measured at free-end extremity of the tip, was modelled and compared with the results of deflection at reference temperature (T_{ref} = 20°C). The static response at temperature range from 20 to 100°C was calculated, defined with temperature increment of 1°C. The data for cantilevers of various lengths and with two different thicknesses of the AlN film is presented in the Table 4.8. The changes in deflection of the 800 μm long cantilever tip are shown in the Fig.4.7. The ANSYS modelling allowed to evaluate the corresponding stress distribution induced by thermal effects, making easier the identification of areas of the highest stress concentration. The shape and the stress distribution of the 800 μm long cantilever maintained at the temperature of 100°C are illustrated the Figs.4.8b and a, respectively. The thermal flux generated by the thermal loading of 100°C is presented in the Fig.4.9.

Table 4.8: Free-end deflection change induced by increase of temperature

h_{AlN} [μm]	L [μm]	$\Delta\delta_{Th}$ at Δ1°C [nm]
1.4	800	-54
	600	-30
	400	-14
	200	-4
1.0	800	-53
	600	-30
	400	-13
	200	-4

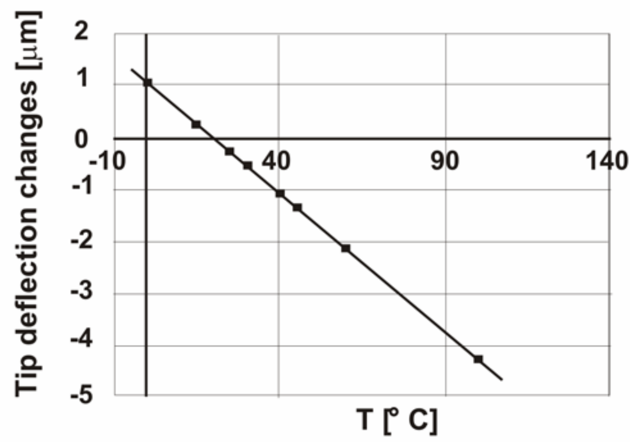

Fig.4.7: Deflection changes of free-end tip of 800 µm-long cantilever vs. various temperature (at T_{ref} = 20°C)

(a)

(b)

Fig.4.8: Results of temperature influence obtained for 800 µm long cantilever modelled with h_{AlN} = 1.4 µm: von Mises stress (a) and shape, i.e. out-of-plane displacement (b) distribution at 100°C relating to T_{ref} = 20°C

The obtained results pointed out, that the stable environmental conditions during the operation of the investigated actuators are indispensable. Especially temperature has to be controlled. Even small temperature variation (see Table 4.8) causes the cantilever displacement changes which should be considered. The temperature influence is induced by the differences in the thin film thermal expansion coefficients. Moreover, analysing the combined stress distribution (see von Mises stress, Fig.4.8a) corresponding to the thermal loading showed that the critical areas of stress concentration are not only at expected clamped cantilever side, but also are attributed to the thin films. Simulations showed that thermal flux related to thermal gradient and the stress generation has the largest value in the bottom thin metal electrode (see Figs.4.8a and 4.9a). This effect can explained the failures observed during the experiments (section 6.3.1) related to the thin film stack delaminations induced by the electrical breakdown and the abrupt heat flow.

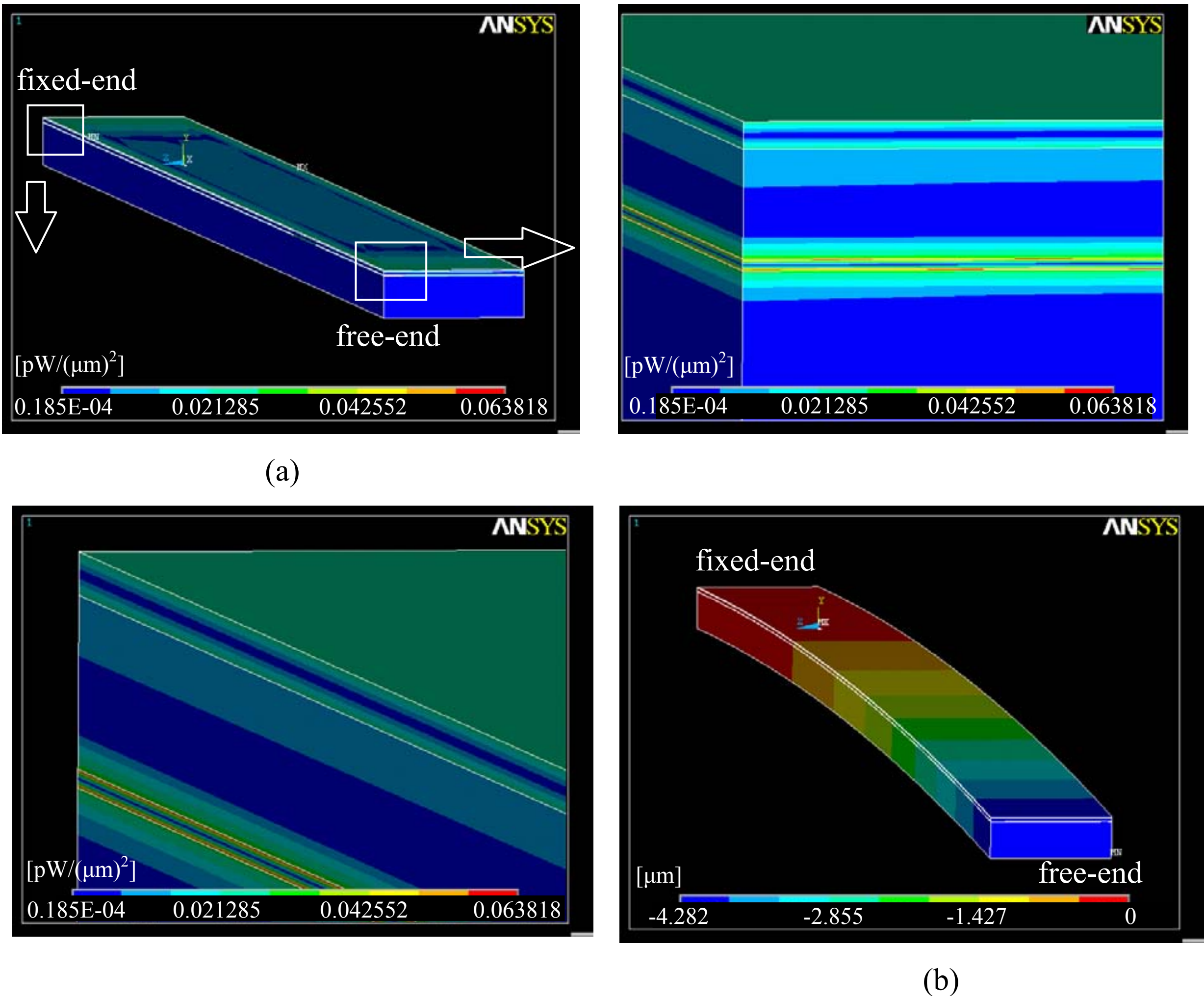

Fig.4.9: Temperature influence results obtained for 800 μm long cantilever modelling with h_{AlN} = 1.4 μm: thermal flux vector sum (a) and shape, i.e. out-of-plane displacement (b) distribution at 100°C relating to T_{normal} = 20°C

Analysis of piezoelectric response: out-of-plane displacement vs. constant voltage

The piezoelectric response of the AlN-driven cantilever was modelled setting a constant driving voltage. The sequentially coupled piezoelectric–structural calculation, present the ANSYS module of multiphysic analysis was performed, where the finite element solutions represented the map of displacements. The cantilever free-end displacement produced by the constant voltage was determined. The changes of displacement as a function of driving voltage for the 800 and 200 µm long cantilevers with two different thickness of the AlN film: 1.4 and 1.0 µm are illustrated in the Fig.4.10. Assuming d_{31} = -2 pm/V and setting the driving voltage at 10 V_{DC} (see section 6.3.1) the simulated free-end displacement is -199 nm for the 800 µm long sample having 1.4 µm thick AlN film. These data matches very well with the theoretical displacement (-213 nm) calculated according the Eq.4.12.

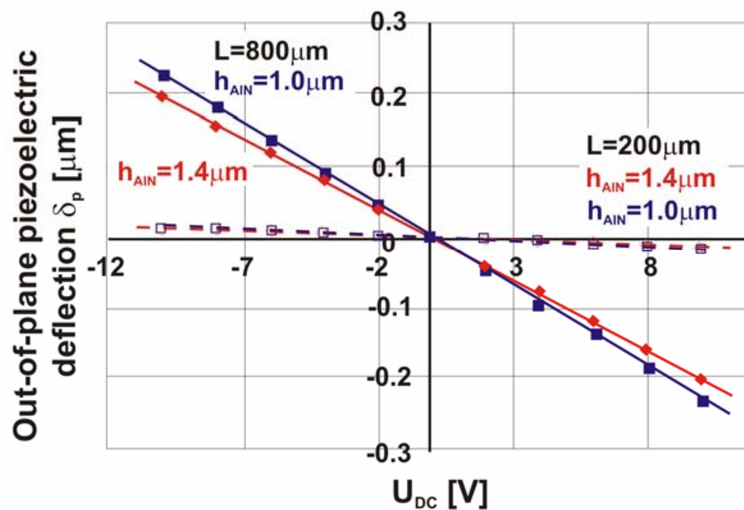

Fig.4.10: Relationship between cantilever free-end displacement and DC driving voltage

The stress resulting from piezoelectrically induced displacement was also analysed. The stresses were concentrated in the thin films having the maximal values in the AlN layer. Such a conclusion is crucial according to the reliability study (see section 6.3) and the operation behaviours. Observed phenomenon could explain the top electrode damage appeared during the dynamic tests of mechanical fatigue discussed in the section 6.3.4 as a result of the concentration of cyclic stress within the thin films. The performed simulations took also into account the measured cantilever initial deflection (see section 5.2). However, obtained results did not show a noticeable influence of the mentioned parameter on piezoelectric response of the cantilever.

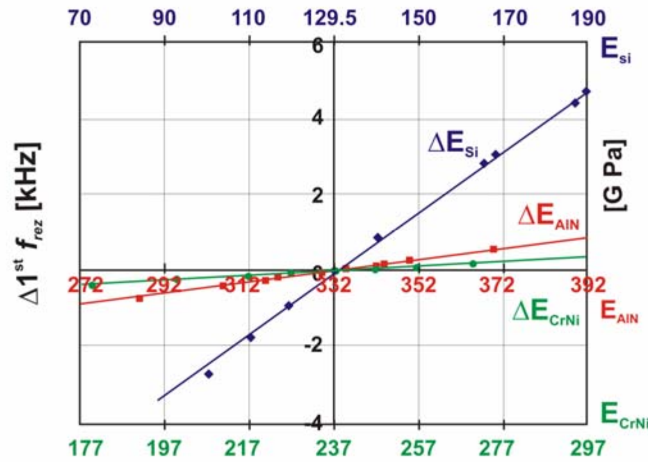

Fig.4.11: Variation of resonance frequency as a function of Young modulus' of materials incorporated in 800 μm long cantilevers with 1.4 μm of AlN

(a)

(b)

(c)

(d)

Fig.4.12: Variation of resonance frequency versus thickness of top and bottom CrNi electrode (a), AlN thin film (b), Si substrate and cantilever's length (c, d)

To obtain a better understanding of our piezoelectric devices, it is crucial to identify the reasons of the deviations between the characteristics of designed and realised cantilevers. In particular, such deviations can result from the technological imperfections producing the geometrical imperfections, the material constant discrepancies or earlier mentioned residual stress introduced by deposition technique of thin films (see sections 3.3.3 and 5.2). The influence of the mentioned causes was simulated. The effect of cantilever length, Si and thin film thickness variations as well as Young modulus differences on the resonance frequency are presented in the Fig.4.12 [Krupa 2008 a] and in the Fig.4.11, respectively. Moreover, according to the design (see section 3.1), the geometrical imperfections measured by SEM (see Figs.3.15a and b, section 3.3.3) were taken into account. Because of the time-consuming FEM simulations, only length deviations (see Figs.3.15a and b, section 3.3.3) caused by silicon underetching and electrode misalignment process (see section 3.3.2) were modelled and numerically analysed. The last assumption was justified due to the resonance cantilever behaviour dependence on the square of length (1st $f_{res} \sim 1/L^2$, see Eq.4.10). The simulations used the model built on the basis of SEM images, shown in the Fig.4.13. The mechanical, dynamic and thermal responses of the 800 μm long devices were analysed.

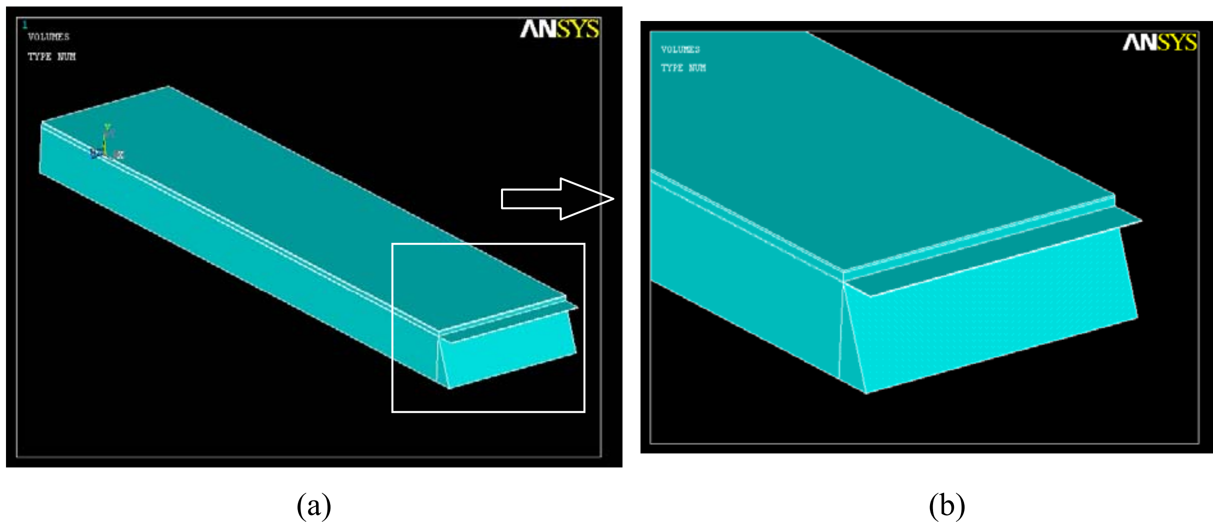

(a) (b)

Fig.4.13: Perspective view of cantilever based on SEM measurements: oblique view (a), zoom on the extremity of tip (b)

The FEM simulations of dynamic response demonstrated that variation of the cantilever length and variation of the silicon substrate thickness, as well as Young modulus of silicon (see Figs.4.12 and 4.11) have the strong influence on the resonance frequency. The ranges of considered parameter changes obtained experimentally (see section 3.3.3) were taken into account. However, it was found that only first two of the mentioned parameter variations could explain the discrepancies observed in the resonance response between the theory, the simulations and the measurements (see section 5.3), what was confirmed and validated by SEM measurements. The influence of the object length and the thickness of Si cantilever was then analysed in detail including the simulations for the 200 and 800 μm long cantilevers with 1.4 and 1.0 μm thick AlN film (see Figs.4.12c and d). Moreover, taking into account the measured values of first resonance frequency f_{res} (see section 5.3), the proper cantilever's length L' and silicon beam thickness h_{Si}' were extracted separately from the analytical model (see Eq.4.10). Afterwards, the FEM modal simulations were accomplished again (1st f_{res}'). The resulting values of L' and h_{Si}' are presented in the Tables 4.9 and 4.10, respectively. However, the found deviations were too large with comparison to the measured geometrical imperfections (see section 3.3). The Si underetching process and the electrode misalignment,

as a length decrease, are unable to explain such large changes. Therefore, the observed deviations in the dynamic response of the piezoelectric actuators were found as results of the both mentioned effects occurred simultaneously.

Table 4.9: Lengths corresponding to first resonance frequencies of fabricated cantilevers analised at nominal value of Si thickness (h_{Si}= 15μm)

h_{AlN} [μm]	L [μm]	L' [μm]	$1^{st} f_{res}$ [kHz]	$1^{st} f_{res}'$ [kHz]
1.4	800	763.90	34.858	38.232
	400	376.36	139.53	157.61
	200	203.88	557.67	536.70
1.0	800	761.66	33.494	36.953
	600	571.03	59.563	65.764
	400	376.89	134.08	151.04
	200	204.64	536.14	512.16

Table 4.10: Si thicknesses corresponding to first resonance frequencies of fabricated cantilevers analised at nominal lengths of the samples L

h_{AlN} [μm]	L [μm]	h_{Si}' [μm]	$1^{st} f_{res}$ [kHz]	$1^{st} f_{res}'$ [kHz]
1.4	800	16.70	34.858	38.257
	400	17.27	139.53	157.61
	200	14.35	557.67	537.04
1.0	800	16.77	33.494	36.973
	600	16.78	59.563	65.779
	400	17.16	134.08	151.01
	200	14.24	536.14	512.40

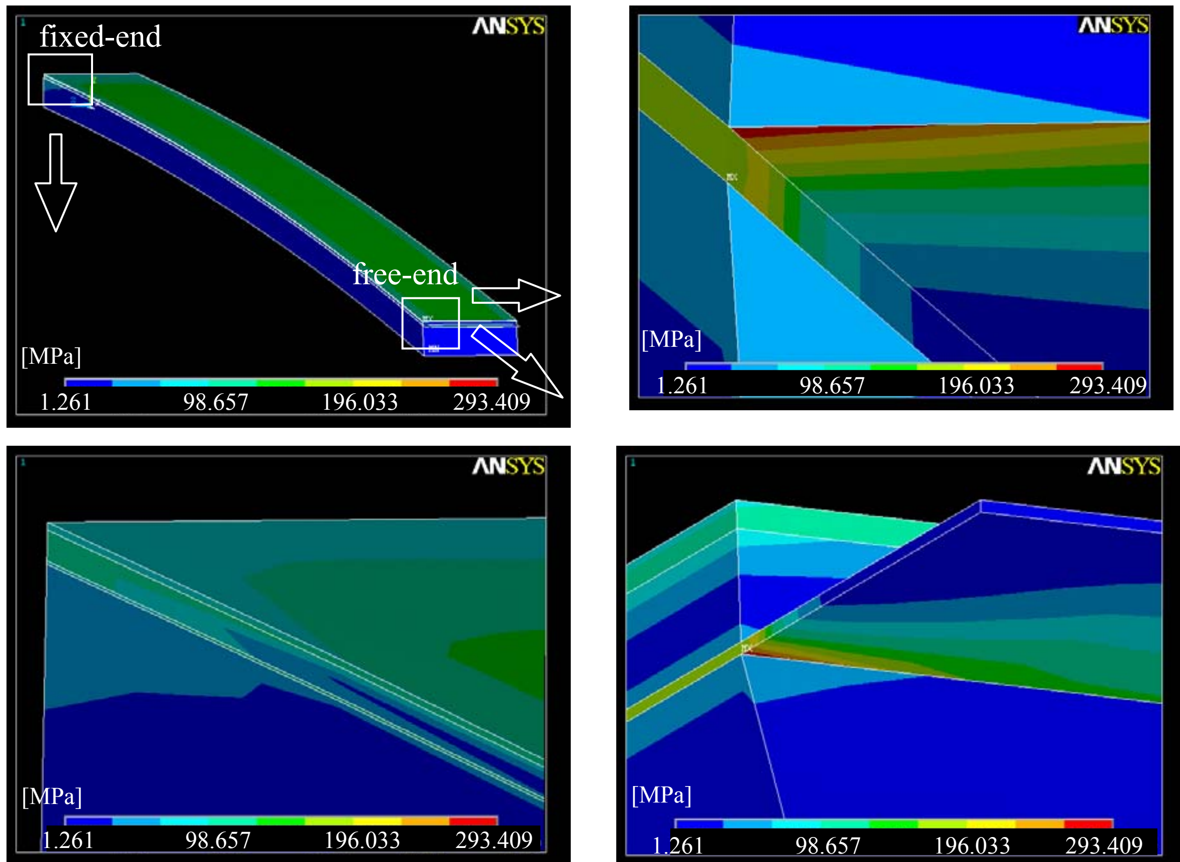

Fig.4.14: Simulation results obtained for 800 µm long cantilever (h_{AlN} = 1.4 µm) model basing on SEM images: map of thermally induced von Mises stress

The measured geometrical imperfections of the fabricated microcantilevers were analysed too. The calculated distribution of von Mises stress and the thermal flux were compatible with those received for the devices modelled on the basis of their designed geometry (see Figs.4.4a and 4.9a). Namely, the area of the mechanical stress concentration of thin film was situated near the extremity of the device fixation. While, the heat flew through the thin film of the bottom electrode. However, according to the thermally induced von Mises stress distribution, the highest stresses were generated in the discontinuity areas of the multiple material interfaces. Such stress concentration areas are illustrated in the Fig.4.14. They are localised near to the bottom electrode at the cantilever free-end. This observation allowed to explain the delamination failure noticed during the reliability tests (see section 6.3.1). In these tests the failure has started just from the free-end of the investigated microelements. The area of high stress concentration, limited the voltage level which could be applied without delamination. Thus, by improving technology to eliminate Si underetching it could be possible to avoid delamination or to increase the voltage level which could be applied without delamination.

4.3. Conclusions

We performed the analysis of the single-clamped microcantilevers, actuated by thin film AlN transducer. The analytical and numerical 3D models taking into account the tri-layer structure and relevant materials incorporated in these devices were developed. The numerical simulations evaluating the performances of such piezoelectric microactuators were obtained using the ANSYS software based on the Finite Element Methods FEM. The modelling data

served as a basis for the subsequent static and dynamic sample analyses. The mechanical, thermal and piezoelectric responses were evaluated. The analyses of cantilever tip deflections and stress distributions induced by the concentrated force applying to the free end of cantilever and the thermal load were accomplished. Moreover, the vibration modes associated with the resonance frequencies and the mechanical response under constant electrical excitation were modelled. The various cantilever geometrical dimensions including the length and the AlN thickness were considered. According to the piezoelectric actuation the good consistence of the simulation response with the experimental results was obtained. Piezoelectrically induced displacement caused the maximal stress introduced to the thin films. It explains the damage of top electrode appearing during the reliability fatigue tests, when the cyclic stress concentrated in thin films was generated. The effects of the thin films on the mechanical performances of the resulting microactuator, including the stress distribution and resonance frequency, were discussed. This last study was based on the comparison between the model of the tri-layer structure and of the homogeneous one. Thus, the symmetrical stress distribution was disturbed and the neutral plane was shifted from the middle position in the Si substrate (valuable for the homogeneous structure). This introduces the maximal stress generation in the thin films close to the cantilever fixed-end. The significant deviations between the measured resonance frequencies and the simulated responses were discussed too. Therefore, the effect of deviations of the various geometrical and material parameters was modelled taking into account the received measurement data. The effect of initial deflections (i.e. internal stress present in the thin films) was also considered as well. The analysis showed that the object length and Si thickness mainly affected its resonance property. Fabricated final microcantilevers were found to be shorter and have thicker Si substrate compared to the designed values. Therefore, these technologically induced imperfections caused increase of the experimentally obtained resonance frequency. The initial deflection did not show significant discrepancies in the actuator dynamic operation. Only slight increase of the resonance frequency was noticed for all tested object lengths, which was found to be higher for the shorter structures. The temperature effect and the thermally induced stresses were discussed too. The results of the thermally generated cantilever tip displacement were in convergence with the experiments. Found high temperature sensitivity confirmed the need of environmental conditions control during the actuator operation. However, the analyses of the combined stress distribution (von Mises stress) introduced by temperature changes was more interesting showing that the stress was concentrated in the electrode thin films. The thermal simulations taking into account the change of the fabricated device geometry were also accomplished. The difference between the designed and fabricated profiles has been resulted from the technologically induced silicon underetching and electrode misalignment processes. Obtained modelling results showed that the highest stresses were generated in the discontinuity areas of the object multiple material interfaces. They were found to be introduced to the bottom electrode from the cantilever free-end. The thermal flux related to thermal gradient and the stress generation had the largest value in the bottom thin metal electrode. Mentioned numerical modelling allowed to explain the mechanism of the failures observed during the reliability tests. Namely, the thin film stack delaminations started from the microelement free-end which were induced by the electrical breakdown and the abrupt heat flow. Performed simulations allowed then to identify the object areas of stress concentration, which are the most critical ones for the failure and damage generations. The interactions between the modelling and the measurements were crucial to develop the model of piezoelectric microactuator which describe more closely the real device. The finite element analysis could be employed to the operational behaviour prediction at the design stage as well as to the analyses of the performances obtained for the fabricated piezoelectric thin film microactuators.

Chapter 5

Material properties and electromechanical performances of AlN thin films incorporated in microcantilever actuators

In this chapter the characterisation of the AlN driven microcantilevers basing on the interactions between measurements, FEM simulations and analytical considerations will be presented. The material properties and the electromechanical performances of the tested objects will be determined. Namely, their measured static and dynamic parameters as well as calculated using these measured quantities the material, piezoelectric, thermal and electric characteristics will be presented. Their deviations over entire wafer will be statistically analysed and estimated to determine the technological reproducibility of the performances, crucial for applications of the considered devices. The obtained parameters will be given basing on the statistics of median and standard deviation calculated from a serie of randomly chosen microcantilevers with the same design. They will allow to infer about the properties of the investigated microelement parent population. The geometrical deviations of the cantilever length, silicon substrate thickness and thin film thickness' will be taken into account. Moreover, the influence of the bottom electrode, AlN deposition conditions and AlN piezoelectric film thickness on the residual stress, the crystallographic, elastic and piezoelectric properties will be also analysed. The influence of environmental and electrical conditions focused on temperature and resistance effects will be presented, as well. It will allow to determine the performance stability and reproducibility of the devices during their operation in the standard weather conditions. The functionality analysis as well as the quality and the long-term stability evaluation of the fabricated AlN thin film used in dedicated for MEMS actuator microcantilevers will be discussed basing on the proposed hybrid methodology. Obtained results will allow to identify the geometrical and the functional discrepancies between the designed and the real objects. It will be shown that the proper selection of the design, materials and manufacturing processes is crucial. Performed researches will give valuable information concerning the design and the fabrication of the high quality piezoelectric microactuators with low internal stress level and demanded performances for the microsystems.

5.1. Material behaviours – crystallographic and elastic properties

A serie of test structures especially designed for process control was fabricated to determine the crystallographic and mechanical properties of the AlN thin film focused on its structure orientation, nanoindentation modulus, hardness and intrinsic residual stresses (see section 5.2). The influence of the bottom electrode nature on these parameters was investigated. Mentioned test objects consisted of the arrays of 0.5 mm wide and 13 μm thick silicon cantilevers with the lengths varying from 0.5 mm up to 3.5 mm. On the top of such elements the metal – AlN film stack was deposited. Two metals serving as the bottom electrodes were tested: 160 nm thick CrNi and 240 nm thick Pt film. The CrNi was deposited using the same conditions as those for the final, investigated devices (see section 3.3). While, the Pt was sputtered on a non biased, non heated substrate at 120 W (0.22 A) using a 1.1 Pa Ar gas. The AlN film had the thickness of 0.8 μm and was deposited also using the same

conditions as those for the final devices fabrication (*fast recipe*, see Table 3.1, section 3.3.1). The X-ray diffraction (XRD), nanoindentation and AFM measurements were performed to determine the relevant properties [Oliver 1992, Banks 2006 d, Delobelle 2006, Osten 2007, Andrei 2008].

Crystallographic properties

According to the experiments the AlN thin film morphology depended strongly on the used electrode (see Fig.5.1). In the Fig.5.1a [Andrei 2007 a, Andrei 2008] the X-rays diffraction spectrum of the AlN films deposited on the CrNi and Pt electrodes are presented. For the CrNi metal the AlN film crystallites were perfectly (002) oriented. The peaks related to the CrNi film were also identified. Moreover, the XRD image shows the presence of additional peaks (denoted as stars in the Fig.5.1a), which probably correspond to the various compounds of the CiNi electrode (e.g. an oxy-nitride of CrNi). According to the structures with (111) oriented Pt as the substrate for AlN deposition, the (002) direction of the AlN crystallites was found to be more pronounced (see Fig.5.1a). However, in this case besides the Pt related peak, the important flat hill at about 45° was also identified in the more rough XRD spectrum. It could be explained by the presence of amorphous phase or AlN material impurities. This means that the morphology of the films was more complex. Studying the morphology of the AlN thin film, the rc FWHM for (002) AlN was measured too. The value of this parameter was found to be smaller in the case of the Pt electrode (1.37°) than the CrNi one (2.68°) as presented in the Fig.5.1b [Andrei 2007 a, Andrei 2008]. It showed a better quality of (002) oriented crystals for the Pt electrode. Discussed measurement results indicated then that the choice of the CrNi electrode is more suitable for MEMS applications. Since, the AlN thin film deposited on this material exhibited better, pure (002) orientation (without any non-(002) traces or impurities) despite its poorer crystallinity (weaker (002) XRD peak and wider rc FWHM of up to 2.68º). The AlN pure oriented crystallographic texture without any impurities is more critical for the piezoelectric response than the rc FWHM parameter (see section 1.5) [Iborra 2004].

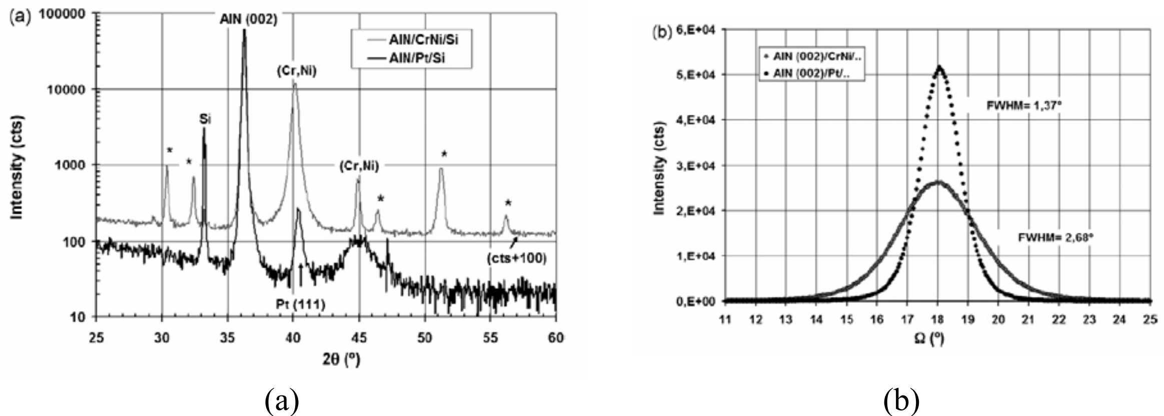

(a) (b)

Fig.5.1: X-ray spectrums obtained for AlN on CrNi and Pt (a), rc FWHM for (002) oriented AlN (b)

Elastic properties

The nanoindentation modulus $M_{<hkl>}$ [Delobelle 2006] and the hardness $H_{b<hkl>}$ of the AlN thin film were measured and analysed. The nanoindentation tests using a nanoindenter IIS (Nano-Instruments) with a Berkovich tip were performed [Andrei 2008]. The $M_{<hkl>}$ modulus of a single crystal for the crystallographic direction determined by a director cosine α_i is given by:

$$M_{<hkl>} = 16\pi^2 \left[\int_0^{2\pi} \alpha_m \beta_{km}^{-1}(c_{ij}, \gamma) \alpha_k d\gamma \right]^{-1} . \tag{5.1}$$

While, $M_{<hkl>}$ measured in nanoindentation test is determined by:

$$M_{<hkl>} = \left[\frac{1}{M_r} - \left(\frac{1-\nu^2}{E} \right)_{ind} \right]^{-1} = \left(\frac{E}{1-\nu^2} \right)_{mat} \tag{5.2a}$$

and $$M_r = \frac{\sqrt{\pi}}{2\beta\sqrt{A}} \frac{dP}{dh}, \tag{5.2b}$$

where A is a projected contact area, P – an applied load, h – penetration depth, β = 1.034 for the Berkovich's tip, $(E/(1-\nu^2))_{ind}$ is a reduced modulus of the diamond indenter, $(E/(1-\nu^2))_{mat}$ is a reduced modulus of the tested material, E – Young's modulus, ν – Poisson coefficient, γ - an angle in surface plane and $\beta_{km}(c_{ij},\gamma)$ – a matrix as a function of stiffness c_{ij} and γ [Delobelle 2006].
The measured hardness is given by:

$$H_{b<hkl>} = \frac{P}{A}. \tag{5.3}$$

There are no general analytic equations allowing to calculate the $M_{<hkl>}$ modulus. However, for some configurations the approximated solutions of the Eq.5.1 are available giving the $M_{<001>}$ and the $M_{<100>}$ modulus calculated on the base of the elastic (stiffness) constants c_{ij} (see Eqs.5.4) [Delafargue 2004, Delobelle 2006].

$$M_{<001>} = \frac{2}{\sqrt{\left(\frac{c_{11}}{c_{11}c_{33} - c_{13}^2} \right) \left(\frac{1}{c_{44}} + \frac{2}{\sqrt{c_{11}c_{33}} + c_{13}} \right)}} \tag{5.4a}$$

$$M_{<100>} = M_{<110>} = \sqrt{\left(\frac{c_{11}^2 - c_{12}^2}{c_{11}} \right) \sqrt{\frac{c_{11}}{c_{33}}} M_{<001>}}\ . \tag{5.4b}$$

Various c_{ij} parameter values of sputtered AlN thin films [Carlotti 1995], epitaxial AlN thin films grown at high temperature [Tsubouchi 1981, Wright 1997] and bulk AlN have been reported in the literature. These elastic constants and the corresponding nanoindentation modulus of $M_{<001>}$ and $M_{<100>}$ are then given in the Table 5.1.

Table 5.1: Values of c_{ij} elastic (stiffness) constants (for an hexagonal symmetry $c_{12}=c_{11} - 2c_{66}$) and $M_{<hkl>}$ indentation modulus of AlN material

AlN	c_{11}	c_{13}	c_{33}	c_{44}	c_{66}	$M_{<001>}$	$M_{<100>}$
High quality sputtered [Carlotti 1995]	360	123	410	116	119	342	319
Low quality sputtered [Carlotti 1995]	326	122	401	118	108	316	286
Epitaxial [Tsubouchi 1981]	345	120	395	99	110	335	306
Bulk [Wright 1997]	396	108	373	116	129.5	329	344

As reported the elastic constants c_{ij} of the sputtered AlN film exhibit an appreciable dependence on the microstructural properties (i.e. the crystal orientation forming in the deposition process) of this film, which are strongly affected by the deposition conditions. Therefore, according to the presented above AlN film crystallographic properties the $M_{<hkl>}$ modulus should not be constant. Obtained experimental results shown in the Fig.5.2

[Andrei 2007 a, Andrei 2008] confirmed this consideration. The measured evolution of the mean values of the $M_{<hkl>}$ and the hardness $H_{b<hkl>}$ vs. the reduced indentation depth h/h_f are presented in the Figs.5.2a and b, respectively. The experiments were accomplished for the AlN thin film deposited on the two kinds of tested electrodes (CrNi/Si and Pt/Si). The quantities h and h_f represent a depth of nanoindenter penetration and AlN film thickness, respectively. Because of the presence of the substrate the $h/h_f \leq 10\%$ should be required [King 1987, Saha 2002] to study the elastic parameters in the relation with the AlN microstructural morphology. Thus, $h = 25$, 50 and 75 nm ($3.1\% \leq h/h_f \leq 9.4\%$) were taken into account and analysed. The mean values of the nanoindentation modulus $M_{<hkl>}$ (for $h/h_f \approx 0$) were found to be 340 ± 10 GPa for AlN/CrNi/Si and 305 ± 10 GPa for AlN/Pt/Si. Obtained measurement results (see Fig.5.2a) showed that the $M_{<hkl>}$ decreased in term of h/h_f for higher indentation depth h (i.e. for $h/h_f \geq 10\%$), what was explained by the $M_{<hkl>}$ (AlN) > $M_{<100>}$(Si) = 129.5 GPa and $M_{<hkl>}$ (AlN) > $M(SiO_2)$ = 80 GPa.

While, the hardness $H_{b<hkl>}$ of the tested AlN film was determined as an increasing function of the reduced indentation depth for $h/h_f \leq 10\%$ because of the spherical shape of the used indenter tip whose radius was in the order of 400 nm [Xue 2002]. Thus, only the values for $h/h_f \geq 10\%$ have to be taken into account as the Berkovich hardness is considered. However, for $h/h_f \geq 10\%$ discussed parameter slightly decreased vs. h/h_f since the hardness of silicon is lower than those of the AlN film H_b(AlN) > H_b(Si) = 13.5 GPa. For the two different investigated electrodes, the mean value of the AlN film hardness was then found to be around $H_{b<hkl>} \approx 26.0 \pm 1.5$ GPa (see Fig.5.2b).

It is worth to emphasise that the elastic property analysis could lead to evaluate the crystallographic structure of the tested material. The relative standard deviation of σ_E/E_{mean} (or σ_H/H_{mean}) is related to the dimensionless parameter of R_{ms}/h by the following equation [Bobji 1999, Qasmi 2006]:

$$\frac{\sigma_E}{E_{mean}} = \alpha\left(\frac{R_{ms}}{h}\right)^m, \tag{5.5}$$

where E_{mean} represents the mean value of the isotropic material Young's modulus, σ_E – the standard deviation determined over more than 25 indents [Bobji 1999] and R_{ms} – the film average roughness. For many metallic films deposited by sputtering technique α and m are equal to 0.346 and 0.64, respectively [Qasmi 2006]. Thus, the multiplicative factor corresponding to the relation between the experimental value of $\sigma_E/E_{mean} = \sigma_E/[(1-\nu^2)\, M_{<hkl>}]$ and that calculated from the Eq.5.5 can be considered as an indicator of the degree of the crystallite disorientation as shown the study of PZT films reported in literature [Wang 2005, Delobelle 2007]. According to the tested AlN thin films, the relative standard deviation of the nanoindentation measurements determined for AlN/CrNi (AlN/Pt) was found to be 7.7% (6.9%) and 5.0% (4.4%) for h=25 and 50 nm, respectively. Performed calculations took into account R_{ms} value of 2.4 ± 0.4 nm (2.0 ± 0.3 nm) for AlN/CrNi (AlN/Pt) measured by AFM [Andrei 2008]. The experimental results of σ_E/E_{mean} (with $\nu = 0.25$) were then of 11% and 7% for AlN/CrNi and 35% and 24% for AlN/Pt. These values were found to be greater than those estimated with the Eq.5.5 with the multiplicative factor of about 1.4 and 5.2 for AlN/CrNi and AlN/Pt, respectively. Thus, a good agreement between the calculation and the experimental values of σ_E/E_{mean} (factor 1.4) confirmed already reported well (i.e. pure) (002) oriented crystallites of the AlN deposited on CrNi (see the XRD spectrum shown in the Fig.5.2a). Observed not pure (002) orientation of AlN on Pt electrode was also justified by the larger multiplicative factor of 5.2. Moreover, to deeply analyse the signification of the considered factor values the histograms of the measured $M_{<hkl>}$ for h = 25 and 50 nm, and for both tested films were presented in the Fig.5.2c. For well (002) textured AlN/CrNi (factor 1.4) only one peak centered at $M_{<hkl>}$ = 332 GPa was found. This value is close to the determined

mean value (see Fig.5.2a) and moreover corresponds to $M_{<001>}$ reported for both the high quality sputtered AlN films ($M_{<001>}$ = 342 GPa) and the epitaxial ones ($M_{<001>}$ = 335 GPa) (see Table 5.1). For AlN/Pt (factor 5.2 and a mean value equal to 305 GPa) two well defined peaks at 370 and 260 GPa were found. The first one is certainly related to the set of well (002) oriented crystallites with high crystal quality (see Fig.5.1b). While, the second one (at 260 GPa) could be corresponded to the amorphous phase of AlN. However, related measured $H_{b<hkl>}$ = 17 GPa and E = 244 GPa (calculated for ν = 0.25) seem to be too high to confirm this consideration. According to the literature the amorphous phase shows different values of mentioned parameters ($E \approx 140$ GPa, H_b = 9.2 GPa [Xiao 2004] and $80 < E < 220$ GPa, $3.5 < H_b < 20$ GPa [Dagdag 2006]). Presented elastic constants are more consistent with those of the crystalline AlON phase obtained on Si substrates (E = 261 GPa, H_b = 17.8 GPa [Xiao 2004]). The absence of this phase for the AlN on CrNi was probably linked to the oxidation of this electrode as shown in the XRD spectrum (stars marked in the Fig.5.1a). Concluding presented analyses, between the two metal electrodes that were tested, the CrNi electrode proved to be considerably better choice allowing to obtain a well, pure (002) orientated AlN film and a well defined value of $M_{<001>}$ important to obtain very good piezoelectric properties. The Young's modulus calculated from the c_{ij} values [Carlotti 1995] was equal to 332 GPa in the c-axis direction, very close to $M_{<001>}$, and equal to 284 GPa in the perpendicular direction.

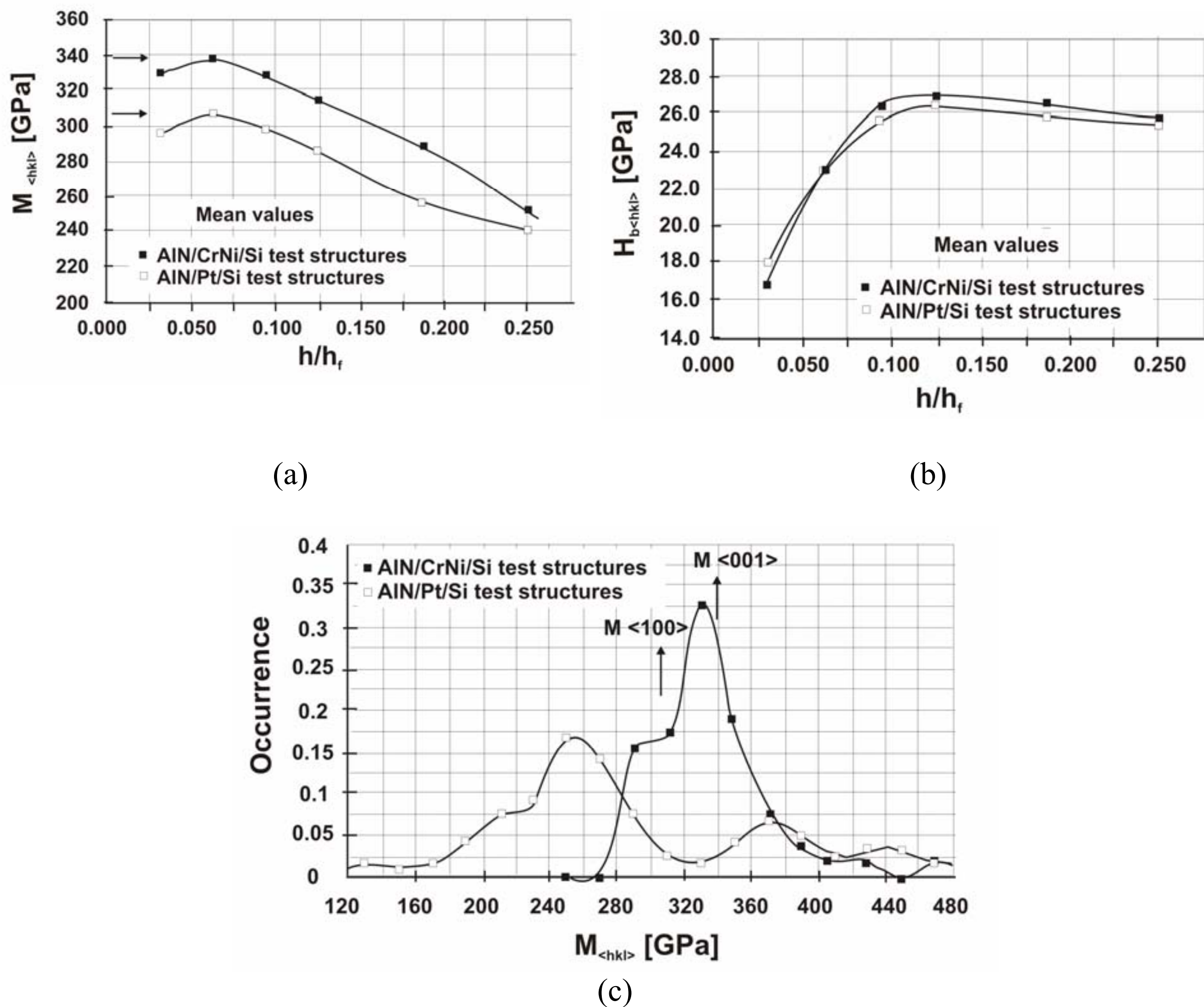

(c)

Fig.5.2: Elastic properties measurements: evolution of indentation modulus $M_{<hkl>}$ (a) and hardness $H_{b<hkl>}$ (b) as a function of reduced depth for AlN deposited on CrNi/Si and Pt/Si substrate; histogram of $M_{<hkl>}$ values (c)

5.2. Static behaviours – shape and residual thin film stress

The static behaviours of the AlN driven cantilevers will be studied. Their shape, the out-of-plane initial deflections and the thin film residual stresses (see section 4.1) will be considered. The influence of their design and the technology process will be analysed focusing on the bottom electrode nature and the AlN film thickness. All found results for the three types of cantilever structures, which differed mainly in the electrode materials and the film thickness' will be discussed. They concerned the devices fabricated during the process of amended microcatilever technology, i.e. the objects with bottom electrode of Aluminium (see Table 3.3, section 3.3.1), the test structures (see section 5.1) and the final actuators (see Table 3.6, section 3.3.2). However, the most detailed analysis will be performed on the last mentioned devices, i.e. those manufactured during the already improved process including the both electrodes from CrNi and AlN thickness of 1.4 and 1.0 μm.

The hybrid methodology and the interferometric multifunctional system described in the Chapter 2 were used to perform the experiments presented in this section. Considering the test structures, the out-of-plane initial deflections were measured before and after the AlN thin film deposition on the both CrNi and Pt electrodes. Their values as a function of the square cantilever length are presented in the Fig.5.3 [Andrei 2007 a, Andrei 2008]. The surfaces of the Si membranes used as substrates for the cantilever fabrication were assumed to be flat (i.e. without presence of the stresses) according to the earlier testing [Józwik 2004 a]. Therefore, obtained results (see Fig.5.3) showed that the residual stresses presented in the CrNi thin film were tensile, while those in the Pt electrode were compressive. While, the change of the slope observed in the both mentioned characteristics induced by the AlN deposition indicated the generation of compressive stress in this piezoelectric film. Basing on the discussed initial deflection measurements the values of the residual stresses presented in the both electrodes and the AlN thin films were calculated using the Eqs.4.2÷4.4 (see section 4.1). The certain assumptions concerning the cantilever geometry (see section 5.1) and the elastic properties of the used materials (i.e. $\sigma_{\mathrm{Si}} = 0$, $E_{\mathrm{Si}} = 129.5$ GPa, $E_{\mathrm{AlN}} = 332$ GPa, $E_{\mathrm{CrNi}} = 237$ GPa, $E_{\mathrm{Pt}} = 168$ GPa and $\nu = 0.3$) were made. The values of +1110 MPa tensile stress and −700 MPa compressive one were found for CrNi and Pt films, respectively [Andrei 2008]. Taking into account these results the residual stress introduced to the AlN film was determined to be $\sigma_{\mathrm{AlN}} = -174$ MPa and $\sigma_{\mathrm{AlN}} = -506$ MPa for the CrNi/Si and Pt/Si substrate, respectively. The mentioned cantilevers with Al as a bottom electrode were also tested. Assuming thus $\sigma_{Al} = -50$ MPa and $E_{Al} = 70$ GPa the residual stress in the AlN film was found to be -1360 MPa when deposited on the Al/Si substrate. Thus, the choice of the CrNi material for the bottom electrode proved again (see section 5.1) to be better giving the less stressed AlN film. This material was then used in the final actuator structures containing the 1.0 μm and 1.4 μm thick piezoelectric films.

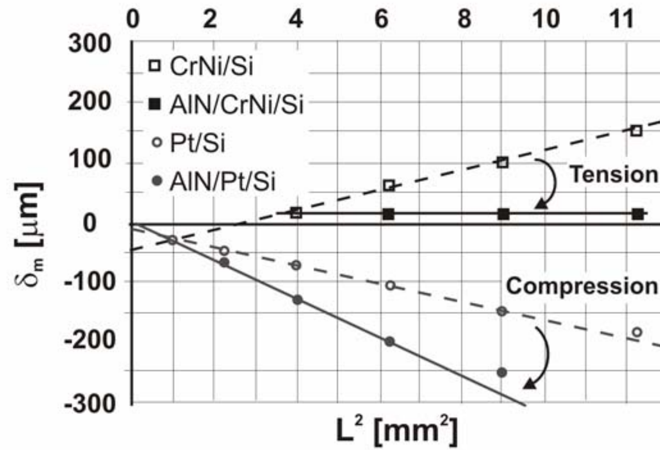

Fig.5.3: Static bending of test structure cantilevers measured before and after AlN film deposition as a function of their L^2

These devices, after the fabrication, were characterised and the initial deflections, the global residual stress and the AlN thin film stress were determined basing on the interferometric measurements. The exemplary interferogram acquired during these measurements is illustrated in the Fig.5.4 [Krupa 2008, Krupa 2009]. While, the exemplary measurement result of the initial deflection obtained for the 800 µm long final cantilever in the form of the 3D map and the object cross section profile are presented in the Figs.5.5a and b, respectively [Krupa 2008, Krupa 2009]. The experimentally received static parameters are given in the Table 5.2 [Krupa 2008 a, Krupa 2009] compared with those received for the devices previously manufactured to develop the technology of the AlN thin film actuators. According to the theory (see section 4.1), the measured relation of the initial deflections vs. L^2 could be approximated by a linear function with the residual stress as the slope parameter related to the considered structure types (see Fig.5.6). The dependencies of the calculated global and AlN thin film stresses on the piezoelectric film thickness for all analysed structure designs were analysed and shown in the Figs.5.7a and b, respectively. While, the influence of the cantilever length on the discussed global stress level introduced to the structures is presented in the Fig.5.8 [Krupa 2008 a, Krupa 2009].

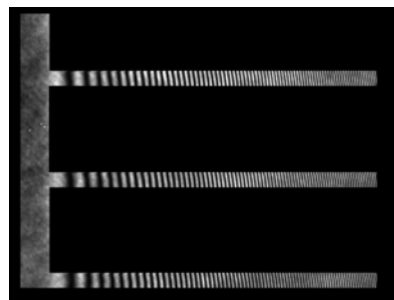

Fig.5.4: Initial deflection measurement of 800 µm long cantilever – exemplary interferogram

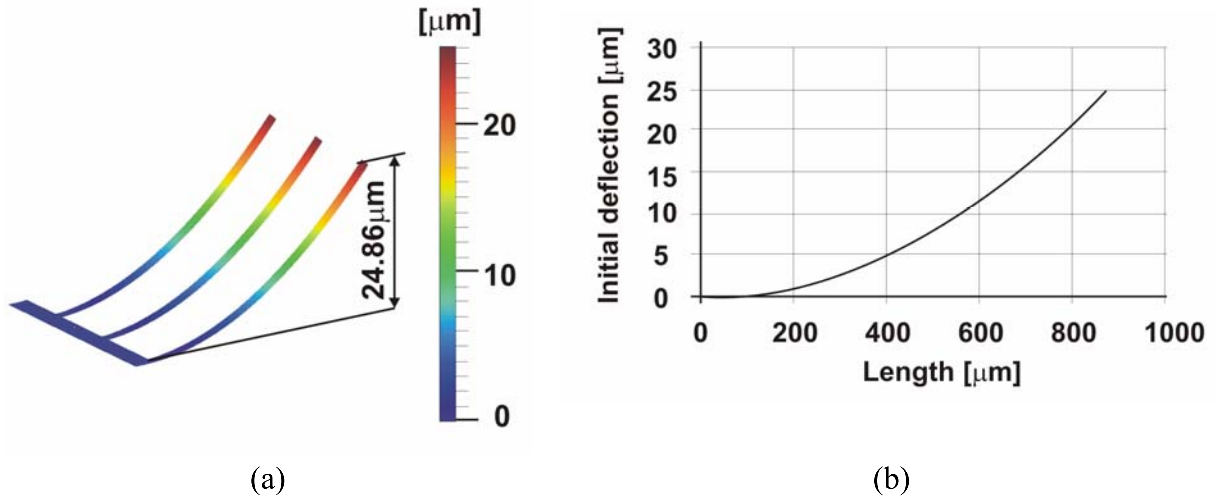

(a) (b)

Fig.5.5: Initial deflection measurement of 800 μm long cantilever with h_{AlN} = 1.4 μm: 3D view of deflection (a), cross section profile (b)

Table 5.2: Median values of initial deflection δ_m induced by residual global stress σ_0 values determined for various cantilever structure designs

	h_{AlN} [μm]	L [μm]	δ_m [μm]	σ_0 [MPa]
CrNi final structure	1.4	800	26.130	86.64
			SD=3.440	SD=11.38
		400	6.990	92.6
			SD=0.650	SD=24.5
		200	2.000	106.1
			SD=0.170	SD=8.9
CrNi final structure	1	800	16.430	45.99
			SD=2.230	SD=6.24
		600	10.880	54.14
			SD=2.230	SD=20.24
		400	5.164	58.0
			SD=0.622	SD=16.0
		200	1.020	45.7
			SD=0.110	SD=16.2
CrNi test structure	0.8	3500	15.00	1.67
		3000	15.00	2.27
		2500	15.00	3.27
		2000	15.00	5.11

Pt test structure	0.8	3500	-220.00	-24.63
		3000	-250.00	-38.09
		2500	-200.00	-43.89
		2000	-127.00	-43.54
Al initial structure	0.4	800	-11.980	- 22.78
			SD=0.400	SD=0.77
		700	-13.500	-33.54
			SD=0.560	SD=1.38
		500	-3.659	-17.82
			SD=0.129	SD=2.45
		200	-1.140	-34.5
			SD=0.030	SD=0.9
Au initial structure	1.0	200	-2.480	-99.5
			SD=0.020	SD=1.0

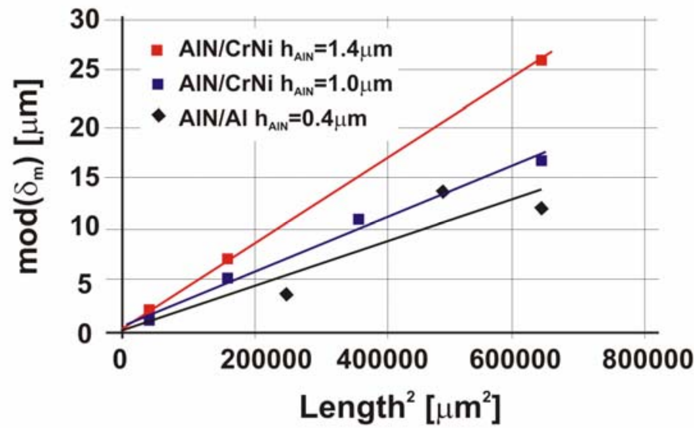

Fig.5.6: Initial deflection vs. L^2 measured for devices with CrNi and Al bottom electrode

The analyses of the performed experimental results (see Table 5.3) allowed to study also the influence of the AlN technology (see Table 3.2, section 3.3.1) on the residual stress level. The sputtering time and rate related to the AlN film thickness as well as the electrode nature were considered. The residual stress determined for the 0.4 μm thick AlN film deposited on the Al/Si substrate with the deposition rate of 3 nm/min (133 min of sputtering time) was equal to -1360 MPa (see Table 5.3). This value was found to correspond to the curve which approximates the stress results received for the final microcantilevers (see Fig.5.9). While, for the AlN deposited on the Pt electrode larger discrepancies were noticed in spite of the same deposition conditions (see Fig.5.9 and Table 5.3). Therefore, according to the performed researches it was difficult to distinguished the effect of the AlN thickness, its sputtering time and electrode nature and explain observed results.

Table 5.3: Internal stress (median) values of AlN film σ_{AlN} as a function of bottom electrode nature, AlN film thickness h_{AlN}, deposition rate v and deposition time t

Bottom electrode	h_{AlN} **[µm]**	v **[nm/min]**	t **[min]**	σ_{AlN} **[MPa]**
CrNi (final structures)	1.4	17	82	774
				SD=138
CrNi (final structures)	1.0	17	59	338
				SD=260
CrNi (test structures)	0.8	17	47	-173.63
				SD=26.30
Pt (test structures)	0.8	17	47	-506.38
				SD=158.05
Al (initial structures)	0.4	3	133	-1360
				SD=319

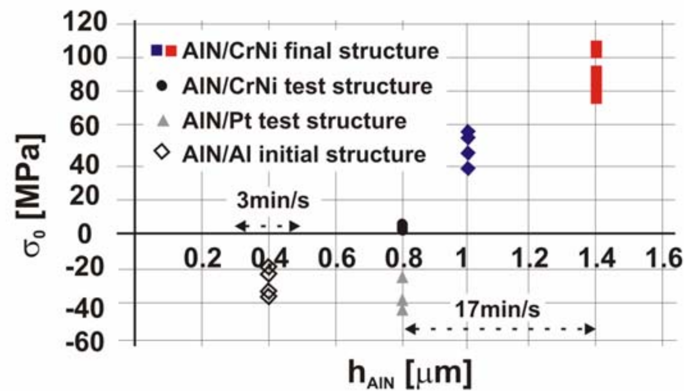

(a)

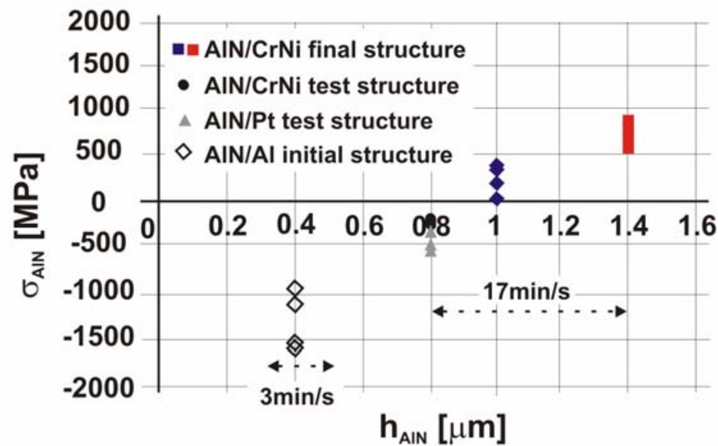

(b)

Fig.5.7: Calculated residual global stress (a) and AlN thin film stress (b) as a function of AlN thickness obtained for all tested cantilevers

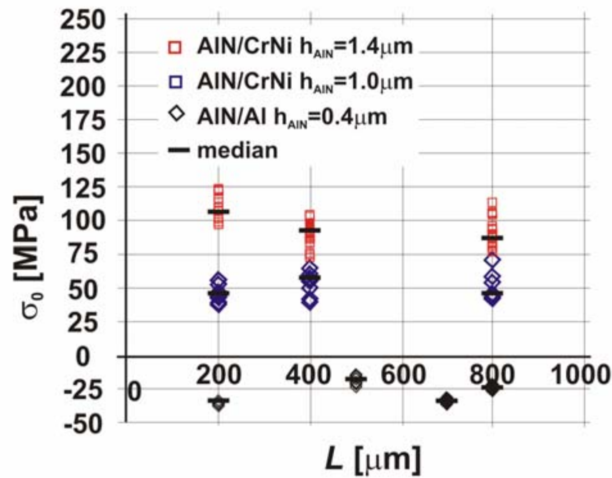

Fig.5.8: Global residual stress versus length accumulate in devices with CrNi and Al bottom electrode

Obtained results indicated that the residual stress presented in the AlN film is a function of the AlN film thickness passing from the compressive to the tensile values as presented in the Fig.5.9 (see section 1.5). Such an effect is in accordance with the literature [Meng 1993, Martin 2004]. Moreover, it was shown that the residual stress has a minimum value for the particular thickness range and increased for the greater thickness'. However, the position of mentioned stress minimum on the stress - AlN thickness characteristic depends on the thin film deposition conditions and the electrode nature [Meng 1993]. Thus, the obtained level of the AlN thin film stresses has been influenced by both the electrode and the AlN film thickness. These observations were confirmed by the performed measurements as shown in the Table 5.3 and in the Fig.5.9. Obtained results indicated thus that the correct choice of the film thickness' (both electrodes and piezoelectric film) and used materials are crucial to fabricate the devices with a zero global stress (i.e. $\delta_m \approx 0$) at a given constant temperature. Such requirements were well fulfilled in the case of the test structure having electrode from CrNi. These objects showed very low global stress as presented in the Fig.5.7a and in the Table 5.2. Thus, to fabricate the AlN driven structures with low global stress, not only the electrode thickness should be adjusted to the AlN thickness value, but also the dependence of the AlN stress value on its thickness need to be taking into account.

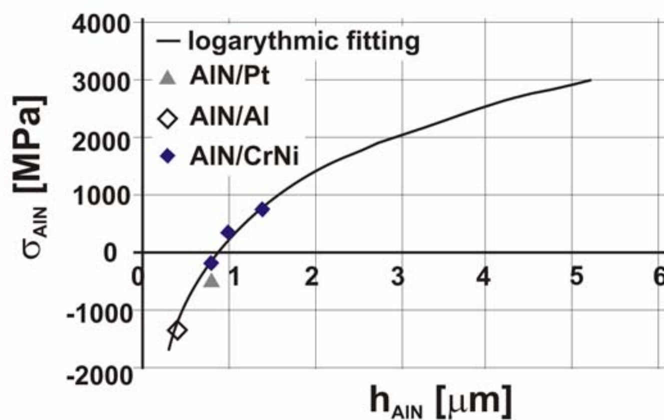

Fig.5.9: Measured AlN thin film residual stress vs. AlN film thickness obtained for cantilevers with bottom electrode from CrNi

Summarising, to study how the fabrication process affects the static properties of the AlN actuated cantilevers the series of devices with various lengths and AlN film thickness' incorporated different materials of bottom electrodes were investigated focusing on the final objects. Performed analysis showed a great influence of the technology on the flatness and the initial shape of the tested microelements. The choice of the used structure geometry (the film thickness'), the materials (the electrode nature) and the film deposition conditions were found to be crucial because they determine the level of the stress accumulated in thin films which affects the object initial deflection. Besides the very good actuation behaviours, the MEMS actuators require also to have straight profile. For the AlN film it means that except a good piezoelectric response it should display the controlled residual stress to obtain device with a flat surface [Iborra 2004].

5.3. Dynamic behaviours – resonance frequency and transient mode shape

The dynamic operation functionality of the microcatilevers actuated by AlN thin film was tested. There were measured only the first fundamental bending modes because the higher bending modes and twisting modes were too weak to be properly analysed. The resonance frequencies, the resonance curve, the transient shapes and the vibration amplitude values were determined using various interferometric methods implemented in the multifunctional platform and the relevant procedures (see Chapter 2). The sections of the cantilevers were excited to the resonant vibration by applying the sinusoidal voltage from 0.18 V_{PP} for the 800 μm long elements up to 8 V_{PP} for the 200 μm long ones. The relevant resonance frequency matched to the selected one particular object was used. The values of voltage were chosen in order to obtain the vibration amplitude value of 2 μm. Performed analysis was focused on the final devices fabricated during the improved technology (see section 3.3.2). However, the effects discussed in this section are related also to the other tested in this thesis work microcantilevers (see Table 3.3, section 3.3.1).

The resonance frequency determination

To analyse more exact the device dynamic response, the first resonance frequencies were determined by the measurements, the FEM simulations and the analytic considerations (see Eq.4.10, section 4.1). Obtained results are given in the Table 5.4 [Krupa 2008 Krupa 2009]. Relevant values varied from several kHz to hundreds of kHz depending on the cantilever dimensions (length in particular). According the theory (see Eq.4.10, section 4.1) the good linear fitting of the experimental frequency vs. $1/L^2$ was noticed (see Fig.5.10a). However, the certain discrepancies were observed being represented as a slope of the mentioned linear characteristic (see Fig.5.10a). The measurement frequency values were found to be higher from the theoretical ones, except the case of the 200 μm long cantilevers. The short length of elements (i.e. 200 μm) caused greater influence of their geometrical imperfections on the behaviours. The theoretical frequency values were calculated assuming the nominal (i.e. designed) dimensions (see Table 3.6, section 3.3.2), the material constants (see Table 4.3, section 4.2.2) and the flat profile of cantilever (without residual stresses). Thus, the noticed deviations could be attributed to the differences between the cantilever nominal geometry assumed in the theoretical considerations and their real technologically formed values. Another possible explanation of mentioned discrepancies could be the considerable initial deflections δ_m measured in the fabricated devices (see section 5.2). Both reasons were then analysed to explain the appeared effect. Performed numerical simulations described in the section 4.2.2 showed the negligible influence of

the initial deflection on the resonance frequency. During the experiments it was difficult to distinguish unequivocally between the effects of the geometrical imperfections and the initial deflections. The theoretical and measured resonance frequencies vs. AlN film thickness with the stress values (the initial deflections) as a parameter are illustrated in the Fig.5.10b. These characteristics were obtained for the 800 μm long cantilevers. Presented data showed that the difference in the shifts of the frequency values noticed for the devices with both AlN film thickness was possibly induced by the differences in mentioned thickness, not by the possible higher experimental relation $f_{rez}(\delta_m)$. The residual stresses presented in the objects with $h_{AlN} = 1.4$ μm were then nearly two times larger than for those with $h_{AlN} = 1.0$ μm. Thus, to explain mentioned deviation in the resonance frequencies the first mentioned reason concerning the object dimension imperfections should be taking into account. The numerical simulations described in the section 4.2.2 indicated that both the length and the Si substrate thickness are those factors which mainly affect the resonance frequency values. Performed measurements showed that the median values of the Si thickness over the wafers were 16.37 ± 0.11 μm (for wafer with $h_{AlN} = 1.0$ μm) and 16.41 ± 0.26 μm (for wafer with $h_{AlN} = 1.4$ μm) instead of designed 15 μm (see section 3.3.3). Thus, the first resonance frequency was determined also with the same assumptions taking into consideration the measured values of Si thickness. However, the thicker silicon substrate did not fully eliminate noticed discrepancies. The residual ones indicated that probably the real device lengths deviated from their designed values. Basing on the measurement results the cantilever lengths L^* ensuring the experimentally obtained resonance frequencies were calculated using the Eq.4.10 (see section 4.1) and the measured h_{Si}. Then, the dynamic simulations (f_{rez}^*) were carried out again taking into account these new values. All results are given in the Table 5.4. In the simulations the simplified model was used (see section 4.2.2). Performed analyses showed that the lengths of the fabricated cantilevers should be smaller than designed ones of about -8.3 ± 1.1 μm (and bigger of about 12.28 ± 0.81 μm for 200 μm long devices). This observation was confirmed by SEM measurements. Because in the SEM images the results of silicon structure underetching at the object free-end (see technological step 8, section 3.3.2 and Figs.3.15a and b, section 3.3.3) and the electrode mask misalignment appearing during the fabrication process were well visible (see Figs.3.15a and b, section 3.3.2). In the Table 4.4 the standard deviations SD determined for all sets of the tested cantilevers are given. These observed deviations were caused by the differences in the device geometry observed between the adjacent elements induced by the technological imperfections related to the dimensions and the quality of the Si substrate structure. The porosity and other damages of the silicon substrate are shown in the Figs.3.15a, b and c, respectively.

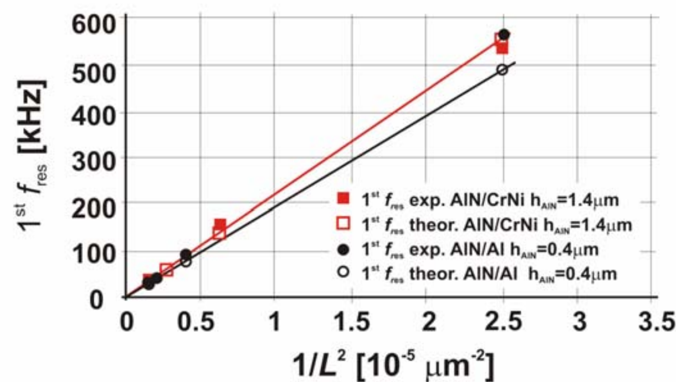

(a)

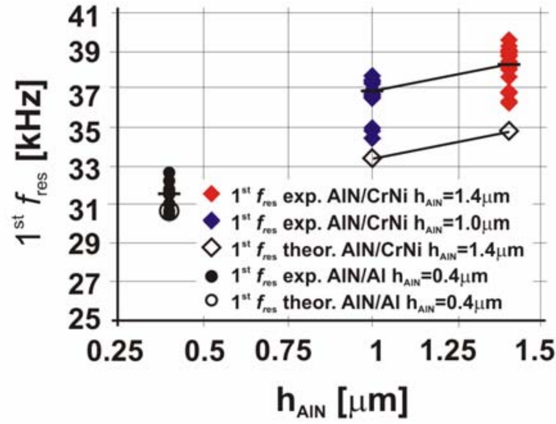

(b)

Fig.5.10: Theoretically and experimentally determined first resonance frequency as a function of $1/L^2$ (a) and AlN thickness obtained for 800 µm long cantilevers with bottom electrode of CrNi and Al taking into account accumulated residual stresses (b)

Table 5.4: Analyses of length and Si thickness changes on the values of 1st f_{rez} presented for final devices

h_{AlN} [µm]	L [µm]	1st f_{res} [kHz]					L^* [µm]	1st f_{res}^* [kHz]
		Theory	FEM	Theory	FEM	measurement median value	(h_{Si} – measured values)	FEM
		(h_{Si} =15µm – nominal value)		(h_{Si} – measured values)				(h_{Si} – measured values)
1.4	800	34.794	34.858	37.576	37.659	38.160 SD=0.939	793.85	38.245
	600	61.856	61.986	66.801	66.962	-	-	-
	400	139.18	139.53	150.30	150.70	157.205 SD=5.339	391.11	157.63
	200	556.71	557.67	601.21	601.80	535.71 SD=13.76	211.87	536.46
1	800	33.402	33.494	36.079	36.189	36.850 SD=0.795	791.58	36.963
	600	59.382	59.563	64.141	643.51	65.555 SD=2.371	593.47	56.775
	400	133.61	134.08	144.32	144.84	150.420 SD=7.024	391.69	151.05
	200	534.44	536.14	577.27	578.66	510.50 SD=18.95	212.68	511.89

The resonance curve and quality factor determination

The resonance curves of the investigated microcantilevers vibrating at the first resonance frequencies were determined. The devices were excited by the sinusoidal voltage with 0.180, 0.885 and 1.8 V_{pp}. The measurement results for the 800 µm long objects with 1.4 µm thick AlN films are presented in the Fig.5.11. Obtained resonance curves allowed to calculate the quality factor Q_m (see Eq.A1.5, Appendix 1), which strongly determines the resonant behaviours of the tested AlN driven actuators. This parameter was found to be 335.

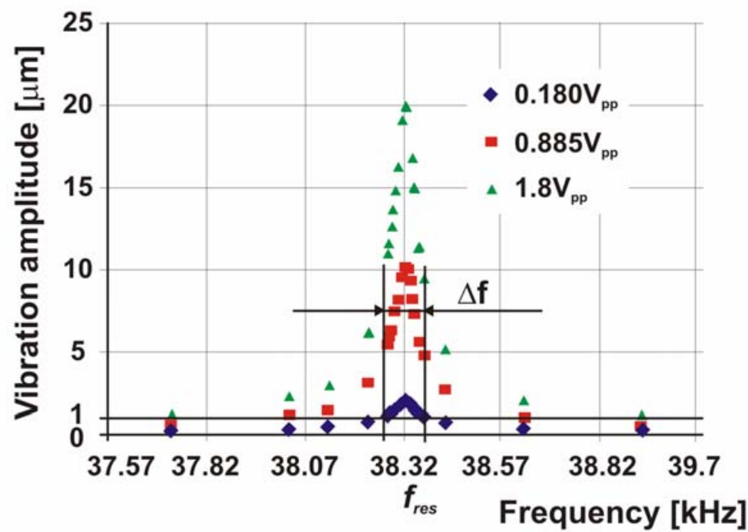

Fig.5.11: Resonance curves for exemplary 800 µm long cantilever with $h_{AlN} = 1.4$ µm obtained at first resonance frequency

The vibration mode amplitude determination

The vibration amplitude of the cantilever free-end measured at the first resonance frequency was determined. The measurement results concerning the amplitude vs. voltage value U_{pp} are presented in the Fig.5.12 [Krupa 2008, Krupa 2009]. The exemplary 3D views of the extreme transient shapes obtained for the 800 µm long cantilever are illustrate in the Fig.5.13. Performed experiments showed that the device vibration amplitude increased linearly as a function of driven voltage and for the same voltage was higher in the case of the samples with thicker AlN film (i.e. 1.4 µm). This effect could be explained by the study of the AlN film piezoelectric properties, which will be presented in the section 5.5. The relevant results will show that more important value of the piezoelectric coefficient d_{31} was found for the cantilevers with AlN film of 1.4 µm (see section 5.5). Moreover, carried out dynamic experiments demonstrated the symmetry of the vibration profile of the investigated objects (see Fig.5.13).

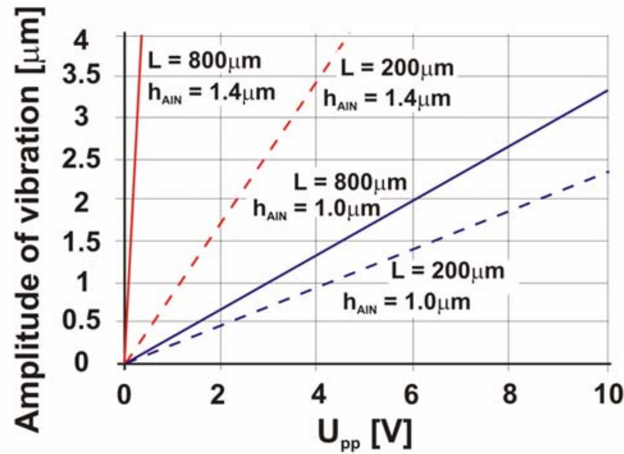

Fig.5.12: Amplitude of cantilever vibration as a function of sinusoidal voltage for 200 and 800 μm long final cantilevers with 1.0 and 1.4 μm thick AlN film

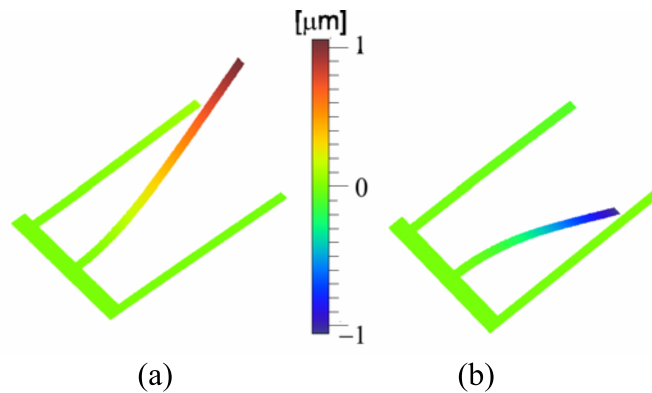

(a) (b)

Fig.5.13: 3D view of 1st resonant mode transient shape measured for 800 μm long cantilever with h_{AlN} = 1.4 μm at 0.18 V_{PP}: upper (a), lower (b) extremities

5.4. Electrical behaviours – resistance

In this section the study of piezoactuator electrical properties influencing their operation will be presented. The resistance of these devices and their electrical performance stability will be discussed. The final cantilevers including top and bottom electrode of CrNi and two values of AlN thin film thickness (h_{AlN} = 1.4 μm and 1.0 μm) will be considered. The one resistance value measured between both electrode films will be related to the section of 9 (or 8) cantilevers combined by the one top electrode.

The test square chips consisted of such 8 sections (see section 3.1). The experiments were performed over two wafers consisting of the devices with 1.4 μm and 1.0 μm thick AlN film, respectively. Obtained results showed that there were 86% and 75% of sections having infinite resistance value for the wafers with thicker and thinner AlN film, respectively. The correct cantilever electrical conditions, i.e. the isolation properties of the AlN thin film, ensured the actuator proper functionality. It means the linear characteristic (i.e. the out-of-plane displacement vs. constant voltage) of the piezoelectric response and the high value of the resonant amplitude. However, for the microcantilevers the finite resistance values (of the order of Ω or kΩ) as a result of short circuit were found. Such behaviour could be explained by certain voids appeared in the AlN thin film during the technological process.

The short circuit was considered as a failure mode causing the same effects as described in the section 6.3.1. It means the important parabolic bending caused by the constant voltage load having the Joule effect origin, and the damping of the resonance amplitude. These phenomena were explained basing on the developed simple model described in the section 5.5. The short circuit could be thus induced during the fabrication process or during the operational use as a result of failure. Performed investigations showed also the resistance value instability noticed for some cantilevers affecting their performances. In the Fig.5.14 there is illustrated the example of such phenomenon, it means that during the measurement of the displacement vs. constant voltage, the resistance changed from firstly small one in the order of hundred Ω to infinity. The initial parabolic behaviour turned then to linear one. This effect could be also reversed, i.e. the device with insulating properties could change to be in short circuit.

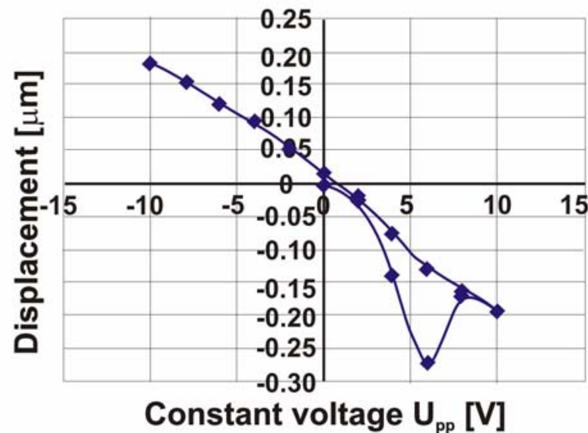

Fig.5.14: Electrical instability of 800 μm long cantilever with h_{AlN} = 1.4 μm relating to changes of R value and then to changes of parabolic dependence of displacement vs. V_{DC} to linear one

The electrical stability is important for the microdevice correct operation. However, comparing the top electrode surface quality of the investigated devices just after fabrication (see Fig.5.15a) and then after few months of their storing (see Fig.6.15b) in the non hermetic box (see Fig.5.16), the degradation of this electrode was observed. It could be explained by the corrosion (oxidation) process proceeding in the standard weather conditions being other possible reasons of the mentioned resistance instability.

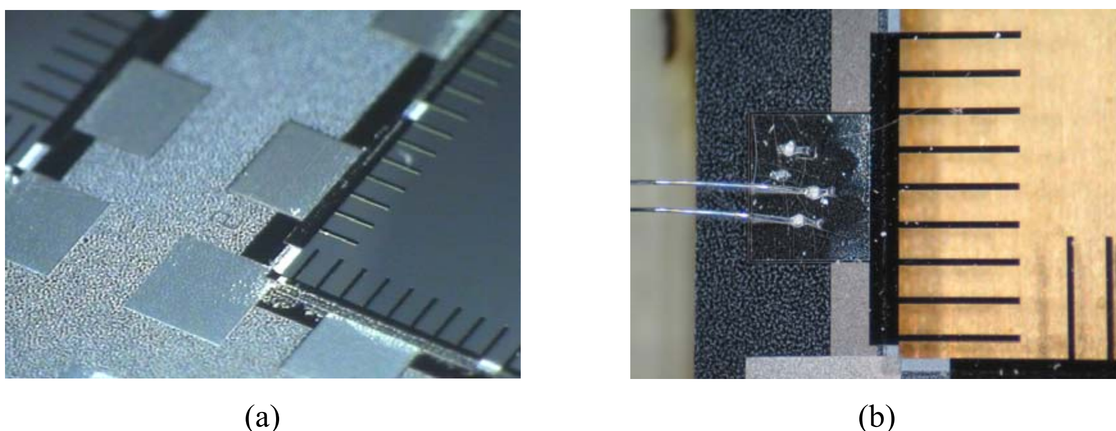

(a) (b)

Fig.5.15: Photograph of cantilever chip performed just after fabrication (a) and after storing it for a few months in non hermetic box (b)

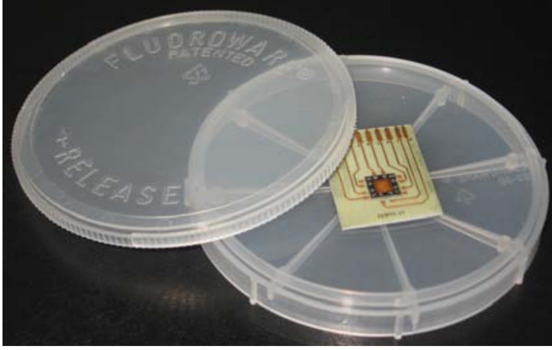

(a) (b)

Fig.5.16: Photograph of non hermetic box serving for storing cantilevers

Moreover, when breakdown appeared after voltage loading without any stable damages like burning or delamination, the voltage decrease could make returning the cantilever electrical properties to the correct value (i.e. the infinity resistance). This is the advantage of the AlN thin film being a semiconductor material [Wiki].

5.5. Piezoelectric behaviours and Joule effect

Table 5.5: Values of piezoelectric coefficients reported in literature

	d₃₁ **[pm/V]**
deposited at 200°C by pulsed reactive DC sputtering	−2.0 ± 0.1 [Guy 1999]
deposited at 90°C by pulsed reactive DC sputtering	−1.6 ± 0.1 [Guy 1999]
Epitaxial	−1.8 ± 0.1 [Lueng 2000]
Bulk	$d_{33}^{b} = 5.6 pm/V$ $d_{31}^{b} = -2.8 pm/V$ [Guy 1999] $d_{33}^{b} \cong 5.0 pm/V$ $d_{31}^{b} = -2.5 pm/V$ [Ho 2004]

The AlN thin film piezoelectric properties used for the microcantilever actuation will be discussed. Such behaviours determine the functionality of the investigated actuators. The piezoelectric coefficient d_{31} will be calculated basing on the performed measurements. The dependence of the AlN film thickness on the piezoelectric response will be presented.

The piezoelectric devices could operate in the static and dynamic modes which were investigated using the multifunctional interferometric platform (see Chapter 2). To determine the d_{31} of AlN, the static displacement δ_p of cantilever free-end induced by the constant voltage load was measured. The exemplary results approximated by linear function obtained for the 800μm long final cantilevers with AlN film thickness' of 1.4 μm and 1.0 μm are

presented in the Fig.5.17. Basing on the slopes of the measured characteristics, the AlN piezoelectric coefficient d_{31} was calculated using the Eq.4.12 (see section 4.1). It was found to be −2.00 ± 0.10 pm/V for the cantilevers with thicker (i.e. 1.4 μm) AlN film and only −1.30 ± 0.11 pm/V for those with thinner (i.e. 1.0 μm) piezoelectric layer (see Fig.5.18) [Andrei 2008, Gorecki 2008, Krupa 2008 a, Krupa 2009]. The values reported in literature are given in the Table 5.5. The first obtained value (i.e. −2.00 ± 0.10 pm/V) is in accordance with the literature while the second one related to the cantilevers with thinner piezoelectric film is much smaller (−1.30 ± 0.11 pm/V). The piezoelectric properties depend on the deposition conditions, the film structural orientation and the thin film thickness (see sections 1.4 and 1.5). The last of the mentioned relations was confirmed by the investigation results presented in the section 3.3.1. The deposition conditions for the both considered devices with thicker and thinner AlN film were the same. Therefore, the mentioned small value of d_{31} noticed for the objects with thinner piezoelectric film could indicate the need of further AlN deposition process improvement. However, the another possible explanation could be the influence of AlN film thickness on this film clamping to the substrate. This dependence could correspond to the relation between the AlN thickness and its piezoelectric properties [Martin 2004]. Basing on the determined d_{31} coefficients which in our case are considered as clamped ones d_{31}^{c}, the d_{31}^{b} factors related to the unconstrained bulk material were calculated using the Eq.3.1 (see section 3.2). Thus, the perfect clamping (clamping factor $\alpha = 1$, $0 \leq \alpha \leq 1$) was assumed and the s_{ij} parameters (elastic compliances) were obtained from the c_{ij} values (see Table 5.1). The bulk piezoelectric coefficients were found to be $d_{31}^{b} = -2.85 pm/V$ for the measured $d_{31}^{c} = -2.00 pm/V$ (1.4 μm of AlN) and only $d_{31}^{b} = -1.85 pm/V$ for $d_{31}^{c} = -1.30 pm/V$ (1.0 μm of AlN). The first value of d_{31}^{b} is very close to the reported ones (see Table 5.5), but the second parameter is somehow small compared to those for the bulk material. However, according to the Eq.3.1 (see section 3.2) for the same value of d_{31}^{b}, d_{31}^{c} decreases with the α decrease what justifies the obtained smaller value of the d_{31} measured for the thinner AlN thin film (i.e. 1.0 μm). The lower factor α indicates the worse clamping conditions found for thinner AlN film indicating the observed worse piezoelectric properties. Described observations noticed between the measured and the reported piezoelectric response were confirmed by the FEM simulations assuming perfect film clamping ($\alpha = 1$). The piezoelectric displacement induced by applying 10 V_{DC} to the 800 μm long cantilevers was analysed. It was found to be -204 nm for the objects with h_{AlN} = 1.4 μm (-160 nm for the objects with h_{AlN} = 1.0 μm) in comparison to -197 nm for those with h_{AlN} = 1.4 μm (- 229 nm for those with h_{AlN} = 1.0 μm) obtained form the experiments and the numerical simulations, respectively (see Fig.5.17). Moreover, during the thin film growth its crystal structure is being aligned. Its texture orientation improves with the thickness increase reaching perfect preferred orientation at the particular value. For lower thickness' the non-(002) traces could appear in the film texture reducing the piezoelectric activity. This effect could be other possible explanation of the lower piezoelectric coefficient value found for the thinner AlN film as a result of its lower deposition time (see section 1.5). In addition, the performed investigations showed that the slope coefficients of the deflection versus constant voltage characteristics had either negative or positive value dependently on the measured microobjects (see Fig.5.17). However, for the most devices the determined piezoelectric coefficient d_{31} had negative sign. It means that the AlN thin film expands when a positive voltage is applied causing downward displacement of the cantilever tip. This effect could be explained by the polarity of the AlN crystal structure which is installed during the nucleation [Dubois 2001, Iborra 2004, Martin 2004]. Most investigated AlN films were oriented in <002> direction but some of them had $(00\bar{2})$ texture with opposite polarity.

The investigated piezoelectric devices could operate also in the dynamic mode excited to the vibration by sinusoidal voltage loading. The resonance response study is presented in the section 5.3. The analyses of both mentioned operation regimes clearly showed that the microcantilevers fabricated with thicker AlN film (i.e. 1.4 μm) found better piezoelectric functional properties. The microdevice behaviours were greatly influenced by the technology. The experimental results presented in the section 3.3.1 confirmed this strong dependency on the structure fabrication process and the electrode materials. They concern the investigations of the initial microcantilevers with AlN thin film deposited on the Au and Al metal electrode using *slow recipe* of the sputtering method (see section 3.3.1). These objects showed very poor electromechanical efficiency in comparison to the final elements in spite of the same AlN film thickness for the objects with electrode of Au (i.e. 1.0 μm). Except of technological imperfections discussed in the section 3.3 mentioned effect could be explained by the lower deposition rate (see Table 5.3, section 5.2) of the AlN thin film causing increase of the piezoelectric film thickness for which the well (002) oriented AlN texture is achieved. Although the type of electrode also influenced the piezoelectric response (see section 1.5). Moreover, instead of the linear piezoelectric activity the initial objects revealed non linear behaviour, characteristic for electrostrictive materials. The curves of their responses under constant voltage load seemed to exhibit the same trends as those for the PZT material. However, the deflection values were much lower (tens times) [Walter 2002]. Likewise, the initial devices also required to be initially polarised using offset voltage as described in the section 3.3.1.

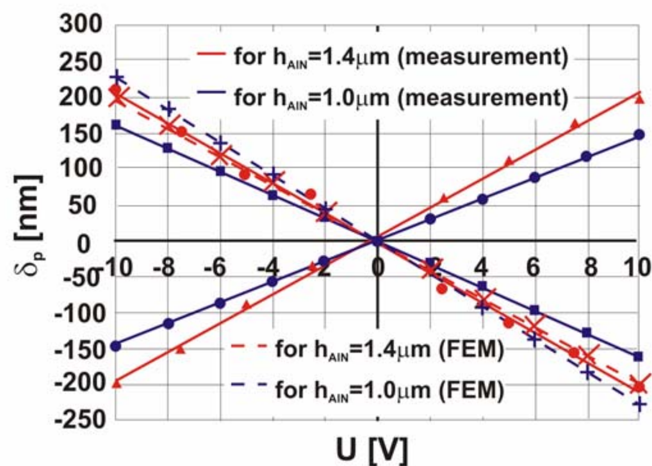

Fig.5.17: Measured and FEM simulated piezoelectrically induced displacement variation as a function of applied DC voltage for 800 μm long cantilever with 1.0 and 1.4 μm of AlN thickness

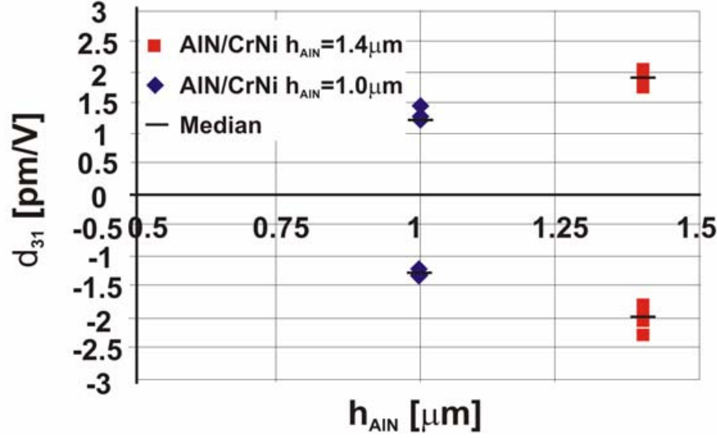

Fig.5.18: The d_{31} piezoelectric coefficient value as a function of AlN film thickness determined for 800 μm long final cantilevers

Joule effect

Performed measurements of the cantilever electrical properties (i.e. resistance) showed that some devices were in short circuit (see section 5.4) changing their piezoelectric behaviours. The constant voltage applied to the electrodes induced the important displacement of the structure free-end proportional to the square of the voltage (see Fig.5.19) [Andrei 2008]. Apart of this effect considerably lower vibration amplitude was also noticed. At the resonance the amplitude was more than 5 times lower than for the objects with the insulating properties working at the same voltage level. According to the static operation mode, the observed significant parabolic bending originated from a Joule effect related to the heating of the AlN and Si films. The explanation of the observed phenomena was developed in the cooperation with the group from the Département de Mécanique Appliquée R. Chaléat LMARC of the Institute FEMTO-ST, in Besançon, in France, and in particular with dr Patrick Delobelle. It brought to establish the simple model, which described the noticed effect (see Eqs.5.6÷5.11). This model allows to determine the area of the short circuit appearance or generation.

Thus, from the Fig.5.19 it can be deduced the relation:

$$\delta_{Th} = A_{exp} U^2, \tag{5.6}$$

which combined with the Eq.4.13 (see section 4.1) gives

$$\Delta T = \frac{E_{eq} h_{eq}^3 (E_f h_f + E_s h_s + E_e h_e)}{3[E_s h_s^2 - (E_f h_f + E_e h_e)(h_e + h_f)][\alpha_s (E_f h_f + E_e h_e) - (E_f \alpha_f h_f + E_e \alpha_e h_e)]L^2} A_{exp} U^2 = A^*_{exp} U^2 \tag{5.7}$$

In the case of a very simple thermal conduction model of a wall heating on one side by an electric resistance r, we have:

$$\Delta T = \beta \frac{U^2}{r}. \tag{5.8}$$

Hence, taking into account that the resistances r of each cantilevers were associated in parallel configuration we obtained:

$$A^*_{exp} = \frac{\beta}{nR}. \tag{5.9}$$

The representation

$$A^*_{exp} = f\left(\frac{1}{nR}\right) \tag{5.10}$$

for all tested sections (see section 3.1) being in short circuit and generally consisting in n = 9, is presented in the Fig.5.20 [Andrei 2007 a, Andrei 2008]. The slope of these curves allowed to calculate the β coefficient which was found to be $357 < \beta < 600$ K/W.
Then the considered model leads to the following relations [Andrei 2007 a]:

$$\beta = \frac{h_{Si}}{\lambda_{Si} L L_S}, \tag{5.11}$$

where λ_{Si}, h_{Si}, L, L_s are a Si thermal conductivity, a Si thickness, a cantilever length and a distance from cantilever fixation to a place where short cut is formed, respectively. Assuming the cantilever geometry (see Table 3.6 section 3.3.2) and λ_{Si} = 167 W/mK (at T = 50°C), L_s were found to be in the range of 0.18 µm < L_s < 0.30 µm, i.e. very close to the cantilever fixation. The short circuit could be induced not only by technological imperfections (see section 5.4), but also by voltage breakdown appeared during device operation (see section 6.3.1). Therefore, the heating related oxidation areas of the top electrode damages, well visible near the object fixation in the Fig.6.2 (see section 6.3.1) could be a confirmation of determined the L_s low value.

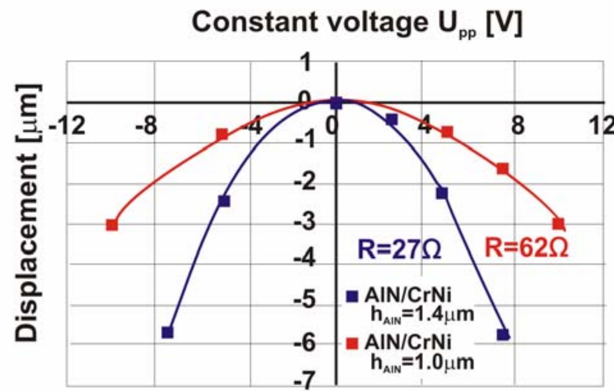

Fig.5.19: Displacement induced by constant voltage V_{DC} measured for 800 µm long final cantilevers in short circuit

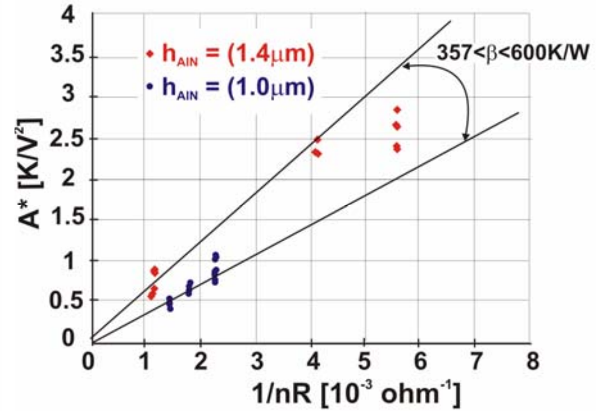

Fig.5.20: Coefficient A^*_{exp} vs. inverse of device resistance measured for 800 µm long cantilevers in short circuit

5.6. Thermal behaviours

In this section the thermal properties of the AlN thin film based microcantilevers will be presented. The study will be focused on the influence of temperature variation on their static initial deflection and their resonance response. It will allow to determine the operation stability of the investigated devices dedicated for MEMS actuators working in the standard weather conditions. More detailed analysis will be performed on the 800µm long final cantilevers.

The thermal FEM simulations (see section 4.2.2) showed that the temperature affects more the longer structures, what ensured the higher confidence of the measurements. To set the cantilever temperature, the heating plaque of the climatic chamber described in the section 6.3.2 was integrated with the interferometric platform (see section 2.3.2). It allowed to measure the static and dynamic parameters of the objects at various temperature. The obtained results led to determine the thermal expansion coefficient (TEC) of the AlN thin film. Thus, because the materials incorporated in the cantilever multilayer structures (i.e. AlN,

Si and CrNi) have different TECs, the thermal mismatch at their interfaces caused generation of the thermal stresses induced by the temperature changes. It generated an additional deflection δ_{Th}. The six exemplary measurements of the total deflections (δ_{m} + δ_{Th}) vs. the temperature for the 800µm long microelements with h_{AlN} = 1.0 µm and 1.4 µm three ones for each thickness are shown in the Fig.5.21a. Basing on the slope of obtained linearly approximated characteristics ($\Delta\delta_{\mathrm{Th}}/\Delta T$) the AlN thin film thermal expansion coefficient ($\alpha_{\mathrm{f}} = \alpha_{\mathrm{AlN}}$) was thus determined using the Eq.4.13 (see section 4.1). It was found to be $4.3 \cdot 10^{-6} < \alpha_{AlN} < 4.6 \cdot 10^{-6}$ 1/K [Andrei 2008, Krupa 2008 a] in accordance with the values reported in the literature for AlN bulk material (i.e. $4.4 \times 10^{-6} < \alpha_{\mathrm{AlN}} < 5.3 \times 10^{-6}\ \mathrm{K}^{-1}$ [Ceramic_center] and $4.03 \times 10^{-6} < \alpha_{\mathrm{AlN}} < 4.84 \times 10^{-6}\ \mathrm{K}^{-1}$ [Memsnet a]). For calculations the designed cantilever geometry (see Table 3.6 section 3.3.2) and the relevant material parameters (i.e. $\alpha_{\mathrm{s}} = 2.44 \times 10^{-6}\ \mathrm{K}^{-1}$, $\alpha_{\mathrm{e}} = 9.5 \times 10^{-6}\ \mathrm{K}^{-1}$) were assumed. Mentioned characteristics allowed to evaluate the thermal performance stability of the investigated piezoelectric actuators concerning both their static operation. However, to analyse their dynamic functionality the resonance frequency changes vs. temperature were investigated, as well. Received data are illustrated in the Fig.5.21b. Similarly to the static behaviours the dynamic ones also demonstrated linear dependencies on the ambient temperature. Basing on the obtained experimental results the variations of the device free-end static deflection and first resonance mode induced by temperature increase of 1°C were determined. The values for the 800µm long final cantilevers are given in the Table 5.6 [Krupa 2008 a]. The initial deflections were compared with those obtained from the FEM simulations (see Table 4.6, section 4.2.2) and the analytical considerations (see Eq.4.13, section 4.1) finding to be consistent.

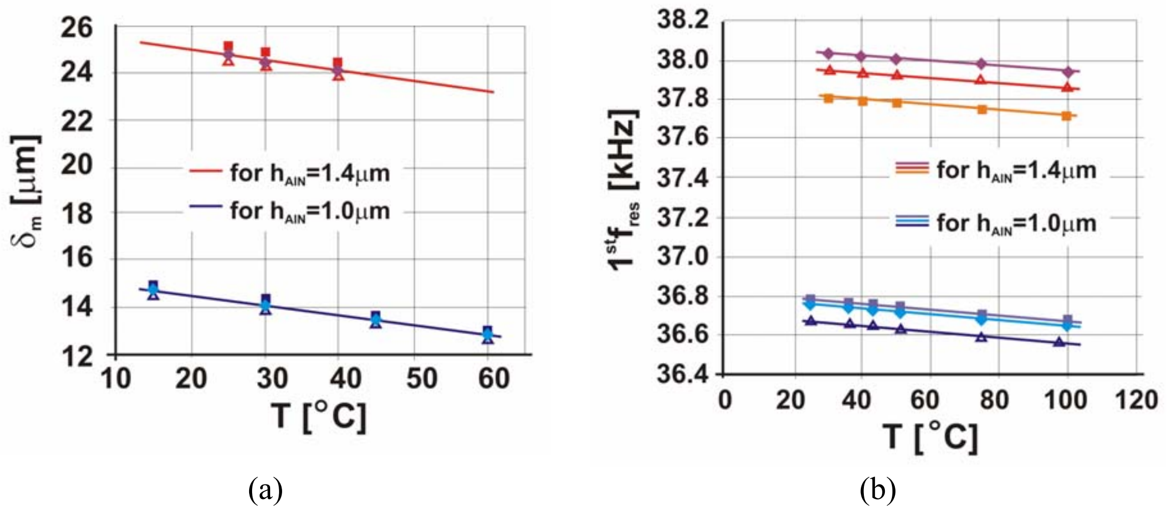

(a) (b)

Fig.5.21: Influence of temperature T on static deflection (a) and 1st resonance frequency (b) for 800 µm long final cantilevers with AlN thickness of 1.4 µm and 1.0 µm

Table 5.6: Thermal additional deflection and resonance frequency induced by temperature increase of 1°C

h_{AlN} [μm]	L [μm]	$\Delta\delta_{Th}$ for ΔT = 1°C [nm]		
		measurement	FEM	theory
1.4	800	-44	-53	- 45
1		-42	- 52	- 44

h_{AlN} [μm]	L [μm]	$\Delta 1^{st} f_{res(Th)}$ for ΔT = 1°C [kHz]
		measurement
1.4	800	-0.0012
1		-0.0014

Thus, performed study of the thermal behaviour showed that a temperature increase has caused a decrease of both the static deflection and the first resonance frequency of the investigated objects. The significant conclusion is that to ensure the stable operation conditions of the AlN based actuators it is crucial to control the temperature.

5.7. Conclusions

The characterisation of the AlN thin film and the AlN driven microcantilevers was performed basing on the hybrid methodology. The analytical equations developed for tri-layer structures and the FEM simulations carried out in the ANSYS software were applied. The experimental results were obtained from the interferometric, AFM, SEM and X-ray diffractive measurements as well as the nanoindentation tests. The material properties and the electromechanical performances of the tested objects were studied. Namely, their optically measured static and dynamic parameters as well as the crystallographic, mechanical, piezoelectric, thermal and electrical behaviours were determined. It was found that the functionality of the AlN thin film applied in microcantilever actuators was strongly influenced by the technology. The proper choice of the design, the materials and the AlN deposition conditions as well as the development of the fabrication process flow are crucial to manufacture devices with demanded operational characteristics. Presented investigations of the bottom electrode influence showed that CrNi is the most suitable material among the other tested metals. The AlN deposited on it exhibited better (002) structure orientation, well defined Young modulus and lower residual stresses at much higher piezoelectric coefficient. Moreover, because the applied materials determine the fabrication process flow, the use of CrNi allowed to improve the quality of the microcantilever surface and then the electrical properties. Therefore the considerable decrease of the supply voltage can have been achieved improving the electromechanical behaviours of the devices. Much better piezoelectric activity was also found when the AlN thin film was sputtered in the conditions defined by *fast recipe* causing higher growth rate of the structure. In addition, the influence of the AlN thickness on the piezoelectric properties was confirmed giving probable explanation of this effect. Increase

of the piezoelectric coefficient d_{31} was noticed for the thicker film (i.e. 1.4μm) and the obtained values corresponded well with those reported for the bulk material. This coefficient was also found to have either negative or positive value dependently on the measured microobjects what was explained by the polarity of the AlN crystal structure installed during nucleation. The AlN films were then oriented in <002> or $\langle 00\bar{2} \rangle$ direction with advantage over the first one. It was shown that except used electrode also the AlN thickness affects the residual stresses introduced to this film during deposition. In accordance with the literature, these stresses changed from highly compressive to highly tensile as a function of AlN thickness. However, because the stresses are generated in every films, the used fabrication process flow determined the initial deflection of the cantilevers. Therefore, the proper selection of the materials and their thickness' could lead to manufacture required flat objects. Except static performances the dynamic ones were also discussed. The experimentally obtained resonance frequencies were higher than designed ones. Noticed discrepancies were explained by the technologically induced geometrical imperfections. Namely, the tested devices had thicker Si substrates and smaller lengths. The results of the vibration amplitude confirmed better electromechanical activity obtained for the thicker AlN film. The quality factor was also determined based on the resonance curve. Considering the measured initial deflections and resonance frequencies the standard deviations SD of these parameters estimated over entire wafer were about 12.0% and 3.4%, respectively. It allowed to determine the performance technological reproducibility which are crucial for parallel applications of the tested actuators. According to the electric properties, for some microstructures the resistance determined between both metal electrodes was finite because of the short-circuit generated during fabrication. Changes in the piezoelectric behaviours were observed and their generation mechanism was discussed. This phenomenon deteriorated the dynamic response causing significant decrease of the resonance vibration. The operational reproducibility and the stability were presented as well. Performed investigations showed the resistance value instability noticed for some objects affecting their correct performances. However, it is worth to emphasise that when the short-circuit, induced by the breakdown appeared after voltage loading, was generated without any stable damages, the voltage decrease could make returning the electrical properties to the insulation one. The environmental stability was also investigated. The AlN based actuator functionality exhibited strong dependence on the temperature. The temperature increase of 1°C caused a noticeable decrease of both the static deflection and the first resonance frequency. Therefore, the need of stable operation conditions was crucial. Moreover, the degradation of the device electrode surfaces was observed. The oxidation process proceeding in the standard weather conditions also introduced the mentioned resistance instability. To summarise, the results presented in this section show that using low temperature method of DC reactive magnetron sputtering for the AlN thin film deposition, it is possible to fabricate devices with very good piezoelectric activity. The flat structures could be also manufactured focusing on the proper selection of the materials and their thickness'.

Chapter 6

Reliability study

In this chapter, first a short introduction to the reliability matter will be presented. Next some reliability aspects oriented on the dissertation problems will be discussed. The procedures of chosen qualitative accelerated reliability tests and their results will be described in detail. The reliability experiments will include the resonant fatigue tests stimulated by high voltage as well as the ageing ones generated independently by electrical shock, high temperature and high humidity. These reliability investigations will lead to the quality estimation of durability and long-term stability of the microcantilevers driven by the AlN thin film as well as the identification of their probable damages, failures and behaviour changes. The range of the supply voltage determining the device operating conditions will be also presented.

6.1. Introduction

The dynamic development of the microsystem technology observed in the last ten years has brought a rapid increase of applications of piezoelectric materials implemented in MEMS actuators, sensors, transducers, etc. [Andersen 2000, Srikar 2002, Andersen 2004] (see sections 1.3 and 1.4). However, to put them successfully into commercially available products, their reliability and controllability are required. Manufacturers have to guarantee their correct operation for a certain time which has a fundamental influence on the competitiveness and the acceptance of this new technology. It is crucial to market devices which are functional, reliable safe, especially when their applications concern the security problems. Thus, the reliability of a product (component, assembly or system) is defined as the probability, at a given confidence level, that this product will perform a required function satisfactorily or without failure, i.e. within pre-defined specifications for a set amount of time when using for the intended applications in the operation environments [Wolf 2003 a, Birolini 2004, Berghmans 2006]. Regarding the reliability, it is essential to investigate especially microdevices serving as actuators. For such elements, affecting an environment through operating under applying external signal, fatigue and ageing processes are the most significant causes of various damages. It justifies the goal of the Ph.D. thesis (see Introduction).
In the first years of MEMS emerging, researchers were focused mostly on the technology development and microstructure functionality demonstration. Only in recent years, the significance of reliability testing has been noticed, creating considerable interest in this subject. Many well-known, world research centers [Tanner 2000, Wolf 2003, Duong 2005, Sarihan 2006], have started dealing with problems of MEMS reliability (e.g. Sandia National Laboratories in USA), which have become a matter of numerous organizing international conferences (e.g. Eurosensors, MEMS, etc). Extensive studies have been conducted for many materials and microdevices. However in spite of a dynamically growing, MEMS reliability subject still remains in its infancy [Hartzell 1999, Andersen 2004, Muratet 2006]. One of the reasons of the reliability data lack is still not-well developed methodology, tools and standards for performing reliability tests. It concerns also failure analysis of complex microelements incorporating new materials and new fabrication processes. The considerable

amount of know-how is available for macro- and IC-device reliability testing. Their failure modes and test procedures described in the standards are well known. Unfortunately, this knowledge can not be directly transferred for the study of MEMS without the proper validations. Despite that certain failure modes can be similar, microdevices have some unique phenomena and damages related to their microstructures through the scaling effect, e.g. a stiction problem defined as the continued adhesion of the surfaces after removing the external forces which brought them into contact [Ali 2004]. Another reason for missing reliability data is that performed reliability investigations are mostly focused on a certain specific microsystems and their particular applications. It causes that they can not be used for other applications. According to the definition the reliability of MEMS highly depends on its intended uses. The same device can have different reliability when serves for various applications or operates in various environmental conditions. Required possible range of performance limitations is then different. Moreover, it is essential to consider reliability aspects from the beginning through all phases of the product development (a conception, a design, production processes) and finally to practical uses. The goal always is to identify potential reliability problems as early as possible in the product lifetime. Changes introducing in the early part of the design phase are much less expensive than when the product is already manufactured and in service [Brown 1997, Wolf 2003 a, Andersen 2004, Weibull].

In order to understand, measure or predict any event, it is necessary to observe it. Thus, to understand the reliability of any material or device, it is mandatory to get knowledge about their failure behaviour, and the factors that invoke this failure. One has to take into account and answer the series of questions, like for instance:

- What failure mode appears in investigated material or device ?
- What are the causes of these failure mechanisms?
- What is the lifetime and the failure rate?
- What tests are necessary to perform to reveal these mechanisms?
- If it is possible to accelerate its damaging?, etc.

Talking about reliability study, one should classify tested object either to repairable or non-repairable one. Non-repairable devices are those which do not get repaired when they fail. This does not necessarily mean that they cannot be repaired, rather that repair it is not economically reasonable [Weibull]. In the dissertation the AlN driven microdevices are considered, which belong to non-repairable elements. This chapter is then related to this kind of devices.

There are various reliability approaches. One of them treats that reliability can be estimated on the base of statistical analysis of performed laboratory reliability tests. Certain reliability parameters serving for its quantifying can be derived from Failure Distribution Density (or Probability Density Function *pdf*) $f(t) = dF(t)/dt$ or Failure Distribution Function (or Cumulative Distribution Function *cdf*) $F(t) = \Pr(\tau \le t)$, which are obtained from the collected life data. Reliability parameters, the most often used, are the following:

- Reliability Function *R(t)*

$$R(t) = 1 - F(t), \tag{6.1}$$

- Mean Time To Failure *MTTF*

$$MTTF = \int R(t)dt, \tag{6.2}$$

- Failure Rate *λ(t)*

$$\lambda(t) = \frac{f(t)}{1 - F(t)} = \frac{f(t)}{R(t)}. \tag{6.3}$$

Reliability function $R(t)$ defines the probability of success, i.e. the probability that a unit survives beyond time t. Mean Time To Failure *MTTF* is an expected value, i.e. a mean of the collected data. *MTTF* represents then only one point in the whole reliability function curve. Therefore $R(t)$ better describes the reliability aspects. The third of listed above parameter – Failure Rate $\lambda(t)$ - is defined as the instantaneous rate of failure in certain instant time t for one particular falrure mechanism determining the number of failure appearing during 1000 mln hours of operation [Birolini 2004, Berghmans 2007, ITL]. According to distribution functions, their various types exist having adequate predefined form of $f(t)$. Among them, families of statistical distributions serve for mathematically modelling or representing certain behaviours. Some of them tend to better represent life data and are commonly called lifetime distributions. The most widely used for life data analysis and reliability data modelling, lifetime distributions are Weibull, exponential and lognormal distribution [Birolini 2004, ITL, Weibull]. The correct choice of lifetime distribution can be justified by several reasons, i.e. the probabilistic arguments based on the physics of the failure mode, the good empirical fitting obtained failure data to particular distribution, or the previous success of certain distribution obtained for the same or a similar failure mechanism. However, whatever method is used, the chosen distribution should "make sense". Therefore, it is important trying to find a theoretical justification for this choice [ITL].

In reliability study, the objective is to obtain information if tested device or material will perform its function successfully for long, required periods of time. Because all failures cannot be eliminated from a fabrication and design, another goal of reliability study is to identify the most likely failures and then develop appropriate actions to mitigate the effects of those failures by improving technology and design. The reliability evaluation can include a number of various methods. Traditional life data analysis involves tests performing under normal operating conditions in order to quantify the life characteristics of the material, system or component. In many situations, and for many reasons, such life data (or times-to-failure data) is very difficult, and often impossible to obtain, because of the long life time of the products. This difficulty and a need to observe damages of tested devices to better understand their failure modes, mechanisms and their life characteristics, make necessary to develop methods for forcing these material and elements to fail more quickly than they would under normal use conditions. Such practices involving acceleration of the failures are termed 'accelerated life testing'. Its techniques allow to quantify the reliability of the product at normal use conditions. More specifically, accelerated life testing can be divided into two areas: qualitative accelerated life testing and quantitative accelerated life testing. Both of them have to be designed properly to not cause damages which would have never been encountered in real life. These tests have to then produce the same failure modes caused by the same mechanisms as at normal-use stresses. The only difference is that they occur much quicker. Failures may be then generated due to mechanical fatigue, corrosion, chemical reaction, diffusion, migration, etc., and their relevant accelerated factor can be e.g. higher temperature, voltage, humidity, duty cycle, etc. Acceleration techniques require that there be a stress dependent physical process causing object changes or degradation leading to failure. In general, different failure modes are affected differently by applied stress. Therefore, during test only one type of failure has to be investigated at time. The qualitative methods are then mostly focused on identifying failure modes and mechanisms without making any predictions concerning the product's life under normal use conditions. However, the quantitative ones concern the predictions determining reliability parameters from data obtained in an accelerated life tests. Qualitative tests are performed to obtain information only about damages, to quickly reveal failure modes probably occurring under normal use conditions.

They are carried out on small samples which can be subjected to a single severe level of stress, to a number of stresses or to a time-varying stress (i.e. stress cycling, etc.). They allow

to perform feedback to design and technology, and making appropriate actions to improve product reliability by eliminating the causes of revealed failures. The qualitative techniques may provide then valuable information about the types and level of stresses which can be employed during subsequent quantitative tests. However, they do not answer the question about quantitative reliability during operation. This is the purpose of quantitative accelerated life testing methods which consist of tests designed to quantify the life characteristics of the material, the product, component or system under normal use conditions and thereby provide reliability information. They allow to determine certain reliability parameters including e.g. the probability of failure, the mean time to failure *MTTF* or the failure rate $\lambda(t)$, all under use conditions. Quantitative accelerated life testing can take the form of usage rate acceleration or overstress acceleration. The first techniques are addressed for devices that do not operate continuously. In this case, the time is accelerated by testing these elements continuously, causing earlier encountering induced failures. Although, for other products, stresses can be applied at levels which exceed the levels that a device encounters under normal operation in order to accelerate the failure modes. Data obtained in this manner is then extrapolated to use conditions. This is the second form of quantitative accelerated life tests called overstress acceleration and they are dedicated to the products with very high or continuous operation. The accelerated life tests serve for stimulating them to fail. A life distribution (like the exponential, Weibull and lognormal lifetime distributions) can be then chosen to fit collected times-to-failure data (life data) to derive overstress *pdf*s for each applied stress level. While, life-stress relationships applied in so-called acceleration models are chosen to make extrapolation from the overstress *pdf*s to a use level *pdf*, and project obtained reliability results to the use conditions. From obtained use level *pdf*, a variety of functions, including reliability, failure rate, mean time to failure, etc. can be then derived. Accelerated life tests can be performed at high or low temperature, humidity, voltage, pressure, vibration, etc. in order to accelerate the failure mechanisms. A combination of these stresses can be also applied. However, accelerated tests can not introduce failure modes that would never occur under normal operation [ITL, Weibull].

Empirical acceleration models constructed from the measured data are related to the various failure mechanisms dependently on type of these models. There is variety of powerful and useful acceleration models as following [ITL]:

- Arrhenius;
- Eyring;
- Other Models.

It is crucial to choose an appropriate one similarly to choosing a life distribution model. The failure mode and its relevant stresses (i.e., accelerated this failure mechanism) have to be identified. Certain acceleration models are then related to the particular stress and failure mechanisms. The Arrhenius model for example is one of the earliest and most successful empirical acceleration models which predicts how time-to-fail varies with temperature. While, the Eyring model is more complicated and can be used to model acceleration when not only the temperature but also other additional stresses like voltage, current etc. are involved.

Many well-known models namely above as other models are simplified versions of the Eyring model. Some of these are the following [ITL]:

- The (Inverse) Power Rule for Voltage;
- The Exponential Voltage Model;
- Two Temperature/Voltage Models;
- The Electromigration Model;
- Three Stress Models (Temperature, Voltage and Humidity);
- The Coffin-Manson Model.

6.2. Chosen problems of the reliability

In the doctor work, the properties of the AlN thin films and the performances of AlN driven microcantilevers intended to work as MEMS actuators (see Introduction) were studied. It concerned their operation stability (resistance variation and influence of environment, i.e. temperature), reproducibility and quality testing (see Chapter 5). Because the success of microsystem product marketing is strictly related to their reliability [Wang 2000, Moraja 2003, Muratet 2006], this problem, including long-term stability and durability, had to be also investigated. As MEMS structures evolve from laboratory prototypes to commercial devices, the reliability of microsystem components need to be established during all phases of product development [Ali 2004]. Nevertheless, in this dissertation author was focused on the some in-use reliability study considering operational generated damages and failures (electrical breakdown and short-circuit, electrode damages, fatigue, etc.) caused by e.g. environmental as well as mechanical and electrical stresses. Because the reliability is a wide subject area, the author had to limit the range of the considered tasks. It was also linked with some experimental restrictions concerning the number of available test samples giving the reliability results. By reason of it, the author's interests were focused only on the certain part of the reliability problems. Therefore, among lots of existing methods for reliability study, the quality accelerated life tests were chosen. They allowed to identify and monitor the object behaviour changes as well as the probable damages and the failures with understanding their causes. Performed tests served to obtain quickly approximate estimation only about the probable property changes and damages, which could occur under normal uses during an expected lifetime. They contained the accelerated aging and the accelerated resonant fatigue. The first tests consisted in loading of the samples by a harsh conditions (i.e. in our case by high temperature, high humidity and high or abruptly changing voltage, all defined with comparison to the normal weather conditions) during certain time. While, during the fatigue tests the devices were working at resonance being exited by applying high sinusoidal voltage. In the presented dissertation the aging and the fatigue will be considered separately.
Aging will be defined as a mechanism impacting the microelement lifetime which relies in changing properties of material with time [Noliac]. However, considering aging induced by operation, this process will be called as a fatigue. Fatigue will be then understand as a mechanism caused by a stress introducing by repeatedly motions which even can be significantly below the crack strength. [Chang 2003]. The investigation of fatigue processes seem to be important since it is the primary technique currently studied in MEM reliability research being a critical issue for ensuring device reliability [Muhlstein 1997, Hartzell 1999].

The general procedure proposed in the Ph.D. thesis to study chosen reliability problems is presented in the Fig.6.1. It is a part of the research methodology described in the Chapter 2 for the investigation of the AlN thin films applied in the microcantilevers. Thus, the reliability study procedure consists in the monitoring of effects which could occur during the mentioned quality accelerated reliability tests. These effects concern the static and dynamic property changes as well as the damages and failures appearance detected on the base of the measurements carried out every particular period of time, chosen for each kind of the investigations. Reliability tests were accomplished in the various climatic chambers (except the aging under electrical shock and the fatigue tests which were performed in the standard weather conditions) described in the section 6.3. The measurements were performed after taking out the samples from the chamber, but not later than 48 hours after it (according to the norm ISO PN-EN 60749-6). Studied properties were determined in the both states, namely the static (i.e. determined initial deflection, out-of-plane displacement

vs. constant voltage) and dynamic (i.e. determined 1st resonance frequency, resonance curve of 1st resonance mode, vibration amplitude at 1st resonance mode) conditions. As it was mentioned in the Chapter 2, these behaviours provide the most amount of information about microelements. This means they allow to identify their geometric, material (i.e. piezoelectricity), mechanical (stress) and electrical (i.e. resistance) properties. Moreover, such properties are significant for intended applications of the investigated AlN driven cantilevers as actuators. Among the dynamic parameters the variations of the resonance frequency are especially important. They can be correlated with the changes in the specimen mechanical response and with the damage accumulation in the device material. Furthermore, the environmental variations such as e.g. temperature can also affect the material and dynamic parameters of the tested element [Muhlstein 1997, Petigrand 2001 a]. In the dissertation it is presented the reliability of the cantilevers for the lengths between 200 and 900 µm as well as the AlN film thickness of 1.0 and 1.4 µm. The same measurement tools as described in the Chapter 2, i.e. the Twyman-Green interferometer platform and the Scanning Electron Microscope SEM and the optical microscope, were used in the mentioned part of the research methodology. These non-destructive methods were successively applied for MEMS reliability studies allowing to monitor damage development and analyse performance changes.

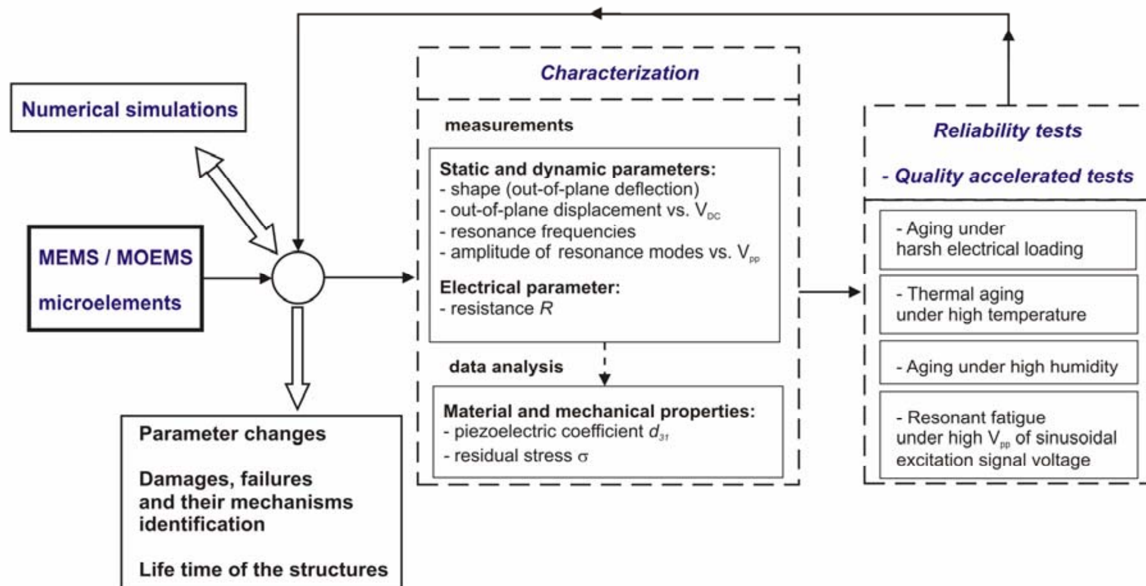

Fig.6.1: Diagram of proposed reliability procedure

6.3. Reliability study – results

In this section, the results of reliability study of the microcantilevers driven by the AlN thin film will be presented. These results were obtained from the qualitative accelerated life tests which idea was already discussed in the previous section (see section 6.1). These tests allowed to reveal and study artificially activated failures as a result of applying factors forcing them to appear quicker. The microcantilevers piezoelectrically driven by AlN thin film have been intended to use as actuators, it means that they present moving parts in the MEMS devices. Therefore, their resistances against the electrical shock, the fatigue and the aging have needed to be considered. Thus, the results of accelerated aging tests stimulated either by electrical shocks, high temperature or high humidity and accelerated resonant fatigue tests generated by high voltage signal were discussed. These tests were performed on the base of the general procedure described in the section 6.2. The received outcomes led to a quality

estimation of the durability (lifetime) and the long-term stability of the AlN based microelements. They allowed to identify their possible failure modes and relevant mechanisms. They gave the knowledge about the types and levels of stresses which can be withstand by the studied elements, as well. The static and dynamic parameters, the piezoelectric and electric behaviours and the appeared damages and failures were monitored. In particular, the initial deflection caused by internal stresses σ, the piezoelectric coefficient d_{31}, the resistance R and the resonance frequency f_{res} were considered. The received quality relations based on the accelerated fatigue studies have allowed to project the probable reliability to the normal conditions. The investigations were carried out on the small amount of samples and therefore their outcomes can not be considered as quantitative information. However, the results presented in this section can be used in the subsequent quantitative tests. During performed reliability tests, shift of 1st resonance frequency, change of vibration amplitude, short-circuit and delamination of thin films were assumed as failures of the AlN driven cantilevers. Failures have been understood as a termination of ability to perform a certain function. While, damages could, but do not have to lead to the failures.

6.3.1. Accelerated aging under electrical shock

Considering durability of the AlN driven devices, electrical shock relating to the high level of the applied voltage and its abrupt changes should be studied. These factors affect the operation and can lead to the microdevice failure. The AlN cantilevers with length of 800 µm will be tested. The maximal voltage values will be defined verifying the microdevice proper (stable) operation. The bias voltage and the resonant sinusoidal signal peak-to-peak voltage V_{pp} (without bias) will be considered.

Performed reliability investigations showed that the maximal values of sinusoidal signal exited the 800 µm long elements to the resonance vibration have been about 2 V_{pp} and 40 V_{pp} for samples with h_{AlN} of 1.4 µm and 1.0 µm, respectively. Higher voltage values have caused operation instability in the tested devices appearing as a slight variation of their vibration frequency noticed using stroboscopic interferometry (see Appendix 3) and/or an electrical breakdown. Higher voltages have introduced too high electrical stress for the proper (stable) cantilever operation.

According to the bias voltage, ±15 V were proved as too high for some of the 800µm long objects with both value of the AlN thickness leading to their failure. Therefore, it was decided to not exceed ±10 V of bias determining the range of the supply voltage. Thus, after using too high electric signal a severe damage of the top metal electrode was noticed and surely the AlN film. It was caused by the generation of too high electric field appearing near to the cantilever fixation area. This field can propagate then through the element resulting in electrode burn (see Fig.6.2) or delamination observed for some microelements (see Fig.6.3). The SEM images presented in the Fig.6.3 show the delamination of multiple thin film stack (i.e. CrNi-AlN-CrNi) from the Si substrate. This failure mode can be explained by various reasons: e.g. inadequate adhesion, thermal expansion coefficient mismatch between the AlN thin film and the Si substrate, and/or Si substrate underetching creating the area of high stress concentration localized at the free-end of the cantilever (see section 4.2.2). The locally burned electrodes were caused by appearing electric breakdown. The abrupt drop of the insulation resistance between the top and bottom electrodes (see section 3.1) caused current flow and heating of the AlN and the Si films. Therefore, well visible in the Fig.6.3 the areas of damages were probably the oxidation type related to the mentioned heating process [Andrei 2007 a, Andrei 2008, Krupa 2008 a]. Described effect resulted in degradation of the isolation property (infinity resistance) of the AlN thin film leading to creation of short

circuit. Discussed effect caused that the linear relation, between the out-of-plane displacement and the applied constant voltage V_{DC} (see Fig.6.4a) characteristic for piezoelectric behaviour, changes to the parabolic one (see Fig.6.4b) (see section 5.5). The cantilevers revealed then an important displacement $\delta >> \delta_p$ proportional to the square of the applied voltage (see Eq.5.6.6, section 5.5 and Fig.6.4a), which had Joule effect origin [Andrei 2007 a, Andrei 2008]. The explanation of this phenomenon was discussed in the section 5.5. Other result of the discussed failure mode, apart of the parabolic bending, was also the considerable decrease of vibration amplitude at resonance of more than 5 times as presented in the Fig.6.5. The similar phenomena were induced by the abrupt change of the supply voltage which caused drop of the structure resistance degrading its insulating properties.

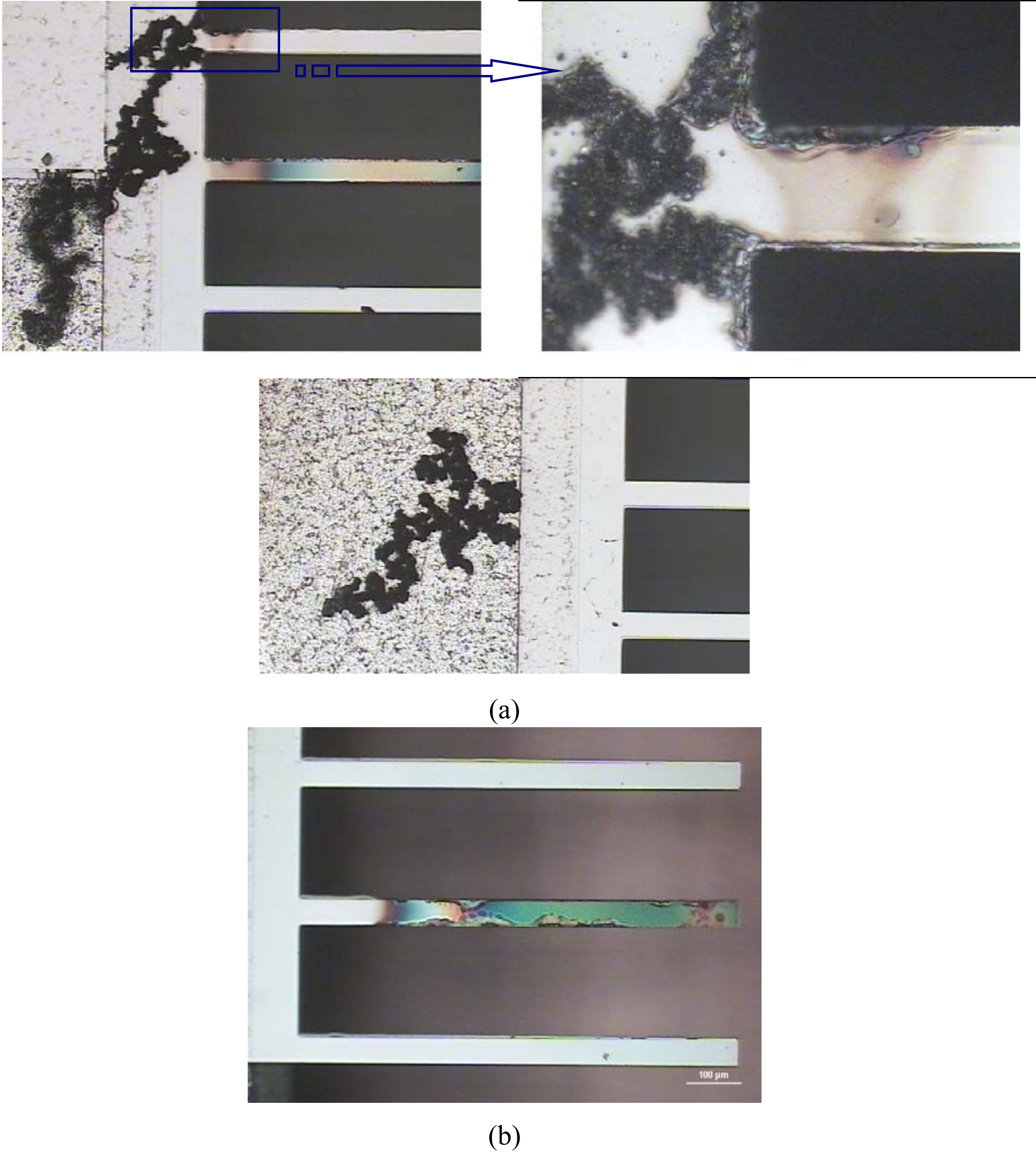

(a)

(b)

Fig.6.2: Optical microscope images of electrode damages for various 800 µm long microcantilevers with 1.0 µm (a) and 1.4 µm (b) of AlN thickness as a result of applying 15 V bias generating short circuit

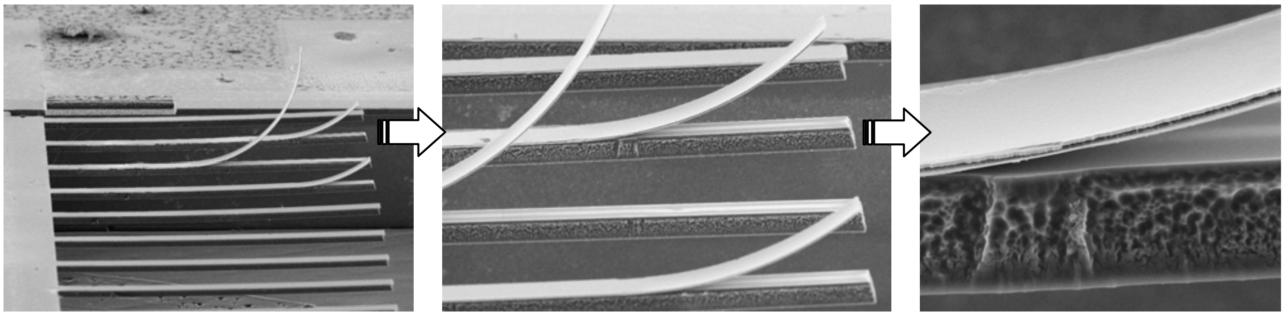

(a)

(b)

Fig.6.3: SEM (a) and optical microscope (b) images of delamination occurred in 800 μm long microcantilevers with 1.4 μm of AlN thickness as a result of applying 15 V bias and then short circuit

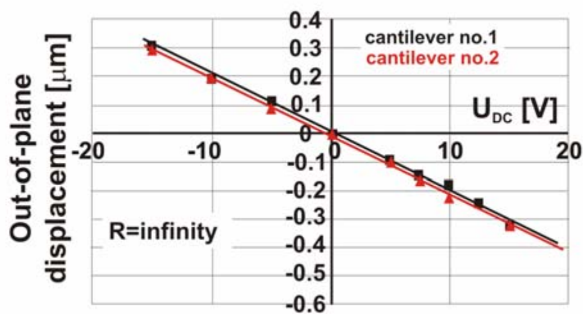

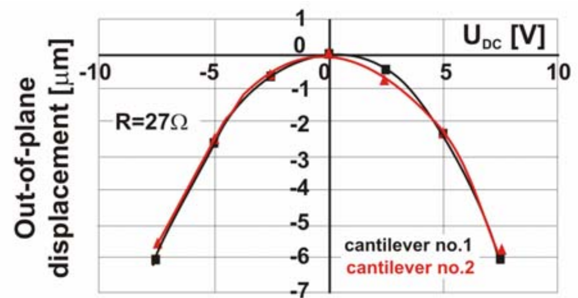

(a) (b)

Fig.6.4: Displacement induced by constant voltage V_{DC} measured for 800 μm long cantilevers with h_{AlN} of 1.4 μm and resistance R a) infinity and b) 27 Ω (in short circuit)

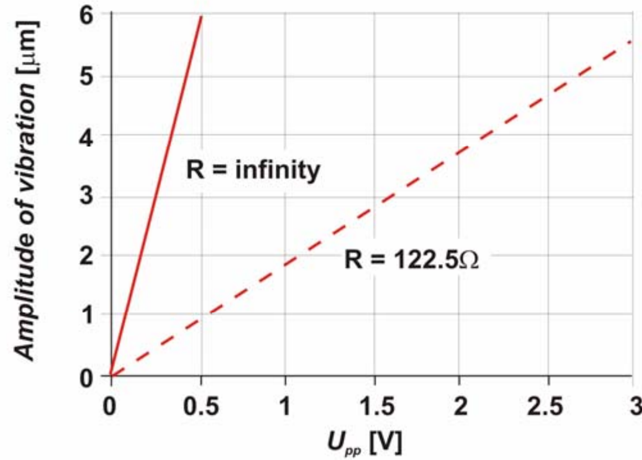

Fig.6.5: Resonance vibration amplitude as a function of applied V_{pp} voltage for 800 µm long cantilevers with h_{AlN} of 1.4 µm and infinite and finite 122.5 Ω (in short circuit) resistance R

6.3.2. Accelerated thermal aging

The aging tests accelerated by elevated temperature (130ºC) were performed according to the ISO PN-EN 60749-6 norm. This norm concerns high temperature storage of semiconductor structures and describes destructive studies recommended for device certification. The goal of mentioned tests is to determine the influence of storage at specified temperature without electrical load. Investigated elements should be storing at 150°C during 1000 hours. However, in the procedures used for the AlN driven microcantilever studies the temperature was decreased to 130°C because of the thermal restrictions related to the object packaging (see section 3.3.2). The storing time was also limited because of the number of available test samples. Applied procedure which general form is shown in the Fig.6.1, consists in monitoring of the first resonance frequency 1st f_{rez} and the initial deflection δ. The measurements were carried out in three cycles: I cycle after 48 hours, II cycle after 96 hours and III cycle after 192 hours of thermal loading. The samples were thermally exposed in the Vacuo-Temp 4000474 climatic chamber of Selecta Company (see Fig.6.6) with stability of ± 1ºC. They were maintained under vacuum of -60 cmHg to avoid possible object deterioration by e.g. metal oxidation. Obtained results are given in the Table 6.1. They present median values calculated from the measurements of a serie of 20 randomly chosen objects with the same design. The exemplary experimental resulted for 10 cantilevers are shown in the Figs.6.7 and 6.8 for the first resonance frequency and the initial deflection, respectively. While, the exemplary comparison of the object profile cross-section is demonstrated in the Fig.6.9. There were tested the 800 µm long microcantilevers with 1.4 µm thick AlN film. These devices reveal the best operation performances (see Chapter 5). Moreover, the temperature influence for longer samples is more significant (see carried out modelling results presented in the section 4.2.2). Measurements were performed in 25.5 ± 1°C of ambient temperature and 45 ± 5% of relative humidity. To obtain the 1st resonance vibration frequency, the sinusoidal voltage with V_{pp} of 0.180 V was applied. This value was chosen to generate 2 µm vibration amplitude.

Fig.6.6: Photograph of Vacuo Temp 4000474 climatic chamber of Selecta Company used for thermal aging reliability tests

Table 6.1: Results of thermal aging tests performed at 130ºC for 800 µm long cantilevers with 1.4 µm of AlN film thickness – median values

Annealing time [h]	**1st resonance frequency f_{res} [kHz]**	**Changes of 1st f_{res} [kHz]**	**Initial deflection δ [nm]**	**Changes of δ [nm]**
0	37.016	–	25970	–
	SD=0.555	–	SD=2150	–
48	37.022	0.006	25700	-270
	SD=0.553	SD=0.006	SD=2430	SD=130
96	37.025	0.009	25540	-430
	SD=0.558	SD=0.018	SD=2170	SD=190
192	37.027	0.011	25480	-490
	SD=0.554	SD=0.008	SD=2010	SD=220

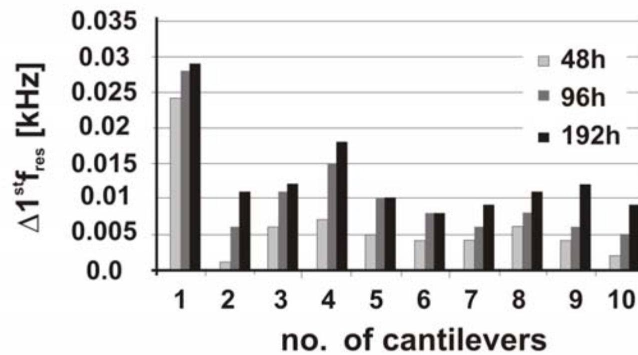

Fig.6.7: Results of 1st resonance frequency changes induced by thermal aging tests for 10 exemplary 800 µm long cantilevers with h_{AlN} = 1.4 µm

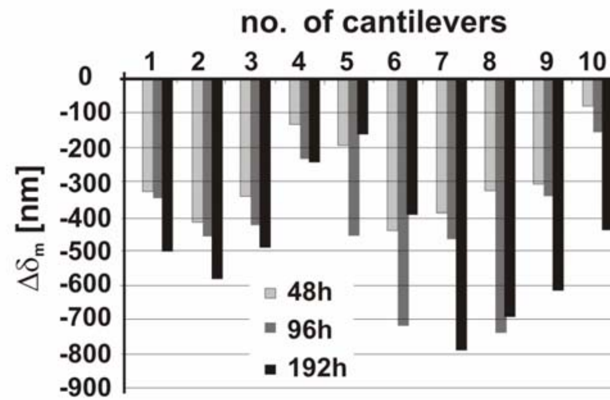

Fig.6.8: Results of initial deflection changes induced by thermal aging tests for 10 exemplary 800 μm long cantilevers with h_{AlN} = 1.4 μm

Received results showed the initial deflection decreased and the first resonance frequency increased. It could be explained by the stiffening process of the tested structures. A decrease of the initial deflection was observed also in the first, initial thermal aging tests performed in the same conditions (T = 130°C). These tests concerned the AlN driven cantilevers coming from the initial technological series (see section 3.3). However, that tentative experiment was accomplished during one thermal exposure cycle of 96 hours. It was tested cantilevers with the bottom aluminium electrode with various length (200, 500, 700, and 800 μm) and 0.400 μm of the AlN film thickness deposited in the different sputtering conditions (see section 3.3). Obtained results (being a median value of measurements of 10 objects) are shown in the Tables 6.2 and 6.3 for the 1st f_{res} and δ, respectively [Andrei 2006 a, Berghmans 2006, Gorecki 2006, Józwik 2006, Krupa 2007]. Thus, the decrease of initial deflections was observed for all tested samples. However, the 1st f_{res} values varied only within the measurement accuracy (see section 2.3.4). The results of the initial deflections obtained for 10 initial microcantilevers of 200 μm length are presented in the Fig.6.10 [Andrei 2006 a, Krupa 2007]. They illustrate the reproducibility of the noticed effect. Thermal aging seems then to release internal stresses. Their decrease was corresponded in percentages to the decrease of the initial deflections. The measurements of the 1st f_{rez} demonstrated constancy of material parameters incorporated in the tested structures (including Young modulus E).

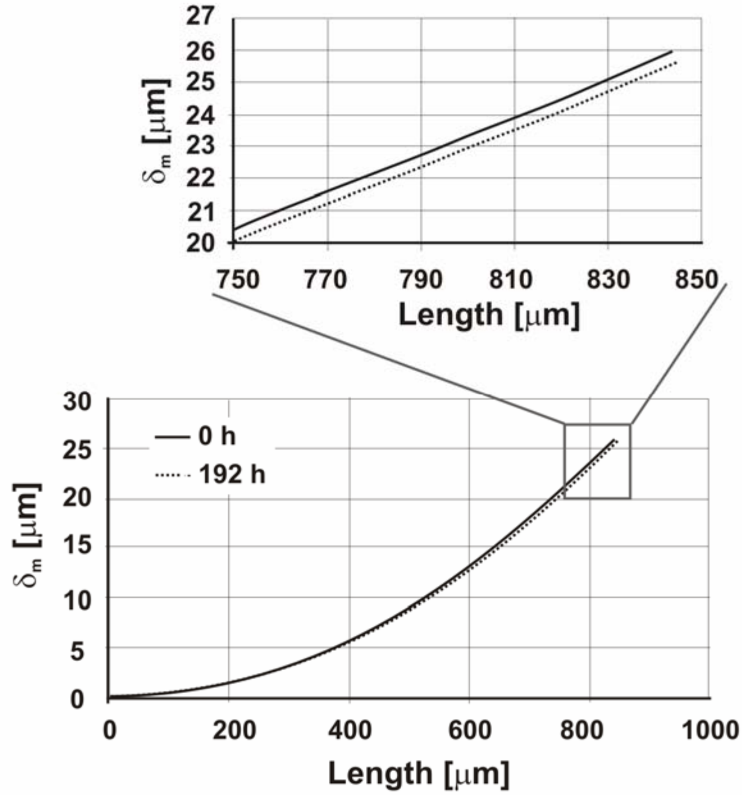

Fig.6.9: Change of object profile cross-sections for exemplary 800 µm long cantilever with h_{AlN} = 1.4 µm induced by thermal aging at 130ºC during 192 hours

Table 6.2: First resonance frequency results of thermal aging tests performed for first run of AlN driven microcantilevers with bottom electrode from Aluminium – median values

Length [µm]	**1st resonance frequency [kHz]**		**Changes of 1st resonance frequency [kHz]**	**Percentage changes of 1st resonance frequency [%]**
	before *T* = 130°	**after *T* = 130° and *t* = 96 h**		
200	566.0	565.7	-0.3	-0.05
	SD = 8,9	SD = 9.2	SD = 0.6	
500	94.80	94.75	-0.05	-0.05
	SD = 0,14	SD = 0.21	SD = 0.07	
700	41.65	41.70	0.05	0.12
	SD = 0.67	SD = 0.68	SD = 0.04	
800	31.80	31.80	0.00	0.0
	SD = 0.43	SD = 0.41	SD = 0.45	

Table 6.3: Initial deflection results of thermal aging tests performed for first run of AlN driven microcantilevers with bottom electrode from Aluminium – median values

Length [μm]	**Initial deflection [μm]**		**Changes of initial deflection [μm]**	**Percentage changes of initial deflection [%]**
	before T = 130°	**after T = 130° and t = 96 h**		
200	-1.140	-0.950	0.190	16.7
	SD = 0.030	SD = 0.030	SD = 0.020	SD = 1.7
500	-3.659	-3.491	0.168	4.6
	SD = 0.129	SD = 0.132	SD = 0.003	SD = 2.3
700	-13.500	-13.020	0.480	3.6
	SD = 0.560	SD = 0.550	SD = 0.020	SD = 0.2
800	-11.980	-11.690	0.290	2.4
	SD = 0.400	SD = 0.390	SD = 0.030	SD = 0.2

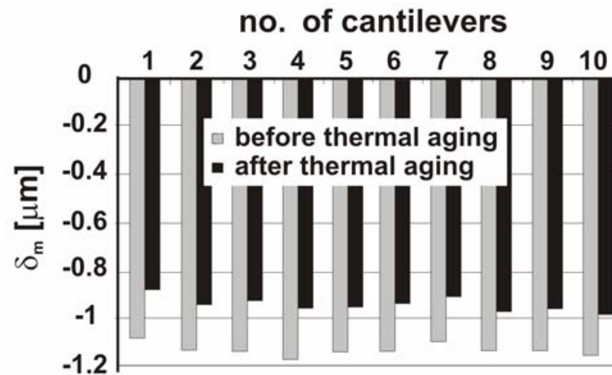

Fig.6.10: Results of initial deflection measurements for 10 exemplary 200 μm long cantilevers before and after thermal aging

6.3.3. Accelerated aging under high humidity

Considering aging accelerated by high humidity, two tests were carried out: one performed in the cooperation with the Space Research Centre of Polish Academy of Sciences and the second one with the Institute of Aviation situated in Warsaw in Poland. The 1st resonance frequency $1^{st}f_{res}$ and the initial deflection were considered. Moreover, the investigations were focused also on the detection of probable damages which can be induced by the humidity. It is the important parameter which should be taken into account during device operation in the standard weather conditions. The following cantilevers were used in the experiment:

- L = 900 μm and h_{AlN} = 1.0 μm;
- L = 200 μm, 400 μm and 600 μm and h_{AlN} = 1.0 μm;
- L = 400 μm and h_{AlN} = 1.4 μm.

These samples were exposed on the temperature T = 85°C and the relative humidity RH = 85% during 18 hours in the climatic chambers (see Fig.6.11) of type VEB Neutron

KPK 400V as well as during two 48-hour cycles in the climatic chamber of type WEISS SB2-300, placed in the Space Research Centre and the Institute of Aviation, respectively. The ISO PN-EN 60749 - 5 norm was applied. This norm is recommended for durability study of semiconductor devices performed at steady-state conditions of temperature, humidity and polarization. Used parameters are given in the Table 6.4. Such investigations have the priority in comparison with the accelerated tests (HASP) described by the norm ISO PN-EN 60749-24 which are oriented to the humidity resistance study. The 1st resonance frequency variations were monitored (median results, see Table 6.5). Median values were taken on the base of measurements of a serie of 14 randomly chosen cantilevers with the same design. Whereas, the initial deflection and the resonant vibration amplitude vs. the sinusoidal voltage V_{pp} changes observed during testing performed in the Institute of Aviation are shown in the Figs.6.12 and 6.13, respectively. Despite the mentioned multiple shorter time of the carried out studies (about 2 and 10% of the time proposed by the chosen norm) certain changes can be noticed. Namely, slight negative changes of 1st f_{res} and changes in resonant vibration amplitude can probably have been caused by the mass migration and the film imbibe. The cantilever mass increased. It resulted in a decrease of the resonance frequency and the electromechanical efficiency causing decrease of the vibration amplitude observed for the same excitation voltage. However, the influence of high humidity on the cantilever initial deflection is not unique.

Table 6.4: ISO PN-EN 60749-5 norm abstract

Temperature (dry-bulb thermometer) [°C]	Relative humidity [%]	Temperature (wet-bulb thermometer) [°C]	Pressure [kPa]	Time [h]
85 ± 2	85 ± 5	81	49.1	1000

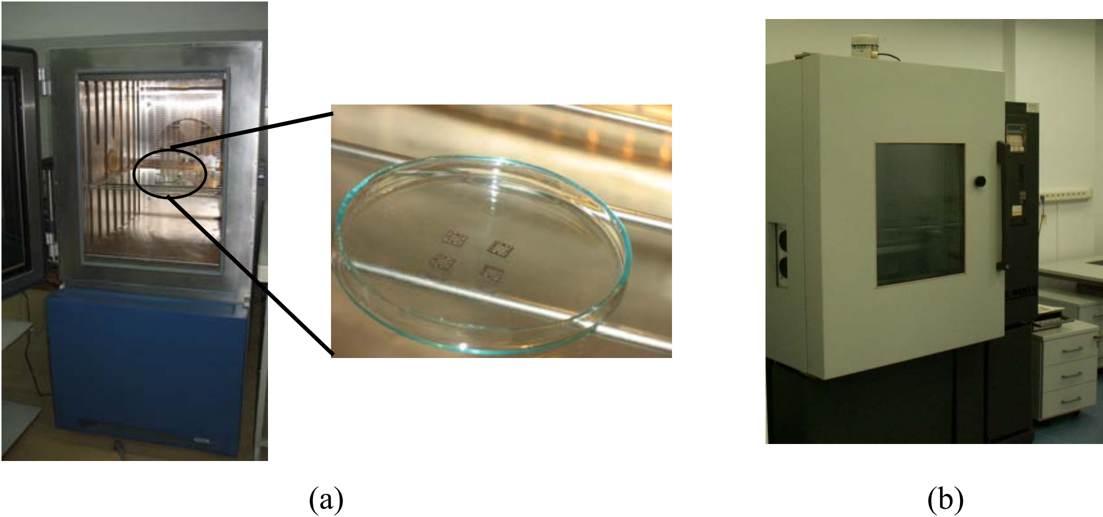

(a) (b)

Fig.6.11: Photograph of climatic chambers used for aging reliability tests under high humidity: WEISS SB2-300 chamber placed in the Institute of Aviation (a) and VEB Neutron KPK 400V chamber from the Space Research Centre (b)

Table 6.5: Results of accelerated aging tests in high humidity – median values

Tests performed in the Institute of Aviation						
h_{AlN} [µm]	**L [µm]**	**1st resonance frequency f_{res} [kHz]**			**Changes of 1st f_{res} [kHz]**	
		before	**after I cycle (48 h)**	**after II cycle (48 h)**	**after I cycle (48 h)**	**after II cycle (48 h)**
1.0	200	511.94	511.75	511.77	-0.19	-0.17
	SD	20.35	20.15	20.23	0.46	0.48
	400	155.193	155.188	155.178	-0.005	-0.015
	SD	5.015	5.009	5.005	0.0316	0.154
1.4	400	158.631	158.508	158.639	-0.123	0.008
	SD	1.636	1.698	1.620	0.312	0.062
1.0	600	62.399	62.398	62.396	-0.001	-0.003
	SD	1.847	1.845	1.842	0.010	0.009

Tests performed in the Space Research Centre of Polish Academy of Sciences				
h_{AlN} [µm]	**L [µm]**	**1st resonance frequency f_{res} [kHz]**		**Changes of 1st f_{res} [kHz]**
		before	**after 18 h**	**after 18 h**
1.0	900	27.075	27.065	-0.005
	SD	0.381	0.419	0.005

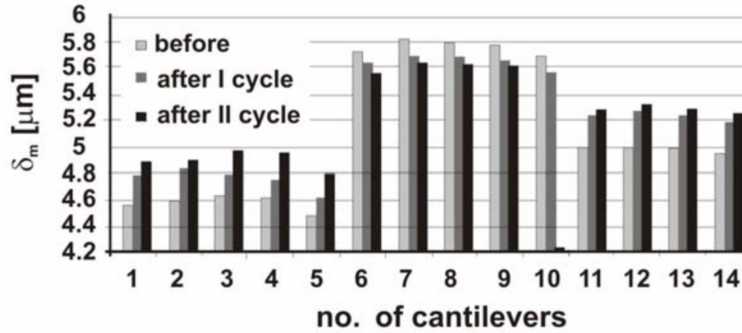

Fig.6.12: Initial deflection changes induced by aging under high humidity performed in the Institute of Aviation for 400 µm long sample with h_{AlN} = 1.0 µm

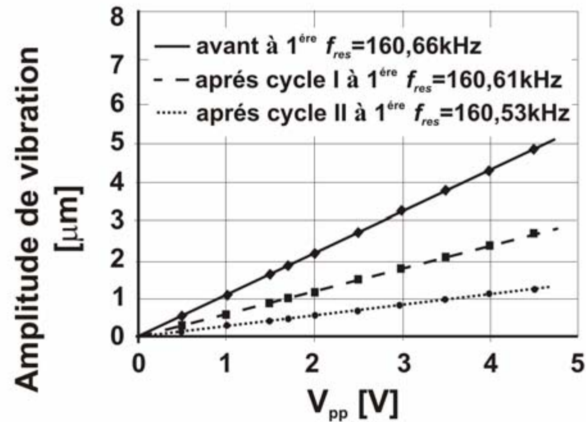

Fig.6.13: Changes of resonant vibration amplitude vs. sinusoidal voltage V_{pp} induced by aging under high humidity performed in the Institute of Aviation for 400 µm long sample with h_{AlN} = 1.0 µm

During investigations of the 900 µm long cantilevers under high humidity, the significance decreases of resonance frequency (of about Δf_{res} = - 0.17 kHz) for some of the samples were observed. This negative change of the resonance frequency can have been caused by a slight decrease of stiffness of the tested microelements. Possible explanation of the observed effect can be a local vapour condensation appeared on the objects. Observed surface deteriorations occurred through the corrosion process are visible in the photograph presented in the Fig.6.14. The obtained results showed that the level of humidity should be monitored as the one of possible reasons of the sample failures.

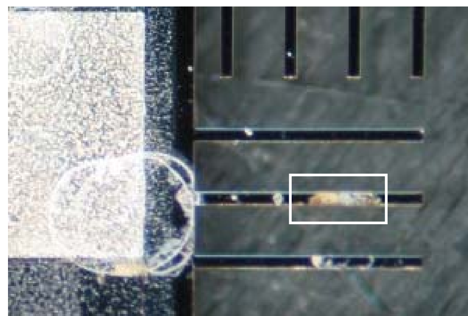

Fig.6.14: Photograph of 900 µm long cantilever damaged by vapour condensation

6.3.4. Accelerated resonant fatigue under high voltage

The accelerated tests were performed to study the resonant fatigue of the AlN driven microcantilevers and its influence on the device operation. Therefore, the objects were excited to the resonant vibration and their static (displacement vs. constant voltage and then piezoelectric coefficient d_{31}) and dynamic parameters (1st f_{rez} and amplitude of the vibration at resonance) were monitored in the day cycle (see Fig.6.1). As an accelerated factor high values of peak to peak voltage V_{pp} of excitation sinusoidal signal were used. The tests were carried out at 1.8 V, 0.885 V and 0.180 V of V_{pp}. It caused the cantilever vibration with the amplitudes of 20 µm, 10 µm and 2 µm, respectively. The 800 µm long microcantilevers with 1.4 µm thick AlN film were tested. Such a choice resulted from their best operation performances (see Chapter 5). Obtained experimental data showed that during the fatigue tests the 1st resonance frequency was shifting into the lower values. This effect occurred quicker when higher V_{pp} was applied (see Fig.6.15). The shift rate vs. the used voltage values are shown in the Fig.6.16. Observed dependencies could be approximated by linear functions.
If the first resonance frequency was decreasing, then the vibration amplitude measured at its initial value was decreasing too. Such an effect was confirmed with the resonance curve (see Fig.5.11, section 5.3). However, the vibration amplitudes measured at the current value of the resonance frequency (see Fig.6.17) were changing only within the measurement accuracy (see section 2.3). Moreover, the cantilever tip displacement vs. constant voltage leading to the piezoelectric coefficient d_{31} determination was not changing, as well. These linear characteristics measured before and after the reliability test are presented in the Fig.6.18.

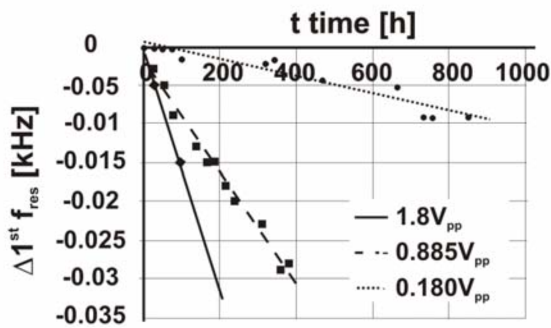

Fig.6.15: Changes of 1st resonance frequency vs. operation time at various V_{pp} of sinusoidal excitation voltage signal for 800 µm long cantilevers with h_{AlN} = 1.4 µm as a results from resonant fatigue tests

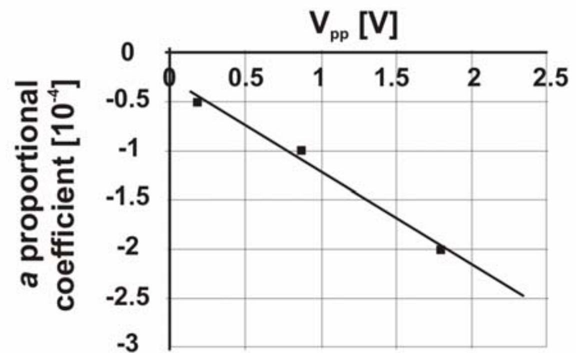

Fig.6.16: 1st resonance frequency change rate vs. V_{pp} of sinusoidal excitation voltage signal for 800 µm long cantilevers with h_{AlN} = 1.4 µm as a results from resonant fatigue tests

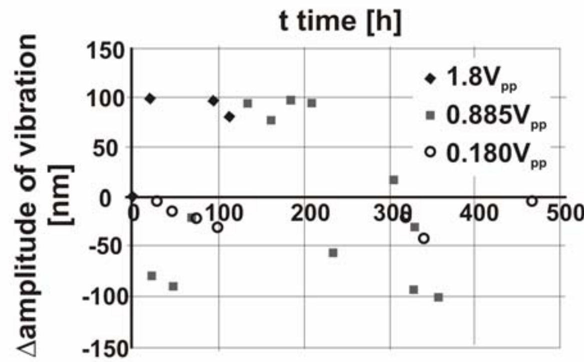

Fig.6.17: Variations of 1st resonance mode amplitude for 800 μm long cantilevers with h_{AlN} = 1.4 μm induced by resonant fatigue tests

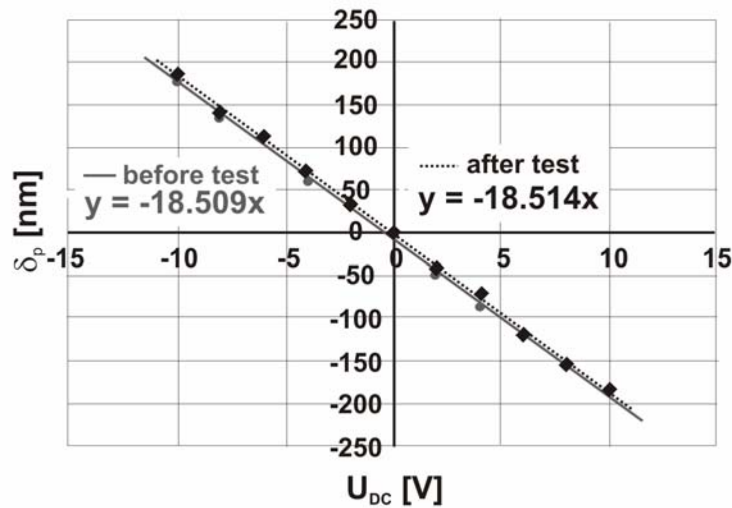

Fig.6.18: Displacement vs. constant voltage DC before and after fatigue test accelerated by 1.8 V_{pp} voltage signal

Thus, the obtained results demonstrated that the fatigue process does not deteriorate the piezoelectric response, however it affects the mechanical properties. Moreover, during the tests the object surface damages corresponded to the mentioned resonance behaviour changes were noticed. The cantilever top electrode degradation was caused by the crack generation in the metallic film. Observed negative shift of the resonance frequency and crack related fatigue effect are in accordance with the literature [Kazinczi 2000]. Both mentioned phenomena were considered to limit the life-time of the investigated objects. Since, the AlN driven microcantilevers could be applied as MEMS actuators dedicated to the AFM microscopy. However, the surface quality was found to be more crucial factor leading to the device failure. Instrument proper operation affected by the resonance parameter changes could be mended by the calibration process. The AlN thin films show then the very stable piezoelectric properties (see Figs.6.17 and 6.18). Because of the high levels of the vibration amplitude applied in the accelerated fatigue tests, the visible damages of the cantilever top electrode were noticed just after 37 and 90 hours of the resonant operation at 1.8 V_{pp} and 0.885 V_{pp}, respectively. The surface quality changes observed during the tests performed at two mentioned peak-to-peak voltage are presented in the Figs.6.19 and 6.20 for the structures marked by

the white rectangles. Deterioration was expected to occur in the object fixation area because of the highest stress concentration localized there. However, the damages were generated starting from the microcantilever free-end likewise the noticed delamination (see Fig.6.3), what confirmed obtained results. Both mentioned effects were found to appear in the film discontinuity area providing convenient conditions for their generation (see section 4.2.2).

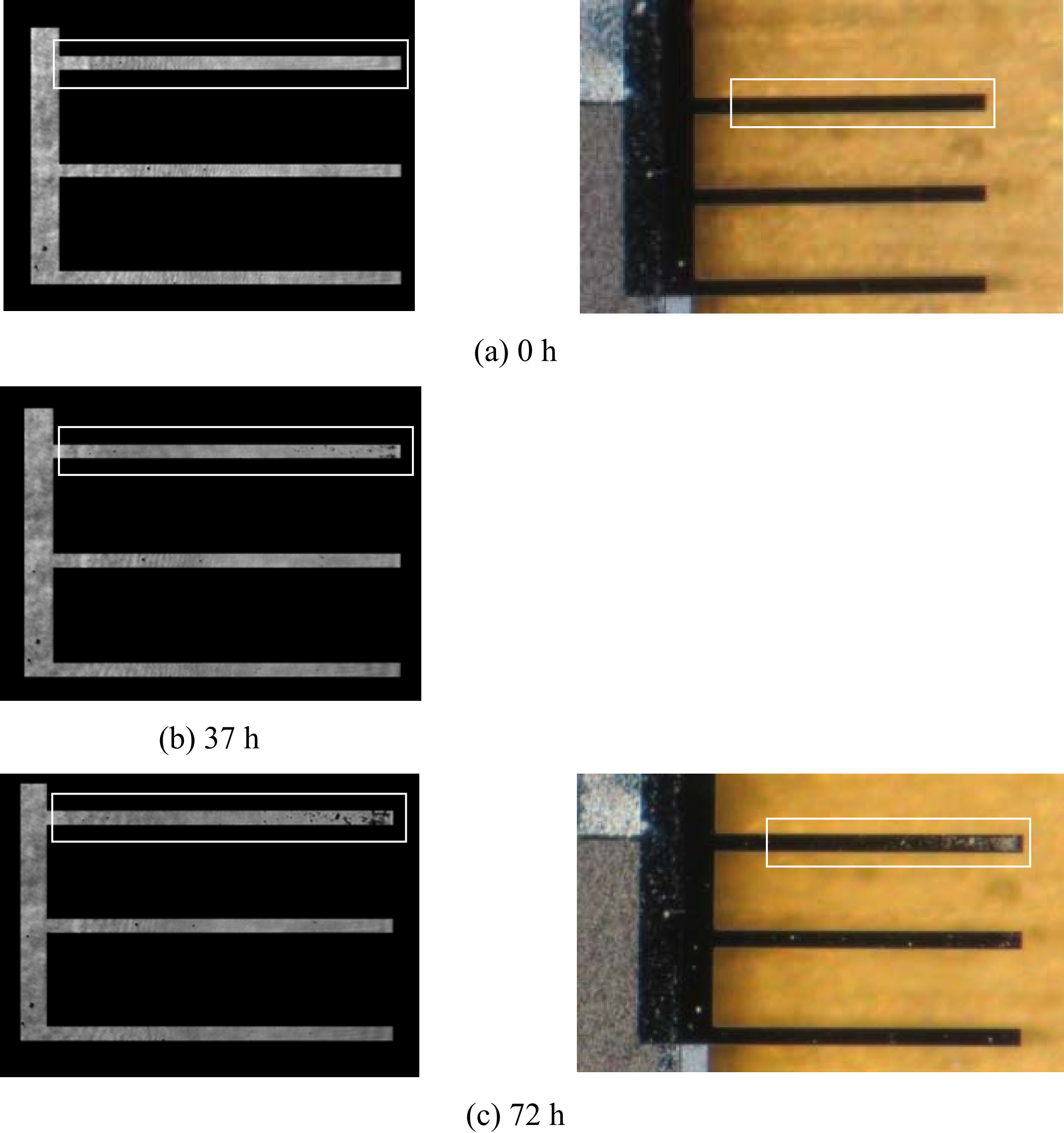

(a) 0 h

(b) 37 h

(c) 72 h

Fig.6.19: Photographs illustrating damages of top electrodes induced by accelerated fatigue tests at 1.8 V_{pp} voltage signal (induced amplitude of 20 μm) for certain time

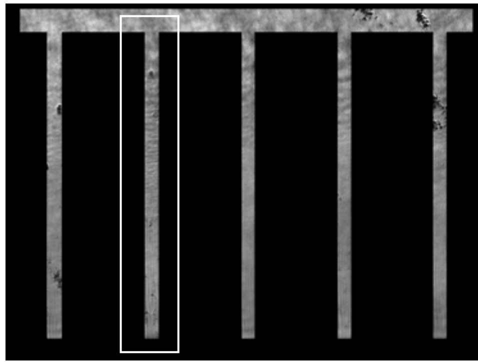
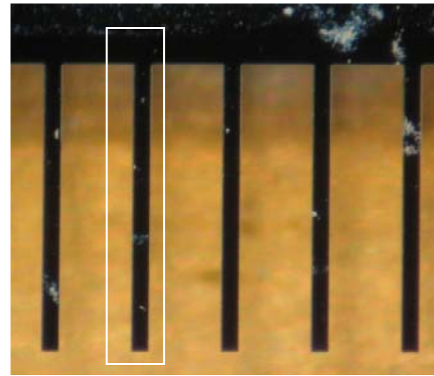

(a) 0 h

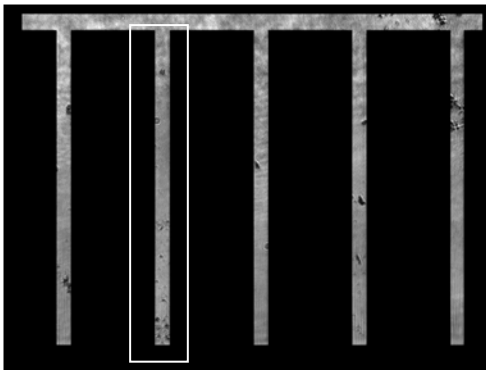

(b) 90 h

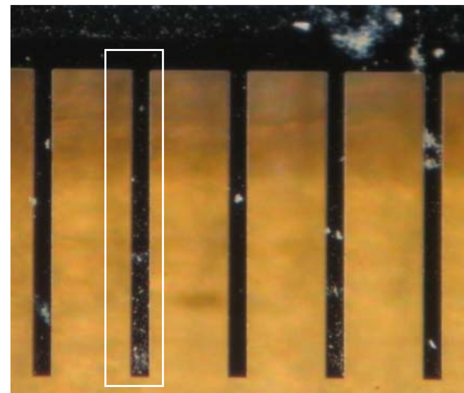

(c) 190 h

Fig.6.20: Photographs illustrating damages of top electrodes induced by accelerated fatigue tests at 0.885 V_{pp} voltage signal (induced amplitude of 10 μm) for certain time

Basing on the performed fatigue tests the acceleration models could be determined for the specified failure conditions, which in our case concern the dynamic parameter and electrode quality changes. Such models allow to estimate the life times (i.e. times-to-failure) of the devices operating at resonance with the specified vibration amplitudes. Assumed that the microcantilever top electrode deterioration observed after 72 hours of the resonant operation at 1.8 V_{pp} (and after relevant 190 hours at 0.885 V_{pp}) is considered as a failure. It corresponds to the resonance frequency shift of -0.015 kHz and according to the measured resonance curve (see Fig.5.11, section 5.3) to the -10% change of the vibration amplitude. Considering these conditions as maximal acceptable for proper device operation,

the accelerated model presented in the Fig.6.21 was determined. It led to formulate the hypothesis about the life-time of the AlN driven microcantilever, which assumes that for every two-times lower vibration amplitude the life time increases over 2.5 times. In the case of the 2 μm amplitude the operation time was found to increase up to 1560 hours (i.e. about 2 month). Developed model allows to project obtained results to the arbitrary chosen normal use conditions of studied actuators. Assuming for instance 300 nm of the vibration amplitude the life time will be almost 3 years.

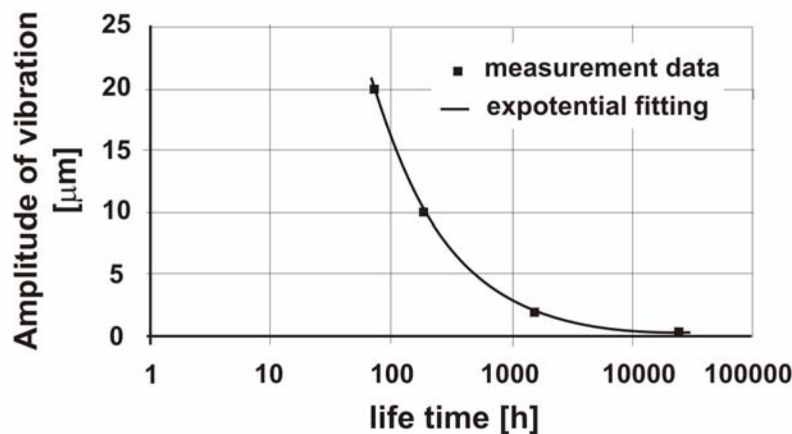

Fig.6.21: Life time vs. demanded vibration amplitude causing its 10% decrease determined for AlN based microcantilever

6.4. Conclusions

The reliability studies based on the quality accelerated tests relating to the chosen problems were performed. The AlN driven microcantilever static and dynamic operational parameters were measured using the multifunctional interferometric platform (see Chapter 2). The initial deflection and the first resonance frequency changes resulted from the accelerated aging induced by the high temperature, humidity and electrical shock were done. Additionally, the resonant fatigue tests accelerated by high voltage were accomplished. The voltage failure threshold was determined, as well. The studies of the accelerated fatigue process allowed to formulate the hypothesis concerning to the tested device lifetime. It was received due to the projection of the obtained data to the normal use conditions. Moreover, the constant voltage higher than 15 V was found to be too large, because of the piezoelectric film abrupt breakdown. Such an effect led to the metal electrode damages and, in some cases, the loss of adhesion and the structure delamination. Moreover, the generated short circuit induced changes in the sample piezoelectric response from linear to parabolic one of the Joule effect origin. According to the dynamic operation mode, the sinusoidal resonant signal amplitudes V_{pp} causing the sample unstable operation was evaluated. They were found to be higher than 2 V_{pp} and 40 V_{pp} for the 800 μm long samples with h_{AlN} of 1.4 μm and 1.0 μm, respectively. The electrical operation conditions were then determined for the static and dynamic operation mode. Considering the reliability results of the thermal aging at 130°C, the first resonance frequency increase and the initial deflection decrease were noticed as a result of a Young module increase. This phenomenon was observed for the piezoelectric actuators coming from both the initial and the improved technological process. The results of the tests performed under high humidity relating to the initial deflection were ambiguous.

However, the dynamic studies allowed to notice changes in the resonant vibration amplitudes and the slight negative shifts of the first resonance frequencies. The mass migration or the film imbibe could be a possible explanation of these behaviours. The higher decrease of the resonance frequency was observed also, induced by the noticed local vapour condensation on the microcantilever top surface. Moreover, fatigue tests at the three values of the resonant sinusoidal voltage were performed too. The results concerned the 800 μm long cantilevers from the improved fabrication process. They showed the top metal electrode damages occurred just after 37 hours of testing (at 1.8 V_{pp}) causing the first resonance frequency decrease. These damages began from the cantilever free-end indicating the high stress concentration in the film discontinuity area. This phenomenon was confirmed by the delamination process (see section 6.3.1) and the border electrode irregularity (see section 3.3), both observed at the object tip. In addition, the hypothesis concerning the life-time of investigated actuators was formulated evaluating this operation time to be about 3 years in the case of assumed 300 nm resonant vibration amplitude.

Concluding remarks

During the dissertation work many various studies were being performed. At the end it is worth to enumerate the main novel achievements concerning the investigation of the piezoelectric thin films and the MEMS cantilever piezoactuators. Moreover, the directions of the future researches, which are important for further device improvement, but which were out of the accepted dissertation scope will be proposed.

The goal of this Ph.D. thesis was the analysis and the determination of the properties of piezoelectric aluminium nitride (AlN) thin film used as an actuation layer of piezoelectrically driven microcantilevers and the evaluation of their micromechanical performances. The work was accomplished using a hybrid methodology, which was based on the interaction between the physical and the mathematical models of the tested sample. The operational parameters of the microdevice under investigation were studied, including their micromechanical behaviours, operational stability and life-time.

In the Chapter 1, the Ph.D. manuscript introduced various types of smart materials applied in MEMS actuators, demonstrating the specific advantages of piezoelectric actuators. In particular, the thin films of aluminium nitride were shown as a very interesting material for this purpose, presenting a good piezoelectric efficiency and a strong compatibility with IC processes of fabrication that is necessary in manufacturing of the MEMS devices. These excellent properties of AlN were not yet fully explored in the case of bulk actuators because the main market of AlN devices is the telecom market requiring mainly the use of systems based on surface acoustic waves. The bulk actuator applications require higher degree of controlling of the micromechanical properties of AlN. However, the mentioned properties are not precisely known and the actuator performances are strongly dependent on manufacturing. It is caused by the scaling effect, the multilayer structure of the devices and the interface interactions between the thin films in presence. In this Ph.D. dissertation we decided to focus on the study of AlN film properties playing the role of actuation layer in the bimorph cantilevers being our objects under tests described in the Chapter 3. In this MEMS structure, the thin film of AlN, sandwiched between two metal electrodes, was deposited on top of silicon substrate. The AlN layer introduced a controlled bending of the structure which was actuated by application of a voltage. The Chapter 2 reviewed the metrology methods applied to MEMS focusing on the two-beam interferometry, particularly well adapted for this purpose. It ensures full-field and non-contact measurements of out-of-plane displacements and fast (without time-consuming scanning) extraction of 3D shape with a required nanometer accuracy and a high sensitivity. Therefore, for the experiments performed within the framework of this doctor work, the multifunctional interferometric platform based on the Twyman-Green interferometer was chosen, providing the data on the static (i.e. shape, out-of-plane displacement) and dynamic (i.e. resonance frequencies, transient vibration shape profiles) behaviours of investigated sample. Using these parameters the geometric and material constants related to the mechanical properties (i.e. Young modulus, hardness, residual stress), thermal expansion coefficient and piezoelectric coefficient d_{31} were determined in the Chapter 5, basing on the developed procedures. Moreover, this platform gave the possibility to perform a limited number of the reliability tests. The analytical and numerical models of the rigidly one-side-clamped tri-layer microcantilevers actuated by AlN thin film were implemented. These models described the static and dynamic performances as well as the mechanical, piezoelectric and thermal properties of the tested samples were shown in the Chapter 4. Combining the measurements with the numerical simulations and

the analytical models the appropriate hybrid opto-numerical methodology for analysis of MEMS actuators was developed in the Chapter 2. The hybrid approach consisting in the feedback between the physical and mathematical models allowed then to complex and detailed characterisation of the AlN piezoelectric thin film microcantilevers presented in the Chapter 5. In this dissertation the two mentioned models were developed in parallel and completed mutually during the analysis process. The opto-numerical techniques are dedicated especially to the objects without well proved design and modelling methods, which are fabricated using new materials incorporated in multilayer structures or using new technological processes. They are to characterise such elements and study their reliability. Understanding better the behaviour of real elements allows to predict and control their functionality in a more accurate and reliable way. To successfully commercialize the microdevices their reliability and controllability have to be ensured. Studying these issues is crucial to get knowledge about the most likely failure modes and the factors that invoke these failures. However, because the study of reliability issues is a very wide subject, only certain quality accelerated life tests were performed, focusing on the some in-use problems, which were presented in the Chapter 6. They contained aging accelerated by harsh conditions (electrical shocks, high temperature and humidity) and resonant fatigue accelerated by high sinusoidal voltage. However, the reliability studies were carried out on the small amount of samples and therefore received results are only estimated. Moreover, basing on the proposed hybrid methodology the analysis and the evaluation of the AlN driven microcantilever technology was performed in respect of their performances (see Chapter 3). The fabrication critical remarks causing the discrepancies in the device functionality were determined. They allowed the optimisation of their technology and the offering the structures with improved performances.

Data obtained from the performed researches showed that AlN thin film could be successfully used for actuation purposes since it could provide excellent and stable in time piezoelectric behaviours comparable with the bulk material. Acquired knowledge gave reliable information to be able to realise the AlN-driven actuators of high quality. The important role of a hybrid methodology for analysing multilayer microstructures was proved. Performed study demonstrated also that technology (including used materials and geometry) has strong influence on the properties and the functionality of AlN based devices needed to be precisely controlled. While, the stable environmental conditions are indispensable during the operation of the investigated actuators, and especially the temperature has to be controlled.

Novelty elements

The main new scientific achievements concerning the investigation of the piezoelectric thin films and the MEMS cantilever piezoactuators are as follows:

- in the theoretical – numerical study domain
    - development of the analytical model describing the AlN driven cantilever behaviours;
    - development of the numerical model of the fabricated AlN driven tri-layer microcantilevers. The FEM simulations of the microactuator performances were performed using ANSYS software. They concerned the static and dynamic response including force induced displacement, resonance frequency, vibration mode shapes, piezoelectric behaviours and temperature influence. The measurement data of the tested objects were taken into considerations. Obtained results allows to understand better the functionality of the real devices and the mechanisms of their failures identifying the critical areas of the stress concentration;

- in the experimental study domain
  - development of the hybrid methodology concerning the non-destructive study and the modelling of the thin film properties, as well as the functionality and chosen reliability problems of the microstructures. This methodology consists in the interaction between the analytical, numerical and experimental data;
  - development of the reliability test procedures applied to the microdevices;
  - determination of the operational voltage range and the operational stability under standard weather conditions, i.e. influence of environmental (temperature) and electrical conditions (resistance);
  - reliability measurements based on the chosen quality accelerating life tests of aging and resonant fatigue. Identification and monitoring of damages, failure modes and behaviour changes which could appear during the object life cycle, as well as explanation of their generation mechanisms;
  - formulation of the hypothesis about the lifetime of the investigated AlN thin film microactuators and their operation time determination;
- in the domain of the hybrid methodology implementation
  - complex analyses of the AlN thin film properties and the performances of the microcantilevers actuated by this piezoelectric layer basing on the combination of the experiments, simulations and theoretical considerations. Determination of the static and dynamic responses as well as the crystallographic, elastic, mechanical, thermal and piezoelectric properties. Estimation of the reproducibility based on the deviations of the tested parameters over entire wafer. Identification and explanation of the main sources of behaviour discrepancies between the physical and theoretical model. The influence of various geometrical dimensions of the cantilevers, AlN thicknesses, AlN crystal structure and electrode nature were considered. Performed studies are one of the most detailed as have been carried out for the AlN thin films and the AlN driven devices;
  - development of the basis for improving the quality of the AlN thin films and the devices by introducing the feedback to their design and fabrication.

Summarizing, it can be found that the fundamental goal of this Ph.D. dissertation related to the complex study of the AlN piezoelectric thin films incorporated in the microcantilevers dedicated for the MEMS actuators was achieved.

The design and the fabrication process of the microactuator with AlN piezoelectric thin film oriented for MEMS applications were proposed.

It is worth to emphasise that obtained results related to the study of the AlN thin films could be valuable also for other microstructures driven by this piezoelectric materials. Acquired knowledge allowing to improve technological process could lead to design and manufacture in the future, high quality and reliable AlN based piezoelectric actuators and other various microdevices increasing a number of their applications. Moreover, obtained data could allow to fabricate objects with low deviation of the technical characteristics over entire substrate. High performance reproducibility is a crucial issue for manufacture the systems which use parallel network elements integrated over a chip.

The received results and proposed hybrid methodology are crucial for developing and getting more exact knowledge about fabrications, behaviours and reliability of microstructures. Created relevant data base which includes parameters characterising AlN thin films and microcantilevers, could be an information source for hybrid analyses, as well as for modelling and manufacturing of various piezoelectric actuators.

Worked out hybrid (opto-numerical) methodology is found to be significant for developing methods which supports the technology improvement in fabrication of high quality microelements. Presented approach for the characterisation as well as the life-time (durability) and the operational stability evaluation could be also extended to other thin film materials and microelements. Its implementation could allow to study and improve their properties, reliability and performance controllability by introducing feedback to their design and fabrication. Precise knowledge about technical characteristics of microdevices and materials properties in microscale is necessary for their further applications. It could help the designer to control better the microelement technology leading to improve their quality, reliability and behaviour stability. Therefore, presented research works are important for developing methodology to determine the reliability in microscale.

The proposed methods and procedures have extended the metrological capability of the laser interferometry techniques and then could lead to develop the smart measurement systems and their applications.

Future research directions

Performed studies and obtained results showed that the aluminium nitride is a very good material which can be successfully used for piezoelectric thin films in MEMS microactuators. It was proved that low temperature deposition of the AlN thin film showing very good piezoelectric properties comparable with bulk material is realisable. It is important for microobject design to assure the compatibility with IC technology. Moreover, the dynamic development of more complex microdevices can bring for the AlN based piezoelectric actuators wide range of potential applications. Therefore, further works concerning the study of the AlN thin films and AlN driven microelements are significant. Thus, the future tasks are proposed. They will be focused on:

- developing methods and fabrication processes leading to improve the technology in order to:
  - manufacture planar AlN based devices with controlled global residual stress;
  - minimise the deviation of the parameters which characterise the fabricated devices over entire Si wafer substrate;
- developing methodology and performing studies of the packaged active microobjects paying a special attention to the reliability aspect;
- developing methods and performing further more detailed studies concerning the reliability of AlN thin film microstructures which consist in:
  - continuation of the carried out research works related to the investigation of the variable environmental load effects on the performances of the devices working in the static and dynamic (i.e. resonant) modes;
  - carrying out of the quantity accelerated reliability tests using the presented in this dissertation qualitative life data. The further researches will be based on the method of the planning reliability assessment test called “backwards L” design using two accelerated parameters, i.e. temperature and supply voltage. The investigated objects will be loaded by constant or time-variable resonant signal voltage which excites the structures to work in the static or dynamic regimes, respectively. These investigations leading to create acceleration model will allow to estimate statistically the reliability of studied AlN driven cantilevers. Determined reliability parameters (e.g. life time distribution for the investigated samples, their time to fail, reliability function, failure rate, etc.) will allow to predict the object life time with higher confidence level.

Author's publications

High standing of the performed scientific works were confirmed by publishing the two articles in the high quality journals included in the ISI Master Journal List:

- "Static and dynamic characterization of AlN-driven microcantilevers using optical interference microscopy", K. Krupa, M. Józwik, C. Gorecki, A. Andrei, Ł. Nieradko, P. Delobelle, L. Hirsinger, Optics and Lasers in Engineering, v.47 (2), pp.211-216, 2009;
- "AlN as an actuation material for MEMS applications: The case of AlN driven multilayered cantilevers", A. Andrei, K. Krupa, M. Józwik, P. Delobelle, L. Hirsinger, C. Gorecki, Ł. Nieradko, C. Meunier, Sensors and Actuators A, v.141, pp. 565-576, 2008.

The subject area of this Ph.D. dissertation was also presented in the several international and polish conferences (13 publications in SPIE Proceedings, Springer publisher, etc.).

Bibliography

[Agilent] http://www.home.agilent.com/agilent/product.jspx?nid=-536902257.536883183.00&cc=US&lc=eng

[Ali 2004] S. M. Ali, J. M. Jennings, L. M. Phinney, "Temperature dependence for in-use stiction of polycrystalline silicon MEMS cantilevers", Sensors and Actuators A 113, pp.60-70, 2004

[Andersen 2000] B. Andersen, E. Riggaard, "Static and dynamic performance of stacked multilayer actuators based on hard and soft PZT", Seventh International Conference on New Actuators, pp.423-426, 2000

[Andersen 2004] B. Andersen, F. Jensen, S. Ouchouche, "Reliability of piezoelectric actuators at extreme operating conditions", ACTUATOR 2004, pp.64-67, 2004

[Andrei 2006 a] A. Andrei, **K. Krupa**, M. Józwik, Ł. Nieradko, C. Gorecki, L. Hirsinger, P. Delobelle, "Fabrication, characterisation and reliability study of AlN-driven cantilevers", Proceedings of SPIE 6188, pp.196-203, 2006

[Andrei 2006 b] A. Andrei, **K. Krupa**, P. Delobelle, L. Hirsinger, C. Gorecki, Ł. Nieradko, "AlN as an actuation material for mems; the case of AlN driven cantilevers", Eurosensors Proceedings, 2006. EuroSensors XX, Göteborg, Sweden, 17-20 September 2006

[Andrei 2006 c] A. Andrei, "Process optimization and reliability study concerning the use of piezoelectric Aluminium Nitride films as actuation layers in MEMS", Post Doctoral Report, 2006

[Andrei 2007 a] A. Andrei, **K. Krupa**, M. Józwik, P. Delobelle, L. Hirsinger, C. Gorecki, Ł. Nieradko, C. Meunier, „Fabrication, caractérisation et modélisation de micropoutres multimorphes intégrant un film piézoelectrique d'AlN comme actionneur", Mécanique & Industries 8, EDP Sciences 2007, pp.267-278, 2007

[Andrei 2007 b] A. Andrei, **K. Krupa**, Ł. Nieradko, C. Gorecki, L. Hirsinger, P. Delobelle, J. Kacperski, M. Józwik, "Opto - Mechanical Reliability Studies of ALN driven cantilevers", ICEM13, Experimental Analysis of Nano and Engineering Materials and Structures, E. E. Gdoutos (editor), Springer, pp.539-540, 2007

[Andrei 2008] A. Andrei, **K. Krupa**, P. Delobelle, L. Hirsinger, M. Józwik, C. Gorecki, Ł. Nieradko, C. Meunier, "AlN as an actuation material for MEMS applications: The case of AlN driven multilayered cantilevers", Sensors and Actuators A 141, pp.565-576, 2008

[ANSYS] Release 10.0 Documentation for ANSYS

[Argillon] http://www.argillon.com

[Auger 2004] M. A. Auger, L. Vazquez, M. Jergel, O. Sanchez, J. M. Albella, "Structure and morphology evolution of AlN films grown by DC sputtering", Surface and Coatings Technology 180-181, pp.140-144, 2004

[Azom] http://www.azom.com

[Banks 2006 a] D. Banks, "Micromachnining – Introduction", Part 1 in "Microengineering, MEMS, and Interfacing. A Practical Guide", Taylor & Francis Group, CRC Press, Boca Raton 2006

[Banks 2006 b] D. Banks, "Photolithography", Part 1, Chapter 1 in "Microengineering, MEMS, and Interfacing. A Practical Guide", Taylor & Francis Group, CRC Press, Boca Raton 2006

[Banks 2006 c] D. Banks, "Silicon Micromachining", Part 1, Chapter 2 in "Microengineering, MEMS, and Interfacing. A Practical Guide", Taylor & Francis Group, CRC Press, Boca Raton 2006

[Banks 2006 d] D. Banks, "Nanotechnology", Part 1, Chapter 10 in "Microengineering, MEMS, and Interfacing. A Practical Guide", Taylor & Francis Group, CRC Press, Boca Raton 2006

[Beck 1991] R. B. Beck, “Technologia krzemowa”, PWN, 1991
[Berghmans 2006] F. Berghmans, M. Van Uffelen, S. Eve, E. Ernst, A. Last, D. Rabus, N. Huber, O. Kraft, A. Andrei, Ł. Nieradko, **K. Krupa**, M. Józwik, C. Gorecki, L. Hirsinger, P. Kniażewski, L. Sałbut, M. Kujawińska, “Reliability studies of microoptical components in NEMO Network of Excellence in Microoptics”, Proceedings of SPIE 6193, pp.61930A 1-11, 2006
[Berghmans 2007] F. Berghmans “Reliability of Optical Components – An Introduction”, NEMO SUMMER SCHOOL Micro-Optics Measurement and Characterisation, Warsaw, 3-14 September 2007
[Birolini 2004] A. Birolini “Reliability Engineering –Theory and Practice”, Springer-Verlag, Berlin Heidelberg, 2004
[Bobji 1999] M. S. Bobji, S. K. Biswas, “Hardness of a surface containing uniformly spaced pyramidal asperities”, Tribology Letters 7, pp.51–56, 1999
[Boeshore 2006] S. E. Boeshore, “Aluminium Nitride Thin Films on Titanium: Piezoelectric Transduction on a Metal Substrate”, Ph.D. thesis, 2006
[Bosseboeuf 2007] A. Bosseboeuf, S. Petitgrand, “Interference microscopy techniques for microsystem characterization”, Chapter 8 in “Optical inspection of microsystems”, W. Osten (editor), CRC Taylor & Francis Group, 2007
[BPiezo] www.bostonpiezooptics.com
[Brissaud 2003] M. Brissaud, S. Ledren, P. Gonnard, “Modelling of a cantilever non-symmetric piezoelectric bimorph”, Journal of Micromechanics and Microengineering 13 (6), pp.832-844, 2003
[Brown 1997] S. B. Brown, W. Van Arsdell, Ch. L. Muhlstein, “Material Reliability in MEMS Devices”, TRANSDUCERS’97 International Conference on Solid State Sensors and Actuators 1, pp.591-593, Chicago, June 16-19, 1997,
[Carlotti 1995] G. Carlotti, F. S. Hickernell, H. M. Liaw, L. Palmieri, G. Socino, E. Verona, “The elastic constants of sputtered aluminium nitride films”, IEEE Ultrasonics Symposium 1, pp. 353–356, 1995
[Cattan 1999] E. Cattan, T. Haccart, G. Vélu, D. Rémiens, C. Bergaud, L. Nicu, “Piezoelectric properties of PZT films for microcantilever”, Sensors and Actuators 74, pp.60-64, 1999
[Ceramic_center] http://www.ceramic_center.com/cttc_pdf/nitrure_al.pdf
[Chang 1999] S. H. Chang, C. C. Chou, “Electromechanical Analysis of an Asymmetric Piezoelectric / Elastic Laminate Structure: Theory and Experiment”, IEEE Transactions on Ultrasonics, Ferroelectrics and Frequency Control 46 (2), pp.441-451, 1999
[Chang 2003] Ch. P. Chang, “MEMS for Telecommunications: Devices and Reliability”, IEEE Custom Integrated Circuits Conference, pp.199-206, 2003
[Choujaa 1995] A. Choujaa, N. Tirole, C. Bonjour, G. Martin, D. Hauden, P. Blint, A. Cachard, C. Pommier, “AlN/silicon lamb-wave microsensors for pressure and gravimetric measurements”, Sensors and Actuators A 46-47, pp.179-182, 1995
[Clement 2004] M. Clement, L. Vergara, J. Sangrador, E. Iborra, A. Sanz-Hervas, “SAW characteristics of AlN films sputtered on silicon substrate”, Ultrasonics 42, pp.403–407, 2004
[Dagdag 2006] S. Dagdag, J. Alexis, J. D. Beguin, J. A. Petit, M. Ferrato, J. Durand, “Propriétés méchanique de revêtenements d’AlN sur carbure de Silicium fritté par dépôt chimique en phase vapeur assisté plasma”, Matériaux 2006, pp.13–17, 2006
[Delafargue 2004] A. Delafargue, F. J. Ulm, “Explicite approximations of the indentation modulus of elastically orthotropic solids for conical indenters”, International Journal of Solids and Structures 41, pp.7351-7360, 2004

[Delobelle 2006] P. Delobelle, E. Fribourg-Blanc, D. Rèmiens, "Mechanical properties determined by nanoindentation tests of [Pb(Zr, Ti) O_3] and [Pb($Mg_{1/3}Nb_{2/3}$)$_{1-x}Ti_xO_3$ sputtered thin films", Thin Solid Films 515, pp.1385-1393, 2006
[Delobelle 2007] P. Delobelle, G. S. Wang, E. Fribourg-Blanc, D. Remiens, "Indentation modulus and hardness of Pb(Zr-Ti)0_3 sol–gel films deposited on Pt and LaNi0_3 electrodes. An estimation of the C_{ij} compliances", Journal of the European Ceramic Society 27, pp.223–230, 2007
[Dobosz 2001] M. Dobosz, "Wspomagana komputerowo statystyczna analiza wyników badań", Exit 2001
[Dogheche 2005] K. Dogheche, "Réalisation de transducteurs piézoélectriques intégrés sur silicium : Applications à l'imagerie acoustique", Ph.D. thesis, 2005
[Duong 2005] Q.-H. Duong, L. Buchaillot, D. Collard, P. Schmitt, X. Lafontan, P. Pons, F. Flourens, F. Pressecq, "Thermal and electrostatic reliability characterization in RF MEMS switches", Microelectronics Reliability 45, pp.1790–1793, 2005
[Dubois 1999] D. A. Dubois, P. Muralt, "Properties of AlN thin films for piezoelectric transducers and microwave filter applications", Applied Physics Letters 74 (20), pp.3032-3034, 1999
[Dubois 2001] D. A. Dubois, P. Muralt, "Stress and piezoelectric properties of aluminum nitride thin films deposited onto metal electrodes by pulsed direct current reactive sputtering", Journal of Applied Physics 89 (11), pp.6389-6395, 2001
[Dziuban 2004] J. A. Dziuban, "Technologia i zastosowanie mikromechanicznych struktur krzemowych i krzemowo-szklanych w technice mikrosystemów", Oficyna Wydawnicza Politechniki Wrocławskiej, Wrocław, 2004
[Edgar 1994] "Basic Physical Properties", Chapter 1 in "Properties of Group III Nitrides", J. H. Edgar (editor), The Institution of Electrical Engineers INSPEC, London 1994
[Edge] http://www.edgepolishing.com/aluminum-nitride.htm
[Efunda] http://www.efunda.com
[Gahide 2001] S. Gahide, "Exploration of micromachines to textiles: monitoring warp tension and breaks during the formation of woven fabrics", Chapter 2 in Ph.D. thesis, 2001
[Gambin 2005] W. L. Gambin, A. Zarzycki, "Termo-sprężysta analiza struktur bimorficznych stosowanych w układach typu MEMS", paper in "Analiza i modelowanie wybranych procesów mechanicznych", report on the research project for the year 2005, Department of Applied Mechanics, Warsaw University of Technology, Faculty of Mechatronics, W. L. Gambin (leader), Warsaw, 2005
[Gilbertson 1996] R. G. Gilbertson, J. D. Busch, "A survey of micro-actuator technologies for future spacecraft mission", The Journal of The British Interplanatary Society 49, pp.129-138, 1996
[Gorecki 2005 a] C. Gorecki, M. Józwik, L. Sałbut, "Multifunctional interferometric platform for on-chip testing the micromechanical properties of MEMS/MOEMS", Journal of Microlithography, Microfabrication and Microsystem 4 (4), pp.1-10, 2005
[Gorecki 2005 b] C. Gorecki, "Association of MEMS technology with Integrated Optics: demonstration of active membrane in-situ read-out by monolithic integration of silicon-based Mach Zehnder interferometer", Optica Pura y Applicada 38 (3), pp.65-69, 2005
[Gorecki 2005 c] Ch. Gorecki, "Integrated Optics and Mems (Guided Wave Moems)", NEMO SUMMER SCHOOL Highlights in Microtechnology, Neûchatel, 4 – 15 July 2005
[Gorecki 2006] C. Gorecki, A. Andrei, M. Józwik, **K. Krupa**, K. Dogheche, S. Balandras, L. Hirsinger, P. Delobelle, "Static and dynamic measurements of active MEMS by Twyman-Green interferometry: case of AlN-based microactuators", Proceedings of SPIE 6293, pp.629309, 2006

[Gorecki 2007] C. Gorecki, M. Józwik, P. Dellobelle, "An interferometric platform for static, quasi-static and dynamic evaluation of out-of-plane deformations of MEMS and MOEMS", Chapter 10 in "Optical Inspection of Microsystems", Osten (editor), CRC Press, Taylor & Francis Group, Boca Raton, 2007

[Gorecki 2008] C. Gorecki, **K. Krupa**, A. Andrei, M. Józwik, Ł. Nieradko, P. Delobelle, L. Hirsinger, "Twyman-Green interferometry in study of AlN material as an actuation layer in MEMS", Proceedings of SPIE 7064, pp. 706402-1-10, 2008

[Guy 1999] L. L. Guy, S. Muensit, E. M. Goldys, "Extensional piezoelectric coefficients of gallium nitride and aluminium nitride", Applied Physics Letters 75 (26), pp.4133–4135, 1999

[Hartzell 1999] A. Hartzell, D. Woodilla, "Reliability methodology for prediction of micromachined accelerometer stiction", IEEE of 37th Annual International Reliability Physics Symposium, pp.202-205, 1999

[Chauffleur 2004] X. Chauffleur, L. Rabbia, P. Pons, K. Grenier, R. Plana, L. Dantas, F. Flourens, J. Kuchenbecker, D. Dubuc, A. Boukabache, "Effect of membrane shape on mechanical behavior of RF switches.", Sensors and Actuators A 112, pp.148-154, 2004

[Ho 2004] C. J. Ho, T. K. Shing, P. C. Li, "Preferred orientation control and characterization of AlN thin films using reactive sputtering", Tamkang Journal of Science and Engineering 7 (1), pp.1-4, 2004

[Hodge 2001] G. Hodge (leader), "Micromachine Based Fabric Formation Systems", NTC Annual Report F98 S12, November 2001

[Iborra 2004] E. Iborra, J. Olivares, M. Clement, L. Vergara, A. Sanz-Hervás, J. Sangrador, "Piezoelectric properties and residual stress of sputtered AlN thin films for MEMS applications", Sensors and Actuators A 115, pp.501-507, 2004

[Ishihara 1998] M. Ishihara, S. J. Li, H. Yumoto, K. Akashi, Y. Ide, "Control of preferential orientation of AIN films prepared by the reactive sputtering method", Thin Solid Films 316, pp.152-157, 1998

[ITL] http://www.itl.nist.gov/div898/handbook/index.htm

[Jakubowicz 1984] A. Jakubowicz, Z. Orłoś, "Wytrzymałość materiałów", Wydawnictwa Naukowo-Techniczne, Warszawa, 1984

[Józwik 2004 a] M. Józwik, "Opto-numeryczne metody wyznaczania wielkości mechanicznych charakteryzujących mikroelementy stosowane w urządzeniach typu MEMS/MOEMS", Ph.D. thesis, 2004

[Józwik 2004 b] M. Józwik, C. Górecki, A. Sabac, P. Delobelle, M. Kujawińska, "Evaluation of micromechanical properties of buckled SiO_xN_y loaded membranes by combining the Twyman-Green interferometry with nanoindentation and point-wise deflection technique", Optics and Lasers in Engeneering 41, pp.703-716, 2004

[Józwik 2006] M. Józwik, **K. Krupa**, A. Andrei, Ł. Nieradko, C. Gorecki, "Badanie niezawodności mikroaktuatorów z warstwą AlN wspomagane metodami interferometrycznymi", IX Konferencja Naukowa Czujniki Optoelektroniczne i Elektroniczne COE'2006, Kraków-Zakopane, pp.475-478, 2006

[Józwik 2008] M. Józwik, **K. Krupa**, C.Gorecki, P.Delobelle, L.Hirsinger, "Numeryczno-eksperymentalna metodyka badania mikrobelek z piezoelektryczną warstwą azotku aluminium", Elektronika 6/2008, pp.110-111, 2008

[Judy 2001] J. W. Judy, "Micromechanical Systems (MEMS): Fabrication, Design, and Applications", Journal of Smart Materials and Structures 10, pp.1115-1134, 2001

[Jüptner 1993] W. Jüptner, "Nondestructive testing with interferometry", Proceedings of Fringe'93, pp.315-324, Akademie Verlag, Berlin, 1993

[Kacperski 2008] J. Kacperski, "Wielofunkcyjna platforma interferencyjna do pomiarów aktywnych elementów MEMS", Ph.D. thesis, 2008

[Kapkowski 1994] J. Kapkowski, M. Kujawińska, “Współczesne zastosowania technik hybrydowych w mechanice ciała stałego”, XVI Sympozjum Mechaniki Eksperymentalnej, Jachranka, pp.132-152, 1994

[Kaszuwara 2004] W. Kaszuwara, “Ceramiczne materiały piezoelektryczne”, Inżynieria Materiałowa 2, pp.65-67, 2004

[Kazinczi 2000] R. Kazinczi, J. R. Mollinger, A. Bossche, “Versatile tool characterising long-term stability and reliability of micromechanical structures”, Sensors and Actuators A 85, pp.84-89, 2000

[Kim 2002] JH. Kim, SH. Lee, JH. Ahn, JK. Lee, “AlN piezoelectric materials for wireless communication thin film components”, Journal of Ceramic Processing Research 3 (1), pp.25–28, 2002

[King 1987] R. B. King, “Elastic analysis of some punch problems for layered medium”, International Journal of Solids and Structures 23, pp.1657-1664, 1987

[**Krupa 2007**] **K. Krupa**, M. Józwik, A. Andrei, Ł. Nieradko, C. Gorecki, L. Hirsinger, P. Delobelle, “Influence study of thermal effects on MEMS cantilever behavior”, 7th International Conference MECHATRONICS 2007, Warsaw, Recent Advances in Mechatronics, Springer, pp.531-535, 2007

[**Krupa 2008 a**] **K. Krupa**, M. Józwik, A. Andrei, Ł. Nieradko, C. Gorecki, P. Delobelle, L. Hirsinger, “AlN driven microcantilever actuators: modeling, fabrication, characterization”, Proceedings of SPIE 6995, 69950E 1-10, 2008

[**Krupa 2008 b**] **K. Krupa**, M. Józwik, A. Andrei, Ł. Nieradko, C. Gorecki, L. Hirsinger, P. Delobelle, “Characterization of MEMS cantilevers”, Proceedings of Technical Digest Of The Fourteenth Microoptics Conference, pp.199-200, 2008

[**Krupa 2009**] **K. Krupa**, M. Józwik, C. Gorecki, A. Andrei, Ł. Nieradko, P. Delobelle, L. Hersinger, “Static and dynamic characterization of AlN-driven microcantilevers using optical interference microscopy”, Optics and Laser in Engineering 47 (2), pp.211-216, 2009

[Kujawińska 1995] M. Kujawińska, T. Tkaczyk, R. Pryputniewicz, “Computational and experimental hybrid study of deformations in a microelectronic connector”, Proceedings of SPIE 2545, pp.54-70, 1995

[Kujawińska 2002] M. Kujawińska, “Modern optical measurement station for micro-materials and micro-elements studies”, Sensors and Actuators A 99, pp.144-153, 2002

[Kujawińska 2005 a] M. Kujawińska, “Podstawy analizy obrazu prążkowego” Charter 2 in “Interferometria laserowa z automatyczną analizą obrazu”, K. Pastorski (editor), Oficyna Wydawnicza Politechniki Warszawskiej, Warszawa, 2005

[Kujawińska 2005 b] M. Kujawińska, “Optyczno-numeryczne systemy wspomagania projektowania, analizy i kontroli struktur inżynierskich”, Charter 9 in “Interferometria laserowa z automatyczną analizą obrazu”, K. Patorski (editor), Oficyna Wydawnicza Politechniki Warszawskiej, Warszawa, 2005

[Kusaka 2000] K. Kusaka, D. Taniguchi, T. Hanakusa, K. Tominaga, “Effect of input power on crystal orientation an residual stress in AlN film deposited by DC sputtering”, Vacuum 59, pp. 806-813, 2000

[Laerman 2002] K. H. Laerman, “Hybrid techniques in experimental solid mechanics” in “Optical Methods in Experimental Solid Mechanics”, K. H. Laerman (editor), Springer, Wien 2002

[Lakin 2001] K. M. Lakin, J. Belsick, J. F. McDonald, K. T. McCarron, “Improved bulk wave rezonator coupling coefficient for wide bandwidth filters”, IEEE Ultrasonics Symposium 3E-5, pp.1–5, 2001

[Laurent 2000] T. Laurent, F. O. Bastien, J. C. Pommier, A. Cachard, D. Remiens, E. Cattan, “Lamb wave and plate mode in ZnO/silicon and AlN/silicon membrane. Application to sensors able to operate in contact with liquid”, Sensors and Actuators A 87, pp.26-37, 2000

[Lueng 2000] C. M. Lueng, H. L. Chan, C. Surya, C. L. Choy, "Piezoelectric coefficient of aluminum nitride and gallium nitride", Journal of Applied Physics 88 (9), pp.5360-5363, 2000

[Madou 1997] M. Madou, "Fundamentals of microfabrications", Boca Raton, FL:CRC Press, Inc., New York, 1997

[Madou 2002] M. J. Madou, "MEMS Fabrication", Chapter 16 in "The MEMS Handbook", M. Gad-el-Hak (editor), CRC Press, Boca Raton 2002

[Malacara 2001] D. Malacara, "Basic Interferometers", Chapter 11 in "Handbook of optical engineering", D. Malacara i B. J. Thompson (editor), Marcel Dekker, Inc., New York, 2001

[Martin 2004] F. Martin, P.Muralt, M.-A. Dubois, A. Pezous, "Thickness dependence of the properties of highly *c*-axis textured AlN thin films", Journal of Vacuum Science and Technology A 22 (2), pp.361-365, 2004

[Matint] http://www.matint.pl

[Meng 1993] W. J. Meng, J. A. Sell, G. L. Eesley, T. A. Perry, "Measurement of intrinsic stresses during growth of aluminium nitride thin films by reactive sputter deposition", Journal of Applied Physics 74 (4), pp.2411–2414, 1993

[Memsnet a] MEMS and Nanotechnology Clearinghouse, www.memsnet.org/material/aluminiumnitride, MEMS Exchange (2001)

[Memsnet b] http://www.memsnet.org/material

[Miller 1999] S. L. Miller, M. S. Rodgers, g. La Vigne, J. J. Sniegowski, P. Clews, D. M. Tanner, K. A. Peterson, "Failure modes in surface micromachined microelectromechanical actuator systems", Microelectronics Reliability 39 (8), pp.1229-1237, 1999

[Moraja 2003] M. Moraja, M. Amiotti, "Advanced getter solutions at wafer level to assure high reliability to the last generations MEMS", 41st Annual Proceedings of the IEEE International Symposium on Reliability Physics, pp.458-459, 2003

[Muhlstein 1997] Ch. Muhlstein, S. Brown, "Reliability and Fatigue testing of MEMS", NSF/AFOSR/ASME Workshop, Tribology Issue and Opportunities in MEMS, Klewer Academic Publications, 9-11 November, 1997

[Muralt 2005] P. Muralt, J. Antifacos, M. Cantoni, R. Lanz, F. Martin, "Is there a better material for thin film BAW applications than AlN ?", IEEE Ultrasonics Symposium 1, pp.315-320, 2005

[Muratet 2006] S. Muratet, S. Lavu, J. Y. Fourniols, G. Bell, M. P. Y. Desmulliez, "Reliability modelling and analysis of thermal MEMS", Journal of Physics: Conference series 34, pp.235-240, 2006

[Nexus] http://www.enablingmnt.com/html/nexus_market_report.html

[Niepewność 1999] "Wyrażanie niepewności pomiaru", guide published by Central Office of Measures, Poland 1999

[Noliac] http://www.noliac.com

[Olivares 2005] J. Olivares, M. Clement, E. Iborra, L. Vergara, J. L. Sanchez-Rojas, J. Vazquez, P. Sanz, "Simulation, fabrication and testing of aluminium nitride piezoelectric microbridges", Proceedings of SPIE 5836, pp.16-26, 2005

[Oliver 1992] W. C. Oliver, G. M. Pharr, "An improved technique for determining hardness and elastic modulus using load and displacement sensing indentation experiments", Journal Materials Research, 7(6), pp.1564-1583, 1992

[Osten 2007] W. Osten (editor), "Optical inspection of microsystems", CRC Press, Taylor & Francis Group, Boca Raton, 2007

[Palacios 2002] T. Palacios, F. Calle, E. Monroy, J. Grajal, M. Eickhoff, O. Ambacher, C. Prieto, "Nanotechnology for SAW devices on AlN epilayers", Materials Science and Engineering B93, pp.154-158, 2002

[Pantojas 2005] V. M. Pantojas, W. Otano-Rivera, J. W. Caraballo, “Statistical analysis of the effect of deposition parameters on the preferred orientation of sputtered AlN films”, Thin Solid Films 492, pp.118-123, 2005

[Patorski 2004] K. Patorski, Z. Sienicki, M. Pawłowski, A. Styk, A. Jóźwicka, “Studies of the properties of the temporal phase shifting method applied to silicone microelement vibration investigations using the time average method”, Proceedings of SPIE 5458, pp.208-219, 2004

[Patorski 2005 a] K. Patorski, “Interferometria laserowa - wprowadzenie” Charter 1 in “Interferometria laserowa z automatyczną analizą obrazu”, K. Patorski (editor), Oficyna Wydawnicza Politechniki Warszawskiej, Warszawa, 2005

[Patorski 2005 b] K. Patorski (editor), “Interferometria laserowa z automatyczną analizą obrazu”, Oficyna Wydawnicza Politechniki Warszawskiej, Warszawa, 2005

[Petersen 1982] K. E. Petersen, “Silicon as a mechanical material”, Proceedings of IEEE 70 (5), pp. 420-457, 1982

[Petitgrand 2001 a] S. Petitgrand, R. Yahiaoui, K. Danaie, A. Bosseboeuf, J. P. Gilles, “3D measurement of micromechanical devices vibration mode shapes with a stroboscopic interferometric microscope”, Optics and Lasers in Engineering 36, pp.77-101, 2001

[Petitgrand 2001 b] S. Petitgrand, R. Yahiaoui, A. Bosseboeuf, K. Danaie, “Quantitative time-averaged microscopic interferometry for micromechanical device vibration mode characterization”, Proceedings of SPIE 4400, pp. 51-60, 2001

[Piezomaterials] http://www.piezomaterials.com

[Poon 1993] C. Y. Poon, M. Kujawińska, C. Ruiz, “Strain measurement of composites using an automated moiré interferometry method”, Measurement 11, pp.45-57, 1993

[Pryputniewicz 1982] R. J. Pryputniewiecz, “Unification of FEM modelling with laser experimentation” in “Unification of Finite Elements, Finite Differences, and Calculus of Variations”, H. Kardestuncer (editor), Univ. of Connecticut, Storrs T’1982

[Pwr] http://www.wemif.pwr.wroc.pl

[Qasmi 2006] M. Qasmi, P. Delobelle, “Influence of the average roughness *R*ms on the precision of the Young’s modulus and hardness determination using nanoindentation technique with a Berkovich indenter”, Surface and Coatings Technology 201, pp.1191-1199, 2006

[Roditi] http://www.roditi.com/SingleCrystal/LiNbO3

[Röll 1976] K. Röll, “Analysis of stress and strain distribution in thin films and substrates”, Journal of Applied Physics 47 (7), pp.3224-3229, 1976

[Ruffieux 2000] D. Ruffieux, M. A. Dubois and N. F. de Rooij, “An AlN piezoelectric microactuator array”, IEEE MicroElectro Mechanical System 23-27, pp.662-667, 2000

[Saha 2002] R. Saha, W. D. Nix, “Effects of the substrate on the determination of the thin film mechanical properties by nanoindentation”, Acta Materialia 50, pp.23-28, 2002

[Sałbut 1996] L. Sałbut, M. Kujawińska, D. Holstein, W. Jüptner, “Comparative analysis of laser weldment properties by grating interferometry and digital speckle photography”, Proceedings of 11th international Conference on Experimental Mechanics, Oxford, pp.1331-1336, 1996

[Sałbut 2003] L. Sałbut, K. Patorski, M. Józwik, J. Kacperski, C. Gorecki, A. Jacobelli, T. Dean, “Active micro-elements testing by interferometry using time-average and quasi-stroboscopic techniques”, Proceedings of SPIE 5145, pp.23-32, 2003

[Sałbut 2005 a] L. Sałbut, K. Patorski, “Interferometria klasyczna”, Chapter 3 in “Interferometria laserowa z automatyczną analizą obrazu”, K. Patorski (editor), Oficyna Wydawnicza Politechniki Warszawskiej, Warszawa, 2005

[Sałbut 2005 b] L. Sałbut, K. Patorski, “Profilometria i mikroprofilometria interferencyjna”, Chapter 4 in “Interferometria laserowa z automatyczną analizą obrazu”, K. Patorski (editor), Oficyna Wydawnicza Politechniki Warszawskiej, Warszawa, 2005
[Sanz-Hervás 2006] A. Sanz-Hervás, M. Clement, E. Iborra, L. Vergara, J. Olivares, J. Sangrador, “Degradation of the piezoelectric response of sputtered c-axis AlN thin films with traces of non-(0002) x-ray diffraction peaks”, Applied physics Letters 88, pp.161915-1-3, 2006
[Samper 2003] V. Samper, A. Trigg, “MEMS Failure Analysis and Reliability”, Proceedings of 10th IPFA, Invited Paper, pp.17-22, 2003
[Sarihan 2006] V. Sarihan, “Role of film intrinsic stress in packaging of multi-layer microelectronic structures”, Materials Science and Engineering A 421 (1-2), pp.109-117, 2006
[Servin 2001] M. Servin, M. Kujawińska, “Modern Fringe Pattern Analysis in Interferometry” Chapter 12 in “Handbook of optical engineering”, D. Malacara i B. J. Thompson (editor), Marcel Dekker, Inc., New York, 2001
[Sharpe 2006] W. N. Sharpe Jr., “Mechanical properties of MEMS materials” in „MEMS: Introduction and Fundamentals”, M. Gad-el-Hak (editor), Taylor & Francis Group, Boca Raton, 2006
[Small 1992] M. K. Small, W. D. Nix, “Analysis of accuracy of the bulge test in determining the mechanical properties of thin films”, Journal of Materials Research 7, pp.1553-1563, 1992
[Smarttech] http://www.smarttech.pl
[Smits 1991] J. G. Smits, WS. Choi, “The constituent equations of piezoelectric heterogeneous bimorphs” IEEE Transaction on Ultrasonics, Ferroelectrics, and Frequency Control 38 (3), pp.256–270, 1991
[Srikar 2002] V. T. Srikar, S. D. Senturia, “The Reliability of Microelectromechanical System (MEMS) in Shock Environments“, Journal of Microelectromechanical Systems 11 (3), pp.206-214, 2002
[SSchool 2005] CD-ROM “World of Microsystems”, Content by FSRM, VDI/VDE-IT, Yole Dèvelopment, NEMO SUMMER SCHOOL Highlights in Microtechnology, Neûchatel, 4-16 July 2005
[Stoney 1909] G. G. Stoney, “The tension of metallic films deposited by electrolysis”, Proceedings of the Royal Society of London Series A 82 (553), pp.172-175, 1909
[Tanner 2000] D. M. Tanner, N. F. Smith. L. W. Irwin, W. P. Eaton, K. S. Helgesen, J. J. Clement, W. M. Miller, J. A. Walraven, K. A. Peterson, P. Tangyunyong, M. T. Dugger, S. L. Miller, “MEMS Reliability: Infrastructure, Test Structures, Experiments, and Failure Modes”, SANDIA REPORT SAND2000-0091, 2000
[Thielicke 2000] E. Thielicke, E. Obermeier, “Microactuators and their technologies”, Mechatronics 10, pp.431-455, 2000
[Tong 1960], Kin N. Tong, “Theory of Mechanical Vibration”, John Wiley & Sons Inc., 1960
[Trimmer 2006] W. Trimmer, R. H. Stroud, “Scaling of micromechanical devices” in “MEMS: Introduction and Fundamentals”, M. Gad-el-Hak (editor), Taylor & Francis Group, Boca Raton, 2006
[Tsubouchi 1981] K. Tsubouchi, K. Sugai, N. Mikoshida, “AlN material constants evaluation and SAW properties on AlN/Al_2O_3 and AlN/Si”, IEEE Ultrasonics Symposium, pp. 375-380, 1981
[Veeco] http://www.veeco.com
[Vergara 2006] L. Vergara, J. Olivares, E. Iborra, M. Clement, A. Sanz-Hervás, J. Sangrador, “Effect of rapid thermal annealing on the crystal quality and the piezoelectric response of polycrystalline AlN films”, Thin Solid Films 515, pp.1814-1818, 2006

[Walter 2001] V. Walter, "Caractérisation et modélisation électroméchanique de dépots de couches épaisses sérigraphiées sur substrate d'alumine. Application au contrôle de forme et à l'amortissement actif d'un bimorphe", Ph.D. thesis, 2001
[Walter 2002] V. Walter, P. Delobelle, P. L. Moal, E. Joseph, M. Collet, "A piezo-mechanical characterisation of PZT thick films screen-printed on Alumina substrate", Sensors and Actuators A 96, pp.157–166, 2002
[Wang 1999] Q. M. Wang, L. E. Cross, "Constitutive Equations of symmetrical triple layer piezoelectric benders", IEEE Transactions on Ultrasonics, Ferroelectrics and Frequency Control 46, pp.1343-1351, 1999
[Wang 2000] L. Wang, J. M. Dawson, J. Cheng, P. Famouri, L. A. Hornak, "Stroke–length control of MEMS device", Proceedings of the IEEE International Symposium on Industrial Electronics 2, pp.535-539, 2000
[Wang 2005] Q. M. Wang, Y. Ding, Q. Chen, M. Zhao, J. Cheng, "Crystalline orientation dependence of nanomechanical properties of Pb(Zr Ti)0_3 thin films", Applied Physics Letter 86, pp.162–903, 2005
[Weibull] http://www.weibull.com/basics/reliability.htm
[Wiki] http://en.wikipedia.org
[Wolf 2003 a] I. De Wolf, "MEMS Reliability", Microelecronics Reliability 43 (7), pp.1047-1048, 2003
[Wolf 2003 b] I. De Wolf, M. van Spengen, R. Mertens, R. Puers, "A low frequency electrical test set-up for the reliability assessment of capacitive RF switches", Journal of Micromechanics and Microengineering 13 (13), pp.604-612, 2003
[Wortman 1965] J. J. Wortman, R. A. Evans, "Young's modulus, shear modulus and Poisson's ration in silicon and germanium", Journal of Applied Physics 36 (1), pp.153-156, 1965
[Wright 1997] A. F. Wright, "Elastic properties of zinc-blende and wurtzite AlN, GaN, and InN", Journal of Applied Physics 82 (6), pp.2833–2839, 1997
[Wu 2003] J. Wu, "Inductive links with integrated receiving coils for MEMS and implantable applications", Chapter 2 in Ph.D. thesis, 2003
[Xiao 2004] W. Xiao, X, Jiang, "Optical and mechanical properties of nanocrstalline aluminium oxy-nitride films prepared by electron cyclotron resonance plasma enhanced chemical vapor deposition", Journal of Crystal Growth 264, pp.165-171, 2004
[Xu 2001] X. H. Xu, H. S. Wu and C. J. Zhang, Z. H. Jin, "Morphological properties of AlN piezoelectric thin films deposited by DC reactive magnetron sputtering", Thin Solid Films 388, pp.62-67, 2001
[Xue 2002] Z. Xue, Y. Huang, K. C. Hwang, M. Li, "The influence of indenter tip radius on the micro-indentation hardness", Journal of Engineering Materials and Technology 124, pp.371–379, 2002
[Yole] http://www.yole.fr
[Zheng 2004] P. Zheng, "Magnetic MEMS and its applications", Ph.D. thesis, 2004
[Zienkiewicz 1977] O. C. Zienkiewicz, "The Finite Element Method", McGraw-Hill Book Company, UK, 1977
[Zink 2004] C. Zink, D. Pinceau, E. Defay, E. Delevoye, D. Barbier, "Development and characterization of membranes actuated by PZT thin film for MEMS applications", Sensors and Actuators A 115, pp.483-489, 2004

Appendix 1

Definitions of parameters characterising piezoelectric materials

Among various parameters characterising piezoelectric materials one of the most significant is the piezoelectric coefficient *d*. Other important properties are a quality factor Q_m, a coupling coefficient k^2 and a dissipation factor *tanσ*. The piezoelectric materials belonging to ferroelectrics are characterised also by their hysteresis parameters. Others often determined properties are a dielectric relative constant ε_r, an acoustic wave velocity v_s, etc [Matint]. Those significant parameters, except the already described piezoelectric coefficient (see Chapter 1), will be briefly explained here, focusing only on a useful background for the late study of the AlN piezoelectric microcantilevers.

Relative dielectric constant ε_r and acoustic wave velocity v_s

Permittivity ε is a physical quantity characterising the electrical properties of a medium, which describes how an electric field affects, and is affected by the dielectric medium. It is determined by the ability of a material to polarise in response to a voltage, and thereby to reduce the total electric field inside the material. It is then linked to a material's possibility to transmit the electric field. In general, the permittivity can vary with a position in the medium, a frequency of the applied field, a humidity, a temperature, and other parameters [Wiki]. The material permittivity is usually given in relation to a free space ε_0, as the relative permittivity $\varepsilon_r(\omega)$. Generally, ε_r is a complex, frequency dependent factor but it is often given for the frequency ω equal to 0 and then is called the relative dielectric constant or the static relative permittivity ε_r. This parameter is a scalar for isotropic materials and a second rank tensor for anisotropic ones. Since, the coefficients of d_{31} and d_{33} are the most often determined for the piezoelectric effect characterisation, the knowledge about ε_{33} and then $\varepsilon_{33,r}$ values is mostly required (see Eq.1.5, section 1.2). Therefore, in the this thesis dissertation, the ε_{33} and $\varepsilon_{33,r}$ factors are noted as described as ε and ε_r. The relative dielectric constant as a dimensionless value is then in general case, defined as:

$$\varepsilon_r(\omega) = \frac{\varepsilon(\omega)}{\varepsilon_0}, \tag{A1.1}$$

where ω is an angular frequency. ε_0 is a permittivity of a free space, also called vacuum permittivity or electric constant, having the lowest value equal to $8.854187817 \cdot 10^{-12}$ F/m [Wiki].

The relative dielectric constant is important because it affects the capacitance of piezoelectric component and then also the electric current required to drive them at the high frequencies [Noliac]. It is an essential information when the used material is intended to introduce capacitance to the system or circuit. If the material with the high relative dielectric constant is placed in the electric field, the magnitude of that field is reduced within the volume of this dielectric. The larger ε leads then to the greater charge stored and thus the greater capacitance achieved. Among dielectrics, the materials showing the ferroelectric effect often have very high relative dielectric constants which correspond to the slope of the curve presenting relation between polarisation and applied electric field [Wiki]. The high value of ε_r allows to

achieve the high electric polarisation and then the stronger piezoelectric effect (large d_{ik}) important for the microsystems. However for MEMS applications, low relative dielectric constant is required allowing to obtain high electric resistivity, low dielectric loss, and high breakdown voltage [Dubois 1999]. It is then necessary to find the compromise during the selection of proper materials in design and fabrication process. The permittivity ε and the magnetic permeability μ of the medium determine also the acoustic velocity v_s of the wave excited in this medium accordingly to the equation:

$$\varepsilon\mu = \frac{1}{v_s^2}. \tag{A1.2}$$

Taking into account the following relation:

$$\lambda_s = v_s f_0, \tag{A1.3}$$

where λ_s and f_0 are a wavelength and a frequency of acoustic wave, a possibility to achieve high acoustic velocity specific for wide band gap E_g materials, allows to produce high frequency filters [Ishihara 1998, Palacios 2002, Auger 2004, Clement 2004, Sanz-Hervás 2006, Wiki].

Dissipation factor *DF*

The dissipation factor *DF* is a parameter that specifies the dielectric losses inherent in the piezoelectric material. It is expressed as the ratio of the resistive power loss to the capacitive power and defined as the tangent of the loss factor $\tan\delta$. The electric power is lost in all dielectric materials, usually in the form of heat. *DF* varies depending on the material. In low dielectric constant and temperature compensating ceramics *DF* is lower than in high dielectric constant ceramics. In a static operation, virtually no heat is generated with a voltage load, but when the voltage is modulated at the high frequency heat is generated inside the material in proportion to the dissipation factor. The dissipation factor is usually specified for the low electric fields and at the frequency of 1000 Hz [Noliac, Wiki].

Electromechanical coupling coefficient k^2

The electromechanical coupling coefficient k^2 is a dimensionless number defined as the ratio of energy stored in the mechanical deformation to the electrical energy needed to produce that deformation. It represents the conversion efficiency between electrical energy and surface acoustic wave energy [Ishihara 1998, Muralt 2005, Noliac]. Similarly to the piezoelectric constant d (see Eq.1.7, section 1.2), the electromechanical coupling coefficient k^2 appears to be a 6 by 3 matrix instead of rank 3 tensor as a result of applying a multilinear algebra. The components k_{ik}^2 can then be described by the following equation [Sanz-Hervás 2006]:

$$k_{ik}^2 = \frac{d_{ik}^2 c_{kk}}{\varepsilon_{ii}}, \tag{A1.4}$$

in which c_{kk} are the components of the elastic stiffness tensor and ε_{ii} are the components of the material permittivity tensor.

To characterise the piezoelectric activity of the materials, k_{33}^2 and k_{31}^2 components of electromechanical coupling coefficient, and in particular the first of them, are quite often determined instead of d_{33} or d_{31} coefficients. However, in order to derive the true value of

these piezoelectric constants from the measured coupling coefficient, it is mandatory to know the elastic and dielectric properties of the tested material with the sufficient accuracy [Dubois 2001]. Although, these behaviours can differ for the bulk and thin film materials being not precisely known because of their technological dependency [Palacios 2002]. k^2 and acoustic wave velocity v_s are the main acoustic properties of the piezoelectric materials significant for the acoustic wave device applications [Clement 2004]. Since, the value of k_{33}^2 has been the most often determined by the researchers, in this dissertation k_{33}^2 is described as k^2.

Mechanical quality factor Q_m

The mechanical quality factor called further quality factor is a dimensionless parameter. Talking about mechanical vibrating resonant system, Q_m strongly influences the resonant behaviours. It is related to the sharpness of the resonant peak. Q_m compares then the frequency at which the system vibrates to the rate at which it dissipates its energy. Equivalently, it compares the decay time constant of oscillating system's amplitude to its vibration period. The higher Q_m indicates a lower rate of energy dissipation relatively to the oscillation frequency resulting in slower decay of vibration. The system with the high Q_m vibrates with a greater amplitude at the resonant frequency which drops more rapidly during the shifting of the frequency from the resonance what allows to produce more selective filters. The quality factor represents then the number of oscillations required to decrease the system's energy to the value of 1 / $e^{2\pi}$ of its original one. It can be given by the following equation:

$$Q_m = \frac{f_0}{\Delta f}, \tag{A1.5}$$

in which f_0 is the resonant frequency, and Δf – the bandwidth for which the energy is higher than half of its peak value.

The quality factor Q_m and described before the mechanical coupling coefficient k^2 are the two material properties important to take into consideration during fabrication of wide band filters, being the primary interest in such applications [Muralt 2005, Noliac, Wiki].

Hysteresis

In the piezoelectric materials, a mechanical hysteresis is observed when the strain does not follow the same track upon charging and discharging. It is expressed as the maximum strain divided by the maximum difference between the two tracks. This phenomenon exists in most of all piezoelectric materials but it is relatively strong in the materials belonging to the ferroelectric groups in which a presented spontaneous polarisation can be reversed by an applied voltage yielding a hysteresis loop. However, ferroelectricity only appears in a certain phase transition temperature, called the Curie temperature. Other piezoelectric materials showing insignificant nonlinearities exhibit linear polarisation with the electric field or a demonstrate linear polarisation in some ranges of the applied voltage. After removing the electric field, then in the ferroelectrics it remains a certain obtained polarisation in contrary to the other dielectric materials which return to their original state [Noliac, Wiki].

Appendix 2

Technology - introduction

Here, the overview of technological processes used for three–dimensional (3D) micromechanical structures will be presented. The content will be limited to the description of processes applied for manufacturing of the studied objects. Knowledge of microdevices technology will allow to better understand their performances, behaviours, principle of operation and also other problems connected with them. Whereas, to facilitate understanding of the fabrication processes, in the section A2.3, it will be presented characterisation of silicon, material used for substrate in the manufacturing of the investigated elements.

A2.1. Silicon as a substrate – micromechanical properties

Since many years, single crystal silicon has been widely used in microelectronics making this Integrated Circuit (IC) technology very well established. However, as early as the sixties, but mostly at the beginning of eighties, it was noticed that thanks to its mechanical or micromechanical properties, silicon could be an excellent constructional material for micromechanical structures manufacturing as well. It was started to develop the fabrication processes of three-dimensional silicon microengineering using know-how micoelectronics technology. Soon, this led to arise microsystem technology, a new and powerful technique, which nowadays is widely used in almost every field of science and industry [Dziuban 2004, Józwik 2004 a, Banks 2006 a].
As a substrate in the microstructures fabrication, silicon turns out to be a mainly used material, but not the only one. As an alternative, quartz, GaAs and recently also titanium are used as well [Boeshore 2006]. However, because silicon is commonly used, it is important to know its mechanical properties making silicon an excellent constructional material. This knowledge also allows to understand the technological process of the microcantilevers, fabricated on the single crystal silicon substrate, which are the subject of the research performed in this dissertation.

In order to be able to use all advantages given by silicon to fabricate the three-dimensional micromechanical devices, it is crucial to know and understand the structure of this material. Crystals of silicon have a regular and cubic structure with lattice parameter *a* equal to 5.43095Å. In the Fig.A2.1, it is illustrated the unit cell of silicon with location of the main crystallographic planes and crystallographic directions denoted with respect to crystallographic notation using Miller indexes [Madou 1997, Madou 2002, Dziuban 2004, Banks 2006 c]. As it could be seen, silicon is highly structured and its crystallographic planes have different density. Therefore, it is very important to know the mutual location of crystallographic planes and directions. This is necessary during shape designing of Si microelements in the wet etching process. In micromechanics, it is mostly used (100), (110) or (111) oriented single crystal silicon substrate. The example of (100) oriented silicon wafer being a substrate during the fabrication process of the tested devices is presented in the Fig.A2.2, which also shows a location of crystallographic planes and directions.

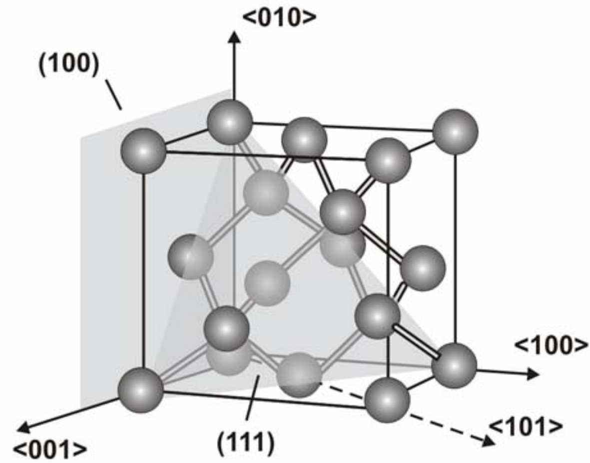

Fig.A2.1: Silicon crystal structure: crystallographic directions and planes indicated with Miller indexes and crystal unit cell (grey box) [Madou 1997, Madou 2002, Banks 2006 c]

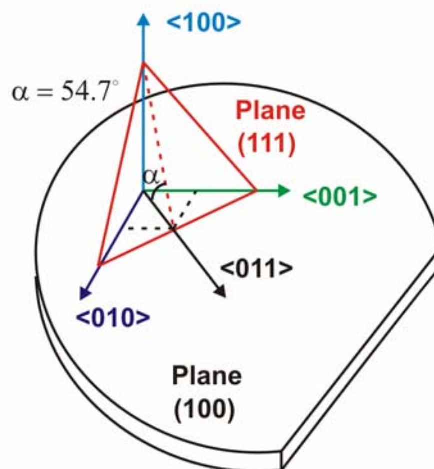

Fig.A2.2: Location of crystallographic planes and directions in (100) oriented silicon wafer [Madou 1997]

Hence, single crystal silicon as a strongly anisotropic material reveals the mechanical properties: Young modulus E and Poisson's ratio v depending on the crystallographic directions [Wortman 1965, Madou 2002, Dziuban 2004] with the values presented in the Table A2.1.

Table A2.1: Silicon mechanical coefficient of E and v for main crystallographic directions, T = 300K [Madou 2002, Dziuban 2004]

Crystallographic direction	***E* [GPa]**	**Expression for *E* calculation**	***v* [GPa]**
<100>	129.5	$c_{11}-2\frac{c_{12}}{c_{11}+c_{12}}c_{12}$	79.0
<110>	168.0	$4\frac{\left(c_{11}^{2}+c_{12}c_{11}-2c_{12}^{2}\right)c_{44}}{2c_{44}c_{11}+c_{11}^{2}+c_{12}c_{11}-2c_{12}^{2}}$	61.7
<111>	186.5	$3\frac{c_{44}\left(c_{11}+2c_{12}\right)}{c_{11}+2c_{12}+c_{44}}$	57.5

As it was already mentioned, silicon shows excellent mechanical properties which are completely described by using the tensor formalism accounting for its anisotropy. The general relationship between stress and strain is then expressed by the following formula:

$$\sigma_{ij}=\sum_{k=1}^{3}\sum_{l=1}^{3}c_{ijkl}S_{kl}\ , \tag{A2.1}$$

where c_{ijkl}, S_{kl}, σ_{ij} are second order stiffness tensor, and strain and stress vectors, respectively. The subscripts ij refer to axes. The stress in x-direction is then denoted as σ_{11} and the stress in the xy plane as σ_{12}. In the cubic crystal such as silicon, the <100>, <010> and <001> directions can be considered as coinciding with x, y, and z-axes, what may not be true for different symmetry. For convenience and better understanding, a matrix notation is often used. Therefore, taking into account the symmetry: $S_{12}=S_{21}$, $S_{13}=S_{31}$, $S_{23}=S_{32}$, and using multilinear algebra to reduce the orders of tensors, the Eq.A2.1 could be rewritten as:

$$\begin{bmatrix}\sigma_1\\ \sigma_2\\ \sigma_3\\ \sigma_4\\ \sigma_5\\ \sigma_6\end{bmatrix}=\begin{bmatrix}c_{11} & c_{12} & c_{13} & c_{14} & c_{15} & c_{16}\\ c_{21} & c_{22} & c_{23} & c_{24} & c_{25} & c_{26}\\ c_{31} & c_{32} & c_{33} & c_{34} & c_{35} & c_{36}\\ c_{41} & c_{42} & c_{43} & c_{44} & c_{45} & c_{46}\\ c_{51} & c_{52} & c_{53} & c_{54} & c_{55} & c_{56}\\ c_{61} & c_{62} & c_{63} & c_{64} & c_{65} & c_{66}\end{bmatrix}\begin{bmatrix}S_1\\ S_2\\ S_3\\ S_4\\ S_5\\ S_6\end{bmatrix}. \tag{A2.2}$$

For silicon, the stiffness matrix c is defined by a crystallographic direction and in the <100> crystal axis is:

$$c = \begin{bmatrix} 1.66 & 0.64 & 0.64 & 0 & 0 & 0 \\ 0.64 & 1.66 & 0.64 & 0 & 0 & 0 \\ 0.64 & 0.64 & 1.66 & 0 & 0 & 0 \\ 0 & 0 & 0 & 0.80 & 0 & 0 \\ 0 & 0 & 0 & 0 & 0.80 & 0 \\ 0 & 0 & 0 & 0 & 0 & 0.80 \end{bmatrix}, \tag{A2.3}$$

where all values are in units of 10^{11} Pa. The Eq.A2.2 allows direct calculation the Young's modulus and the Poisson's ratio. The expressions for Young's modulus in three main crystal directions are given in the Table A2.1. However, since such calculations become complicated, mechanical parameters could be also computed numerically by using inverse matrix of c called compliance matrix $s=c^{-1}$. The Young's modulus is then simply to

$$E_{\langle 100 \rangle} = \frac{\sigma_1}{S_1} = \frac{1}{s_{11}}, \tag{A2.4}$$

and Poisson's ratio to

$$\nu_{ij} = -\frac{S_j}{S_i} = -\frac{s_{ij}}{s_{ii}}. \tag{A2.5}$$

Single crystal silicon showing strong anisotropic properties, is considered as an excellent constructional material. Since, it is light (like Aluminium) with a tensile strength *TS* about two times bigger than constructional steel. Hardness *H* of silicon is also much bigger than for steel with value close to quartz. Moreover, silicon is an elastic material without occurring either fatigue effect in its thin films or mechanical hysteresis, very stable in time with technological repeatable of the mechanical and electric parameters. Silicon is also easy to process – could be grinding and polishing. Strength of silicon microstructures increases with improving surface quality obtain during the fabrication process and reducing defects concentration. And, high quality of planar silicon integrated system and silicon microstructures is strictly connected with it [Madou 1997, Madou 2002, Dziuban 2004, Józwik 2004 a].

However, in the contrary to the single crystal silicon, the polycrystalline silicon is manufactured in the deposited films, what causes differences in their mechanical properties, which depends on the deposition conditions, the parameters of deposition process and many others. Although, on the other hand, such dependence creates potential opportunities allowing to design these properties by properly fabrication process controlling. This is a large advantage in comparison to the single crystal silicon having properties strictly connected with the crystallographic directions. In spite of the strength and the hardness much bigger than for steel, the single crystal silicon is brittle and cracks without plastic strain. In the polycrystalline silicon, whereas, it is possible to observe non-elastic strain. The Young's modulus of polysilicon in films could take the value from the range of 120 ÷ 200 GPa [Józwik 2004 a, Memsnet b] in dependent on the technological process parameters, leading to the presence of variable state of internal stress. In micromechanical applications, controlling the stress released during thermal annealing process is a crucial issue. Therefore, in the microstructure fabrication, it is used doped polysilicon reducing silicon resistivity too.

A2.2. Short introduction to MEMS technological process applied during the fabrication of tested devices

The microstructure fabrication could be defined as a combination of manufacturing techniques and knowledge about materials, processes and their applications considering in micro scale. The proper selection of sequence and parameters of technological processes has a crucial significance in the microstructure fabrication. The manufacturing process usually is composed of three basic techniques, namely a photolithography (a), a deposition (b) and an etching (c) [Judy 2001, Józwik 2004 a, Banks 2006]:

a) Photolithography is a process that uses light or optical technique to transfer a two-dimensional pattern from a mask to a structural material.
b) Deposition is a process of films structuring on the wafer surface.
c) Etching is a process of removing useless parts of substrate or deposited films allowing to form three-dimensional shape of microstructure.

A2.2.1. Photolithography

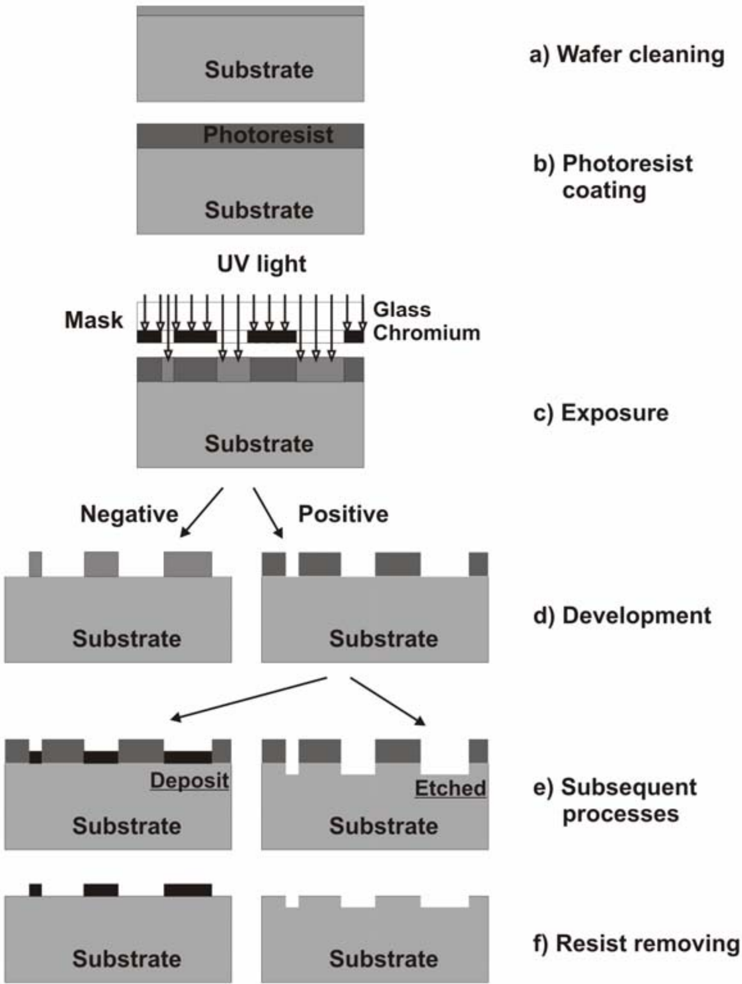

Fig.A2.3: Scheme of photolithography process

In microsystem and microelectronic technologies, the photolithography is a basic and commonly used technique to define shapes of microdevices by forming structured layers on planar substrates. This process is a first step to fabricate most microelements and microelectronics by performing the transfer of a given pattern onto the surface of the wafer for further processes, such as etching or deposition.

Photolithography is based on the selective irradiation of a thin film of photoresist (photosensitive organic materials) deposited on the wafer surface followed by the removal of the exposed (or unexposed) parts of this film. There are distinguished mask and scanning lithographic techniques where the pattern is created through mask imaged by UV or X-rays or directly using laser or electron scanning, respectively. In micromachining applications, mask photolithography with UV-light is commonly used. That is why, the following section will be referred to that type of the process. The main steps of standard UV-lithography are schematically presented in the Fig.A2.3.

To form the pattern, after wafer cleaning the sample is coated by photoresist, then prebaked, exposed, developed and postbaked. It is important to prepare properly the silicon substrate used in the process and masks (usually quartz glass plates with the pattern fabricated in the film of Chrome). The Fig.A2.3a shows Si substrate with deposited thin film (e.g. silicon oxide SiO_2), well prepared. Resist coating is the first step in a photolithographic process (see Fig.A2.3b). It is significant to produce a uniform and adherent film of photosensitive polymer over the entire wafer surface. Resist deposition is usually performed by spin-coating, i.e. dispensing a controlled amount of resist on the wafer surface and spinning the wafer. After coating, a post bake is necessary to evaporate all solvents from the resist. By controlling of whirling time and rotational speed with known, photoresist parameters (given by producer), it is possible to deposit photoresist with required thickness. Next, there is a main step of photolithographic process (see Fig.A2.3c), i.e. exposure used to transfer a pattern from a mask on the wafer surface coated by a photosensitive resist film. The alignment with previous patterns and resolution of the transfer process are the key features of the exposure. It is necessary to ensure perfect alignment of the mask and the wafer. The wafer surface is then exposed by UV light through a mask, generally made of quartz with a patterned chromium layer. The material of the mask depends on the wavelength of the rays used in the projection process. Alignment and exposure can be performed in different ways enumerated below:

- contact printing, where the mask is in direct contact with the wafer;
- proximity printing, where there is a small gap of 10 to 50 μm between the wafer and the mask;
- and by projection printing, where an image of the mask is projected on the wafer surface.

The next step is development process (see Fig.A2.3d) performed by etching techniques. Dependently on the photoresist type (positive or negative one), its exposed or unexposed areas are removed. The development is based on the selective dissolution of the photoresist between UV exposed and unexposed areas, generally performed in alkaline solutions, such as NaOH, KOH, depending on the resist specification. For some special resist, dry development is required. It is either based on a vapour process or a plasma process. Thus, the latent resist image formed during exposure was transferred into a relief image which will serve as a mask for the subsequent process steps, i.e. deposition or etch (see Fig.A2.3e). After these processes there is performed resist stripping as a final step of photolithography used to remove the remaining resist on the wafer surface (see Fig.A2.3f) [Judy 2001, Józwik 2004 a, SSchool 2005, Banks 2006 b].

A2.2.2. Thin film deposition

The deposition techniques are used to deposit a wide variety of materials (see Table A2.2) with thickness from a few tens of nm to several µm on the wafer surface. They can be either selectively deposited (i.e. lift-off) or selectively etched to receive demanded patterns on the substrate.

Table A2.2: Review of materials using in thin film deposition [SSchool 2005]

Metals	Al, Au, Cr, Mb, Pa, Pt, Ta, Ti, Cu
Metal oxides	Aluminium oxide, indium oxide, tin oxide, zinc oxide, tantalum oxide, titanium oxide
Silicon compounds	Silicon dioxide, silicon nitride, polysilicon, silicides
alloys	Nichrome, permalloy, TiNi, Al-Si-Cu, Al-Si

There are developed numerous techniques for thin film deposition. Commonly used in micromachining are as follows [Judy 2001, Zheng 2004, SSchool 2005, Banks 2006 c]:
- Physical vapour deposition (PVD), in which the thin film is created by physical techniques such as the evaporation or sputtering. No chemical reaction is involved.
- Chemical vapour deposition (CVD) and its variations, in which film deposition is obtained through the chemical reaction of selected gases at the wafer surface.
- Thermal oxidation as a particular case of CVD consists in SiO_2 film growing directly at the wafer surface.

The equipment depends on the method used to deposit the thin films, either simple furnaces or high-end plasma reactors can be required.

Evaporation

Evaporation is mostly used to deposit metal films, such as aluminium, gold or silver onto a wafer surface, to realise for example, an interconnection layer or an optical coating. Evaporation illustrating in the Fig.A2.4a consists in the condensation a material in vapour phase on a cold surface. The material to be evaporated is heated up and the vapour particles move towards the wafer surface. Evaporation is a rapid process with deposition rates in the range [1-25Å/s] as a function of the deposit material [Zheng 2004, SSchool 2005, Banks 2006 c, Boeshore 2006].

Sputtering

Sputtering is a widely applied and a very efficient thin film deposition method for a large variety of materials in a fairly uniform and reproducible manner. The resulting layers are a few nanometers to several microns thick with well controlled thickness and material properties. In the reaction chamber illustrating in the Fig.A2.4b, the material to be deposited is bombarded with high energy ions (Ar +) accelerated towards it. Surface atoms are ejected from the target and condense as a film on the wafer surface [Zheng 2004, SSchool 2005, Banks 2006 c]. A sputtering process takes place in a vacuum and is provided by plasma generated inside the chamber. The plasma is usually a noble gas such as argon. The electrical bias dissociates electrons from the gaseous atoms. The electrons drift towards the anode (substrate) while the ions drift towards the cathode (target). This so-called ionic bombardment

causes mentioned ejection of atoms from the target. Some of these atoms condense on the substrate surface, some collide with the plasma and others land on the chamber walls. Sputtering deposition can occur in several typical configurations. Namely, pure direct current DC or radio frequency RF glow discharge, magnetron and reactive sputtering can be used. The RF-coupled power mode increases the ion density while the magnetic field source enhances ion bombardment and minimizes film damage. Reactive sputtering adds addition reactive gas to the main noble plasma gas altering its stoichiometry. To sputter the investigated AlN film by reactive deposition the plasma is composed of an argon and nitrogen mixture in a presence of an aluminium target. Any of mentioned configurations have been the most frequently used techniques to obtain AlN thin films applied in MEMS devices [Boeshore 2006, Vergara 2006]. They allow to deposit these films with different crystal orientation from (002) to (100) and mixed textures (see section 1.5) on the polycrystalline surfaces (usually metal electrodes). Sputtering is also well suited for microsystems due to low process cost, fewer design restrictions than epitaxial methods and fine tuning of the material characteristics. A careful control of its deposition conditions allows to obtain the properties required for MEMS applications, i.e. low residual stress and good piezoelectric behaviours. The combination of all mentioned sputtering modes allows to form the high quality AlN film at fast deposition rates with low temperature (below 200°C) ensuring compatibility with the standard IC technology [Ishihara 1998, Dubois 1999, Dubois 2001, Iborra 2004, Boeshore 2006]. Therefore, according to the dissertation the pulsed reactive DC sputtering method was applied in the fabrication process of the AlN driven cantilevers (see section 3.3).

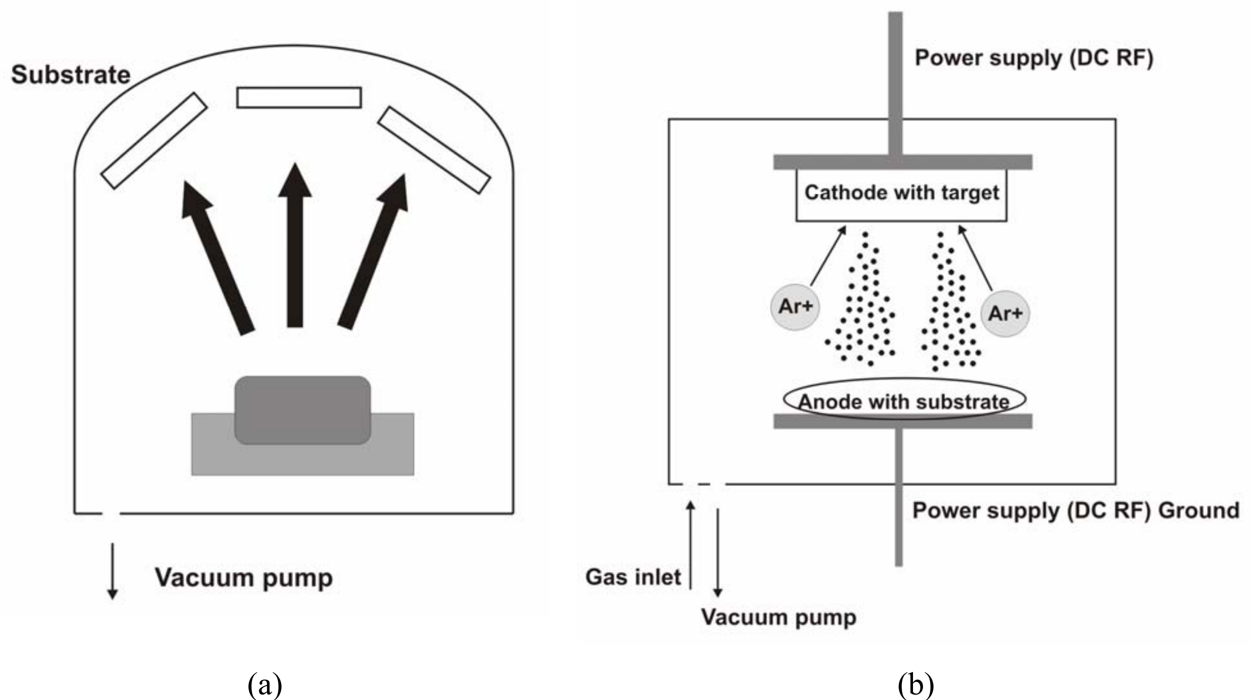

(a) (b)

Fig.A2.4: Scheme of evaporation (a) and sputtering (b) reactors [Zheng 2004]

Chemical Vapour Deposition (CVD)

Chemical Vapour Deposition (CVD) is a method frequently used to deposit thin films of dielectrics (silicon oxide and silicon nitride), semiconductors (single crystal, polycrystal and amorphous silicon films), and also metals (infusible metals) in Si technology. In surface micromachining, CVD deposition is used to create:

- structural layers made of Polycristalline Silicon (Poly-Si) or Silicon Nitride;
- sacrificial layers made of Phosphosilicate Glass (PSG). CVD techniques are also used to form low stress Silicon Dioxide layers.

The wafers are placed and heated in a reaction chamber where a gas flow is maintained. Chemical reactions transform the gaseous molecules into solid material in the form of a new, desired thin film on the wafer surface. Substrate serves a function of mechanical passive carrier and do not participate in a chemical reaction. CVD films may exhibit significant but controllable internal stress as a consequence of fairly elevated deposition temperature.

Several CVD techniques are used:

- Atmospheric pressure CVD (APCVD or just CVD);
- Low pressure CVD (LPCVD);
- Plasma enhanced CVD (PECVD).

Comparison of LPCVD and PECVD processes proceeded in the reactor chambers shown in the Fig.A2.5, are illustrated in the Table A2.3 [Zheng 2004, Gorecki 2005 c, SSchool 2005, Banks 2006 c].

Table A2.3: Comparison of LPCVD and PECVD properties [Gorecki 2005 c]

Process type	**LPCVD**	**PECVD**
Materials	SiO_2, Si_3N_4, SiON P-glass, BP-glass poly-Si	Si, SiO_2, SiON
Temperature / pressure	550-900°C / below 130 Pa	300-400°C / below 650 Pa
Applications	ore of waveguides, insulation, metallic gates, doped and undoped thin films, actuators, structural layers	core/buffer/coat of waveguides, insulation, passivation (nitride)
Advantages	high purity and high uniformity films, high reproducibility, uniform coverage step, low optical loss	high uniformity films, moderate reproducibility, good coverage step, low optical loss, low temperature, good adhesion, low mechanical stress, high deposition rate
Disadvantages	high temperature, low deposition rate, high mechanical stress	moderate film purity (hydrogen content), moderate reproducibility

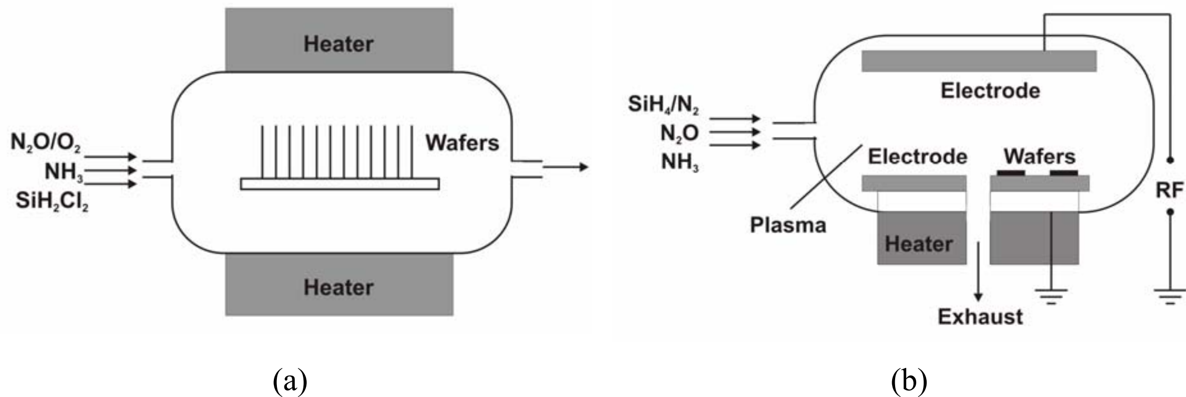

(a) (b)

Fig.A2.5: Scheme of LPCVD (a) and PECVD (b) reactors [Gorecki 2005 c]

The basic kinetic model of deposition process takes into consideration two processes setting up in series:

- transport of reacting substances to the wafer surface; it is proceeded through the area, where due to reaction on the substrate surface, reacting substances decrease and reaction products appear, simultaneously;
- chemical reaction proceeded on the substrate surface.

Their setting-up in series causes that the deposition rate is controlled and determinate by the slower one. In general, in the case of low temperature process, deposition rate is controlled by surface reaction rate, and of high temperature – by reacting substances transport [Beck 1991, Józwik 2004 a, Boeshore 2006].

Oxidation

The oxidation technique gives silicon dioxide layer (SiO_2) with a stable and tenacious film material, commonly used for a variety of applications [SSchool 2005], such as:

- mask for etching processes or diffusion to introduce dopants to the silicon;
- isolation layer;
- buried layer as etch stop;
- sacrificial layer in surface micromachining, defined as a thin film that is later removed to release a microstructure from its substrate.

The oxidation of silicon is enhanced using elevated temperature (above 1000ºC). Two thermal oxidation processes are commonly used:

- dry oxidation uses O_2 as oxidising agent:

$$Si + O_2 \rightarrow SiO_2; \tag{A2.6}$$

- wet oxidation uses H_2O (steam):

$$Si + H_2O \rightarrow SiO_2 + 2H_2. \tag{A2.7}$$

The oxidation process proceeds at the atmospheric pressure, and growing rate decreases with time. The film thickness does not exceed several 100 nm for dry oxidation and 1 to 2 µm for wet one. Thermally grown oxide layers are very high quality but show high compressive stress [Gorecki 2005 c, SSchool 2005, Banks 2006 c].

A2.2.3. Etching

Generally, this process could be divided into the wet and dry etchings. The dry process is proceeded in a bath solution (acid and liquor), where the wafer parts not covered by the photoresist are removed. The dry etching is performed due to the ion beam or plasma techniques, using chemical and physical mechanisms. Both of these etching techniques allow to etch metals, conductors, dielectrics and also photoresists [SSchool 2005, Banks 2006 c].
The etching process is characterised by two main parameters. First one is etch selectivity defined as a ratio of etch rate of different materials in the same process, e.g. $V_{Si} : V_{Al}$ = 100:1. Etching of low selectivity is important in the case of planarisation of substrates and microelectronic devices. Etching of high selectivity is applied in photolithography and in 3D micromechanical structures fabrication processes, where both etched material and mask have to have high selectivity. High selectivity is typical for wet – etching process. For instance, selectivity of silicon etching and silicon dioxide in KOH solution at 80°C is 250:1. For dry-etching, selectivity is usually less, because this process consists not only in chemical etch mechanism but also in physical one. Therefore, because of different selectivity of materials, it is crucial issue to select an appropriate material for mask taking into account its resistance on used chemical processes or dry – etching parameters, i.e. pressure of working gas, power supply, substrate temperature. The second important etch parameter is directivity, defined through so-called anisotropic coefficient, expressed by following formula:

$$A = 1 - V_S/V_P \,, \tag{A2.8}$$

where V_S and V_P are etch rates in tangent and perpendicular direction to etched surface, respectively. The etching could be then isotropic or anisotropic. In the case of anisotropic etching $V_S = 0$ i $A = 1$, however for isotropic etching $V_P > V_S > 0$ i $A < 1$.
The wet etching in acid and liquor solutions is mostly highly isotropic process. The exception is single crystal materials, like silicon, which particular crystallographic planes have different etch rates ($V_{<100>} : V_{<111>}$ = 100:1) allowing to obtain highly anisotropy structure. Whereas, dry etching process can be either isotropic or anisotropic. More detailed description of etching process will be presented in the following section [Józwik 2004 a, Banks 2006 c].

Isotropic wet etching

During isotropic etching, material is etched with similar etch rates in all directions. Metals, semiconductors and glass materials can be structured by this process. The isotropic wet etching is then widely used to etch oxides, nitrides, aluminium, polysilicon and silicon serving as masking layers and also to remove the sacrificial layer in surface micromachining. The etching process is controlled by the diffusion and convection processes. Typical processes are:

- etching of SiO_2 and PSG (phosphorous-doped oxide) in hydrofluoric (HF) solutions;
- etching of monocrystalline silicon in a water solution of HF and nitric acid solution (HNO_3).

As a masking material in this process gold, chromium or silicon nitride (Si_3N_4) can be used [SSchool 2005]. The shape profile after isotropic etching is presented in the Fig.A2.6.

Fig.A2.6: Shape obtained after isotropic etching
[Petersen 1982, Madou 2002, Józwik 2004 a]

Anisotropic wet etching

Anisotropic etching leads to remove Si substrate with etch rates highly dependent on crystallographic directions of the material. As a result, cavities are shaped along particular crystallographic planes. It allows to better control the shape of etched elements. Usual etching solutions are KOH (potassium hydroxide), EDP (ethylendiamine pyrotechol) or TMAH (tetramethyl ammonium hydroxide). Whereas, silicon dioxide (SiO_2) and nitride (Si_3N_4) are classical mask materials used as protection layer during the patterning. The cross section of membrane fabricated by Si wafer etching in KOH through (100) crystallographic plane is shown in the Fig.A2.7. This technique was applied to manufacture membranes used for fabrication cantilevers investigated in this Ph.D. thesis [SSchool 2005, Banks 2006 c].

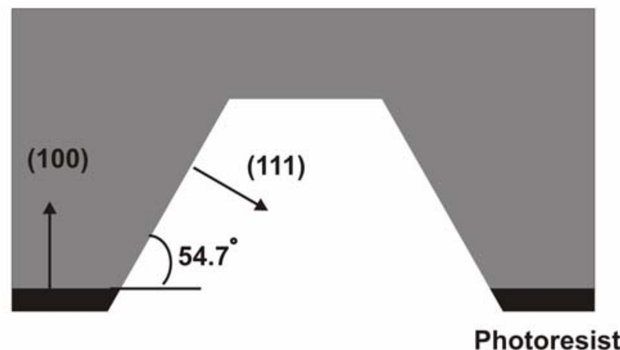

Fig.A2.7: Cross section of silicon membrane across (100) plane
[Petersen 1982, Madou 2002, Józwik 2004 a]

Dry etching

In many technologies, it is a need to obtain vertical walls. These structures form holes, grooves, trench, and precisely done lines of small width, which are applied in MEMS/MOEMS devices and microelectronics. The dry etching is just used to fabricate microstructures with such vertical sidewalls, independently on the crystallographic structure. The aspect ratio up to 50:1 can be achieved. It is define as a ratio of the depth to the width of an etched hole or trench. Other typical applications of dry etching are resist stripping or wafer cleaning in a O_2 based plasma [SSchool 2005]. Using dry etching optimisation process many of the potential problems connected with wet etching could be omitted, what however makes vacuous device etching process itself more complicated. Plasma etching gives for example the following advantages [Józwik 2004 a]:

- dimensions of etched patterns could be smaller than 10 nm (FIBE – Focus Ion Beam Etching). The result depends on used mask;
- profiles of formed structures do not depend on the substrate crystallographic structure;

- etching profile can be chosen according to a device design;
- selective removing of so-called sacrificial layer is possible;
- plasma does not exert any pressure on 3D microstructures causing their bending and/or adhering.

A flux of chemically reactive and ionised gas (plasma) is directed towards the wafer surface in a reactor with plasma environment which provides the activating energy for the etching reaction. Dry etching uses effects proceeded in plasma or interaction of ion beam with etched material. The main mechanisms of dry etching process are then chemical and physical ones. Chemical mechanism consists in reaction of free radicals and etching material, giving gaseous reaction products. For instance, during etching of silicon in plasma of CF_4, gaseous carbon tetrafluoride dissociates according to reaction:

$$CF_4 + e \rightarrow CF_3^* + F^* + e. \quad (A2.9)$$

And free fluoric radical reacts with silicon giving gaseous silicon tetrafluoride:

$$Si + 4F^* \rightarrow SiF_4 \uparrow. \quad (A2.10)$$

Physical mechanism consists in knocking out atoms or molecules of etching material by high energetic ions.

Dependently on the applied mechanism, there are distinguished following commonly used techniques:

- Plasma Etching (PE);
- Reactive ion Etching (RIE);
- Deep RIE (DRIE).

They differ in obtained etch profile shown in the Fig.A2.8 for PE technique (see Fig.A2.11a) and RIE one (see Fig.A2.11b).

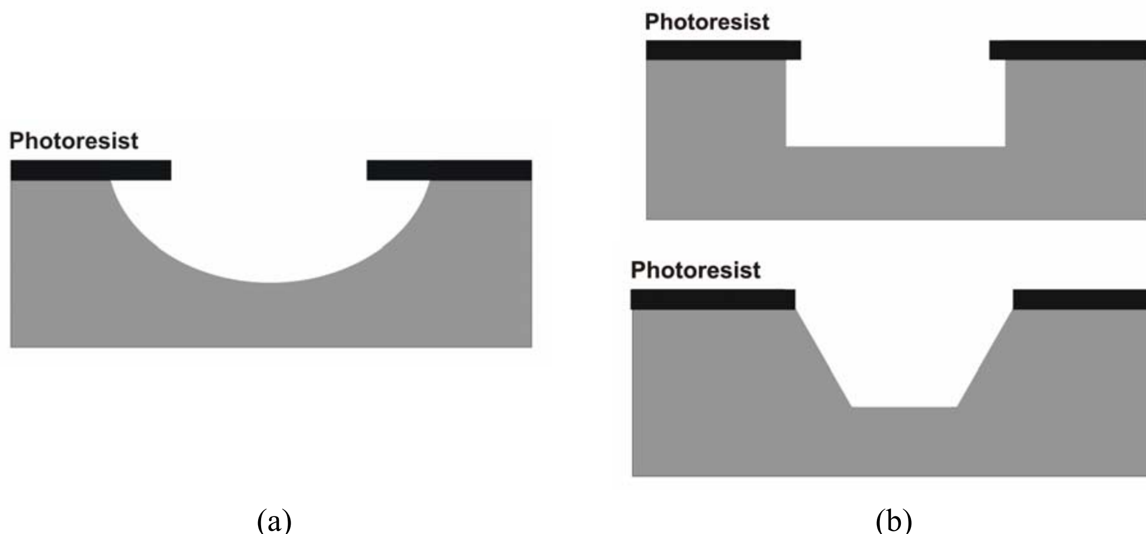

(a) (b)

Fig.A2.8: Typical etch profiles obtained after PE (a) and RIE (b) etching [Petersen 1982, Józwik 2004 a]

In Plasma Etching (PE), chemical mechanism prevails during the process, while in RIE case physical mechanism has a big influence, making the last process more anisotropic and less selective. That is why PE process gives isotropic profiles, high etch rates and high selectivity. Whereas, RIE technique allows to obtain compromise between rate and anisotropy. It is possible to obtain highly anisotropic, isotropic or directional etching of pattern in Si substrate by modification of working gas composition, proper selection of process parameters and mask material.

Almost any material can be dry-etched by choosing the appropriate combination of plasma chemistry and ion bombardment energy. Silicon is for instance usually etched in fluorine or

chlorine plasma based chemistry, using photoresist, silicon dioxide, silicon nitride and metals for masks [Józwik 2004 a, SSchool 2005].

Deep reactive ion etching (DRIE)

Deep reactive ion etching (DRIE) belongs to dry etching techniques. It is used to etch deeply in the silicon wafer while leaving vertical sidewalls and is independent on the crystallographic orientation. This unique capability is very useful and demanded for MEMS manufacturing. This process allows to etch small structures (> 2 μm) with high aspect ratio (> 15) and very good anisotropy (> 99%). The example of the microelement fabricated by this technique is presented in the Fig.A2.9 [Thielicke 2000, Judy 2001].

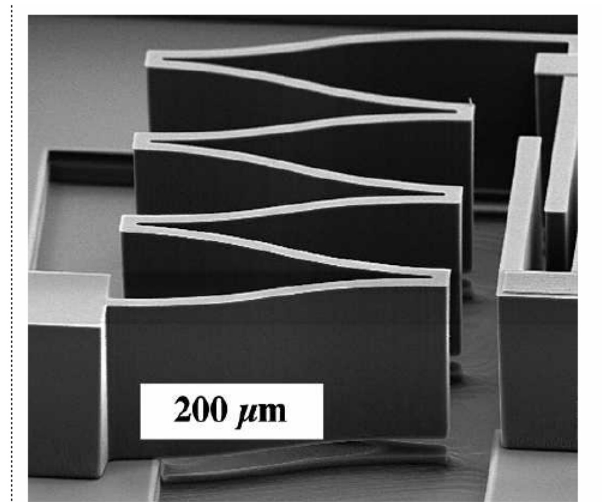

Fig.A2.9: Microflexure created by DRIE [Judy 2001]

A2.2.4. Complementary techniques

In microstructure technology, there are a lot of other complementary techniques, allowing to obtain final devices. Here, there will be presented a few of them applied to manufacture objects tested in these work.

Wafer cleaning

Wafer cleaning is carried out before any process to avoid cross contamination through the equipment and for process reproducibility. The purpose is to remove any trace of organic, ionic or heavy metal contaminations from the wafer surface. A standard method for wafer cleaning, know as RCA, consists of three major wet chemical steps used sequentially [SSchool 2005]:

- removal of insoluble organic contaminations in a oxidizing solution (5:1:1 H_2O:H_2O_2:NH_4OH at 75 ÷ 80ºC during 10 ÷ 15 min.);
- removal of native oxide formed during the previous treatment in a HF solution;
- removal of ionic and heavy metal contaminations in a HCL solution (6:1:1 H_2O:H_2O_2:HCl at 75-80ºC during 10 ÷ 15 min.).

Dicing

Dicing is used to cut finished wafer into individual chips. It usually consists on sawing the wafer with a diamond sawblade that rotates at several thousand rpm. The feed rate is of the order of 1 cm/s, and the kerf width ranges from 50 to 200 μm [SSchool 2005].

Appendix 3

Analytical description of implemented metrological methods

Here, the methods of optical metrology and the fringe pattern analysis algorithms implemented in the selected interferometric platform (see section 2.3) will be discussed. In particular, the two-beam interferometry with the use of time-average and stroboscopic methods and the application of 5-frame Temporal Phase Shift Algorithm (TPS) will be presented. Since, these techniques are well known [Servin 2001, Patorski 2005 b, Bosseboeuf 2007], they will be only shortly presented here.

Concerning the configuration of Twyman-Green interferometer (TGI) the following assumption are given:

- used radiation is quasi-monochromatic noticed by mean wavelength value (λ);
- interfering beams are linearly polarised;
- influence of coherence of light source is negligible – this means that we have full mutual temporal and spatial coherence of interfering beams;
- influence of depth of field of optical system, which images an object surface on CCD matrix on interference pattern is negligible;
- direction of beam illuminating an object and direction of observation (of interferogram registration) are in-line with a normal to the surface of tested element in entire field of view (sensitivity vector is constant);
- imaging system is aberration-free.

These assumptions are fully justified taking into account design and operation principle of the used interferometric system [Patorski 2005 b].

A3.1. Classical interferometry

The intensity distribution of interferogram obtained for in-time static object can be described as:

$$I_{stat}(x,y) = I_0(x,y)\{1 + K(x,y)\cos\Delta\varphi_{stat}(x,y)\}, \tag{A3.1}$$

where

$$K(x,y) = \frac{2\sqrt{I_A(x,y)I_B(x,y)}}{I_A(x,y)+I_B(x,y)} \tag{A3.2}$$

and $$\Delta\varphi_{stat}(x,y) = \frac{2\pi}{\lambda}OPD(x,y), \tag{A3.3}$$

in which $I_0(x,y)$ is a background intensity in the interferogram (a sum of two interfering beams intensities I_A, I_B), $K(x,y)$ is a modulation depth (contrast) of the interference fringes, $\Delta\varphi_{stat}(x,y)$ is a phase difference between the interfering beams, $OPD(x,y)$ represents

the optical path difference between the interferometer arms, $k = \frac{\lambda}{2\pi}$ is a proportionality factor known as a wave number, λ is a light wavelength, and (x, y) are Cartesian coordinates.
The $\Delta\varphi_{stat}(x, y)$ distribution includes information about difference in wave-fronts between the object and reference beams. It then gives information about the shape of the tested object $\Delta w\left(\frac{x}{\beta}, \frac{y}{\beta}\right)$ (assuming in our case the plane shape of reference wavefront) as well.
In order to determine this parameter, the obtained phase map $\Delta\varphi_{stat}(x, y)$ has to be scaled to the units in length according to the equation.

$$\Delta w\left(\frac{x}{\beta}, \frac{y}{\beta}\right) = \frac{\lambda}{4\pi}\Delta\varphi_{stat}(x, y), \tag{A3.4}$$

in which Δw is a difference between the object shape and the reference wavefront shape, and β is a transverse magnification of used microscope. Sensitivity factor of this measurement method ($\frac{4\pi}{\lambda}$) is then doubled because TGI works in reflection.
Two-beam classical interferometry is used to perform static measurements determining the shape and out-of-plane displacement obtained by static initial shape subtraction.

A3.2. Time-average interferometry

Time-average interferometry is applied when the measured object vibrates and is illuminated by a continuous light, and then the resulting intensity distribution of the interferogram is averaged in time.
Height map of object excited to sinusoidal vibration can be described by the equation:

$$w\left(\frac{x}{\beta}, \frac{y}{\beta}\right) = w_{stat}\left(\frac{x}{\beta}, \frac{y}{\beta}\right) + a_0\left(\frac{x}{\beta}, \frac{y}{\beta}\right)\sin\left[\omega t + \varphi_0\left(\frac{x}{\beta}, \frac{y}{\beta}\right)\right], \tag{A3.5}$$

where w_{stat} is an object static shape, a_0 is a maximal vibration amplitude, ω - an angular frequency of vibration, t - a time coordinate, φ_0 - an initial vibration phase and β is a transversal microscope magnification.
Intensity distribution of the registered interferogram during the use of plane reference mirror, can be given by [Bosseboeuf 2007] (for simplicity coordinates were omitted):

$$\begin{aligned} I(x, y, t) = I_O[1 + K\cos\left(\frac{4\pi}{\lambda}h_{stat}\right)J_0\left(\frac{4\pi}{\lambda}a_0\right) \\ + 2K\cos\left(\frac{4\pi}{\lambda}h_{stat}\right)\sum_{n=1}^{\infty}J_{2n}\left(\frac{4\pi}{\lambda}a_0\right)\cos(2n(\omega t + \varphi_0)) \\ - 2K\sin\left(\frac{4\pi}{\lambda}h_{stat}\right)\sum_{n=0}^{\infty}J_{2n+1}\left(\frac{4\pi}{\lambda}a_0\right)\sin((2n+1)(\omega t + \varphi_0))] \end{aligned}, \tag{A3.6}$$

in which J_n is a n-order first type Bessel function.

Assuming sinusoidal vibrations and much longer than vibration period single registration time (averaging time), the intensity distribution of interference fringes registered by a camera is given by [Petitgrand 2001]:

$$I_{aver}(x,y) = I_0(x,y)\left\{1 + K(x,y)J_0\left(\frac{4\pi}{\lambda}a_0(x,y)\right)\cos[\Delta\varphi_{aver}(x,y)]\right\}, \qquad \text{(A3.7)}$$

where $\Delta\varphi_{aver}(x,y)$ is a phase difference between interfering beams during vibrated object passing of a state of equilibrium (usually equivalent to the state of unloaded object). The interference fringe contrast is then modulated by the Bessel function. The number of Bessel fringes increases with the increase of vibration amplitude. Determination of the Bessel function [Sałbut 2003] allows to estimate the tested object vibration amplitude and define the number of resonance vibration modes. The advantage of time-average interferometry is to permit the visual monitoring of the Bessel fringes with dynamic tracking of the resonance frequencies. The observed interferograms give information about shape differences between the tested object and the reference surface, not being directly proportional to the Bessel function [Petigrand 2001]. To enhance the visibility of the obtained Bessel fringes, the simple, 4-frame phase shifting can be applied – so we can speak about the enhanced time-average interferometry technique. It consists in the registration of the four interferograms of vibration object phase shifted by $\pi/2$ and then the realisation of phase calculation. The resulting intensity distribution is described by [Salbut 2003, Patorski 2004] (for simplicity coordinates were omitted):

$$I_{enhanced} = |I_1 - I_3| + |I_2 + I_4| = 2I_0KJ_0\left(\frac{4\pi}{\lambda}a_0\right)\{\sin\Delta\varphi_{aver} + \cos\Delta\varphi_{aver}\}, \qquad \text{(A3.8)}$$

in which $I_1 \div I_4$ are intensity distributions in the consecutive interferograms.
The time-average interferometry is then usually applied to the determination of resonance frequencies, the visualisation of vibration modes shape or the estimation of vibration amplitude.

A3.3. Stroboscopic interferometry

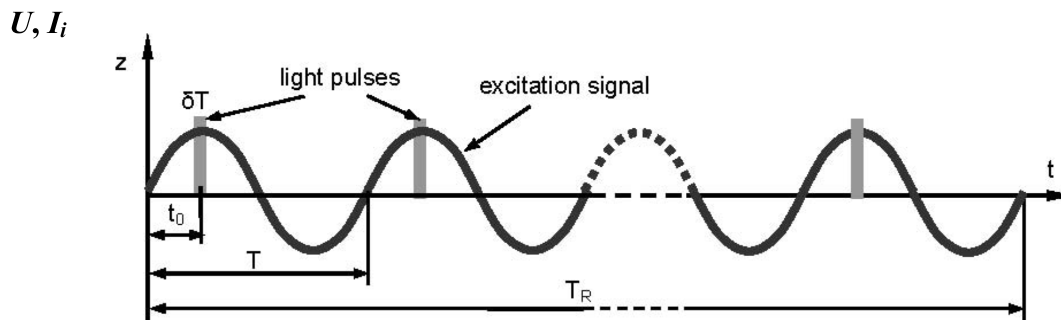

Fig.A3.1: Principle of stroboscopic technique. Denotation: δT – time of pulse light duration, t_0 - time delay of light pulses in relation to excitation signal, T – cycle of excitation signal, T_R – registration time, U – voltage, I_i – light pulses intensity, t – time coordinate

When the system is operating in stroboscopic mode, the diode laser is driven with a duty cycle pulse-train synchronized with a sinosoidal excitation signal of vibrating MEMS (see Fig.A3.1) in order to stroboscopically "freeze" its motion. By changing time delay t_0 of light pulse in relation to the excitation signal, it is possible to perform the accurate measurement of object transient shape in any time of the vibration cycle T.
In the stroboscopic interferometry the registered interferogram intensity distribution obtained by the Eq.A3.6 can be described as [Petigrand 2001 a, Bosseboeuf 2007]:

$$I_{strob}(x,y) = N \int_{t_0-\delta T/2}^{t_0+\delta T/2} I(x,y,t)dt\,, \tag{A3.9}$$

in which N is an integer part of T_R/T and T_R much longer than T is assumed. For small vibration amplitude and short light pulses, intensity distribution similar to the static case will be obtained using approximation $\sin(n\omega\delta T/2)/(n\omega\delta T/2) \approx 1$:

$$I_{strob}(x,y) = N\delta T I_0(x,y)\left\{1 + K(x,y)\cos\left(\frac{4\pi}{\lambda}h_{stat} + \frac{4\pi}{\lambda}a_0 \sin(\omega t_0 + \varphi_0)\right)\right\}. \tag{A3.10}$$

The analysis of this resulting interferogram is performed with the same technique like in the static case. It allows to determine transient shape or indirectly out-of-plane displacement in the selected time of vibration cycle. The out-of-plane displacement is generally a result of two measurements differences (static and dynamic states). For measuring the vibration amplitude, it is necessary to find t_0 for which tested object has the maximal deflection.
When duration of light pulse is less than $1/20T$ and maximum vibration amplitude less than 5λ, the deformation measurement error becomes smaller than 5%.

The stroboscopic interferometry performs the dynamic measurements of objects excited by sinusoidal signal including the determination of the transient shapes, the out-of-plane displacement and the amplitude and phase distribution in vibration modes.

A3.4. Fringe Pattern Analysis Algorithms (FPAA)

During the acquisition of the interferometric data, an information is coded as the following sinusoidal intensity distribution:

$$I(x,y) = a(x,y) + b(x,y)\cos\varphi(x,y), \tag{A3.11}$$

in which $a(x,y)$ is a background function, $b(x,y)$ is a modulation function and $\varphi(x,y)$ is an unknown phase distribution. The Fringe Pattern Analysis (FPA) consists in retrieving phase function from the registered interferogram (or series of interferograms), its scaling, and then determining measured quantities. There are several types of algorithms to process the fringe pattern [Kujawińska 2005 a]. The phase algorithms have advantages over intensity-based techniques. The phase algorithms are less complicated, more accurate and consist in processing of phase-shifted interferograms. In particular, the Time Phase Shifting (TPS) algorithm [Servin 2001, Kujawińska 2005 a] demonstrates the high accuracy of phase determination (up to 2π/100). The TPS algorithms ensure the high spatial resolution of calculated phase map, as well. Each pixel of the acquired interferogram is analysed separately, making these techniques less sensitive on local fluctuations of background or variation of modulation function. However, the sample needs to be stable during the acquisition time of series of interferograms. Although, the measurement of vibrating objects is also possible by applying the stroboscopic technique. The proposed interferometric

platform besides the TPS method implements also the Fast Fourier Transform (FFT) algorithm and Spatial Carrier Phase Shift (SCPS) algorithm to process the received interferograms. However, neither the FFT or the SCPS were not exploited in our work. The FFT provides disadvantages, which occurred during the realisation of this algorithm [Kujawińska 2005 a, Kacperski 2008]. Most of the problems concern the difficulty of FFT automation causing necessity of manually filtrate Fourier spectrum. Since, phase analysing is a global operation, noncareful filtration causes wrong phase determination in many parts of the interferogram. Some information about large phase gradient can easily be lost or phase can be modified by background function or higher order signal components. Moreover, the FFT requires a continuity of the analysed function. Interferogram discontinuity (resulted e.g. from a masking process, see Fig.2.4, section 2.3.3) and sharp frequency-domain filter cause significant leakage of energy between pixels in spatial frequency domain, and consequently errors appearing near discontinuities in the calculated phase. The the SCPS algorithm offers easy automation and is relatively not computationally complicated. However, its disadvantages are a relatively low accuracy and a need of introduction of spatial carrier fringes, what together with the highly deflected cantilever samples provide interferograms too dense to be analised properly.

Time Phase Shift (TPS) algorithm

In general, the Time Phase Shift methods [Servin 2001, Kujawińska 2005 a] require registration of at least three interferograms with (usually) constant phase shift acquired in different discrete time intervals. Consecutive interferograms can be described by general equation:

$$I_i(x,y) = a(x,y) + b(x,y)\cos[\varphi(x,y) + i\Delta\alpha], \tag{A3.12}$$

in which $\Delta\alpha$ is a phase step between following interferograms, $i \geq 3$.
This method consists in matching the cosine function to the intensity value $I_i(x,y)$ (see Eq.A3.12) corresponding to the adequate phase shift $i\Delta\alpha$, where consecutive intensities are obtained in following discrete time intervals.
Among a lot of existing algorithms of the TPS method differing in number of required interferograms, for the experimental part of the Ph.D. thesis the *5-image algorithm* [Servin 2001, Kujawińska 2005 a] was applied. This algorithm is the most often used in the interferometric measurement systems. It is less sensitive on some measurement errors, i.e. the harmonic and linear phase shift errors. Its resistance on many kinds of errors ensures high accuracy of the performed measurement.
This algorithm also known as Hariharan's algorithm consists in registration of 5 interferograms with $\Delta\alpha = 2/\pi$ giving total phase shift of 2π. Demanded phase distribution is then calculated from the following equation:

$$\varphi(x,y) = \arctan\left[\frac{2(I_2 - I_4)}{(2I_3 - I_1 - I_5)}\right]. \tag{A3.13}$$

Due to periodical (with cosine function) intensity distribution in term of phase $\cos\varphi = \cos(\varphi + 2k\pi)$, the Eq.A3.11 (in our case given by the Eq.A3.13) gives the phase distribution modulo 2π with a value range from –π to +π. These data needs to be unwrapped to obtain continuous phase function. Then, the phase is scaled to the measured quantities according to the Eq.A3.4 restoring the 3D shape of sample. There are a lot of algorithms for performing unwrapping process. In the framework of this research, the Minimum Spanning Tree algorithm [Sevrin 2001, Kujawińska 2005 a] was used.

Appendix 4

Theoretical relations for homogeneous Si cantilever

Theoretical relations for the homogeneous Si cantilever with constant cross-section are presented. The considered cantilever is a rigidly single clamped structure. It is oriented along the *z*–axis as presented in the Fig.A4.1. *X*–axis is related to a width and *y*–axis to a thickness of the cantilever. The element deformations in the range of its linear elasticity are acceptable. According to the plane section hypothesis (Bernoulli hypothesis) the cantilever cross-section, plane and perpendicular to the cantilever center line before deformation still remains plane and perpendicular to the bended cantilever center line after deformation [Jakubowicz 1984].

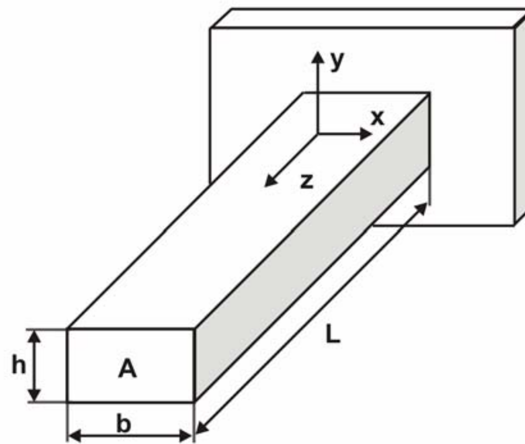

Fig.A4.1: Cantilever model: geometry and clamping conditions

To model the stress distribution corresponded to the experimentally obtained object initial deflection the two approaches are analysed. Namely, the bending cantilever generated by the concentrated force and the pure bending schematically presented in the Figs.A4.2a and b are considered.

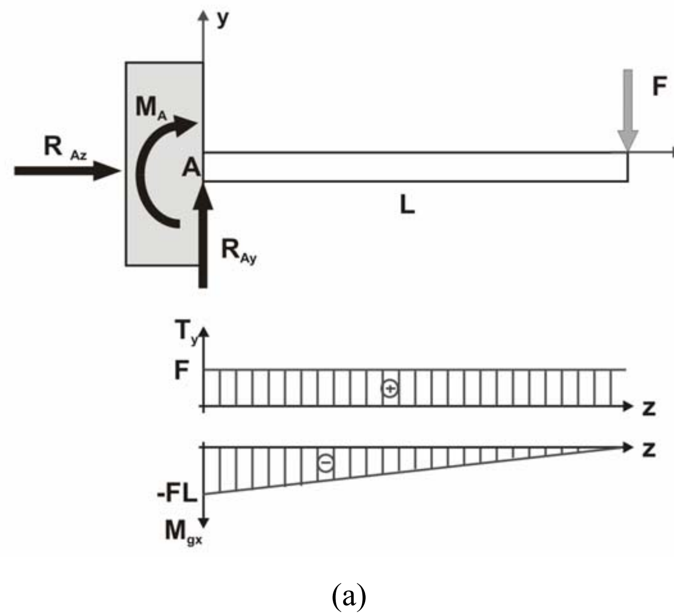

(a)

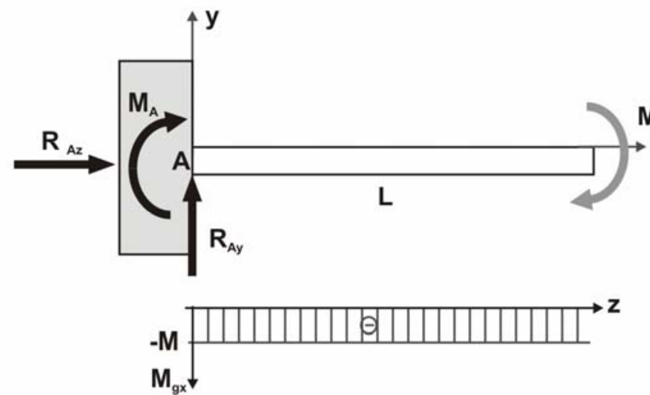

(b)

Fig.A4.2: Scheme of cantilever loaded by concentrated force applied to its free end (a) and constant moment (b) including constraint reactions

Considering the case of cantilever loaded by a concentrated force, the conditions of equilibrium can be written as follows regarding to the sign convention:

$$\begin{cases} \Sigma F_z: \quad R_{Az} = 0; & \text{(A4.1a)} \\ \Sigma F_y: \quad R_{Ay} - F = 0; & \text{(A4.1b)} \\ \Sigma M_{x(A)}: \quad M_A + FL = 0. & \text{(A4.1c)} \end{cases}$$

Thus, internal shearing (transverse) force T_y as an algebraic sum of external component forces perpendicular to cantilever center line and acting in the *xy* section plane has a constant value of F (see Fig.A4.2a and Eq.A4.2a). While, bending moment M_{gx} as a sum of external load moments is expressed by the Eq.A4.2b (see Fig.A4.2b).

$$\begin{cases} T_y = F; & \text{(A4.2a)} \\ M_{gx}\,(z) = Fz - FL\,. & \text{(A4.2b)} \end{cases}$$

Moreover, assuming the pure bending (i.e. generation of only bending moment constant thought the object length (see Fig.A4.2b) and the plane section hypothesis neutral layer for which stress is equal to zero can be found in the bending cantilever. This layer is perpendicular to the bending moment plane and located in the middle of the homogeneous cantilever structure. During bending process one part of the object (i.e. above neutral plane) lengthens, while the other one (i.e. below neutral plane) narrows. The bending cantilever acts thus in uniaxial state of strains and stresses take symmetrical linear distribution (see Fig.A4.3) [Jakubowicz 1984, Brissaud 2003].

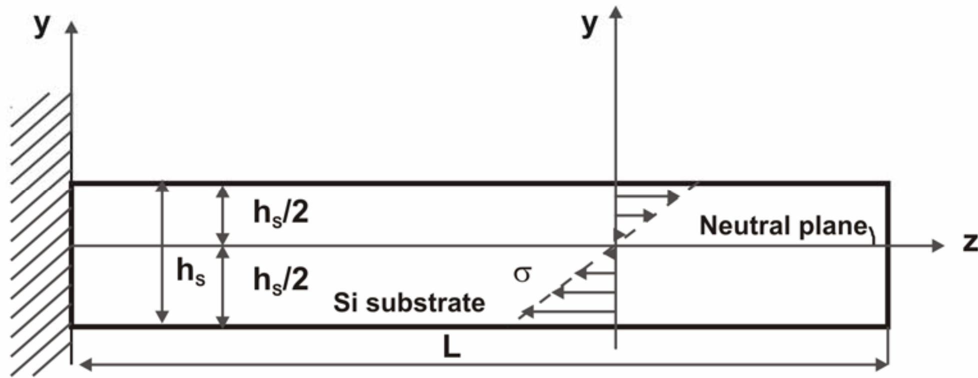

Fig.A4.3: Stress distribution in cross-section of homogeneous bending cantilever

Normal stresses in the film distanced of y from the neutral layer are as follows:

$$\sigma = \frac{M_{gx}}{I_x} y, \tag{A4.3}$$

where, M_{gx} and I_x are a bending moment and a moment of inertia according to x-axis. For the rectangular section of the considered cantilever I_x is expressed by the following equation:

$$I_x = \int_A y^2 dA = \frac{bh^3}{12}, \tag{A4.4}$$

where A, b and h are an area, a width and a thickness of the analysed cantilever [Jakubowicz 1984].

The bending displacement and the resonance frequency are also modelled. Thus, assuming lack of damping, the differential equation of motion for the cantilever bending displacement (Newton's law) is given by [Tong 1960, Brissaud 2003]:

$$EI_x \frac{\partial^4 w}{\partial z^4} + \rho A \frac{\partial^2 w}{\partial t^2} = 0, \tag{A4.5}$$

where w is a deflection in the y–axis direction vs. z–axis length, E – a Young modulus of a cantilever material, ρ is a density, A – cantilever area, t – time.
A solution of above equation (see Eq.A4.5) in harmonic form is as follows:

$$w(z,t) = W(z)e^{j\omega t} \tag{A4.6}$$

It represents a cantilever bending displacement along y–axis. However, inserting the Eq.A4.6 into the Eq.A4.5 we obtain:

$$\frac{\partial^4 W}{\partial z^4} - k^4 W = 0, \tag{A4.7}$$

where k is a flexural wave number given by:

$$k^4 = \omega^2 \frac{\rho A}{EI_x}. \tag{A4.8}$$

Hence, the general solutions of the Eq.A4.7 are [Tong 1960, Brissaud 2003]:

$$W(z) = A\cosh(kz) + B\sinh(kz) + A'\cos(kz) + B'\sin(kz). \tag{A4.9}$$

For determining the constants A, B, A' and B' the following cantilever boundary conditions the Eqs.A4.10a, b and A4.11a, b will be applied. At the clamped end located at $z = 0$ the displacement and its first derivative are equal zero:

$$W(0) = 0; \tag{A4.10a}$$

$$\frac{dW(0)}{dz} = 0, \tag{A4.10b}$$

While, at the free end (z = L) the moment and the transverse shearing stress are equal zero:

$$M(L) = 0; \tag{A4.11a}$$

$$\frac{\partial^3 W(L)}{\partial^3 z} = 0. \tag{A4.11b}$$

Applying the Eqs.A4.10 and A4.11 to the Eq.A4.9, we have:

$$\begin{aligned} &B(\sin(kL) + \sinh(kL)) + A(\cos(kL) + \cosh(kL)) = 0 \\ &B(\cos(kL) + \cosh(kL)) + A(\sinh(kL) - \sin(kL)) = 0 \end{aligned}. \tag{A4.12}$$

For, nontrivial solutions the determinant formed by the coefficients of A and B must vanish.

Hence,

$$\begin{vmatrix} \sin(kL) + \sinh(kL) & \cos(kL) + \cosh(kL) \\ \cos(kL) + \cosh(kL) & \sinh(kL) - \sin(kL) \end{vmatrix} \tag{A4.13a}$$

or

$$1 + \cosh(kL)\cos(kL) = 0. \tag{A4.13b}$$

The roots of this *characteristic* or *frequency* equation (see Eq.A4.13) allow to identify series of first six vibration bending modes:

$$k_n L = p_l \approx 1.8751,\ 4.6941,\ 7.8548,\ 10.9955,\ 14.1372,\ 17.2788. \tag{A4.14}$$

Inserting the Eq.A4.8 into the Eq.A4.14 the resonance frequencies can be determined. Thus, the first resonance frequency is derived from the equation [Tong 1960, Brissaud 2003]:

$$f_{res1} = \frac{p_1^2}{4\pi\sqrt{3}} \frac{h}{L^2} \sqrt{\frac{E}{\rho}}. \qquad \text{(A4.15)}$$

Tortional modes were not be considered in our work because of their considerably low amplitudes and, moreover, lower usability.